Experimental and Numerical Investigation of the Absorption Process in Polygeneration

Vom Fachbereich Maschinenbau

der Technischen Universität Darmstadt

zur Erlangung des akademischen Grades

Doktor–Ingenieur (Dr.-Ing.)

genehmigte

DISSERTATION

von

M.Sc. Adel Jomaa Almoslh

aus Qunaitra (Syrien)

Berichterstatter: Prof. Dr.-Ing. Bernd Epple

Mitberichterstatter: Prof. Dr. rer. nat. habil. Amsini Sadiki

Priv.-Doz. Dr.-Ing. habil. Falah Alobaid

Tag der Einreichung: 19.08.2022

Tag der mündlichen Prüfung: 06.12.2022

Darmstadt 2022

D17

Experimental and Numerical Investigation of the Absorption Process in Polygeneration

Genehmigte Dissertation von M.Sc. Adel Jomaa Almoslh

Tag der mündlichen Prüfung: 06.12.2022

Darmstadt, Technische Universität Darmstadt

URN: urn:nbn:de:tuda-tuprints-233236

Jahr der Veröffentlichung der Dissertation auf TUprints: 2023

Preface

This dissertation "Experimental and Numerical Investigation of the Absorption Process in Polygeneration " is the outcome of my work as a Ph.D. student at the Institute of Energy Systems and Technology (EST) at Technical University of Darmstadt. I would like to acknowledge my warm appreciation and gratefulness towards my supervisor **Prof. Dr.-Ing. Bernd Epple** for his great support and outstanding supervision. I would like to thank **Prof. Dr. rer. nat. habil. Amsini Sadiki**, the reviewer of this Ph.D. thesis, for the takeover of the co-review of this work. I would like to acknowledge my warm appreciation and gratefulness to **Priv.-Doz. Dr.-Ing. habil. Falah Alobaid** for his professional guidance, suggestions, recommendations, and understanding of the research subject.

I am grateful to the sponsor of my Ph.D. study, Al Furat University, for the scholarship that allowed me to work as a Ph.D. student on this research at the Institute EST. I am grateful to Dr. Christian Heinze for his direct support, expert advice, and valuable suggestions. Dr. Christian Heinze helped me in constructing the test rig, understanding the research subject, and guiding me on how to achieve the objectives of the research. I am especially grateful to Dr. Jens Peters for his close cooperation with all issues relating to programming support and for sharing his experience. I would like to thank Eric Langner and Paul Dieringer for their support when I needed it most. It would have been impossible to finish this work without great support, and direct contribution from:

- Mechanical construction: C. Bonk, W. Lau, F. Stender
- Electrical construction: J. Wagner, P. Reinig,
- Administrative: S. Tropp
- Students: D. Freudenreich

I am grateful for the support of the staff at the Institute of Energy Systems and Technology (EST) at Technical University of Darmstadt, who made my work at the institute a memorable and valuable experience.

Darmstadt, August 2022 **Adel Almoslh**

Dedication

I dedicate this work:

To him, who helped me with everything he had, who was like a candle that lit my way, who was like a bridge that brought me to where I am (my dear father).

To her who was the source of tenderness, who struggled greatly for my comfort (my dear mother).

To her, who was my companion in these lands, who is the wonderful person in my life, whose constant support, love, and encouragement has made this work possible (my dear wife).

To her whose love flows in my veins and my heart (my beloved children).

To them, of whom I am proud to be a part (my brothers and my sister).

To them who encourage and support me (my friends). Here I must mention my friends Dr. Naser Almohammed, Dr. Wisam Al-Maliki, and Mr. Raid Almoued.

To them who have contributed to my learning at all levels of education (my honored teachers and professors).

Erklärung

Hiermit erkläre ich, dass ich die vorliegende Arbeit, abgesehen von den in ihr ausdrücklich genannten Hilfen, selbständig verfasst habe.

Darmstadt, den 19.08.2022

Adel Almoslh

Adel Jomaa Almoslh

Abstract

Polygeneration plants play an important role in environmental and energy issues. Polygeneration plants are built to produce chemical products such as petroleum products like naphtha and diesel, or to generate electricity in parallel. The importance of polygeneration plants has increased with the continuous increase in energy demand, as their numerous advantages contribute significantly to the flexibility of chemical products or energy supply and their thermodynamic efficiency is higher than that of single product systems.

The absorption process is considered essential in polygeneration plants, as it removes harmful gases such as acid gas from the produced syngas. The absorption process is usually designed for steady-state operation. However, operating the absorption process varies over time. Sometimes, this is due to the change in load, startup, or shutdown.

The study of the unsteady state of the absorption process due to load changes is interesting because it helps to reconsider design issues or improve the behavior of the absorption process during the unsteady state.

In this work, the background of the main processes in the Polygeneration plant was presented. A laboratory-scale absorber test rig was built at the Institute of Energy Systems and Technology (EST) at Technical University of Darmstadt. The absorber test rig was commissioned to verify that it operates safely and meets the experimental requirements for which it was built. The steady-state and the dynamic state of the absorption process were conducted in the absorber test rig. The models of the absorption process are presented. A simulation of the absorption process was performed using Aspen PLUS and Aspen PLUS Dynamics simulation programs. The simulation results were validated with the experimental results. It was found that the different load changes and the different change rates of the gas and solvent have a significant effect on the acid gas concentration at the outlet of the absorber. The correlation between the behavior of the absorber during the transient state and the hydrodynamic properties of the sieve tray was investigated. It was found that the hydrodynamic properties of the sieve tray have a significant influence on the performance of the absorber during the transient state. Finally, the conclusion and the outlook were presented.

Kurzfassung

Polygenerationsanlagen spielen eine wichtige Rolle in Umwelt- und Energiefragen. Polygenerationsanlagen werden gebaut, um chemische Produkte wie Erdölprodukte wie Naphtha und Diesel zu produzieren oder um parallel dazu Strom zu erzeugen. Die Bedeutung von Polygenerationsanlagen hat mit dem kontinuierlichen Anstieg des Energiebedarfs zugenommen, da ihre zahlreichen Vorteile erheblich zur Flexibilität der chemischen Produkte oder der Energieversorgung beitragen und ihr thermodynamischer Wirkungsgrad höher ist als der von Einzelproduktsystemen.

Der Absorptionsprozess wird in Polygeneration-Anlagen als wesentlich angesehen, da er schädliche Gase wie saures Gas aus dem erzeugten Synthesegas entfernt. Der Absorptionsprozess ist in der Regel für einen stationären Betrieb ausgelegt. Der Betrieb des Absorptionsprozesses variiert jedoch im Laufe der Zeit. Manchmal ist dies auf Änderungen der Beladungen, das Anfahren oder das Abschalten zurückzuführen.

Die Untersuchung des instationären Zustands des Absorptionsprozesses aufgrund von Belastungsänderungen ist interessant, weil sie dazu beiträgt, Konstruktionsfragen zu überdenken oder das Verhalten des Absorptionsprozesses während des instationären Zustands zu verbessern.

In dieser Arbeit wurde der Hintergrund der Hauptprozesse in einer Polygeneration-Anlage vorgestellt. Ein Absorberprüfstand im Labormaßstab am Institut für Energiesysteme und Energietechnik der Technische Universität Darmstadt aufgebaut wurde. Der Absorberprüfstand wurde in Betrieb genommen, um zu überprüfen, ob er sicher funktioniert und die experimentellen Anforderungen erfüllt, für die er gebaut wurde. Der stationäre und der dynamische Zustand des Absorptionsprozesses wurden im Absorberprüfstand durchgeführt. Die Modelle des Absorptionsprozesses werden vorgestellt. Eine Simulation des Absorptionsprozesses wurde mit den Simulationsprogrammen Aspen PLUS und Aspen PLUS Dynamics durchgeführt. Die Simulationsergebnisse wurden mit den experimentellen Ergebnissen abgeglichen. Es wurde festgestellt, dass die unterschiedlichen Beladungswechsel und die unterschiedlichen Wechselraten des Gases und des Lösungsmittels einen erheblichen Einfluss auf die Sauergaskonzentration am Ausgang des Absorbers haben. Die Korrelation zwischen dem Verhalten des Absorbers im Übergangszustand und den hydrodynamischen Eigenschaften der Siebboden wurde untersucht. Es wurde festgestellt, dass die hydrodynamischen Eigenschaften der Siebboden einen signifikanten Einfluss auf die Leistung des Absorbers während des Übergangszustands haben. Abschließend wurden die Zusammenfassung und der Ausblick vorgestellt.

Table of Contents

List of Tables

List of Figures

Nomenclatures

Symbols

Symbol	Description	Unit
L	liquid molar flow rate	$[kmol/s]$
V	vapor molar flow rate	$[kmol/s]$
F	feed molar flow rate	$[kmol/s]$
N	molar transfer rate	$[kmol/s]$
x_i	mole fraction of component i in liquid phase	$[-]$
y_i	mole fraction p of component i in the gas phase	$[-]$
γ_i	activity coefficient of component *i*	$[-]$
Q	heat input to a stage	$[J/s]$
H	enthalpy	$[J/kmol]$
Eff^V	vaporization efficiency	$[-]$
Eff^M	murphree efficiency	$[-]$
U_{nf}	flooding velocity	[m/s]
σ	liquid surface tension	[mN/m]
ρ_l	liquid density	[kg/m^3]
C_{sbf}	capacity parameter	[m/s]
L_w	liquid flow rate	[kg/s]
V_w	vapor or gas flow rate	[kg/s]
ρ_v	vapor or gas density	[kg/m^3].
U_{min}	minimum design vapor velocity	[m/s]
d_h	hole diameter	[mm]
K_2	constant of weep-point correlation	$[-]$
L_{ow}	weir length	[mm]
L_W	liquid flow rate over the crest	[mm]
L_i	liquid molar flow rate of component i	$[kmol/s]$
G_i	gas molar flow rate of component i	$[kmol/s]$
$\dot{N}_L$	liquid molar flow rate	$[kmol/s]$
$\dot{N}_G$	gas or vapor molar flow rate	$[kmol/s]$
Φ_i^v	fugacity	$[bar]$
P_{soi}	saturation vapor pressure of pure component i	$[bar]$
P	vapor pressure	$[bar]$
k_G	mass transfer coefficient of the gas-phase	$[m/s]$
k_L	mass transfer coefficient of the liquid-phase	$[m/s]$
a^*	interfacial area	$[m^2]$
L	molar flow rate of liquid	$[kmol/s]$
V	molar flow rate of vapour	$[kmol/s]$
K	equilibrium ratio	$[-]$

r	reaction rate	$[kmol/s]$
q	heat transfer rate	$[J/s]$
$k_{i,K}^{L}$	binary mass transfer coefficient for the liquid	$[m/s]$
$k_{i,K}^{V}$	the binary mass transfer coefficient for the vapor	$[m/s]$
$D_{i,k}^{L}$	diffusivity of the liquid	$[m^2/s]$
$D_{i,k}^{V}$	diffusivity of the vapor	$[m^2/s]$
Fs	superficial F-factor	
t_L	average residence time for the liquid	$[s]$
$\bar{\rho}^L$	molar density of the liquid	
a^I	total interfacial area mass transfer	$[m^2]$
F_f	fractional approach to flooding	
a	relative froth density	
h_{cl}	clear liquid height	$[m]$
A_b	total active bubbling area	$[m^2]$
u_s^V	superficial velocity of vapor	$[m/s]$
FP	flow parameter	
$\emptyset$	fractional hole area per unit bubbling area	$[-]$
l_w	average weir length	$[mm]$
Q_L	volumetric flow rate for the liquid	$[m^3/s]$
Q_V	volumetric flow rate for the vapor	$[m^3/s]$
u_{sf}^V	superficial velocity of vapor at flooding	$[m/s]$
P	sieve tray hole pitch	$[mm]$
u_s^V	superficial velocity of vapor	$[m/s]$
ρ_G	density of the gas	[kg/m^3]
c_p	specific molar heat capacity	[J/Kmol K]
$M_{w,L}$	molecular weight of the liquid phase	
λ	thermal conductivity	$[W/mK]$
D	diffusion coefficient	$[m^2/s]$
$F_{gas,in}$	inlet gas flow rate	$[Nm^3/h]$
$F_{gas,out}$	outlet gas flow rate, $[Nm^3/h]$	$[Nm^3/h]$
$F_{CO_2,in}$	inlet CO_2 flow rate $[Nm^3/h]$	$[Nm^3/h]$
$F_{air,in}$	inlet air flow rate, $[Nm^3/h]$	$[Nm^3/h]$
$F_{N_2,in}$	inlet N_2 flow rate, $[Nm^3/h]$	$[Nm^3/h]$
N_{CO_2}	the absorbed rate of CO_2, $[Nm^3/h]$	$[Nm^3/h]$
$y_{CO_2,in}$	inlet volumetric fraction of CO_2	$[-]$
$y_{CO_2,out}$	outlet volumetric fraction of CO_2	$[-]$
$\Delta P_{total.tray}$	total tray pressure drop	[kPa]
$\Delta P_{hyd.tray}$	hydraulic tray pressure drop	[kPa]
$\Delta P_{dry,tray}$	dry tray pressure drop	[kPa]

h_L	liquid holdup	$[m^3]$
A_{tray}	tray surface area	$[m^2]$
h_{cl}	liquid holdup level	[m]

Subscripts

Symbol	Description
i	component index
j	stage index
C	last component index
k	last stage index

Abbreviations

Symbol	Description
PID controller	Proportional integral derivative controller
MFC	mass flow controller
kW	kilowatt
Nm^3/h	a cubic meter of gas per hour at the normal temperature and pressure
MEA	monoethanolamine
DEA	diethanolamine
MDEA	methyl diethanolamine
NMP	N-methyl-2-pyrrolidone
THFA	tetrahydrofurfuryl alcohol
MEG	monoethylene glycol
CC5	cyclopentanone
VLE	vapor-liquid equilibrium
MPa	megapascal
kPa	kilopascals
min	minute
sec	second
L	liter
h	hour
mboe/d	million barrels of oil equivalent per day
IGCC	Integrated Gasification Combined Cycle
ppm	parts per million
ppmv	parts per million volume
WGSR	water-gas shift reaction
LTS	Low temperature shift
HTS	high temperature shift
NMP	N-methyl-2-pyrrolidone
PLC	programmable logic controller
K	Kelvin
atm	standard atmosphere
$\Delta H_{298\ K,1\ atm}$	Reaction heat based on 298K and 1 atm
s	solid phase

g	gas phase
HTFT	high-temperature Fischer-Tropsch
LTFT	Low-temperature Fischer-Tropsch
FT	Fischer-Tropsch
SLO	stabilized light oil
DO	decanted oil
RPS	rotating particle separators
CPU	central processing unit
pH	power of hydrogen
PC	personal computer
WinCC	Windows Control Center
GW	gigawatts
PSIG	pound per square inch gauge

Chapter 1 **Introduction**

In this chapter, the motivation for the experimental and numerical investigation of the absorption process in polygeneration plant is presented. The objectives of the study and literature reviews are given. Finally, the outline of the dissertation is presented.

1.1 Introduction and Motivation

The world's urgent need for clean energy with low gas emissions is now better known than ever, especially after the world has experienced numerous global warming phenomena in recent years, such as the increase in average earth temperature, climate change, floods, the extinction of many animal and plant species, and rising sea levels. In addition, the rapid depletion of conventional energy sources and the increasing energy demand encourage the search for other energy sources to achieve energy security.

The world's energy comes mainly from fossil fuels, of which crude oil is an essential fuel. The crude oil formed naturally in the earth's crust from organic materials thousands of years ago under pressure and temperature conditions. The oil formed accumulates in an oil reservoir located in the geological layers at a depth of thousands of meters. After the oil production, the oil is processed, for example by separating the formation water and gases. To use the oil for industrial applications, it must undergo a refining process.

Petroleum refining is an industrial process where petroleum is converted into useful products such as liquefied petroleum gas (LPG), Nephta, Butanes, Sulfur, kerosene, diesel oil, fuel oils, heating oil, kerosene, asphalt, and petroleum coke as shown in Figure 1.1. The main processes which involved in the crude oil refinery are distillation, hydrotreating, reforming, alkylation, polymerization, isomerization, amine absorption, and cracking.

Petroleum coke is a byproduct produced during cracking process. The cracking process takes place in the delayed coker (a type of coker), where the large hydrocarbon molecules are heated to a cracking temperature that breaks them down into smaller hydrocarbon molecules to produce usful products like coker naphtha and gas oil, and byproduct like gas and Petroleum coke. The prudectes fom Petroleum coke is often stored in large amounts as a waste product or it can be combusted for heat or power generation. Petroleum coke has a high carbon content and low ash quality, but often has an undesirably high sulfur content [1].

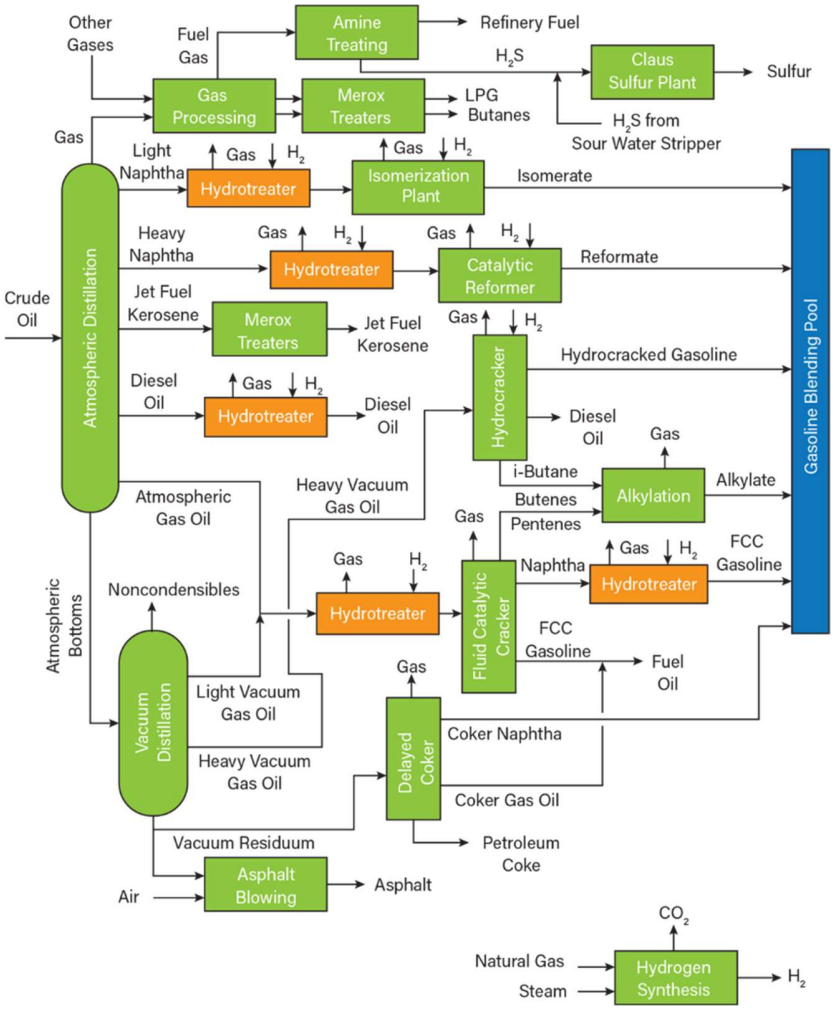

Figure 1.1 General process flow diagram of a petroleum refinery [2]

Increasing demand for energy sources and high energy prices, as well as declining global reserves of fossil fuels, this increases the importance ofsystems that use petroleum coke more efficiently and with environmental considerations increasingly important.

The energy stored in petroleum coke can be released by various methods, such as combustion, destructive distillation, and gasification. Releasing energy by combustion takes place with the presence of oxygen. Since petroleum coke has high carbon content, low volatile content, and high sulfur and nitrogen content, so the combustion products are usually harmful gases that contribute to greenhouse gas emissions that pollute the environment. that make the combustion of petroleum coke is undesirable or even not allowed by the authorities [3], [4]. The destructive distillation or pyrolysis happens absent oxygen, whereas the gasification happens with a little oxygen. The product of gasification and pyrolysis is called raw synthesis gas. After processing the raw synthesis gas, it can be sent to synthesize plants like the Fischer-Tropsch refinery (FT) to produce hydrocarbon products like naphtha and diesel as shown in Figure 1.2.

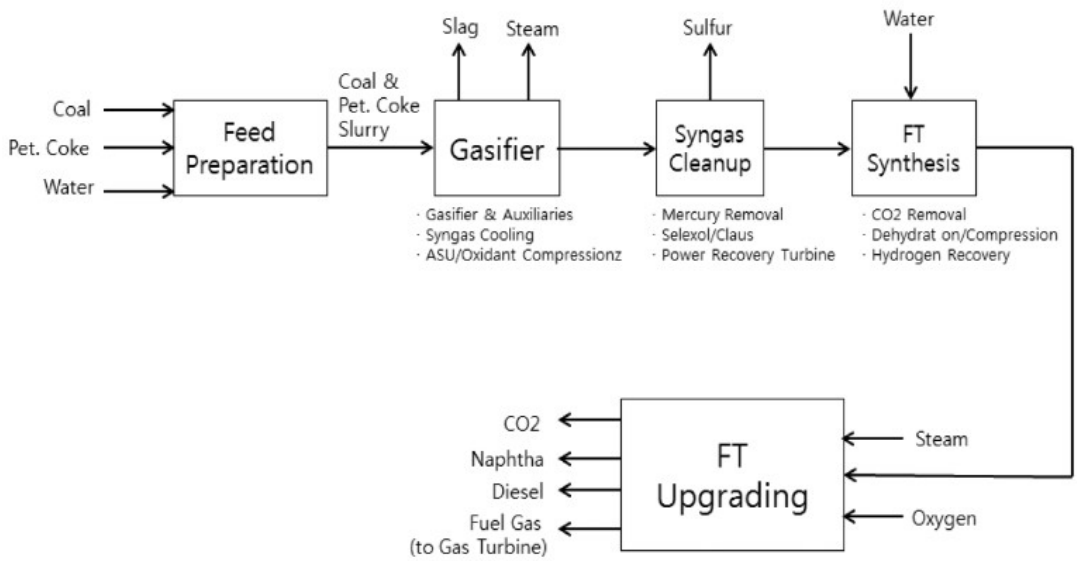

Figure 1.2 Fischer-Tropsch process of indirect liquefaction with co-gasification of petroleum coke and coal mixture [5]

Figure 1.3 shows the electricity generation and consumption in Germany in 2020 from different renewable energy sources. It can be seen that the consumption fluctuations in 12 hours are about 15 GW, while the feed-in fluctuations in 12 hours are 45 GW.

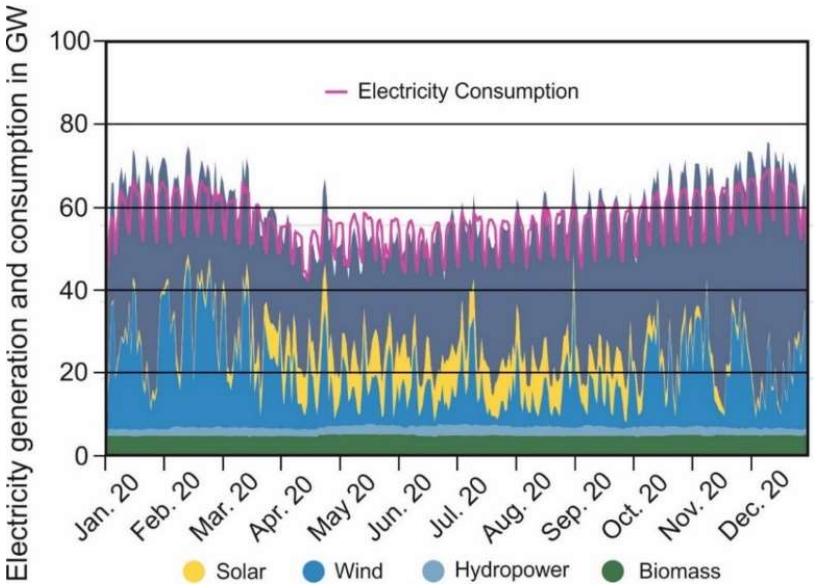

Figure 1.3 Electricity generation and consumption in Germany in 2020 [112]

Some renewable energy sources, such as solar and wind power, encounter difficulties in generating energy regularly and being fully controlled. For example, solar power generation is limited to the time of day. The challenges for renewable energy sources lie in their ability to meet fluctuating electricity demands during the day.

One of the requirements of the power systems is flexibility in power generation. There are two pathways to achieve this target. The first pathway is by using energy storage systems, but the energy

storage should be on a large scale. The second pathway is by making conventional power plants significantly more flexible. Polygeneration is one of the systems based on the flexibility of power generation and hydrocrabons production like naphtha and diesel is promising concepts that can provide a path to clean energy generation and help meet variable energy needs [5].

1.2 Polygeneration Concept

The polygeneration system is one concept that produces clean synthesis gas that is used in parallel to create synthetic fuels or electricity. Figure 1.4 shows a flowchart of the polygeneration concept. The polygeneration system is based on a gasification process that converts the petroleum coke into raw syngas. Raw syngas is a mixture of gases such as H_2, CO, CO_2, H_2S, COS, tar, and solid particles. The raw syngas must be treated before it is sent to downstream applications. This treatment aims to remove harmful components such as CO_2, H_2S, COS, tar components, and solid particles. In addition, the treatment aims to condition the syngas in terms of the H_2/CO ratio to make them suitable for downstream applications. After the gas conditioning phase, the product is clean syngas, which is a mixture of H_2 and Co with a specific ratio. The clean syngas is fed either to the Fischer-Tropsch refinery for fuel production like naphtha and diesel or the combined cycle power plant for energy generation.

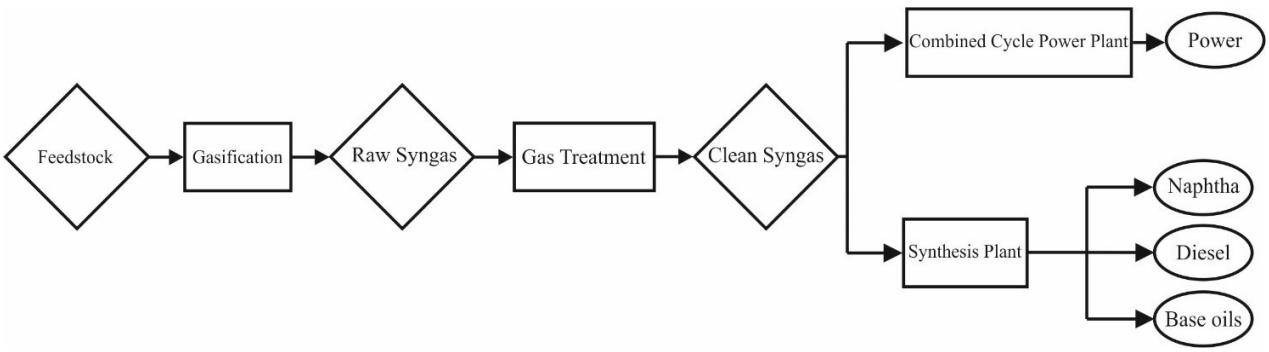

Figure 1.4 Schematic of Polygeneration concept

One goal of polygeneration power plants is to serve the fluctuating energy demand of the local market during the day. There are two operating states for polygeneration plant. In the first state, when electricity demand increases, all the clean syngas is fed into the combined cycle power plant to generate electricity. In the second state, when electricity demand decreases, most of the syngas is directed to the Fischer-Tropsch refinery to produce chemical components such as diesel, naphtha, and base oil. Some of the clean syngas is fed to the combined cycle power plant to generate the heat and steam required to operate the polygeneration processes. When switching between the two states, the polygeneration enters a transient state. In the transient state, the gasification agent in the gasification process is switched from air to oxygen or vice versa. Air is used as the gasification agent when the generated clean syngas is fed into the IGCC plant, while oxygen is used as the gasification agent when the generated clean syngas is fed into a synthesis plant. The reason for switching between air and oxygen as the gasification agent is to increase the efficiency of the polygeneration, because air is cheaper than oxygen and always available. But the quality of the product raw syngas when air is used as a gasification agent is lower than the quality of the product raw syngas when oxygen is used as a

gasification agent in terms of harmful gas content. On the other hand, the requirements for the syngas for the IGCC plants are less stringent than the requirements for the syngas for the synthesis plants concerning sulfur and carbon dioxide.

Chemical syntheses such as Fischer-Tropsch and methanol synthesis require sulfur levels below 1 ppm. [6]. While power generation applications that allow higher sulfur levels require about 10 to 30 ppmv of sulfur [7].

The polygeneration plant encounters a change in load during the transient state. The different load changes result because the flow rate of air used as a gasification agent is higher than the flow rate of oxygen. As a result, the flow rate of the produced raw syngas by using the air as a gasification agent is higher than that of the produced raw syngas when oxygen is used as a gasification agent.

The different load changes of the raw syngas have a significant impact on the downstream processes because the flow rate of the generated raw syngas increases from a low load to a high load when clean syngas is fed into a combined cycle plant, and vice versa when the generated clean syngas is fed into a synthesis plant. One process affected by the different load changes of the raw syngas is the absorption process in the acid gas removal unit. The acid gas removal unit is an essential unit in polygeneration plant, which applies the absorption process to remove harmful acid gases such as CO_2 and H_2S. To ensure stable operation of the absorption process during the transient state of different load changes, the response of the absorption process toward different load changes should be studied.

1.3 Literature Review

1.3.1 Polygeneration Systems

Gao et al. (2004) [8] proposed a new type of polygeneration system and investigated it using graphical exergy analysis. The authors compared the new type of polygeneration system with individual systems and concluded the proposed polygeneration system can significantly improve energy conservation. Their results showed that, by combining a power system with a chemical process, the polygeneration system leads to an energy saving of 3.9%. The authors indicate the synthesis based on the cascade utilization of thermal energy contributes the most to the performance improvement in this polygeneration system. They also state the ratio of capacity between the chemical process and the power supply system has a significant effect on the coordination between the two sides, making it a key factor in the polygeneration system. Besides thermal energy integration, the cascade use of chemical exergy will be the key topic for continued study.

Li et al. (2010) [9] suggested a polygeneration system for methanol and electricity. The raw materials are biomass and natural gas. The authors reviewed that the syngas produced from biomass gas has a comparatively lower H/C ratio to produce methanol, while the syngas produced from natural gas has a comparatively higher H/C ratio to produce methanol. The authors state that if the two kinds of syngas are mixed, the best H/C ratio can be achieved by adjusting the ratio between natural gas and biomass without energy loss. Li reviewed that it can be achieved by the proposed polygeneration with an energy saving of 10% by setting the input ratio of natural gas to biomass to about two.

Gao et al. 2008 [10] reviewed a new type of natural gas-based polygeneration system for methanol and power generation. The proposed system is based on the Sequential Connection of Chemical Production and Electricity Production. The new system uses the innovative integration of partial reforming and partial recycling in the methanol synthesis subsystem. The authors performed an exergetic comparison between the new system and a reference polygeneration system. Their results show the new system can save about 6 percent energy compared to individual production systems. Using the graphical exergy analysis method, it is shown that the synergistic combination of both partial reforming and partial recycling contributes the most to the performance improvement.

1.3.2 Modeling and Simulation of Amine Absorption Process

There are two common simulations in the process industry; steady-state simulation and dynamic simulation. A steady-state simulation is an important tool for designing and operation the plant in a steady-state condition. Dynamic simulation is important in the process industry for operability studies, safety, and risk assessments, analysis of start-up and shut-down operations, and automatic process optimization using optimal control technologies.

Several dynamic simulation studies were performed to investigate the flexibility of the plant to absorb acid gases like CO_2 and H_2S.

Sepideh Ziaii 2009 [11] developed A dynamic rate-based model for the stripping process in CO_2 capture from coal-fired power plants with 30 wt % by using monoethanolamine (MEA). One of the objectives of their study is to investigate the effects of lean loading and packing height on total work equivalents and to determine ideal operating conditions that keep the lost work of the power plant to a minimum. Two dynamic strategies with control configurations are investigated to flexibly operate the stripper during peak power load. One of the control approaches increased CO_2 removal by 1% at a reduced steam rate and caused the stripper to respond more quickly to a step change in the reboiler heating rate.

Harun et al. 2012 [12] developed a dynamic MEA absorption process model to investigate the dynamic behavior of the CO_2 capture process. Harun studied the behavioral response of the monoethanolamine (MEA) absorption process during the transient state of changes in flue gas flow rate and reboiler heating power. The authors found the changes in flue gas flow rate and reboiler heating power are major process parameters that affect the percentage of CO_2 removal, liquid-to-gas ratio, and lean loading. Their results reveal the variation between the reboiler heating capacity and CO_2 removal is in a ratio of about 1:1.4.

Lawal et al. 2009 [13] developed and compared two models (equilibrium-based and rate-based models). Their study is conducted on post-combustion CO_2 capture using monoethanolamine (MEA) as solvent. The objective of this study is to understand the dynamic behavior of the absorber during partial load operation and when the stripper is disturbed. Lawal reviewed that the rate-based model is more accurate in prediction than the equilibrium-based model. Lawal found that absorber operation is more responsive to the L/G ratio. The authors reviewed that increased CO_2 loading in the lean solvent resulted in a significant reduction in absorber performance.

Gáspár and Cormoş 2011 [14] performed modeling and simulation of the CO_2 absorption and regeneration process using abundant amine. This study aims to validate models and understand the dynamic behavior of the whole capture and regeneration stages. One case studied by the authors is the change of power plant load by linearly increasing the ratio of gas flow rate to liquid flow rate (FG/FL) from 625 to 1040. The authors found that the amount of purified CO_2 gas increases with the increase of power plant load, but the exhaust gas stream is richer in CO_2. The authors reviewed that the developed model can predict the dynamic behavior of the columns during operation.

Gaspar and Cormos (2012) [15] developed a rate-based model used for simulating the CO_2 post-combustion process using amine-based solutions in a fixed-bed absorption column. The objective of this study is to investigate the dynamic behavior and absorption performance of four types of alkanolamines (MEA, DEA, MDEA, and AMP) using mass transfer and liquid holding correlation models published in the literature, such as the Wang et al. model, Billet and Schultes model, and Rocha model. The authors found that the mass transfer correlation model proposed by Wang et al. well predicted the effective mass transfer area and the mass transfer coefficient correlation for all alkanolamines.

1.4 Research Objectives

The main objective of this study is to study experimentally and numerically the unsteady state of the absorption process due to the load changes in inlet gas flow rate in a polygeneration plant. The derived objectives of this study are as follows:

1- To experimentally study the influence of different load changes and different change rates of gas flow rate and solvent flow rate on the performance of the absorber during the transient state; an absorber test rig was constructed.

2- Commissioning of the constructed absorber test rig to verify it meets safety and testing requirements.

3- Experimental investigation of the influence of different load changes and different change rates of gas flow rate and solvent flow rate on the performance of the absorber used for CO_2 capture.

4- Experimental investigation of the influence of different load changes and different change rates of gas flow rate and solvent flow rate on the hydrodynamic properties of the sieve tray, such as total tray pressure drop, hydraulic tray pressure drop, liquid holdup level, and liquid holdup.

5- Studying the correlation between a sieve tray's hydrodynamic characteristics and the absorber's performance to capture CO_2 during the transient state.

6- Modeling of the absorption process.

7- Performing a simulation of the absorption process was performed using Aspen PLUS and Aspen PLUS Dynamics simulation programs.

8- Validation of the mathematical models against the experimental data.

9- State suggestions for improving the performance of the absorber during the transient condition.

1.5 Outline of the Thesis

The outlines of this study are as follows:

Chapter 1 Introduction. This chapter presents the motivation for studying the experimental and numerical investigation of the absorption process in polygeneration plant. Literature reviews and the objectives of the study are given. Finally, the outline of the dissertation is presented.

Chapter 2 Background. This chapter presents the background of the units that make up the polygeneration plant. It also presents the technologies used in the polygeneration plant. In addition, the background of the applied processes used in the polygeneration plant is explained.

Chapter 3 Constructing an absorber test rig. This chapter summarizes the construction of an absorber test rig on a laboratory scale built at the Institute of Energy Systems and Technology (EST) at Technical University of Darmstadt. The designing, constructing, sizing, and selecting of the parts of the test rig are illustrated. Furthermore, the programming of the control system is presented.

Chapter 4 Commissioning the absorber test rig. This chapter summarizes the commissioning of the absorber test rig built at the Institute of Energy Systems and Technology (EST) at Technical University of Darmstadt to verify that it operates safely and meets the experimental requirements for which it was built.

Chapter 5 Modeling of the absorption process. This chapter presents two mathematical models (the equilibrium model and the rate-based model) applied to simulate the absorber test rig. In addition, thermodynamic approaches to predict the phase behavior are described. Finally, the correlations for calculating the binary mass transfer coefficients, the heat transfer coefficient, the liquid holdup, and the interface are presented.

Chapter 6 Experimental results. In this chapter, the results of the experiments performed on the absorber test bench are reported and discussed. The methodology of the experimental study is explained, then the results of the CO_2 absorption experiments using aqueous MDEA solutions are presented.

Chapter 7 Simulation results. In this chapter, a steady-state simulation for the absorber test rig was performed. The validation of the steady-state model using the experimental data is shown. Finally, the simulation of the dynamic absorption process was performed and the validation of the dynamic model is presented.

Chapter 8 Conclusion and outlook. This chapter summarizes the conclusions of the present research and provides an outlook for future research.

1.6 Publications

- Ata, A. B., Alobaid, F., Heinze, C., **Almoslh, A**., Sanfeliu, A., & Epple, B. (2020). *Comparison and validation of three process simulation programs during warm start-up procedure of a combined cycle power plant. Energy Conversion and Management*, 207, 112547. https://doi.org/10.1016/j.enconman.2020.112547

- **Almoslh, A**., Alobaid, F., Heinze, C., & Epple, B. (2020). *Comparison of equilibrium-stage and rate-based models of a packed column for tar absorption using vegetable oil*. Applied Sciences, 10(7), 2362. https://doi.org/10.3390/app10072362

- **Almoslh, A**., Alobaid, F., Heinze, C., & Epple, B. (2020). *Influence of Pressure on Gas/Liquid Interfacial Area in a Tray Column*. Applied Sciences, 10(13), 4617. https://doi.org/10.3390/app10134617

- **Almoslh, A**., Alobaid, F., Heinze, C., & Epple, B. (2021). *Experimental Study of the Influence of Gas Flow Rate on Hydrodynamic Characteristics of Sieve Trays and Their Effect on CO_2 Absorption*. Applied Sciences, 11(22), 10708. https://doi.org/10.3390/app112210708

- Aghel, B., Janati, S., Alobaid, F., **Almoslh, A**., & Epple, B. (2022). *Application of Nanofluids in CO_2 Absorption*: A Review. Applied Sciences, 12(6), 3200. https://doi.org/10.3390/app12063200

- **Almoslh, A**., Aghel, B., Alobaid, F., Heinze, C., & Epple, B. (2022). *Experimental Study of the Influence of Different Load Changes in Inlet Gas and Solvent Flow Rate on CO_2 Absorption in a Sieve Tray Column.* Entropy, 24(9), 1318. https://doi.org/10.3390/e24091318

Chapter 2 : Background

This chapter presents the background of the units that make up the polygeneration plant. It also presents the technologies used in the polygeneration plant. In addition, the background of the applied processes used in the polygeneration plant is explained.

2.1 Introduction

The polygeneration plant consists of a group of serial units whose purpose is to create clean synthesis gas that is used in parallel to produce synthetic fuels or electricity. Figure 2.1 shows the units that make up the polygeneration plant. Petroleum coke is fed to the gasifier, where it is converted to raw syngas. The raw syngas is then fed to the filtration unit, where the solid particles are removed. Solid particles like ash cause a lot of problems like blocking equipment, especially heat exchangers. The raw syngas is then washed to remove chlorine compounds, which cause corrosion in the equipment. Next, the raw syngas is fed into the CO shift reactor to modify the H_2/CO ratio and increase the amount of the H_2 in the raw syngas. Then, the raw syngas is fed into the COS hydrolysis to convert the COS gas into H_2S gas, which easily can be separated later in the amine absorption process, where the compound COS is difficult to be separated by the amine absorption process. After the COS hydrolysis process, the raw syngas enters the biodiesel washing process to separate the tar compounds. The tar compounds are condensed gases that may create fouling and soot accumulation in downstream processes. After the biodiesel washing process, the raw syngas enters the amine absorption process to separate the CO_2 and H_2S. CO_2 is counted among the greenhouse gases that cause environmental problems when released into the atmosphere. H_2S is separated because it causes many problems, such as poisoning the catalysts in the reactors in downstream applications.

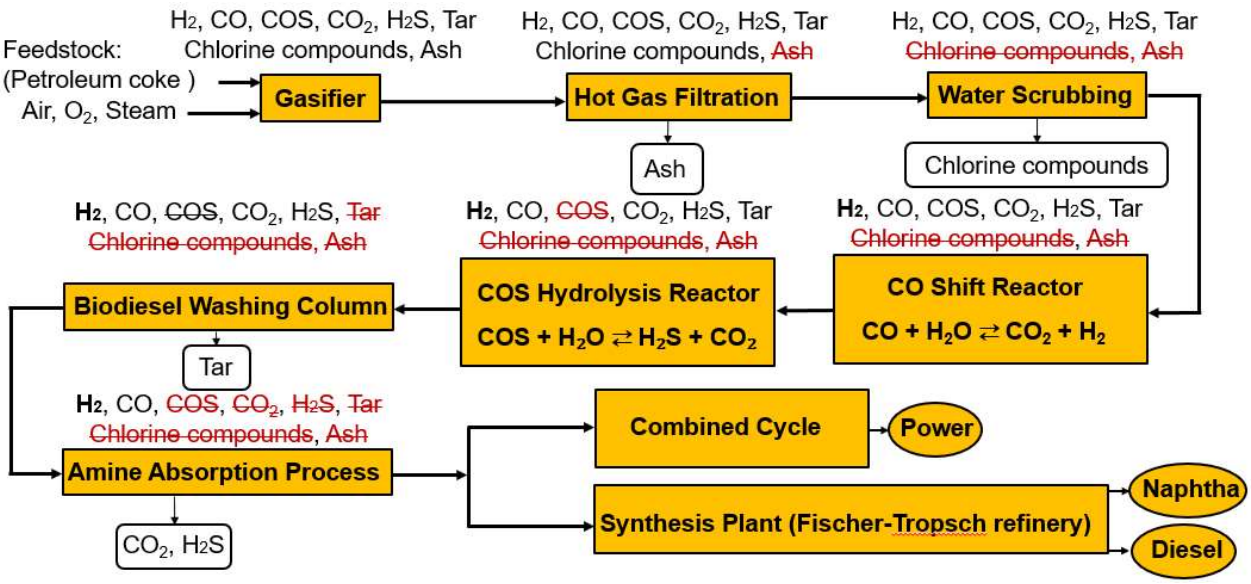

Figure 2.1 Flowsheet of the polygeneration plant

After the removal of harmful components from the raw syngas, the so-called clean syngas is produced, which is a mixture of H_2 and CO with a specific ratio. The clean syngas is fed to an integrated gasification combined cycle for energy production or a chemical processing plant (Fischer-Tropsch process). In the Fischer-Tropsch refinery, hydrocarbons are produced to obtain beneficial petrochemical compounds for industrial use like naphtha and diesel.

2.2 Gasification

Gasification is a process in which the feedstock (like petroleum coke) is converted into syngas. The syngas produced by gasification consists of various gases and components, such as CO, H_2, CO_2, CH_4, tar, H_2S, N_2, hydrocarbons, and particulates. The composition of syngas depends on several parameters, such as feedstock, temperature, gasifier type, and operating conditions (e.g., temperature, pressure, and residence time) [16]. Generally, gasification is carried out in a temperature range of 600°C-1000°C. The materials commonly used for gasification agents are steam, air, CO_2, and H_2 [17]. Several chemical reactions can occur simultaneously during the gasification of feedstock. The reactions can be divided into homogeneous and heterogeneous reactions according to their reaction educts states. Table 2.1 summarizes the main reactions during the gasification process:

Table 2.1 Main gasification reactions [18]

Reaction name	Reaction formula	$\Delta H_{298\,K,1\,atm}$, (kJ/mol)	
Heterogeneous reactions			
Water-gas primary	$C_s + H_2O \rightleftarrows CO + H_2$	131.3	(2.1)
Water-gas primary	$C_s + 2H_2O \rightleftarrows CO_2 + 2H_2$	90.3	(2.2)
Boudouard	$C_s + CO_2 \rightleftarrows 2CO$	172.4	(2.3)
Oxidation	$C_s + O_2 \rightleftarrows CO_2$	-392.5	(2.4)
Partial oxidation	$C_s + 1/2\ O_2 \rightleftarrows CO$	-110.5	(2.5)
Methanation	$C_s + 2H_2 \rightleftarrows CH_4$	-74.6	(2.6)
Homogeneous reactions			
Water-gas shift	$CO + H_2O \rightleftarrows CO_2 + H_2$	-41	(2.7)
H_2(/Steam) reforming	$CO + 3H_2 \rightleftarrows CH_4 + H_2O$	-(/+) 205.9	(2.8)
Oxidation reaction	$CO + 1/2\ O_2 \rightleftarrows CO_2$	-283	(2.9)
	$H_2 + 1/2\ O_2 \rightleftarrows H_2O$	-242	(2.10)
Steam reforming	$CH_4 + 2H_2O \rightleftarrows CO_2 + 4H_2$	164.7	(2.11)
	$C_6H_6O + 5H_2O \rightleftarrows 6CO + 8H_2$	642	(2.12)
CO_2 reforming	$CH_4 + CO_2 \rightleftarrows 2CO + 2H_2$	247	(2.13)

2.2.1 Types of Gasifiers

The size and type of gasifier are determined by various factors, such as desired products, moisture content, fuel source availability, etc. [19]. There are three common types of gasifiers: moving bed gasifiers, fluidized bed gasifiers, and entrained flow gasifiers.

2.2.1.1 Moving-bed Gasifier

Moving bed gasifiers have a simple design and are easy to operate. The feedstock is fed into the gasifier from the top, while the gasification agents are fed from the bottom, as shown in Figure 2.2.

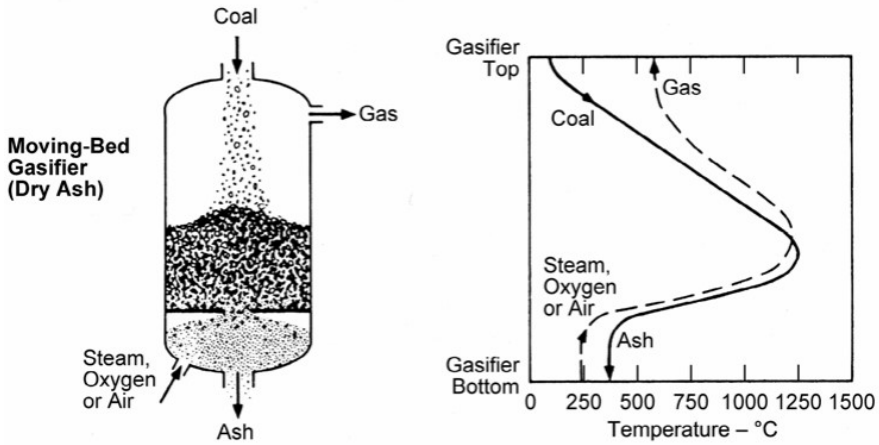

Figure 2.2 Diagram of a generic moving bed gasifier [20]

The gasifier has three main zones: the combustion zone, the gasification zone, and the drying zone. In the combustion zone, the feedstock is burned. The heat released by the feedstock goes up to the gasification zone. In the gasification zone, the temperature is higher than in the combustion zone. The gasification process of feedstock occurs. The produced synthesis gas from the gasification zone goes up to the drying zone. The heat load in the gases heats and dries the feedstock located in the drying zone. The raw syngas exits from the side top part of the gasifier, while the ash is removed from the lower part of the gasifier. In the literature, a common type of gasifier used on an industrial scale is the Lurgi gasifier, shown in Figure 2.3.

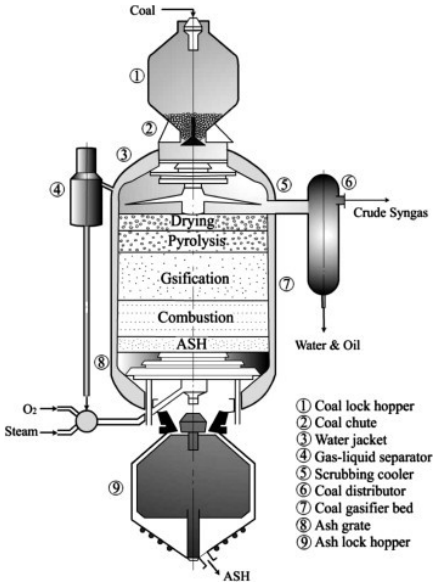

Figure 2.3 Schematic diagram of pressurized Lurgi gasifier [21]

2.2.1.2 Fluidized-Bed Gasifier

Figure 2.4 shows a schematic diagram of a general fluidized bed gasifier. In this type of gasifier, the feedstock is fed from the top, while the gasification agents are fed from the bottom at a sufficient rate to fluidize the coal particles in the bed but not so high that they are carried out of the bed. A cyclone downstream of the gasifier typically collects the larger particles and then recycles them back into the bed. A fluidized bed gasifier creates a homogeneous mixture of fresh coal particles and older, fully gasified, and partially gasified particles. The mixing also keeps temperatures uniform throughout the bed, as shown in Figure 2.4. Temperatures within the bed should be below the initial melting temperature of the ash to avoid agglomeration of the particles [20].

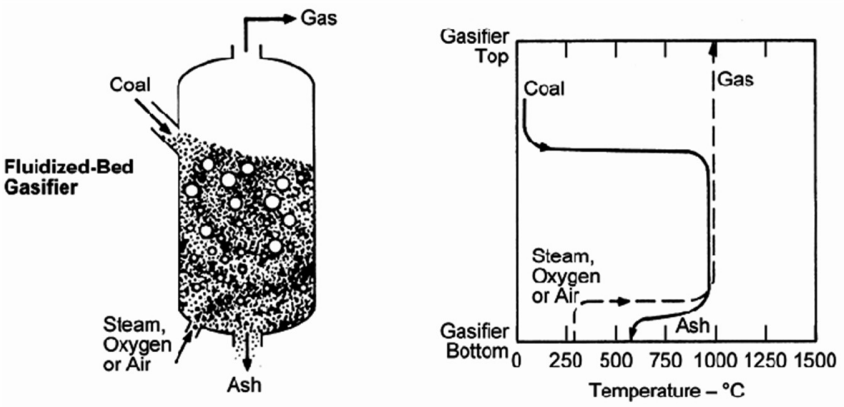

Figure 2.4 Diagram of a generic fluidized bed gasifier [20]

2.2.1.3 Entrained Flow Gasifier

Figure 2.5 shows a schematic diagram of a general entrained flow gasifier. The feedstock (e.g. petroleum coke) and gasification agent are simultaneously fed into the reactor from above in this type of gasifier. To achieve optimal mixing, the feedstocks must be finely ground. Due to the short residence time (about ten seconds), entrained-flow gasifiers must operate at high temperatures to achieve high carbon conversion [20]. Entrained flow gasifiers typically use oxygen to operate at high temperatures above the ash slag temperature [20].

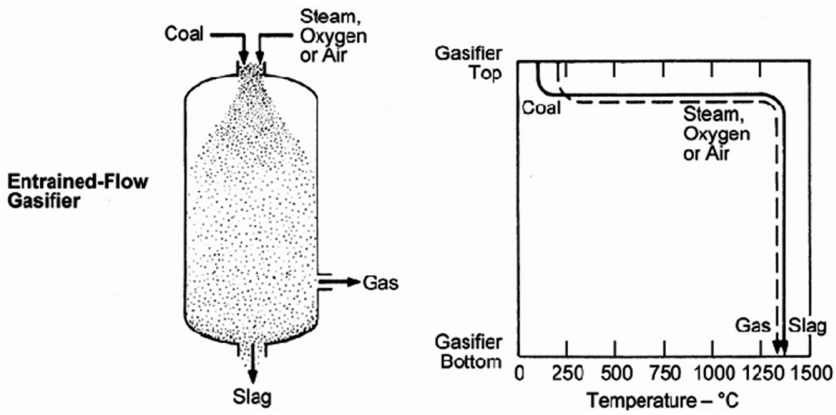

Figure 2.5 Diagram of a general entrained flow gasifier [20]

2.2.2 Gasification Feedstock

The synthesis gas produced depends on the properties of the feedstock used. Figure 2.6 shows feedstock and products of gasification. Gasification technology has been developed to take different types of feedstocks. Coal, petroleum coke, biomass, agricultural waste, industrial and municipal waste, and refinery streams can be used as feedstock for gasifiers. Before feeding feedstock into the gasifiers, the feedstocks must be pretreated by adjusting the moisture content and grain size.

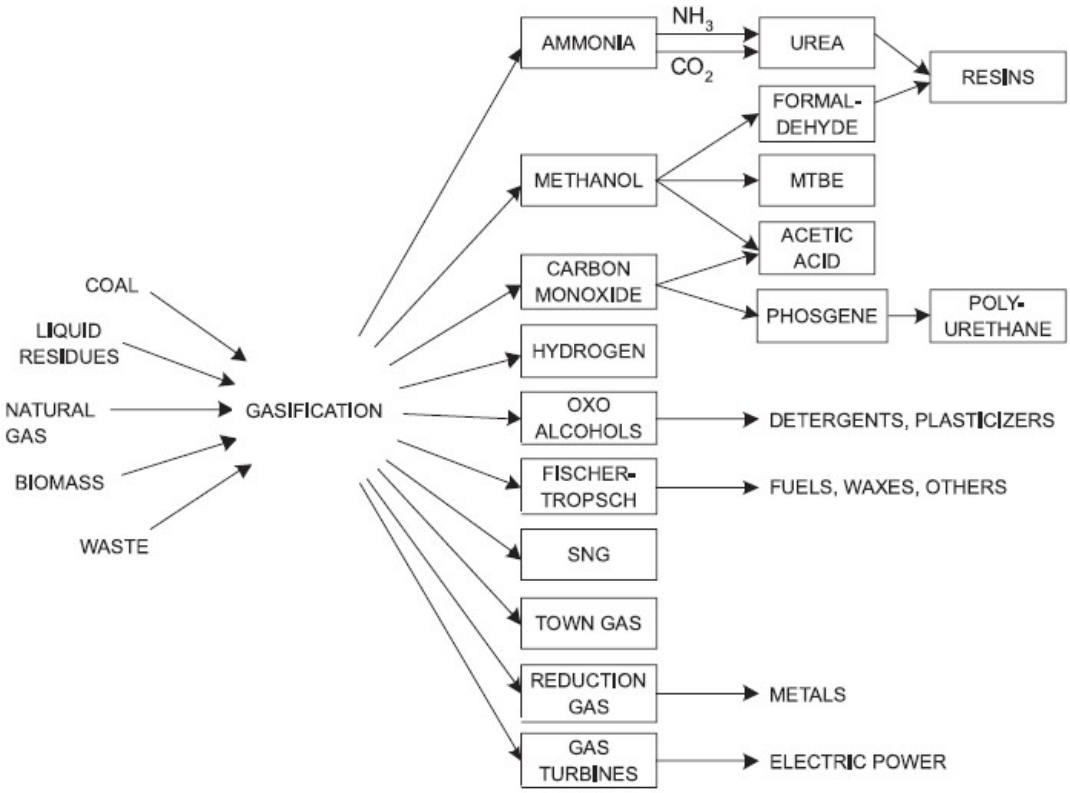

Figure 2.6 Feedstock and products of gasification [22]

2.3 Solid Particles Removal

2.3.1 Introduction

Soltani (2011) [23] defined aerosol as tiny solid particles or liquid droplets with sizes from 0.001 to 1000 µm. Aerosols include various particles such as fine soot, fly ash, drizzle, etc. Removing particulate from a hot gas stream produced in coal-fired power plants has become a potential technology [24], [25]. Removing particulate is crucial to protect heat exchangers, catalyst units, and turbines from corrosion and fouling in a biomass combustion process [26].

Various technologies are used to separate these particles from the producer gas. These technologies can be divided into dry and wet gas cleaning. Dry gas cleaning is usually used before gas cooling when the temperature of the gas is more than 500 ◦C, while wet gas cleaning is used after gas cooling and typically at 20-60 ◦C [27]. Table 2.2 shows the dry and wet gas cleaning systems.

Table 2.2 Classification of mechanical/physical gas cleaning systems [27]

Basic type	Equipment
Dry	Cyclone, rotating particle separators (RPS), electrostatic precipitators (ESP), bag filters, baffle filters, ceramic filters, fabric/tube filters, sand bed filters, adsorbers, etc
Wet	Spray towers, packed column scrubbers (wash tower), impingement scrubbers, venturi scrubbers, wet electrostatic precipitators, OLGA, wet cyclones, etc.

The separation systems presented in Table 2.2 have different separation efficiencies for particles. Figure 2.7 shows the separation efficiency of some equipment for particles, where the separation efficiency of these systems depends primarily on the size of the particles.

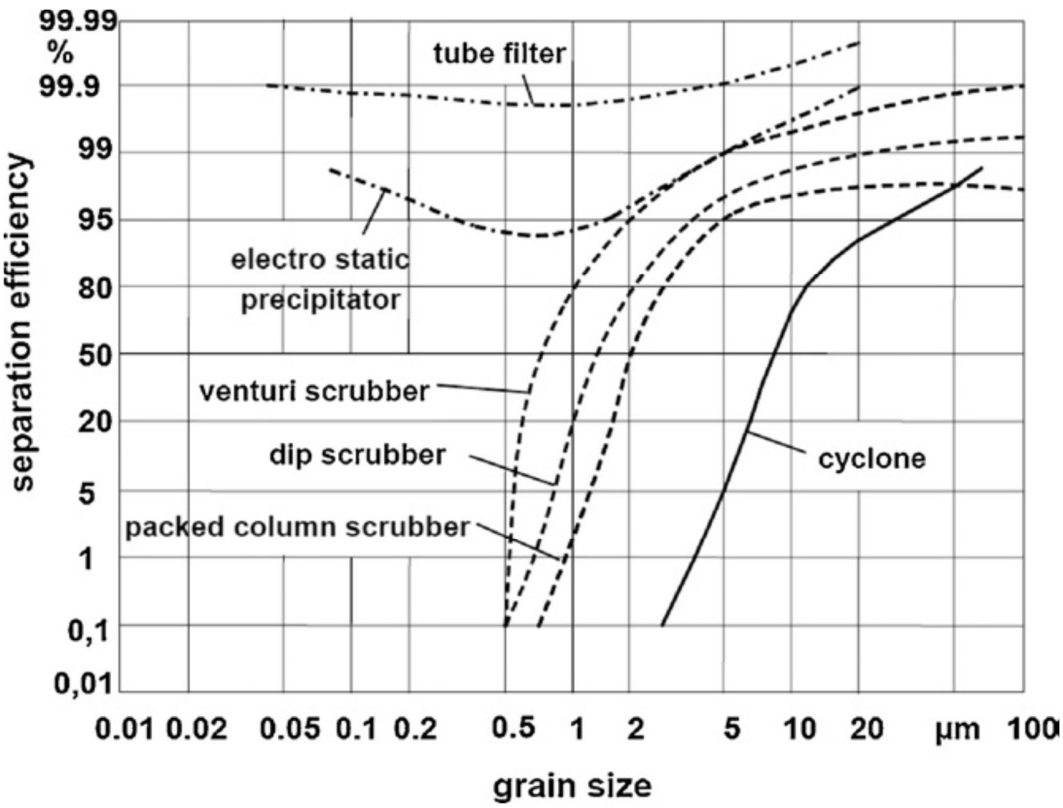

Figure 2.7 Typical separation efficiencies of separation systems [27]

The syngas exiting the gasifier contains solid particles, often of the fly ash type, varying in size from 0.8 to 70 µm [23].To achieve a typical separation efficiency of 99.8%, cyclone and tube filters are the potential separation devices. Based on Figure 2.7. two stages of the separation system are proposed with the first stage is separating particles with a cyclone, followed by the separation stage of the tube filter. With the cyclone, the separation efficiency of 0.1-98% can be achieved for particles of size 3-70 µm, while with the tubular filter, the separation efficiency of 99.8% can be achieved for particles

of size 0.04-20 µm. By these two separation stages, an amount of ash is separated by the cyclone, and the rest of the ash can be separated by the second stage of the tube filter. This contributes to less ash entering the filter and less cake forming on the surface of the filter. The formation of a cake leads to an increase in the gas pressure drop and thus to higher operating costs.

2.3.2 Cyclone

Cyclone separation is the typical method for separating particles from gases because they are simple in design, requires little maintenance, and can also be operated over a wide range of temperatures and pressures [28]. Figure 2.8 shows a schematic flow diagram of a cyclone.

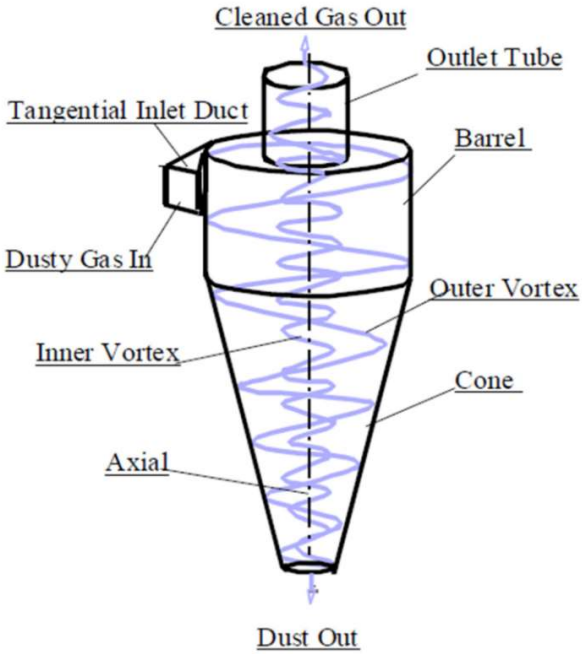

Figure 2.8 Schematic flow diagram of a cyclone [29]

The cyclone consists of four main parts, the stream inlet, the separation chamber, the vortex finder, and the dust chamber. On an industrial scale, two common cyclones are used to separate particles: tangential cyclones and axial cyclones. The main difference between an axial cyclone and a tangential cyclone is the steam inlet. The inlet of the axial cyclone has a guide vane, while the tangential cyclone has a tangential inlet. Tangential cyclones are mainly applied for separating particles from gases, while axial cyclones are favored for separating fine liquid droplets from a gas stream [28].

The principle of separation for tangential and axial cyclones is similar. The particle-laden gas enters the cyclone through the inlet. The tangential cyclone's wall and the axial cyclone's guide vanes turn the gas flow into a rotating motion. The centrifugal forces created by the rotating motion spin the particles towards the cyclone's wall, and the particles fall into the dust container while the clean gas leaves the cyclone at the outlet.

2.3.3 Ceramic Filter Tube

Ceramic filters are widely used in hot gas filtration due to their high filtration efficiency and high thermal resistance to corrosive hot flue gases [30]. Figure 2.9 shows a schematic of a hot gas filter. The raw gas loaded with dust enters the filter from below and then flows to the filter element or candle. The dust sticks to the surface of the filter element while the clean gas passes through the filter element. The ceramic filter element is made of silicon carbide (SiC) because this material has high-temperature stability, high corrosion resistance, high thermal shock resistance, and excellent mechanical properties [26], [31].

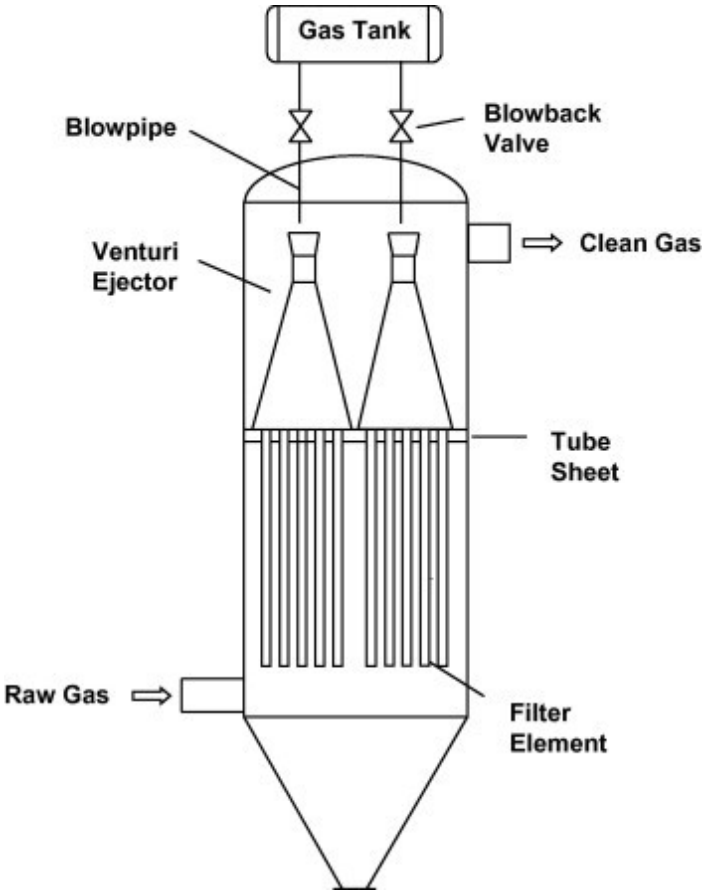

Figure 2.9 Scheme of a hot gas filter [32]

Based on their manufacturing materials, ceramic filters for hot gas treatment can be divided into fibrous ceramic filters and granular ones. Ceramic fibrous filters have high separation efficiency and transmittance but low mechanical strength. In comparison, granular ceramic filters have good mechanical stability, and their filtration characteristics can be easily controlled by changing the size of the powder. In addition, granular filters offer both continuous cleaning efficiency and reusability, which is ideally suited for maintaining steady filtration efficiency in both separation efficiency and pressure drop [30].

2.3.3.1 Mechanism of Filtration

Aust (2007) [33] differentiate between surface filtration and depth filtration, as shown in Figure 2.10. In surface filtration, filtration depends on the diameter of the holes in the structure of the ceramic candle. The particles that have a smaller diameter than the holes pass through the candle, while the particles that have a larger diameter than the holes settle on the surface of the filter and are then separated.

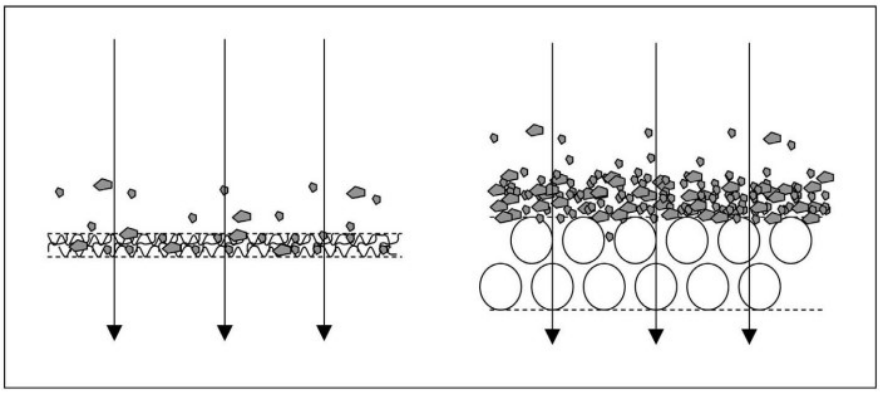

Figure 2.10 Diagram illustrates depth filtration (Left) and surface filtration (right) [33]

By depth filtration, the separation of particles depends mainly on the porous structure of the filter. The most common mechanisms for fibrous filters are deposition, inertial separation, diffusion, and gravity separation. Figure 2.11 illustrates the filtration mechanisms.

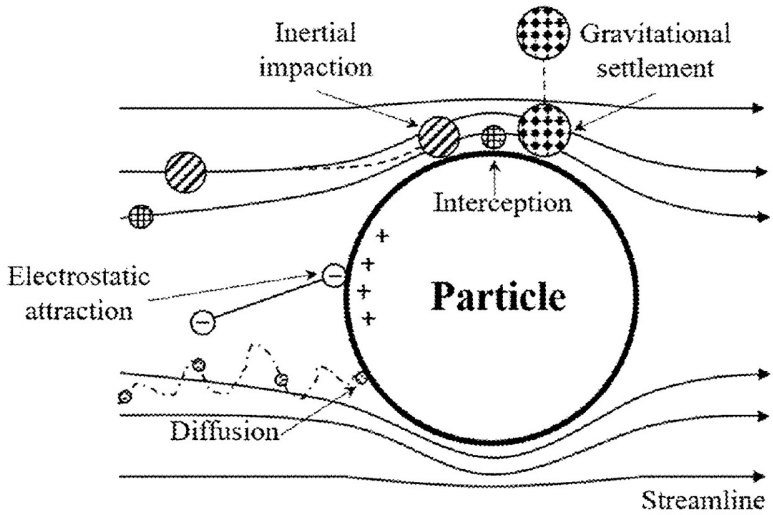

Figure 2.11 Schematic illustration of filtration mechanisms [34]

The interception occurs when a particle follows a streamline that comes into contact with the surface of the filter so that this particle hits the surface of the filter and is intercepted. Impaction occurs when the particles cannot adapt quickly enough to the suddenly changing flow lines near the filter surface due to the inert masses, so the particles fall out of the flow lines and hit the filter. Diffusion occurs by Brownian motion when the particles are tiny, so this motion increases the possibility of the particles hitting the surface of the filter.

2.4 Tar Removal

2.4.1 Introduction

The gasification process converts the feedstocks (e.g. petroleum coke) into raw syngas, a fuel gas mixture consisting primarily of hydrogen, carbon monoxide, tar, and other gases considered contaminants, such as hydrogen chloride, carbon dioxide, and hydrogen sulfide. The produced tar from the gasifier may create fouling and soot accumulation in downstream processes; moreover, tar solubility in the water may generate wastewater treatment difficulties [35].

In literature, many definitions for tar have been reported. All the definitions seek to present a view of the nature of the tar. Besides, these definitions are influenced by the gas quality specifications required for a particular end-use application and how the tar is assembled and analyzed [27]. One of the definitions of tar was described by T. A. Milne et al. (1998) [36] as follows: It is the organics components created under a thermal or partial-oxidation process (gasification) and is supposed to be primarily aromatic. Devi et al. (2005) [37] defined tar as a complex blend of condensable hydrocarbons, which comprises single to multiple ring aromatic compounds along with other oxygen-containing hydrocarbons and complex polycyclic aromatic hydrocarbons. The Energy Research Centre of the Netherlands (ECN) considers that tar consists of organic molecules, which have a higher molecular weight than benzene (benzene is not considered to be tar) [38]. According to C. Unger and M. Ising (2002) [39], tar is a mix of hydrocarbons that can form a highly viscous liquid which may convert to solid accumulations by dropping the temperature of the gaseous phase down to ambient temperature; it consists of carbon, hydrogen, and other organic linked elements such as oxygen (O), nitrogen (N), or sulfur (S).

Tar can be classified based on different criteria. C. Li and K. Suzuki (2009) [40] listed tar into five classes: GC-undetectable, heterocyclic aromatics, light aromatic (one ring), light PAH compounds (two to three rings), and heavy PAH compounds (four to seven rings). Several studies [36], [41]–[43] published that tar can also be classified into primary, secondary, and tertiary tar.

Wolfesberger, Aigner, and Hofbauer (2009) [43] described how the tar components are formed and the influence of temperature on the type of tar components formed. The primary tar components begin to appear during the pyrolysis process, the complex polymers that make the main parts of biomass (cellulose, hemicellulose, and lignin) are broken down from cellulose and hemicellulose, and tar components like alcohols, ketones, aldehydes, or carbon acids are formed, whereas bi-and trifunctional monoaromatics mostly substituted phenols are derived from lignin [43]. By growing temperature and attendance of an oxidant, a portion of the cellulose-contributed primary tars convert to small gaseous molecules. The remaining primary tar creates secondary tar. Examples of secondary tar components are alkylated mono- and diaromatics, including heteroaromatics such as pyridine, furan, dioxin, and thiophene [43]. At a temperature above 800 C, components such as benzene, naphthalene, phenanthrene, pyrene, and benzopyrene (polynuclear aromatic hydrocarbons (PAH)) are created; these components form the tertiary tars components [43].

2.4.2 Tar Treatment

The methods of tar removal can be categorized into primary and secondary measures based on the place where the tar is removed [44]. The primary method is to remove the tar by applying processes such as thermal or catalytic cracking in the gasifier. In contrast, in the secondary methods, the tar is separated outside the gasifier [27]. Although the primary methods have some disadvantages, such as the complex construction of the gasifier and the limited flexibility of feedstock, it promises high tar removal efficiency by promoting this technology with time [27].

Currently, secondary methods are fitting for tar separation from the produced syngas because of their low cost and simple measures [45]. The wet scrubbing process is one of the secondary methods, which applies an absorber to exclude the tar. The absorber can be a plate or packed column. It is recommended to use the packed absorber because of its high capacity [46]. Furthermore, the packed absorber can operate with lower pressure drops than the tray column [47]. The packed absorber materials are categorized into random or structured packing. Modern random packings have a wide range of geometries and shapes and are made from ceramic, metal, or plastics. The structured packings are ideal for lower pressures (i.e., less than 2 bar) and lower liquid rates (i.e., less than 50 $m^3/m^2 \cdot h$) [47]. A suitable solvent must be appropriately selected for the absorption process since the solvent type significantly influences equipment sizing and operating costs [48]. Phuphuakrat, Namioka, and Yoshikawa (2011) [49] summarized that the absorption process should concentrate on separating the components of the tar that cause the fouling problem. These components as per the tar classification of Bergman et al. (2002) [50] are heterocyclic compounds, light polycyclic aromatic hydrocarbons such as naphthalene, and heavier hydrocarbons that condensate easily. According to Phuphuakrat, Namioka, and Yoshikawa (2011) [49], light aromatic hydrocarbon tares (one ring aromatic hydrocarbon) are not the reason for blocking and fouling.

Phuphuakrat, Namioka, and Yoshikawa (2011) [49] reviewed the absorption efficiencies of tar components by different solvents, as shown in Table 2.3. They studied scrubbing liquids such as diesel fuel, vegetable oil, engine oil, and water as a solvent to remove the tar.

Table 2.3 Absorption efficiencies of tar components by different solvents (%) [49]

Absorbent	Water	Diesel fuel	Biodiesel fuel	Vegetable oil	Engine oil
Benzene	24.1	77.0	86.1	77.6	61.7
Toluene	22.5	63.2	94.7	91.1	82.3
Xylene	22.1	-730.1	97.8	96.4	90.7
Styrene	23.5	57.7	98.1	97.1	91.1
Phenol	92.8	-111.1	99.9	99.7	97.7
Indene	28.2	97.9	97.2	97.6	88.7
Naphthalene	38.9	97.4	90.3	93.5	76.2

From Table 2.3, it can be observed that diesel fuel is the most e effective solvent used to remove naphthalene. However, diesel is considered an uneconomic solvent because of its simple evaporation, which raises the losses of the solvent [49]. Vegetable oil has proven to be efficient in separating naphthalene [45]. The water has a comparatively high removal efficiency for phenol because the phenol is a hydrophilic component, and it can lose H+ (ion) from a hydroxyl group, whereas the other components are nonpolar substances [45]. Applying water as a solvent to remove the tar achieves an efficiency of about 31.8%. However, water is not an effective solvent since tar has low solubility in water, and the separation of the tar from the water is difficult and expensive [45].

Phuphuakrat, Namioka, and Yoshikawa (2011) [49] placed the efficiency of the solvent as vegetable oil > engine oil > water > diesel fuel. Paethanom et al. (2012) [51] published the tar removal efficiency of vegetable oil as 89.8% and cooking oil as 81.4%. Bhoi (2014) [52] investigated the effect of two kinds of vegetable oils, soybean, and canola oil, to separate the tar. The author summarized that there is no significant difference between the soybean and canola oils for all the absorbent conditions like temperatures and volumetric flow rates. Ozturk and Yilmaz (2006) [53] analyzed the relationship between the operating time and removal efficiency of some oily solvents like benzene and toluene. They concluded that the removal efficiency declines with time because of increasing the tar concentration in the absorbent.

In the industry, a common system for tar removal, the OLGA process, was developed by ECN [38]. The OLGA process, as seen in Figure 2.12, consists of two main steps: The first step is the collection of the liquid tar by a collector, followed by a second step aimed at separating the gaseous tar by absorption. In the first step, the gas stream enters the collector at a temperature higher than the dew point of the tar. The temperature of the gas stream cools along with the collector due to contact with the scrubbing liquid, causing the tar fraction to be condensed and then collected by scrubbing. The gas stream is then directed into the absorber to remove the remaining gaseous tars that have not condensed and collected in the collector. The gas stream comes into contact with the scrubbing liquid, capable of dissolving the gaseous tar components through the absorption process. The gas stream leaves the absorber at a temperature higher than the dew point of water, and the scrubbing liquid is directed to the stripper for regeneration and then returned to the absorber.

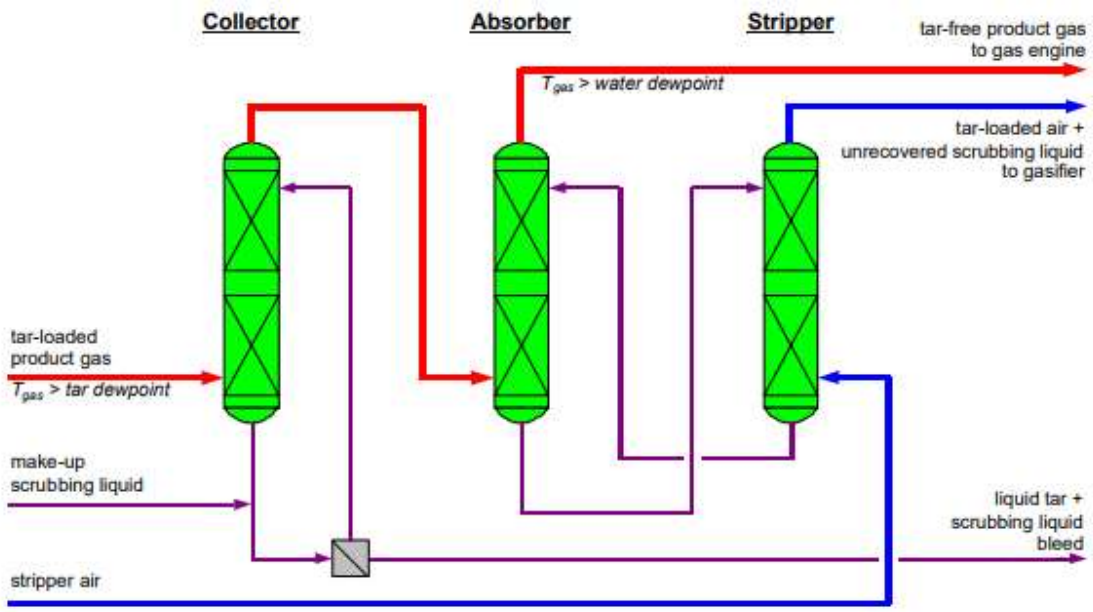

Figure 2.12 Diagram of OLGA process [35], [38]

2.5 Water-Gas Shift Reaction

The water-gas shift reaction (WGSR) is the reaction of carbon monoxide and water vapor to form carbon dioxide and hydrogen as follows:

$$CO + H_2O \leftrightarrow CO_2 + H_2 \qquad \Delta H°298 = -41.09 \text{ kJ/mol} \tag{2.14}$$

The water-gas shift reaction is moderately exothermic, and its equilibrium constant decreases with increasing temperature. The equilibrium is favorable for the formation of products at lower temperatures. Kinetically, the WGSR reaction is favorable at elevated temperatures. The Presence of steam in amounts exceeding the stoichiometric amount enhances the conversion [54].

The water-gas reaction is required to change the CO/H_2 ratio for downstream processes such as methanol synthesis and Fischer-Tropsch reactions. Adjustment of the ratio for Carbon monoxide and hydrogen for mole ratio of (1:3) is ideal and usually required [55].

To achieve high conversion, a suitable catalyst must be selected. The literature includes a comprehensive classification of catalysts used for the WGSR, such as high-temperature catalysts (HTS) and low-temperature catalysts (LTS). Callaghan (2006) [56] reports that the typical composition of a commercial LTS catalyst is 32-33% CuO, 34-53% ZnO, and 15-33% Al_2O_3. The active catalytic species is CuO. The role of the ZnO is to give structural support and inhibit sulfur poisoning of the copper. The Al_2O_3 helps inhibit the dispersion and shrinkage of the pellets. The LTS shift reactor operates in a temperature range of 200-250 °C. The upper-temperature limit is due to the copper being exposed to thermal sintering [57].

Newsome (1980) [58] reports that the typical composition of a commercial HTS catalyst is 74.2% Fe_2O_3, 10.0% Cr_2O_3, and 0.2% MgO. The chromium serves to stabilize the iron oxide and inhibits sintering. HTS catalysts are operated in a temperature range from 310 °C to 450 °C. The temperature

increases with the reactor's length due to the reaction's exothermic nature. Commercial reactors run from atmospheric pressure to 8375 kPa (82.7 atm) [58].

In the conversion plants, the water gas shift reaction is carried out in several adiabatic stages consisting of a high-temperature shift (HTS) followed by a low-temperature shift (LTS) with cooling between the systems [59].

Figure 2.13 shows an industrial process of the WGS reaction. It consists of a two-stage WGR process with an intercooler. The first stage is called high-temperature shift (HTS), and the second stage is called low-temperature shift (LTS). First HTS has the advantage of high reaction rates. However, it leads to incomplete conversion of carbon monoxide. A subsequent low-temperature shift reactor reduces the carbon monoxide content to <1%. [60], [61].

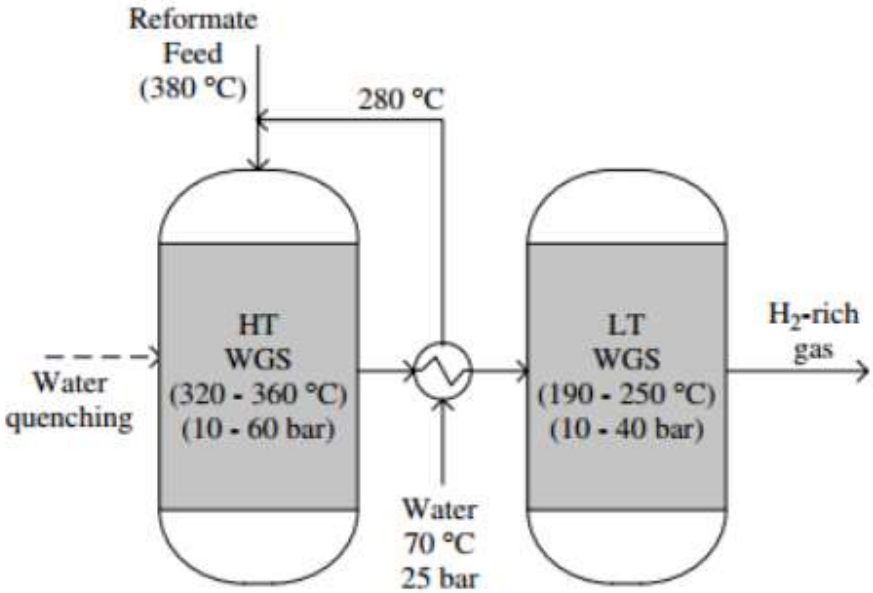

Figure 2.13 Stage water gas shift reaction process flow diagram [59]

The high-temperature shift (HTS) is carried out in the first stage at 320-360 °C, which reduces the CO content to 2-3%, while the second stage is the low-temperature shift (LTS), which is carried out in a temperature range of 190-250o C and reduces the concentration of CO content to 1-0.5% [60]. Various catalysts are used in the two stages; iron oxide/chromium-based catalysts are suitable for HTS, while copper-zinc-based catalysts are used for LTS [60].

2.6 COS Hydrolysis

The COS hydrolysis reaction aims to convert sulfur bound in COS molecules into molecules bound in hydrogen sulfide. Hydrogen sulfide is easily separated in an acid gas removal system that uses amino solutions that selectively separate hydrogen sulfide. The bound sulfur is separated because it poisons the catalysts and causes corrosion to the equipment for subsequent syngas applications. The COS hydrolysis reaction occurs according to the following equation [62]:

$COS + H_2O \rightleftarrows H_2S + CO_2$ $\Delta H^oR = -30$ MJ/kmol (2.15)

The equilibrium for the COS conversion is favorable at low temperatures. On an industrial scale, the reaction occurs in a reactor with catalysts and at a temperature range of 150-200°C. The suitable catalysts for the reaction include pure activated alumina, promoted chromium oxide-alumina, or titanium oxide [62].

2.7 Acid Gas Removal

2.7.1 Introduction

The syngas must be purified from acid gases to protect downstream catalysts for chemical processing or to meet emission regulations. Chemical syntheses such as Fischer-Tropsch and methanol synthesis require sulfur levels below one ppm [6]. For power generation applications that allow higher sulfur levels, about 10 to 30 ppmv sulfur is required [7]. The absorption process is a typical separation process applied to remove acid gases. Absorption is the dissolution of gases or vapors (absorbate) in a liquid solvent (absorbent).

There are two types of absorption, physical absorption, and chemical absorption. Henry's law describes the physical absorption process. Acid gases are absorbed at high pressure and low temperature and desorbed at reduced pressure and elevated temperature. Figure 2.14 shows the partial pressure pi of component i versus the molar fraction xi in the liquid phase. It can be seen that based on Henry's law and Raoul's law, there is a linear correlation between the partial pressure pi and the molar fraction xi. Increasing the partial pressure pi will increase the liquid load capacity of component i. Henry's law is expressed as follows [63]:

$$y_i = \frac{H_i}{p} x_i \tag{2.16}$$

Raoul's law is given as follows [64]:

$$p_i = x_i p_{o,i} \tag{2.17}$$

For real gas the correlation between the partial pressure pi and molar fraction xi can be expressed as follow [64]:

$$p_i = \gamma_i \, x_i p_{o,i} \tag{2.18}$$

Where p_i is the partial pressure of component i, $p_{o,i}$ is the saturation vapor pressure of component i at temperature T, p is the total pressure of the gas, x_i is the mole fraction of component i in the liquid phase, y_i is the mole fraction of component i in the gas phase, and H_i is Henry's law constant, γ_i is activity coefficient.

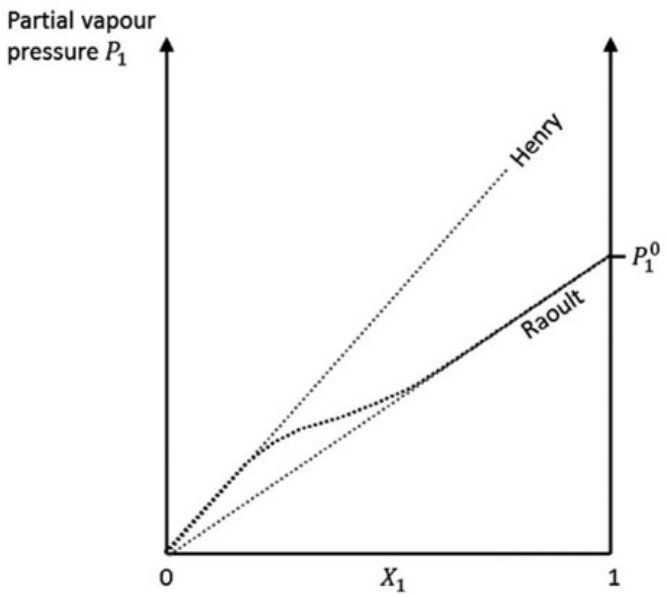

Figure 2.14 Illustration of the correlation between the partial pressure and mole fraction X1 solute in a binary solution [65]

Chemical absorption is based on the transfer of the gases to be separated from the gas phase to the liquid phase, and then these gases react with the solvent. Chemical absorption is desirable at a small partial pressure of the gas which will be separated. Figure 2.15 compares the solvent absorption capacity as a function of CO_2 partial pressure. It can be seen that at low partial pressures of CO_2, chemical Absorption has a higher Absorption capacity for CO_2 than physical absorption. Furthermore, at high partial pressure, physical absorption has a higher Absorption capacity for CO_2 than chemical absorption.

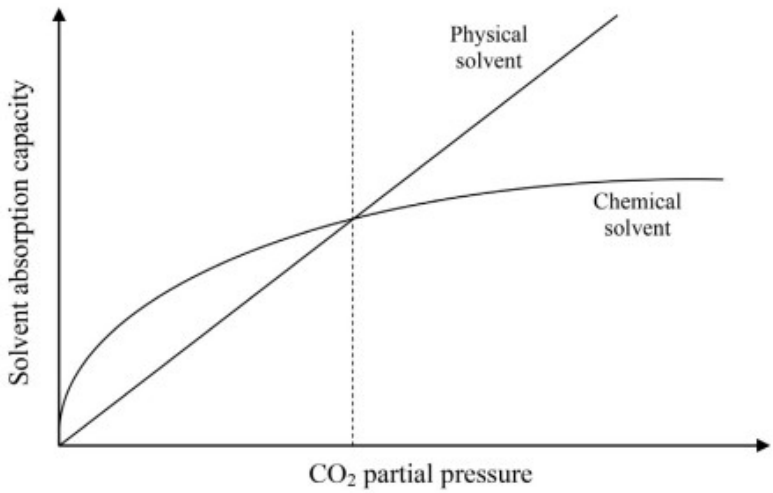

Figure 2.15 Solvent loading for chemical and physical solvents vs. CO2 partial pressure [66]

In the chemical industry, absorption is a broad process that uses mass transfer to separate the gas. The absorption column is considered one of the main parts of the absorption process. Two standard columns are used for the absorption process, the tray column, and the packed column.

2.7.2 Plate Column

The plate column consists of many trays or plates distributed along the column, as shown in Figure 2.16. The liquid is entered from the top of the column and flows down on the trays due to gravity. The gas is entered from the bottom and rises due to pressure. The liquid and gas come into contact on the tray, which causes the mass transfer between the gas and the liquid. The gas to be separated passes from the gaseous phase to the liquid phase, where it is absorbed. The liquid continues to flow down to the next tray below while the gas rises to the upper tray. The clean gas leaves the column from the top, while the liquid leaves the column from the bottom.

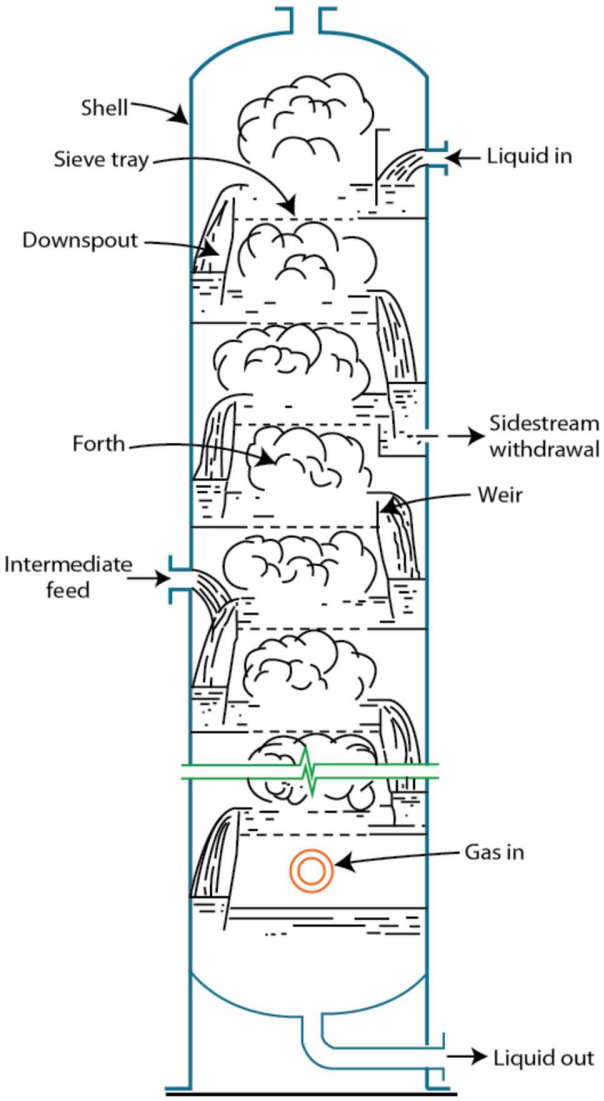

Figure 2.16 Schematic diagram of a plate column [67]

Tray's design plays an essential role in increasing the efficiency of mass and heat transfer, as well as the efficiency of the absorption process. Several calculations are required to design a tray, such as the diameter of the tray, the number of holes, the hole area, the area of the downcomer, the weir height, and the spacing between the trays. Figure 2.17 shows the areas and parts of the tray.

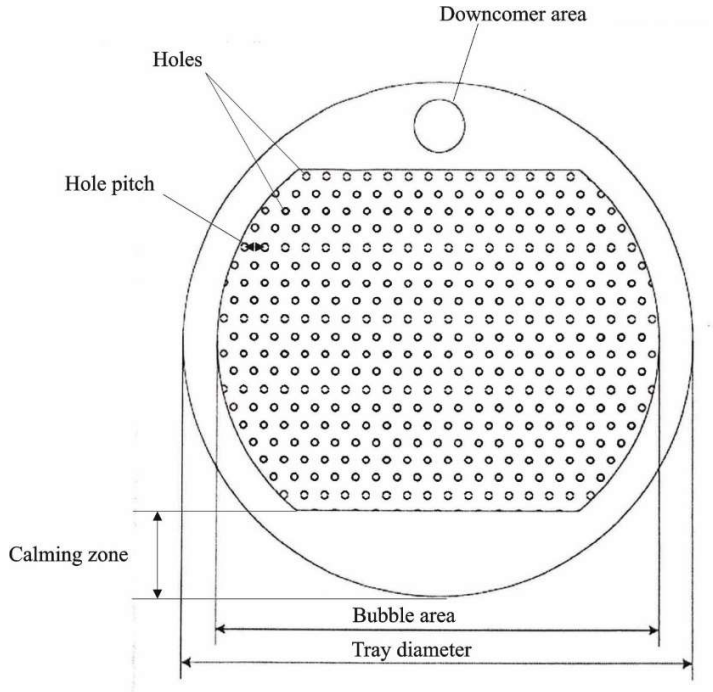

Figure 2.17 Sieve tray areas

There are three common types of trays, bubble cap tray, valve tray, and sieve tray.

2.7.2.1 Bubble Cap Tray

Figure 2.18 illustrate a Bubble cap tray and how it operates. A bubble cap consists of a chimney attached to the tray through a hole and a cap placed above the chimney. The gas flows up through the chimney and is directed down the annular space between the chimney and the cap. Finally, the gas diffuses into the liquid. Bubble cap trays have advantages, such as improving gas-liquid contact under shallow liquid operating conditions [67]. In addition, using a bubble lid can avoid the problem of weeping, but they also have some disadvantages, such as the high cost and the high-pressure drop in the tray [68].

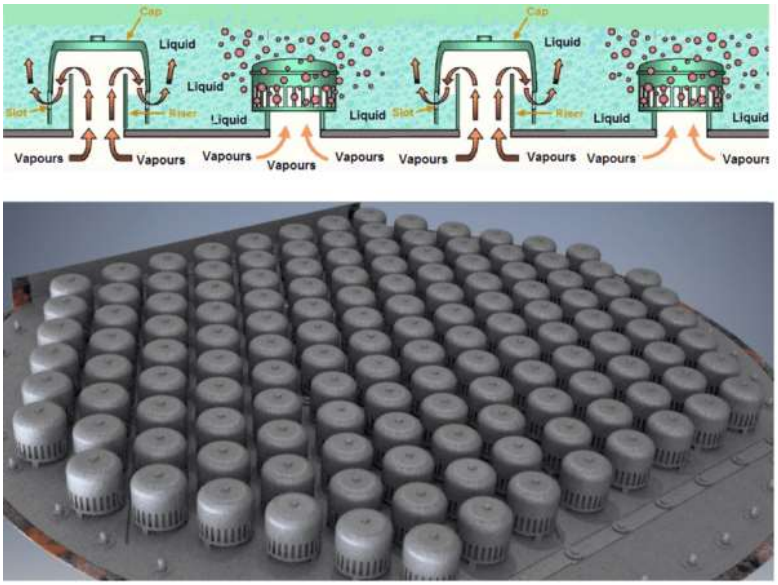

Figure 2.18 Bubble Cap Tray [110]

2.7.2.2 Valve Tray

Figure 2.19 illustrates valve trays and how it operates. The valve tray consists of holes covered with fixed or movable valves that allow the gas to diffuse into the liquid phase. Valve trays have some advantages, such as improving gas-liquid contact at shallow liquid levels and avoiding the problem of weeping [67].

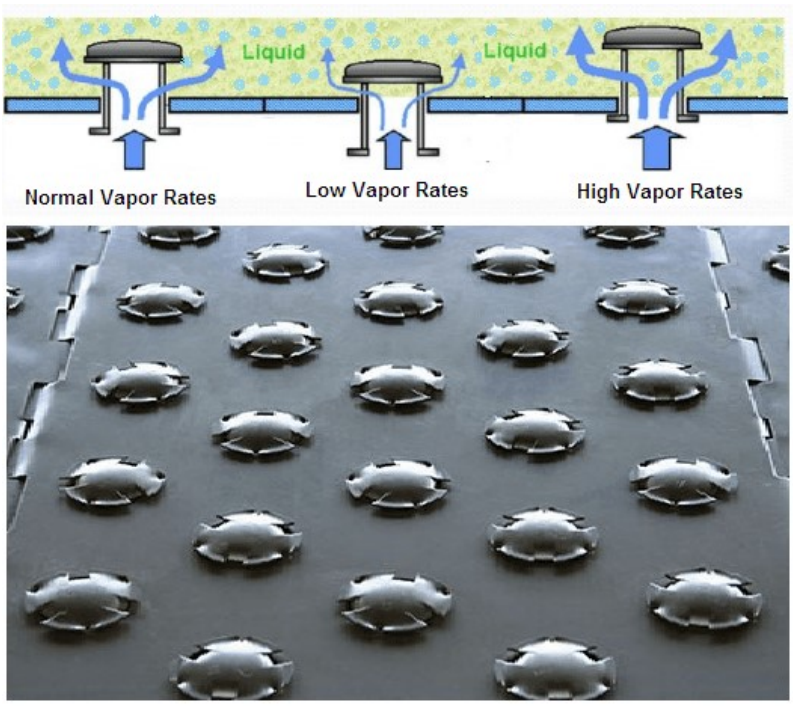

Figure 2.19 Valve Tray [110]

2.7.2.3 Sieve Tray

Figure 2.20 shows the sieve tray and how it operates. The Sieve tray consists of many holes distributed on the tray. The gas flows through the holes and comes into contact with the liquid. The advantage of the tray is that it is too cheap compared with other tray types. However, it has some disadvantages, such as it may cause weeping when the gas velocity is low.

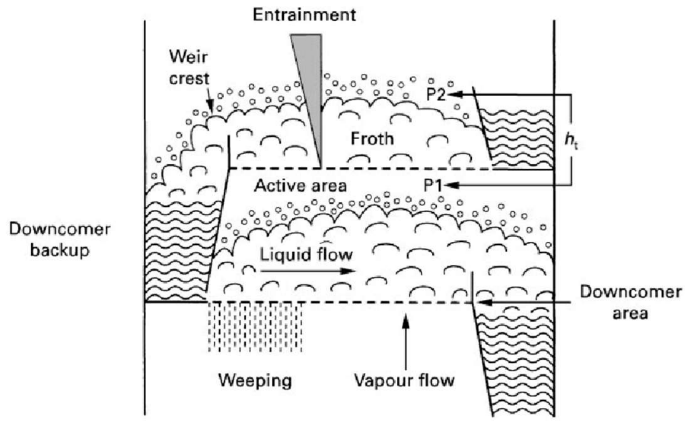

Figure 2.20 Sieve tray operation schematic diagram [69]

Every sieve tray has limited operation conditions regarding gas and liquid flow rate. Figure 2.21 shows the satisfactory operating condition of the sieve tray. It can be said that outside this limited area, some problems occur such as coning, weeping, flooding, and downcomer backup. Coning formation in the tray occurs due to the low flow rate of the liquid in comparison to the flow rate of gas, causing the liquid to be forced away from the opening of the tray. When the flow rate of the gas is too low, that causes weeping. The weeping phenomenon is when the liquid flows through the holes of the tray. Another problem that occurs is entrainment, which happens at a high flow rate of the gas. Entrainment occurs when liquid froth reaches from the lower tray to the upper tray. Flooding occurs at high gas velocities, known as flooding velocities. The downcomer backup occurs at a high flow rate of the liquid. This leads to liquid accumulation on the tray, which increases the pressure drop of the tray. In this case, the liquid backs up into the downcomer.

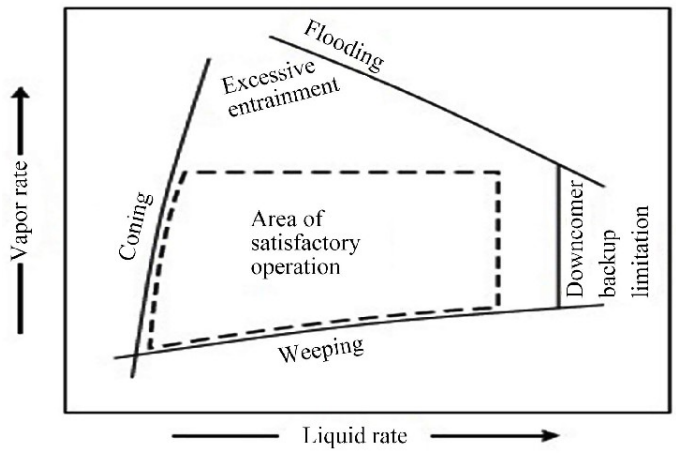

Figure 2.21 Limits of satisfactory sieve tray operation [70]

2.7.3 Packed Column

The packed column consists mainly of a column filled with packing elements. The packing elements are materials of different shapes and sizes. The purpose of these elements is to increase the contact area between the gas and liquid phases. Packing materials are made of metal, plastic, or ceramic. There are different types of packing, such as structural and random packing. The gas enters the column from the bottom, while the liquid enters the column from the top through a liquid distributor. The purpose of the liquid distributor is to improve the distribution of the liquid on the surface of the packing elements. The packing material is located on the packing support. Figure 2.22 shows a packed column and the different types of packing.

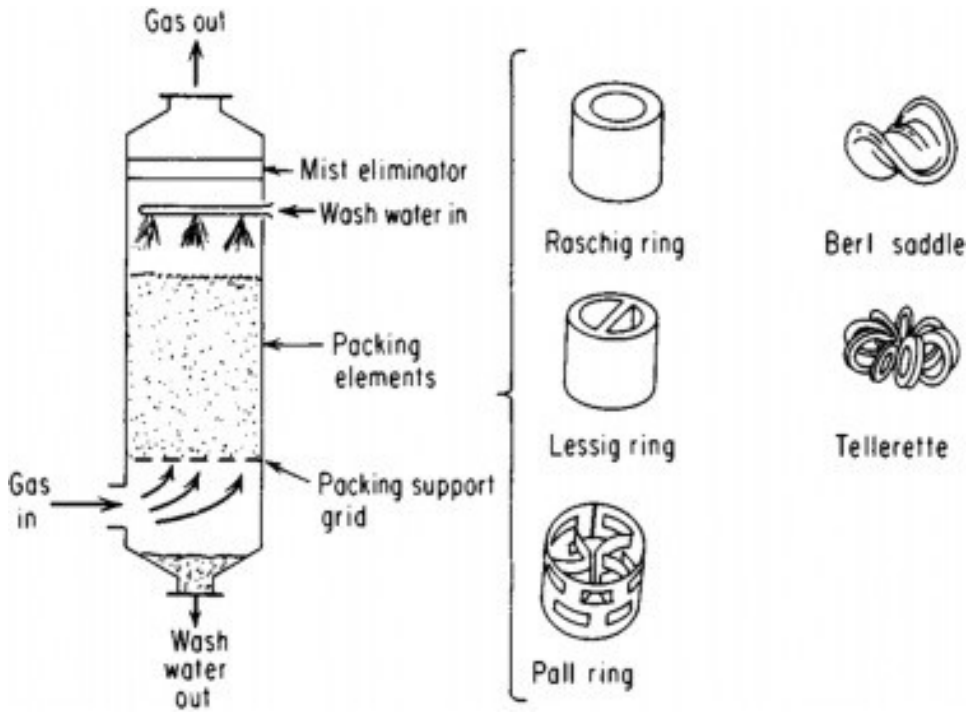

Figure 2.22 Packed column and types of packing elements [71]

2.7.4 Absorption Technology

Figure 2.23 shows a flow diagram of the conventional absorption process. The absorption technology for acid gas removal mainly consists of the absorption column and the stripper. The absorption column can be a plate column or a packed column. The absorbent enters the absorber from the top, and the waste gas containing acid gases enters the absorber from the bottom. The gas and liquid phases come into contact with each other on the trays or packing. The absorbent has properties, such as a high capacity and selectivity to absorb acid gases. The acid gases pass from the gas to a liquid phase and are absorbed. The rich absorbent is sent to the stripper for regeneration and then recycled to the absorber as a lean absorbent.

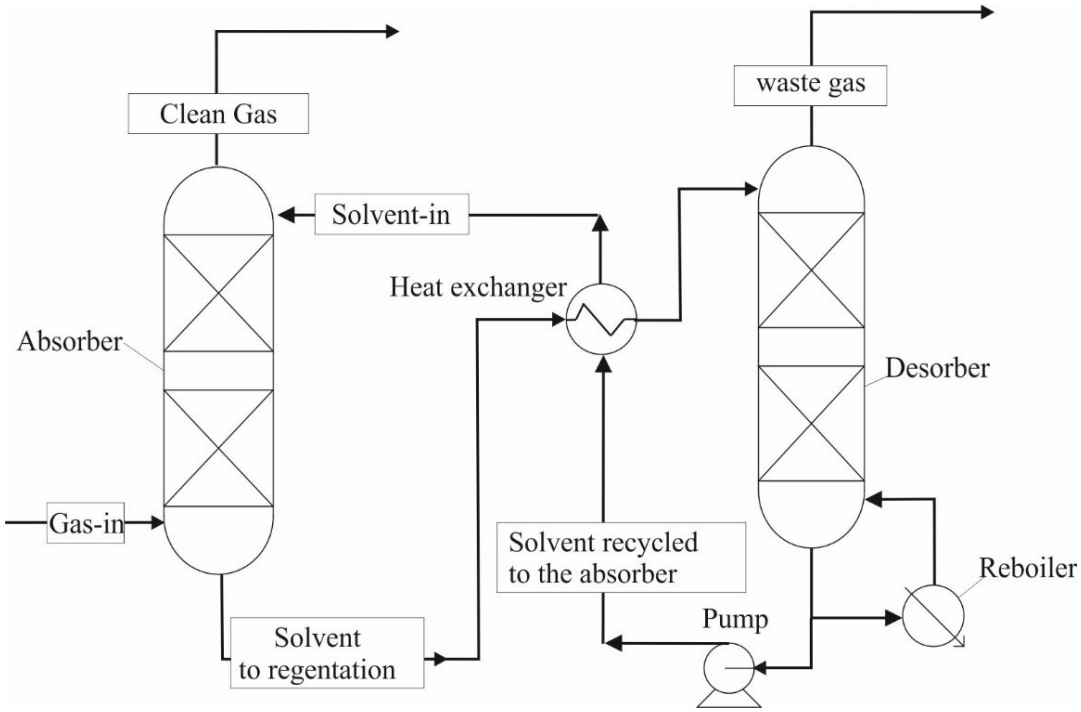

Figure 2.23 Flow diagram of the conventional absorption process

Many commercial processes have been developed based on absorption technologies to absorb acid gas. Some of them are based on the principle of physical absorption, such as the Rectisol process, the Selexol process, and the Purisol process. And others are based on the principle of chemical absorption, such as the absorption with amine solutions.

2.7.4.1 Rectisol Process

The Rectisol process is commercially the most widely used physical absorption process to separate acid gases. In the Rectisol process, methanol (CH_3OH) is used as a physical solvent to remove carbon dioxide, hydrogen sulfide, and carbonyl sulfide. Figure 2.24 shows a possible process layout for the Rectisol process. The methanol enters the absorber from the top at a low temperature of about -40 to -62°C. At these temperatures, the selectivity of methanol for hydrogen sulfide to carbon dioxide is about 6/1, which allows very deep desulfurization. It can be produced as a clean gas containing less than 0.1 ppm of sulfur and carbon dioxide. The advantage of this technique is a low-cost, stable, available solvent and a very flexible process. The main disadvantage of this method is the need to chill the solvent, which has high capital and operating costs [55].

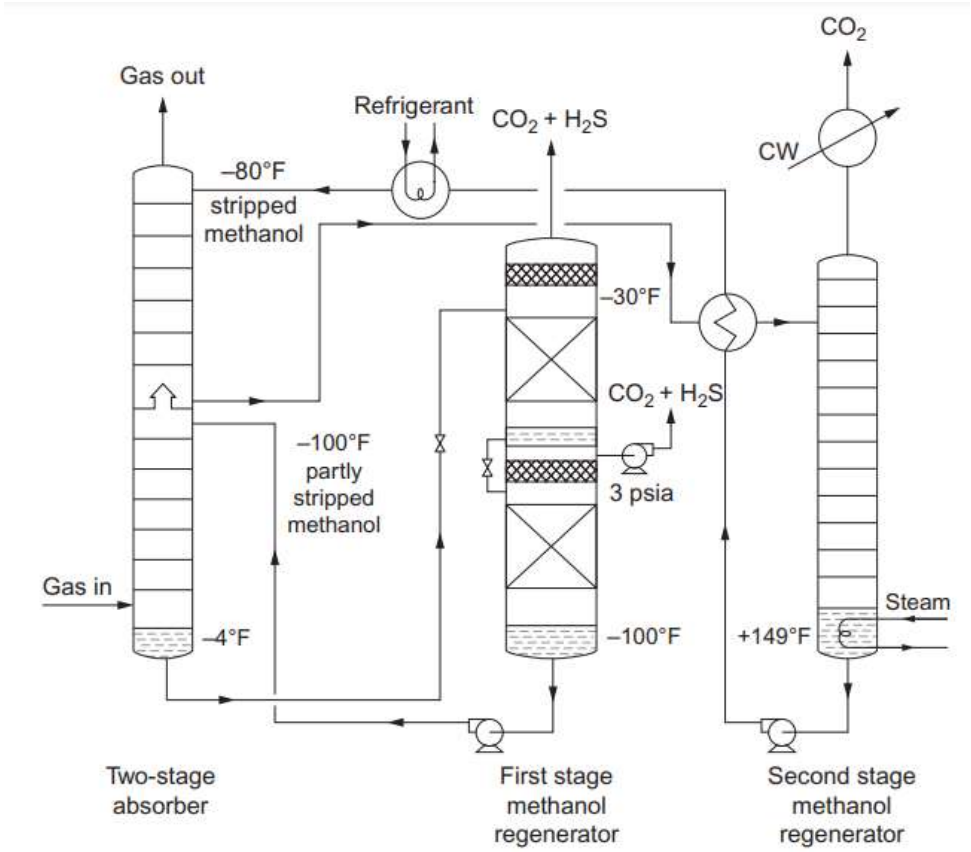

Figure 2.24 Rectisol process [55]

2.7.4.2 Selexol Process

Figure 2.25 shows a possible process layout for the Selexol process. The Selexol process uses dimethyl ether from polyethylene glycol as the physical solvent for acid gases. Operating pressures in the Selexol process are typically 290 to ≈1740 PSIG. The operating temperature is usually between 15 and 100°F. The ratio of absorption coefficients for H_2S, COS, and CO_2 is about 1:4:9. In a gasification system, it is desirable to convert COS to H_2S before Selexol scrubbing. The low viscosity of the solvent, low pressure drop, and low cost make this process so attractive for industrial applications. One of the disadvantages of this process is the high operating pressures [72].

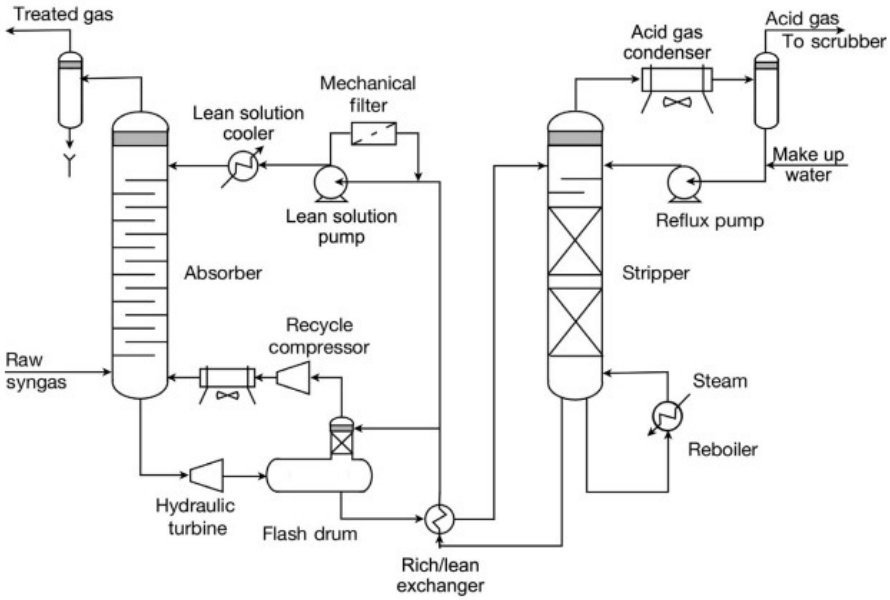

Figure 2.25 Selexol flowsheet for selective H_2S removal [72]

2.7.4.3 Purisol Process

Figure 2.26 shows a possible process layout for the Purisol process. The purisol process uses N-methyl-2-pyrrolidone (NMP Purisol) as a solvent, which has a high absorption capacity for H_2S and CO_2.

The purisol process differs from other widely used absorption methods in that the rich solvent leaves the bottom of the absorber and goes into the reabsorber. In the reabsorber, Acid gases and hydrocarbons are released from the rich solvent at the bottom and go up in countercurrent with the solution.

The advantage of this process is the low regeneration heat requirement and selectivity in removing H_2S over CO_2. The disadvantage of the process is the requirements of high operating pressure and high partial pressure of the acid gas [73].

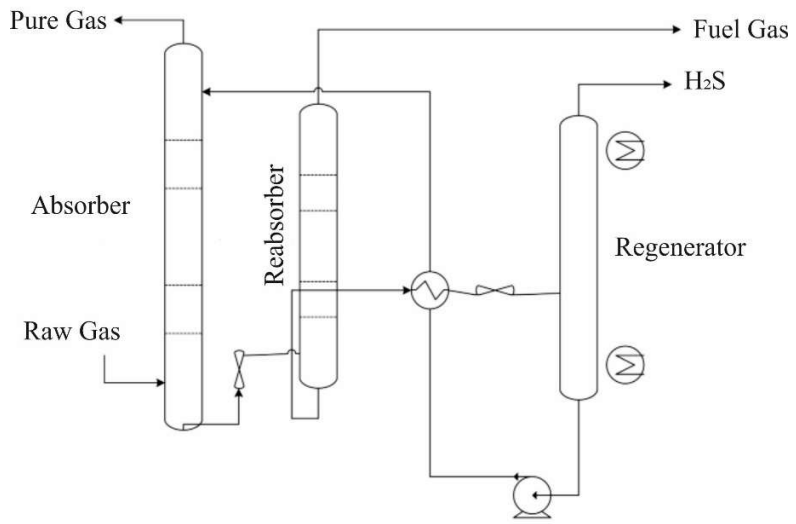

Figure 2.26 Typical process flow diagram for the Purisol process [73]

2.7.4.4 Amine Absorption Process

The amine absorption process is considered a chemical absorption. The Amine absorption process refers to the process in which an aqueous amine solution is used to absorb acid gas. Amine absorption is applied in gas processing plants, oil refineries, and other industries.

One of the advantages of the amine absorption process is that it is suitable when the partial pressure of the gas is low. One of the disadvantages of the amine absorption process is the required energy for the regeneration of the chemical solvent, which needs thermal energy for regeneration.

Three common amines are used for CO_2 capture: primary amines, secondary amines, and tertiary amines. Figure 2.27 shows the structure of the three common amines.

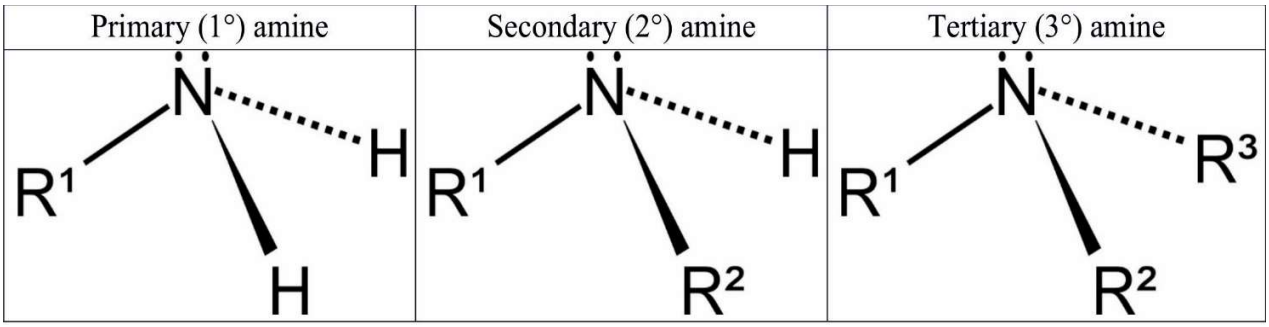

Figure 2.27 Structure of the three common amines (Reproduced) [111]

The three types are distinguished according to the number of carbon atoms in the roots R^1, R^2, and R^3, attached to the nitrogen atom. Each amine type has at least one hydroxyl group and one amino group. The hydroxyl group is responsible for reducing the vapor pressure and increasing the solubility in water. In contrast, the amino group creates the necessary alkalinity in water solutions to allow the absorption of acidic gases [12]. Figure 2.28 shows structural formulas for commercial alkanolamines that belong to the kinds mentioned above: primary amines such as monoethanolamine (MEA) and 2-

(2-aminoethoxy) ethanol (DGA), secondary amines such as Diethanolamine (DEA) and Diisopropanolamine (DIPA), tertiary amines such as triethanolamine (TEA) and methyldiethanolamine (MDEA).

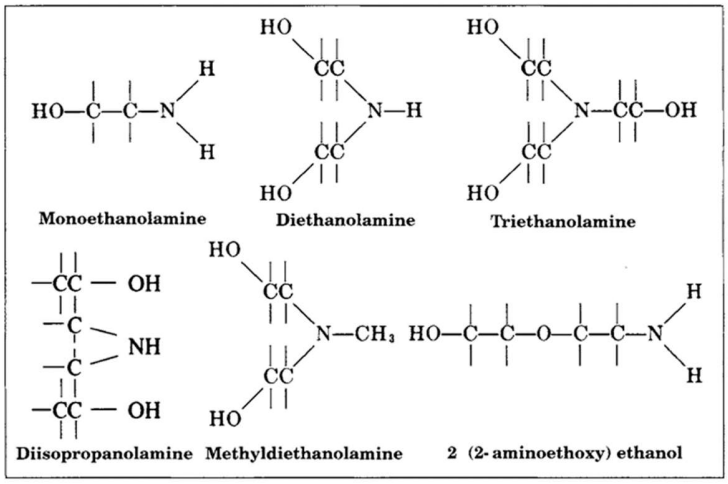

Figure 2.28 Structural formulas for alkanolamines [74]

The mechanism of the reaction between the primary and secondary amine solution and CO_2 is demonstrated as follows: first, the amine reacts with CO_2 to form a zwitterion and then to form a carbamate as follows [75]:

$$RR'NH + CO_2 \leftrightarrow RR'NH^+COO^-(\text{Zwitterion}) \tag{2.19}$$

$$RR'NH^+COO^- + RR'NH \leftrightarrow RR'NCOO^-(\text{Carbamate}) + RR'NH_2^+ \tag{2.20}$$

The overall reaction is,

$$2RR'NH + CO_2 \leftrightarrow RR'NCOO^- + RR'NH_2^+ \tag{2.21}$$

$$RR'NCOO^- + H_2O \leftrightarrow RR'NH + HCO_3^- \tag{2.22}$$

Donaldson and Nguyen (1980) [76] describe the reaction mechanism of a tertiary amine with CO_2 as base-catalyzed hydration. This can be illustrated as follows:

$$RN + H_2O + CO_2 \rightarrow RN^+H + HCO_3^- \tag{2.23}$$

In addition to this reaction, the following reactions can also occur in the case of an aqueous solution [12],

$$RN + H_2O \rightarrow RN^+H + OH^- \tag{2.24}$$

$$CO_2 + OH^- \rightarrow HCO_3^- \tag{2.25}$$

$$CO_2 + H_2O \rightarrow HCO_3^- + H^+ \tag{2.26}$$

The solution's capacity for primary amines is limited to 0.5 moles of CO_2 per mole of amine due to the high stability of the carbamate and its low rate of hydrolysis to bicarbonate. In contrast, the solution's capacity for tertiary amines is one mole of CO_2 per mole of amine, but the CO_2 reactions with tertiary amines are too slow. To handle this problem, primary or secondary amines are added to the tertiary amines to combine the high capacity of tertiary amines and the high reaction rate of the primary and secondary amines [74]. An amine's ability to absorb acid gases is based on its alkalinity [74]. Figure 2.29 shows pH values on titration curves for some amine solutions, which have been performed by bubbling CO_2 gas through the amine solutions. The KOH curve has been added for comparison. It can be seen from Figure 2.29 that the ratio of moles acid gas/moles amine decreases with a decrease in the pH value.

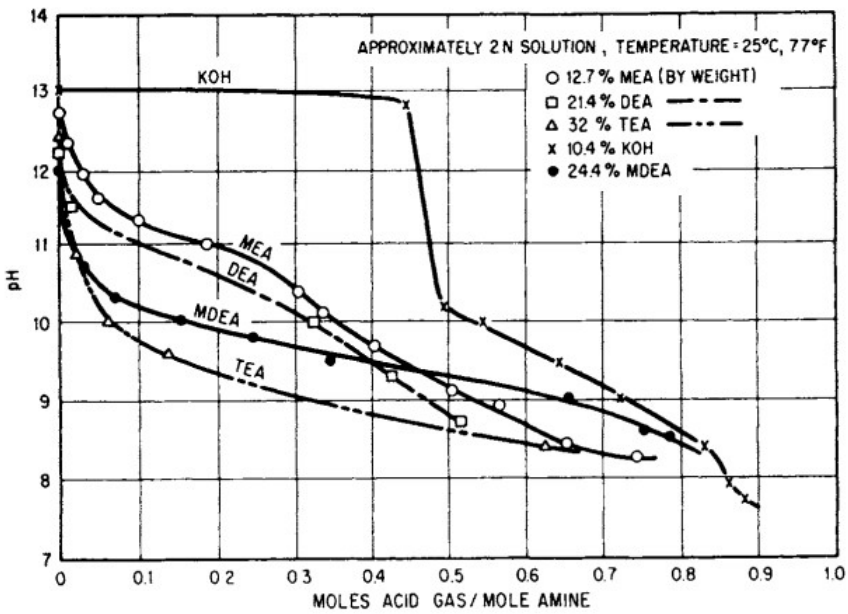

Figure 2.29 Titration curves showing pH during neutralization of ethanolamine and KOH solutions with CO_2 [74]

2.8 Fischer Tropics Synthesis

Fischer-Tropsch synthesis converts a mixture of hydrogen and carbon monoxide, also known as synthesis gas, into hydrocarbons. The general equation of the FT synthesis and its reaction enthalpy is given in the following equation [77] :

$$CO + 2H_2 \rightarrow (-CH_2-) + H_2O \qquad \Delta H = -165 kJ/mole \tag{2.27}$$

"-CH_2-" refers to linear paraffinic hydrocarbons with different chain lengths.

The Fischer-Tropsch reaction occurs typically at temperatures (200 - 300 °C) and pressures (10 - 40 bar) using catalysts based on iron or cobalt. The chain length "-CH_2-" of hydrocarbons depends on several things, such as temperature, the type of catalyst, and the reactor used [77].

Technically, Fischer-Tropsch synthesis is classified based on the operating temperature of syngas into two main categories: the high-temperature Fischer-Tropsch process (HTFT) and the low-temperature Fischer-Tropsch process (LTFT) [77]. High-temperature FT (HTFT) is conducted at 300-350 °C, $H_2/CO << 2$, and a pressure of 20-40 bar. Low-temperature FT synthesis (LTFT) is usually carried out at 190-260 °C, $H_2/CO = 1.7\text{-}2.15$, and 20-45 bar [78].

On the industrial scale, the typical reactors used for the FT process on the industrial scale are fixed-bed, slurry-phase, or fluidized bed reactors. Figure 2.30 shows these types of common reactors.

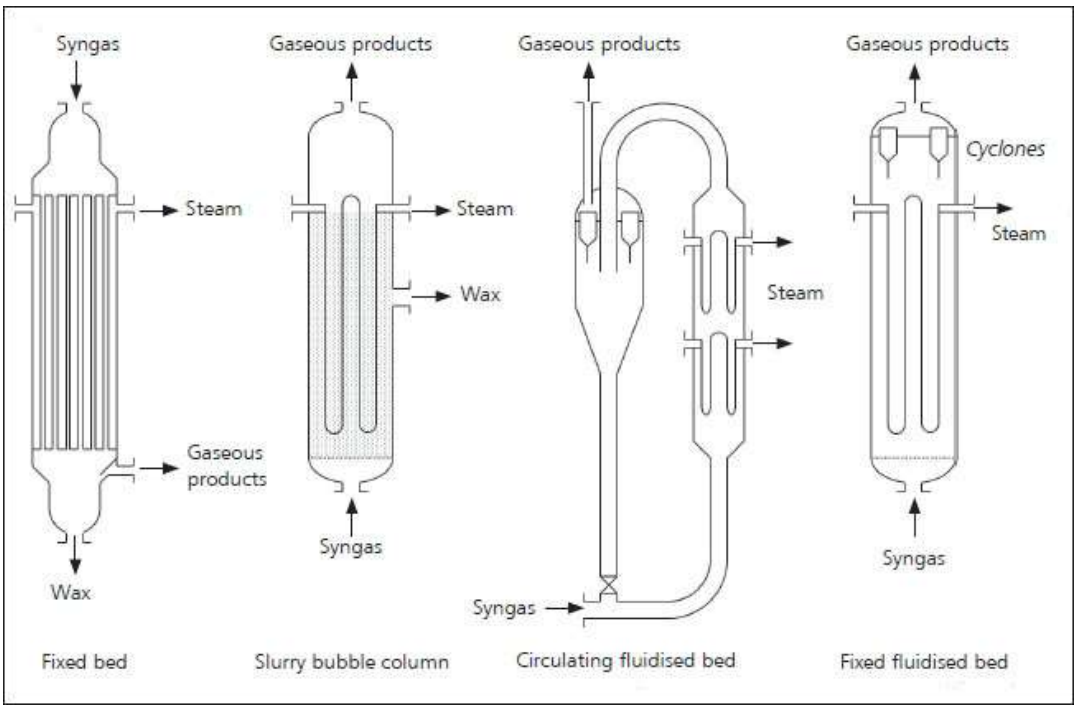

Figure 2.30 Commercial Reactors used in Fischer−Tropsch Synthesis [79]

Synthesis of C_1–C_{15} hydrocarbons, olefins, and oxygenates is carried out in fluidized bed reactors with Fe catalysts in HTFT mode. In comparison, linear long-chain hydrocarbons and light olefins are synthesized in fixed-bed or slurry-phase reactors in LTFT mode. The catalysts can be Co or Fe [78].

2.9 Fischer-Tropsch Refining

Figure 2.31 shows the refinery concept of the Sasol HTFT synfuels plants. After the high-temperature Fischer-Tropsch synthesis, four products are synthesized: a gaseous, aqueous, stabilized light oil (SLO), and decanted oil (DO). The stabilized light oil, whose chain lengths are from C_4 to C_{28}, is fed to the atmospheric distillation unit. In the atmospheric distillation unit, the light products are separated into valuable and industrially useful products such as SLO light naphtha, SLO heavy naphtha, and SLO distillate. The SLO distillate is fed to olefin extraction, where linear 1-olefins are separated. The bottom product from the atmospheric distillation unit contains carbon chains from C_{16} to C_{28}. This bottom product is fed to the vacuum distillation unit.

The decanted oil (DO), whose chain length varies from C_{11} to C_{50}, is sent to a vacuum distillation unit and separated into a vacuum gas oil whose chain length from C_{11}-C_{43} and a waxy oil whose chain length is from a chain length of C_{28}-C_{50}. The vacuum gas oil is sent to a distillate hydrotreater. Three products are separated in the hydrotreating process, namely naphtha, light distillate, and a product whose chain lengths are from C_{15} and C_{43}. The product whose chain lengths are from C_{15} and C_{43} is fed to a selective distillate cracker to produce naphtha, a heavy distillate whose chain lengths are from C_{11} to C_{31}, and fuel oil (C_{32}+).

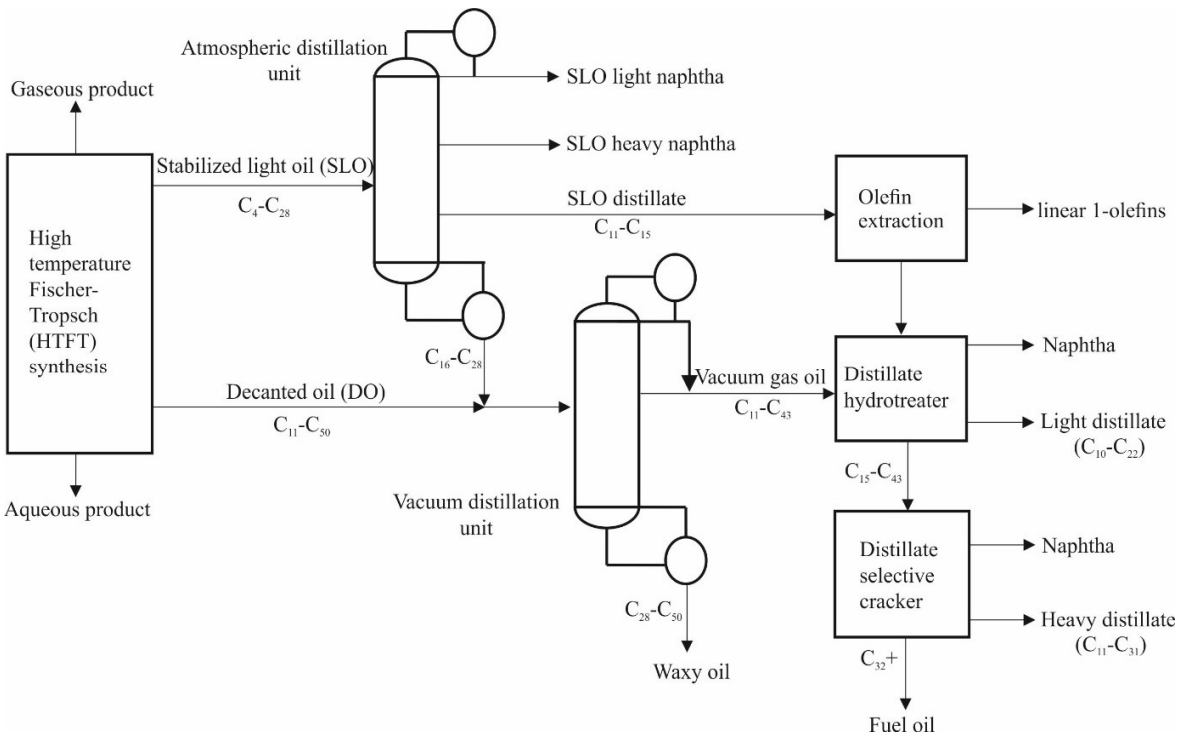

Figure 2.31 Operation of the HTFT heavy-end syncrude conversion and separation units in the Sasol Synfuels facilities at Secunda, South Africa (2008) (Reproduced) [80]

2.9.1 Distillation

Distillation is an important process in Fischer-Tropsch refining. Distillation aims to separate important chemical products which have industrial uses from crude oil. The principle of separation in the distillation process depends on the difference in boiling degrees and volatility of the substances that make up the crude oil. The distillation process is carried out in a distillation column.

Figure 2.32 shows the main parts of an atmospheric distillation column. The distillation column usually consists of trays, a reboiler, a condenser, and a reflux drum. The crude oil or liquid is fed into the column on a tray called the feed tray. The trays on the top of the inlet tray are called the rectification section, while the trays on the bottom are called the stripping section. After the oil is introduced into the column, it flows down the trays until it reaches the reboiler. In the reboiler, the raw oil is heated to a certain temperature. Some oil converts into vapor, while the remaining oil goes out of the reboiler. The steam rises along the trays and exits at the top of the column. The condenser then condenses the vapor. The condensed liquid is directed into the reflux drum and then flows back into the column from

the top. The reflux flows down on the trays. The vapor phase contacts with the reflux liquid on the trays. During this contact, mass and heat transfer occurs. Because of the mass and heat transfer between the liquid and vapor phases, the less volatile material in the vapor phase is condensed and transferred to the liquid phase.

In contrast, the more volatile material in the liquid phase is vaporized and transferred to the vapor phase. The concentration of the components varies from one tray to another. The concentration of the highly volatile substances increases as they rise to the upper tray, and the concentration of the less volatile substances decreases as they rise to the upper trays. And vice versa.

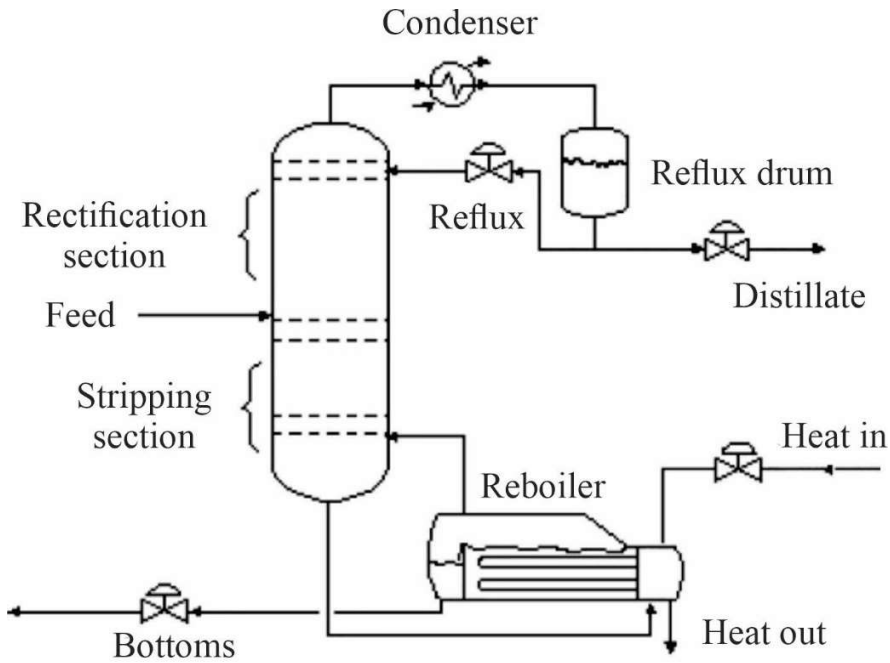

Figure 2.32 Illustration of the parts of an atmospheric distillation column (Reproduced) [81]

The products of the distillation column are withdrawn directly from specific trays and then fed into the downstream processes.

2.9.2 Distillate Hydrotreating

Hydrotreating is an important process that aims to remove impurities such as sulfur and nitrogen from distillate fuels. These impurities should be separated to meet environmental, safety, and technical requirements. Separation of these impurities increases fuel efficiency and reduces combustion by-products such as NOx and Sox [2].

The process is carried out by feeding the hydrogen and distillate fuels into the reactor in the presence of the catalyst at relatively high temperatures and moderate pressures. Cobalt-molybdenum catalysts are advantageous catalysts to use in the hydrotreating reactor when the objective of the process is to remove sulfur. Nickel-molybdenum catalysts are advantageous catalysts when the fuel contains little sulfur and the process is aimed at removing nitrogen [2].

The hydrotreating process is carried out by pressurizing the fuels and mixing them with the hydrogen stream. The mixture is heated to about 290-430°C and then fed into the fixed-bed reactor, where the pressure in the reactor is about 7-180 bar [2]. In the reactor, the hydrogen reacts selectively with fuels components containing sulfur or nitrogen as follows:

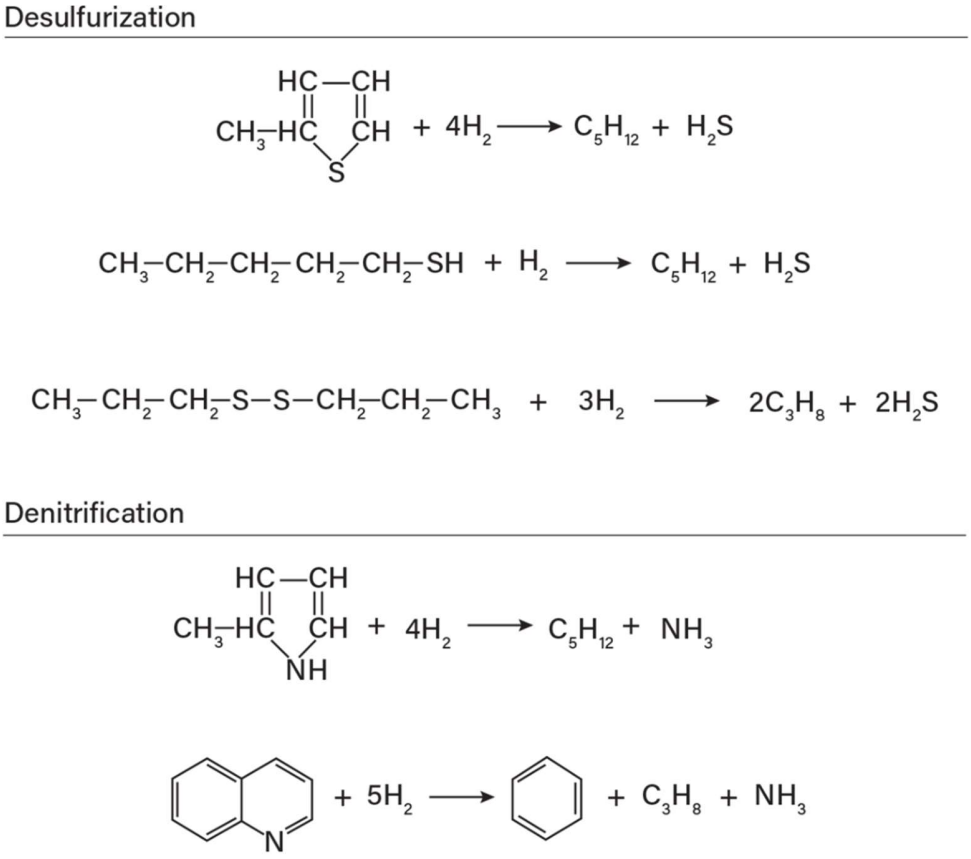

Figure 2.33 Common hydrotreating unit reactions [2]

Chapter 3 : **Constructing an Absorber test rig**

This chapter summarizes the construction of an absorber test rig on a laboratory scale built at the Institute of Energy Systems and Technology (EST) at Technical University of Darmstadt. The designing, constructing, sizing, and selecting of the parts of the test rig are illustrated. The programming of the control system is presented.

3.1 Introduction

To study the behavior of the absorption process in a polygeneration plant during start-up, shutdown, and the transient state, a test rig had to be built to perform the experiments and to study the behavior of the absorption system during the transient state. The derived objectives for the construction of the absorber test rig can be summarized as follows:

- To perform steady-state and unsteady-state experiments in the absorber test rig.
- To validate mathematical models.
- To study the behavior of the absorber in a polygeneration plant during the transient state.
- To analyze the problems that may occur in the absorption process during the transient state and present possible solutions to these problems.
- To study the difference between the behavior of a tray absorber and a packed bed absorber for CO_2 absorption in a polygeneration plant during the transient state.

The phase of building the absorber test stand went through several phases and steps. After the determination of the objectives and requirements to be achieved by the absorber test rig, next was designing and selecting the components of the absorber test rig, followed by the construction of the absorber test stand in the workshop. The programming of the control system, then the commissioning of the absorber test rig to ensure that the basic requirements were met, and then the performance of the absorber was improved to meet the operational requirements. The requirements that the absorber test rig must meet to achieve the main objectives of the study are as follows:

- The ability to mix up to three gases.
- The ability to mix the gases with volume fraction concentrations in the range of 0-1.
- The ability to change the pressure of the absorber from 0.1-0.3 MPa.
- The ability to change the gas flow rate up to 50 Nm^3/h.
- The ability to change the input solvent flow rate up to 250 L/h.
- The ability to recycle the solvent.
- The ability to perform steady-state and unsteady-state experiments.
- The ability to measure continually all the parameters correlated to the absorption process.
- The ability to study the hydrodynamic properties of the sieves tray.
- Fulfillment of the safety aspects and experimental requirements.

3.2 Constructing an Absorber Test Rig

Based on the above requirements, an Absorber test rig was built at the Institute of Energy Systems and Technology (EST) at Technical University of Darmstadt. Figure 3.1 and Figure 3.2 show the constructed absorber test rig. The test rig consists of four main parts: a gas mixing unit, an absorber column, a regeneration unit, and a gas analysis unit. This chapter presents the construction phases of the absorber test rig's four main parts.

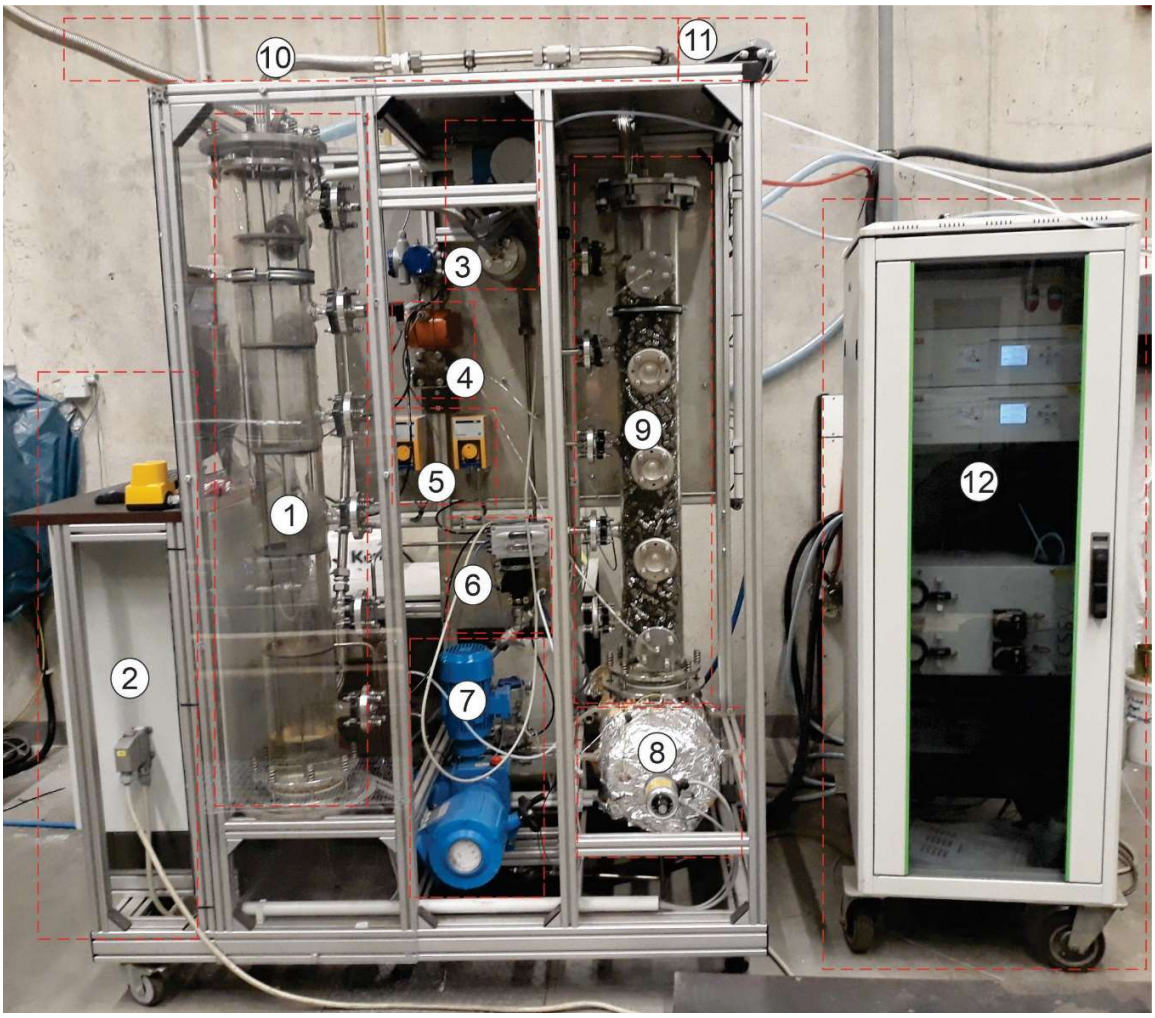

Figure 3.1 Side view of the absorber test rig

1,absorber column; 2,control panel; 3,Coriolis device; 4, pressure difference transmitter; 5,make-up pump; 6,liquid level control valve ; 7,recycling pump; 8,re-boiler ; 9,packed column; 10,gas outlet; 11,pressure control valve; 12,gas analysis unit.

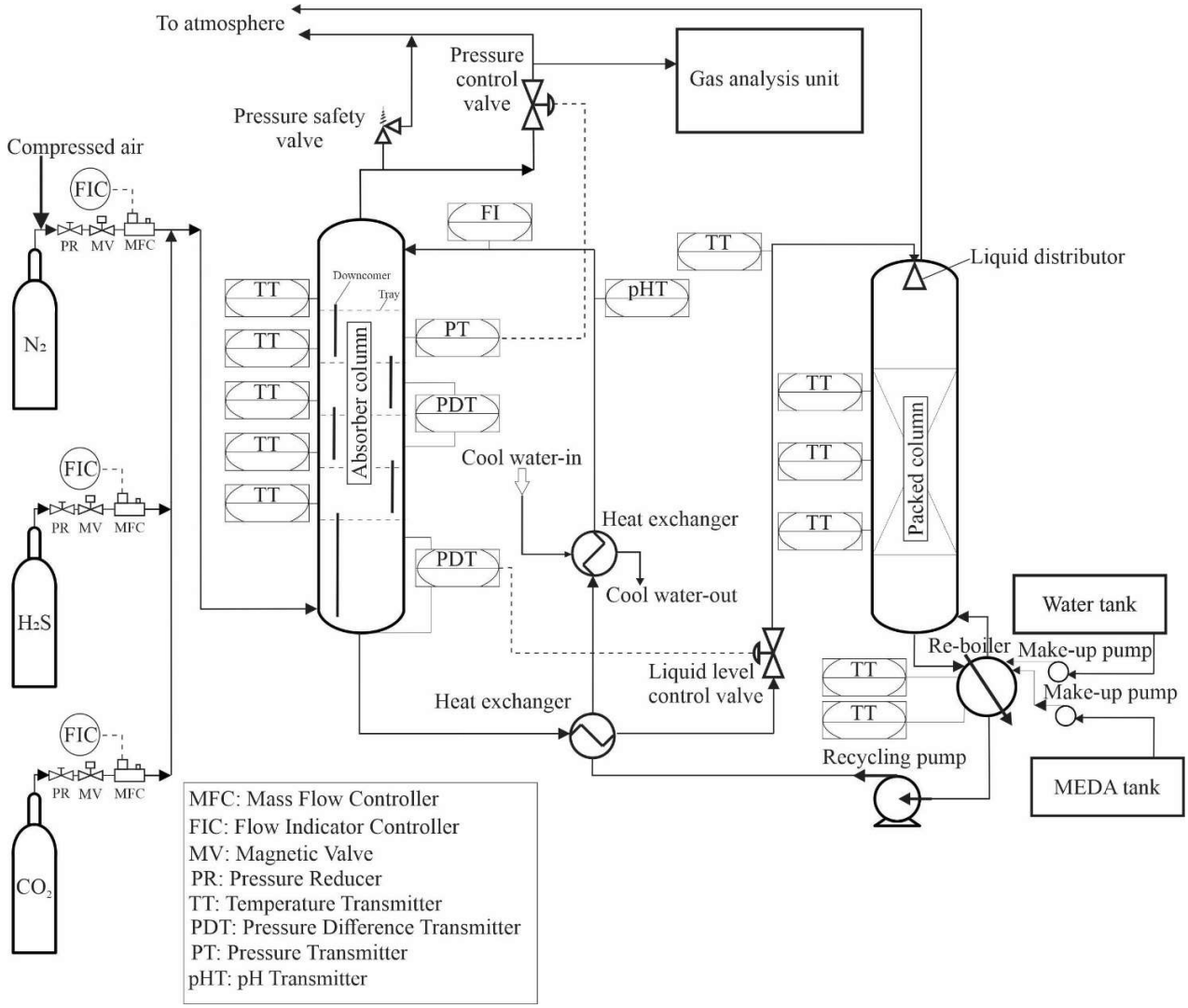

Figure 3.2 Schematic diagram of the absorber test rig

In this chapter, the steps performed during the construction of the absorber test rig will be explained. First, the parts and components that make up the absorber test rig were designed, sized, and selected. Then the test rig was built in the workshop. The system was programmed, and finally, the absorber was commissioned to ensure it met operational and safety requirements. The performance of the test rig has been improved to be suitable for performing steady-state and dynamic operating conditions.

3.2.1 Constructing a Gas Mixing Unit

Figure 3.3 and Figure 3.4 show the gas mixing unit constructed in the workshop. The constructed mixing unit consists of three lines connected to a manifold upstream of the absorber. Each line has a pressure reducer, solenoid valve, and mass flow controller. The pressure reducer controls the maximum pressure of the gas entering the absorber test rig. The pressure reducer can be set to a value lower than the maximum operating pressure in the absorber test rig which is 0.5 MPa. Equipping with a pressure reducer is important and without it, it is not allowed to enter gas into the test rig. The

pressure reducer prevents the pressure from accumulating above the maximum operating pressure and protects the absorber column from exploding. Therefore, it is considered the first safety barrier for the absorber test rig.

The solenoid valve allows or prevents gas from flowing into the absorber test rig, depending on the operator's desire. In addition, the solenoid valve is connected to an emergency control circuit, which will be shown later. In an emergency, the solenoid valves are closed directly by pressing the emergency button to prevent gas from entering the test rig and building up the gas pressure in the absorber test rig. This procedure protects the absorber test stand from the risk of high pressure, which can cause the absorber column to explode.

The mass flow controller controls and measures the volumetric flow rate of the gas entering the absorber column. The installed mass flow controllers are different for each line of the gas mixing unit.

In the first line, the mass flow controller is to measure the volumetric flow rate for air or N_2 gas. The maximum flow rate that can be controlled by this MFC is 78 Nm^3/h. In the second line, the mass flow controller measures the volumetric flow rate for H_2S gas. In the third line, the designed mass flow controller measures the volumetric flow rate of CO_2 gas. The maximum flow rate that can be controlled by this MFC is 48 Nm^3/h.

Figure 3.3 Side view of the gas mixing unit

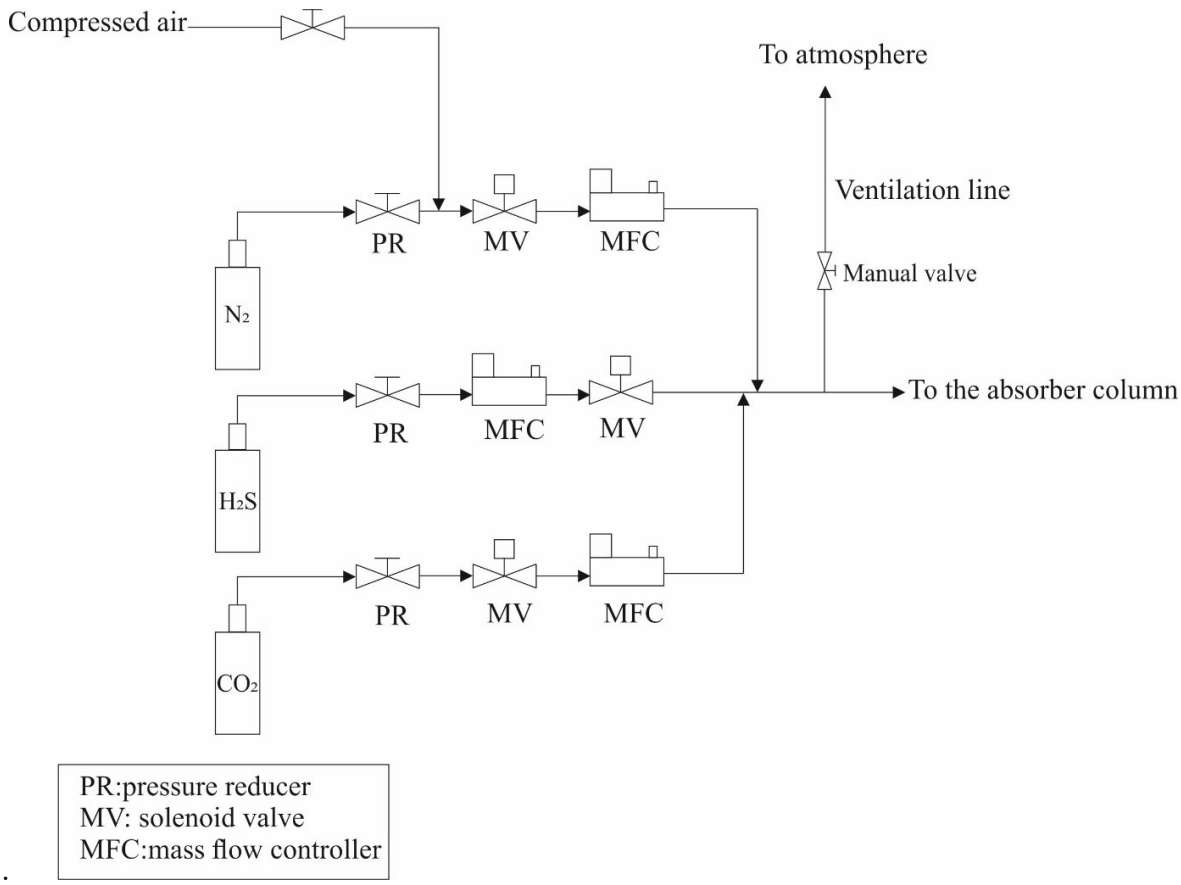

Figure 3.4 Schematic diagram of the gas mixing unit

All gas lines are connected in a manifold located upstream of the absorber. The manifold collects and mixes well all the gases before entering the absorber. Each line of the gas mixing unit can be connected to cylinders filled with pure gas. In addition, a compressed air line has been integrated into the gas mixing unit, which serves in the commissioning phase of the test stand, as the air is cheap and available in the workshop. With this design of a gas mixing unit, the mixing unit can mix up to three gases with volume fraction concentrations in the range of 0-1. For example, if the operator wants to feed 10 Nm^3/h of gas consisting of N_2, CO_2, and H_2S, with a volume fraction of 0.7 for N_2, 0.29 for CO_2, and 0.01 for H_2S, then the operator can set the MCFs of N_2, CO_2, and H_2S to 7 Nm^3/h, 2.9 Nm^3/h, and 0.1 Nm^3/h, respectively.

3.2.2 Constructing a Sieve Tray

For sizing the absorber column and the trays, one needs to know the type of tray to be used in the column, the number of trays, and the geometries of the plate. In the actual study, the chosen tray type is a sieve tray because it has high efficiency and medium pressure drop, and it is the cheapest of all types [82], as these properties are desirable in industries. Figure 3.5 and Figure 3.6 show the designed sieve tray.

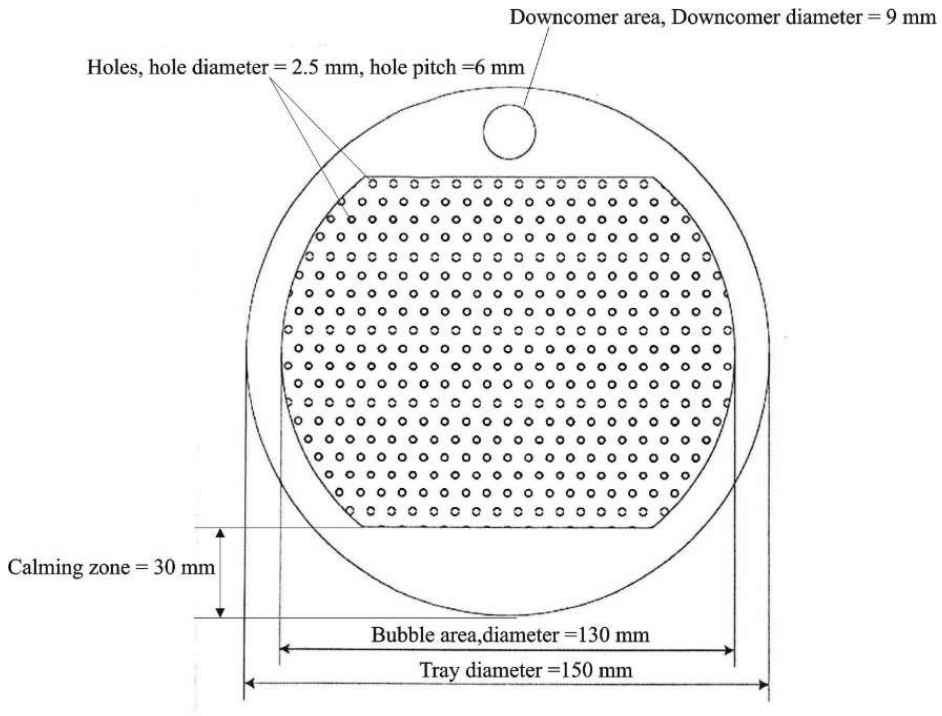

Figure 3.5 Illustration of the geometry of the constructed sieve tray

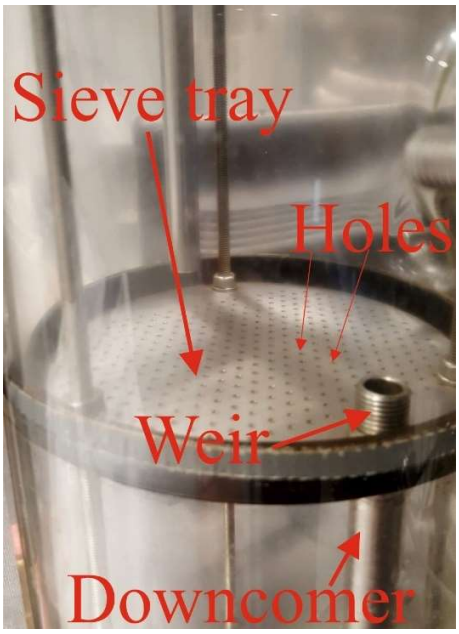

Figure 3.6 The constructed sieve tray

Table 3.1 shows the geometry of the constructed sieve tray. The background for estimating the number of trays and the tray geometry is explained below.

Table 3.1 Geometry of the constructed sieve tray

Parameters	Values
Number of trays,	5
Trays spacing, mm	240
Tray diameter, mm	150
Tray thickness, mm	2
Tray area, m^2	0.0177
Bubbling area or active area, m^2	0.013
The number of the holes	373
Hole diameter, mm	2.5
Holes area, m^2	0.00117
Holes pitch, mm	6
Weir height, mm	10-40
Downcomer diameter, mm	9 mm
Calming zone area, m^2	0.00235

3.2.2.1 Number of the Stages

There are two common methods in the literature for determining the number of stages that make up an absorption column: the graphical method and the algebraic method for determining the number of ideal stages. The graphical determination of the number of ideal stages was developed by McCabe and Thiele [83]. The McCabe-Thiele graphical design method is based on drawing a McCabe-Thiele diagram for the absorption operation, as shown in Figure 3.7.

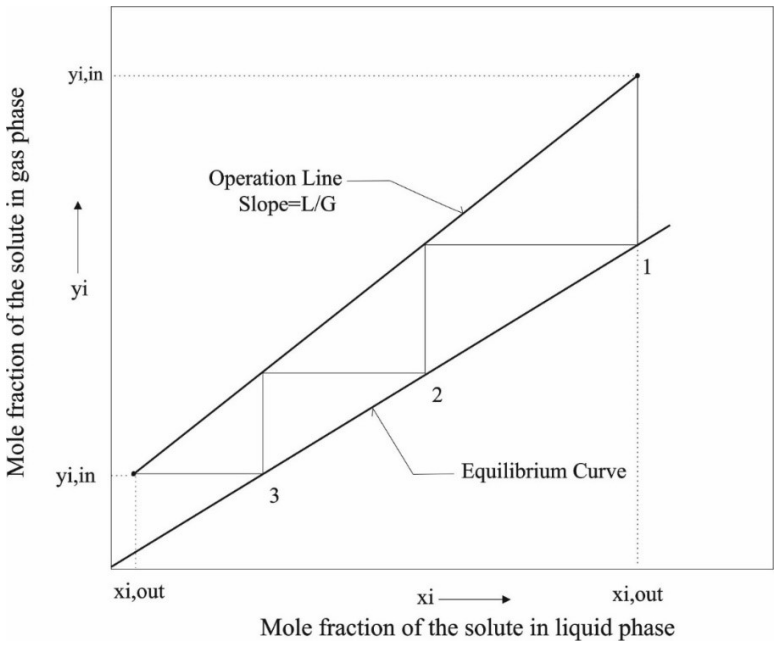

Figure 3.7 A McCabe-Thiele diagram for the absorption operation, modified from [84]

From Figure 3.7 both the operating curve and the equilibrium curve should be drawn. The equilibrium curve can be drawn by employing Henry's law as follows [63]:

$$y_i = \frac{H_i}{P} x_i \tag{3.1}$$

H_i represents Henry's constant, x_i represents the mole fraction of the solute i in the liquid phase, y_i represents the mole fraction of the solute i in the gas phase, and P represent total pressure.
To draw the operation line, a mass balance in the column illustrated in Figure 3.8 can be applied as follows [84]:

$$Gy_{i,in} + Lx_{i,in} = Gy_{i,out} + Lx_{i,out} \tag{3.2}$$

$$GY_{j+1} + LX_{\circ} = GY_1 + LX_j \tag{3.3}$$

$$Y = \frac{y}{1-y} \tag{3.4}$$

$$X = \frac{x}{1-x} \tag{3.5}$$

Where G represents the gas molar flow rate, L represents the liquid molar flow rate, $y_{i,in}$ represents the mole fraction of the solute i in the gas phase at the inlet of the absorber, $x_{i,in}$ represents the mole fraction of the solute i in the liquid phase at the inlet of the absorber, $y_{i,out}$ represents the mole fraction of the solute i in the gas phase at the outlet of the absorber, and $x_{i,out}$ represents the mole fraction of the solute i in the liquid phase at the outlet of the absorber.
The relationship between Y and y, and for X and x is as follows [84]:

$$y = \frac{Y}{1+Y} \tag{3.6}$$

$$x = \frac{X}{1+X} \tag{3.7}$$

$$y_{i,in}G + x_{i,in}L = y_{i,out}G + x_{i,out}L \tag{3.8}$$

$$Y_{j+1} = \frac{L}{G} X_j + \left(Y_1 - \frac{L}{G} X_{\circ}\right) \tag{3.9}$$

By equation (3.9) the operating line can be drawn, which has a slope $\frac{L}{G}$

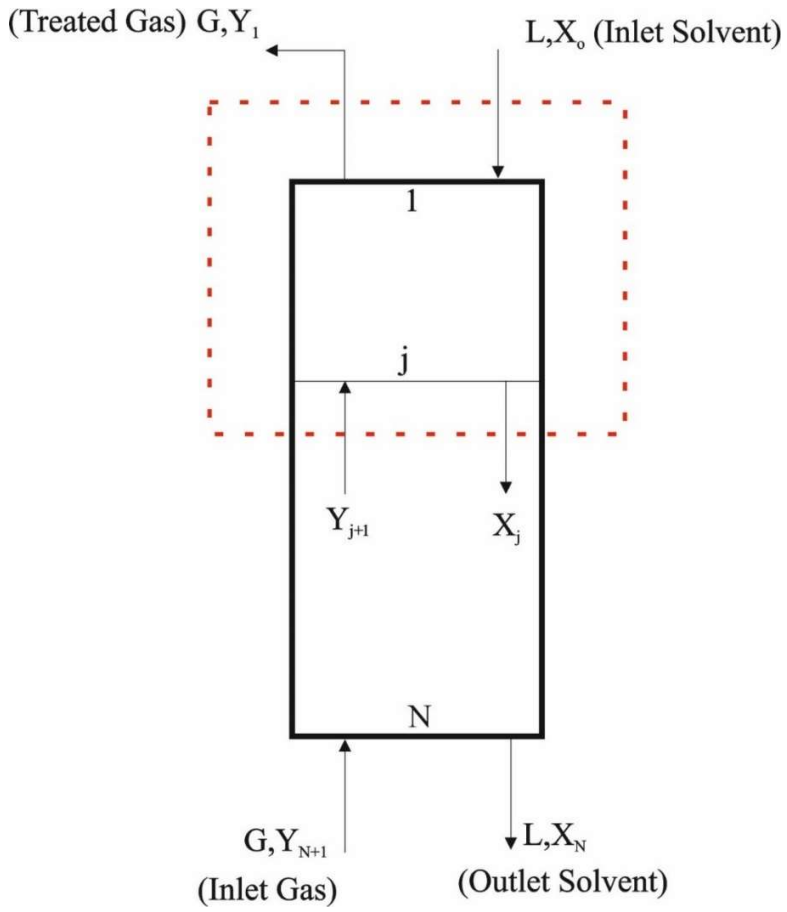

Figure 3.8 Gas absorption column (Reproduced from [84]**)**

3.2.2.2 Diameter of the Tray

The inner diameter of the tray can be estimated based on 80-85% of the flooding velocity of gas for non-foaming liquids and 75% or less of the flooding velocity of gas for foaming liquids [Goud, 2014]. The flooding velocity is gas velocity through the net area under flooding conditions. The flooding condition happens when the froth level of the liquid on the plate reaches the plate above. The flooding velocity can be calculated from the correlation as follows [85]:

$$U_{nf} = C_{sbf}\left(\frac{\sigma}{20}\right)^{0.2}\left(\frac{\rho_l - \rho_v}{\rho_v}\right)^{0.5} \tag{3.10}$$

Where U_{nf} represents flooding velocity [m/s], σ represents liquid surface tension [mN/m], ρ_l represents liquid density [kg/m^3], ρ_v represents vapor density [kg/m^3], and C_{sbf} represents capacity parameter (m/s).

To calculate C_{sbf} from Figure 3.9, one needs the plates spacing and flow parameter F_{LG}. The flow parameter can be calculated using the following correlation [86]:

$$F_{\mathrm{LV}} = \frac{L_w}{V_w}\left(\frac{\rho v}{\rho_l}\right)^{0.5} \tag{3.11}$$

Where L_w represents liquid flow rate [kg/s], V_w represents vapor or gas flow rate [kg/s], ρ_l represents liquid density [kg/m^3], and ρ_v represents vapor or gas density [kg/m^3].

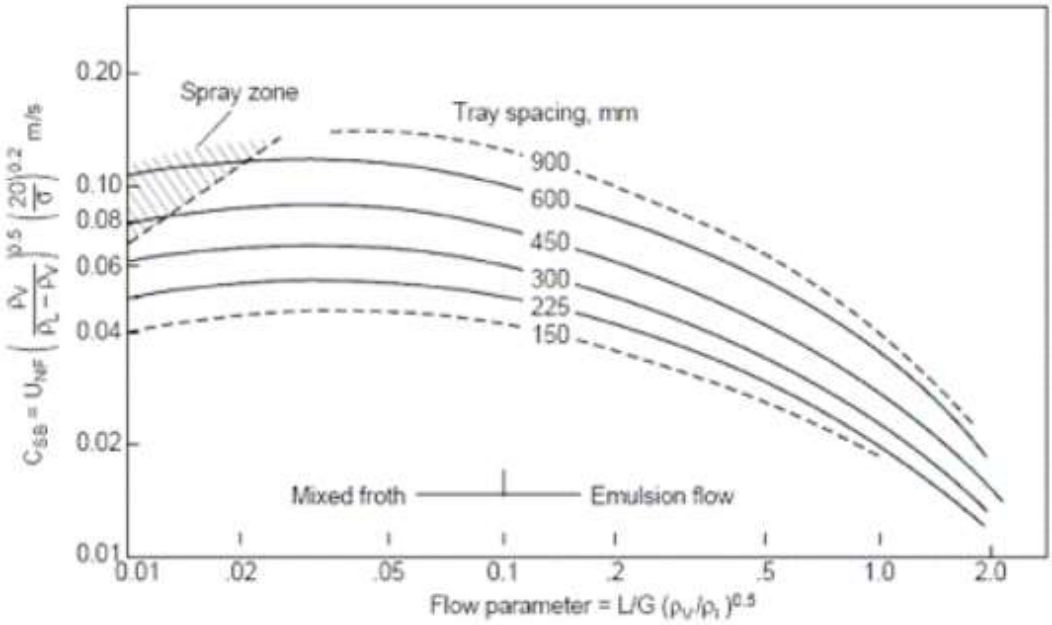

Figure 3.9 Capacity parameter [87]

3.2.2.3 Hole Area

At the stable operation of the sieve tray, the gas phase flows through the tray's holes, and the liquid flows down through the downcomer. Flowing the gas through the holes prevents the liquid from flowing through the holes of the sieve tray. The case of flowing the liquid or part of it through the holes of the sieve tray is called weeping. The weeping occurs at low gas velocity. In the weeping, the liquid or part of it flows through the holes of the sieve tray instead of flowing through the downcomer. The possibility of weeping increases with rising fractional hole area and liquid flow rates.

Operation of the column in weeping conditions reduces the plate's efficiency. So, to avoid weeping, the vapor flow velocity should be higher than the minimum vapor velocity. The minimum vapor velocity, or the minimum design vapor velocity, can be calculated using the following correlation [67]:

$$U_{min} = \frac{K_2 - 0.9(25.4 - d_h)}{\rho v^{1/2}} \tag{3.12}$$

Where U_{min} represents minimum design vapor velocity [m/s], d_h represents hole diameter [mm], ρv represents vapor density [kg/m^3], and K_2 represents a constant of weep-point correlation.
K_2 can be estimated by using Figure 3.10. To get K_2, the sum of $(h_w + h_{ow})$ should be calculated which is the sum of weir height h_w and weir crest h_{ow}.

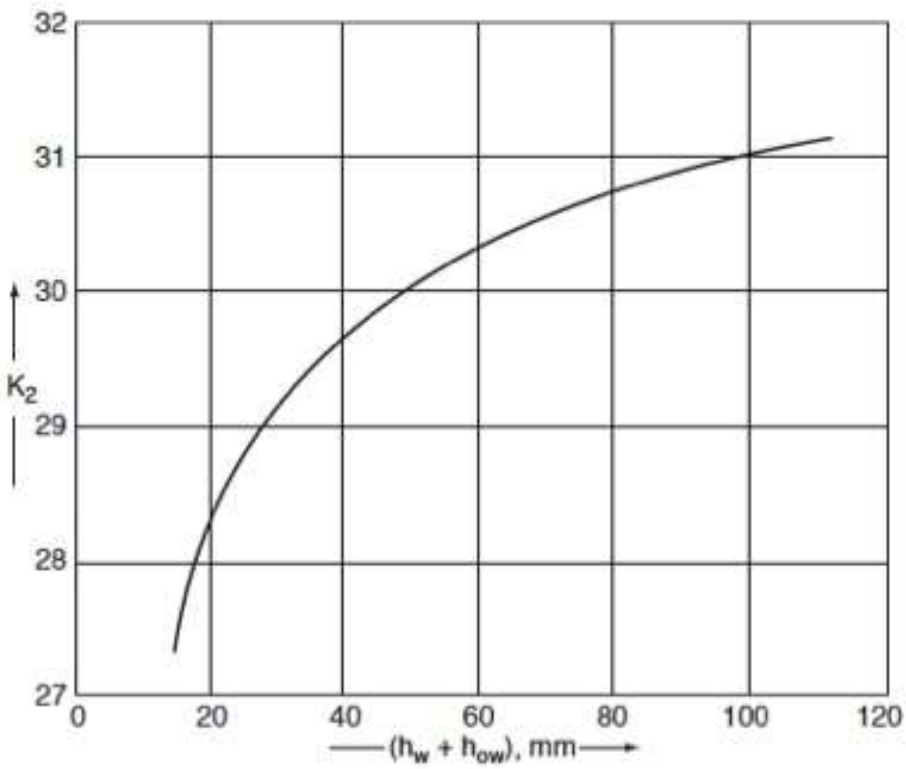

Figure 3.10 Weep-point correlation [88]

The weir crest (h_{ow}) can be estimated by applying the Francis' weir correlation as shown in [67]:

$$h_{ow} = 750\left(\frac{L_{wc}}{L_W \rho_l}\right)^{2/3} \tag{3.13}$$

Where L_{wc} represents weir length [m], L_W represents liquid flow rate over the crest [kg/s], ρ_l represents liquid density [kg/m^3].

To avoid weeping, the operating minimum vapor velocity $U_{min,op}$ should be higher than the minimum design vapor velocity, which means $U_{min,op} > U_{min}$. The operating minimum vapor velocity $U_{min,op}$ can be calculated as follows:

$$U_{min,op} = \frac{\text{minimum vapor flow rate}}{\text{hole area}} \tag{3.14}$$

From equation (3.14), the hole area can be estimated by compensating a value of $U_{min,op} > U_{min}$ which can be as follows:

$$\text{hole area} = \frac{\text{minimum vapor flow rate}}{U_{min,op}} \tag{3.15}$$

3.2.2.4 Hole Diameter, Hole Pitch, and Tray Thickness

The estimated hole diameter in the constructed tray is about 2.5 mm. The hole diameter is an influential parameter determining the minimum design steam velocity. As seen from equation (3.12), a large diameter increases the possibility of weeping problems. But a small hole diameter increases the pressure drop of the gas in the absorber [67]. The hole pitch in the constructed tray is 6 mm. The hole pitch is the distance between the centers of two adjacent holes. The hole pitch helps to arrange the holes on the sieve plate. The holes in the tray can be positioned in a square or equilateral triangular layout concerning the vapor/gas flow direction. The usual range of IP is between 2.5 and 5 times the hole diameter dh [67].

Plate thickness is another parameter that should be considered when sizing the plate, as it affects the pressure drop of the plate. Typical plate thickness is between 0.2 and 1.2 times the hole diameter [67]. The thickness of the tray used in this study is 2 mm.

3.2.2.5 Downcomer, Weir Height, and Weir Length

Segmental downcomers are commonly used in the plate tray. The estimated area of the downcomer used in this study is 6.4 X 10^{-5} m^2. Since the estimated area of the downcomer is too small, it was challenging to make a downcomer with a segmental layout with this area, so in this study, a circular cross-section was used, as shown in Figure 3.11, The diameter of the used downcomer is 9 mm.

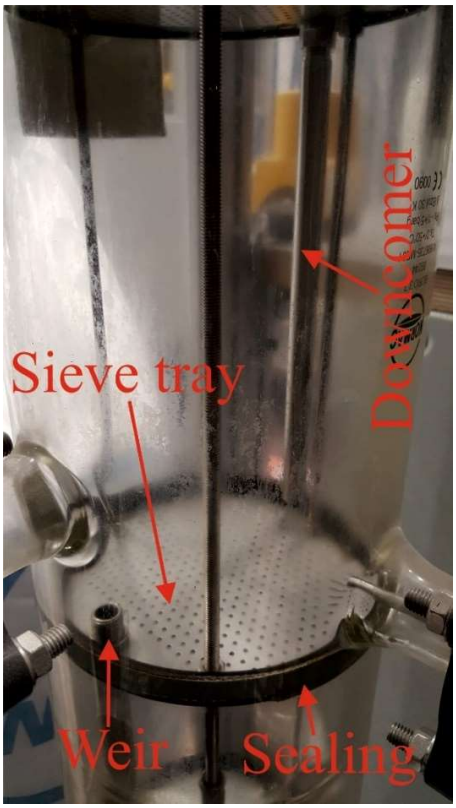

Figure 3.11 Liquid downcomer

Increasing the weir height will increase the liquid holdup and thus increases thus plate efficiency. However, increasing a weir height will increase the tray pressure drop and the potential for washout and entrainment. The common weir heights are from 40 to 90 mm for operation above atmospheric pressure and from 6 to 12 mm for vacuum operation. For a segmented downcomer layout, a weir length of 60 to 80% of the column diameter is recommended [67].

The constructed downcomer in this study is a tube with a length of 250 mm and a diameter of 9 mm. The tube has an external thread with a side length of 40 mm. The downcomer is inserted from the bottom of the tray from the threaded side into a hole drilled in the tray. The inserted length of the threaded side determines the height of the weir. If the inserted length of the threaded side is 10 mm, the height of the weir is 10 mm. For the tray used in this study, the weir height can be adjusted between 5 mm and 40 mm.

3.2.2.6 Calming Zones

A calming zone in the term is a blank area between the perforation area and the inlet downcomer or inlet weir. Since the liquid from the above plate fell with high velocity, it is recommended to provide this calming zone to reduce the weeping. It is recommended that a calming zone is between 50 to 100 mm [67]. The calming zone in the used tray is 30 mm.

3.2.2.7 Constructing Radial Sealing for the Sieve Trays

The diameter of the glass absorber column is 152.6 mm, and the diameter of the tray is 150 mm, so a sealing ring is required to seal the area between the outer wall of the sieve circumference and the inner wall of the glass column. The space between the outer wall of the sieve circumference and the column's inner wall should be closed by sealing. Without closing this area, the gas or liquid will flow through this space, decreasing absorption efficiency. The requirement for this sealing is to close the space between the round edge of the tray and the inner wall of the column tightly, and it should be made from material against corrosion resistance specifications. The chosen material which made the sealing is EPDM (ethylene-propylene-diene rubber).

At first, the sealing shown in Figure 3.12 was designed. But it did not close the space between the round edge of the tray and the column's inner wall, because the inner diameter of the column is not constant, it varies in the range of 152.7 mm + 10 micro millimeters along the column. So, this sealing closes the space between the tray's round edge and the column's inner wall in some areas perfectly and in some areas not, so this design will not prevent leakage. Another form of sealing was designed, as shown in Figure 3.13. As seen, it has a flexible edge. This edge touches the inner wall of the column with a specific force to prevent leakage. With this flexible edge, its diameter changes depending on the touched area from the inner wall of the column.

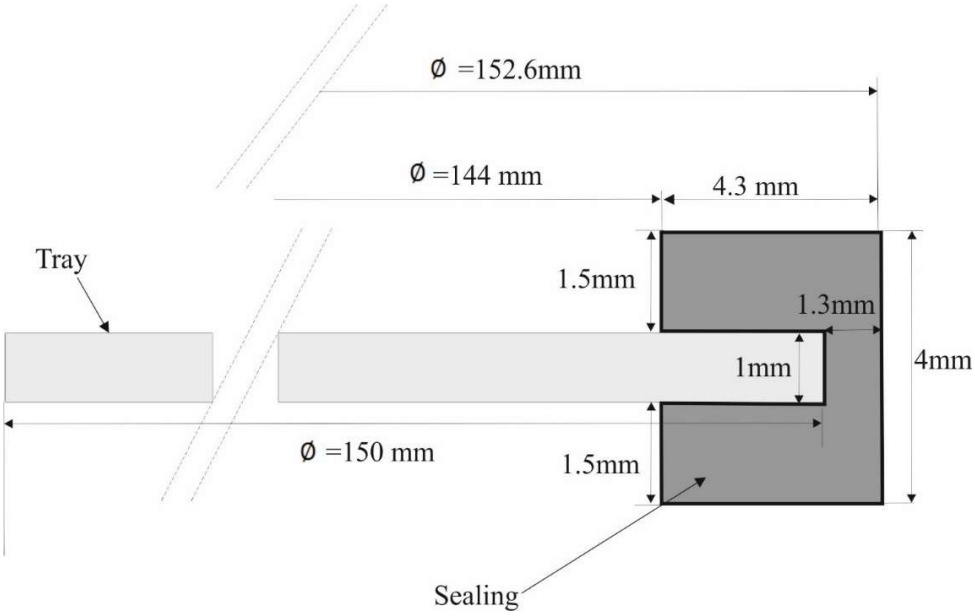

Figure 3.12 Illustration of the geometry of the conventional sealing

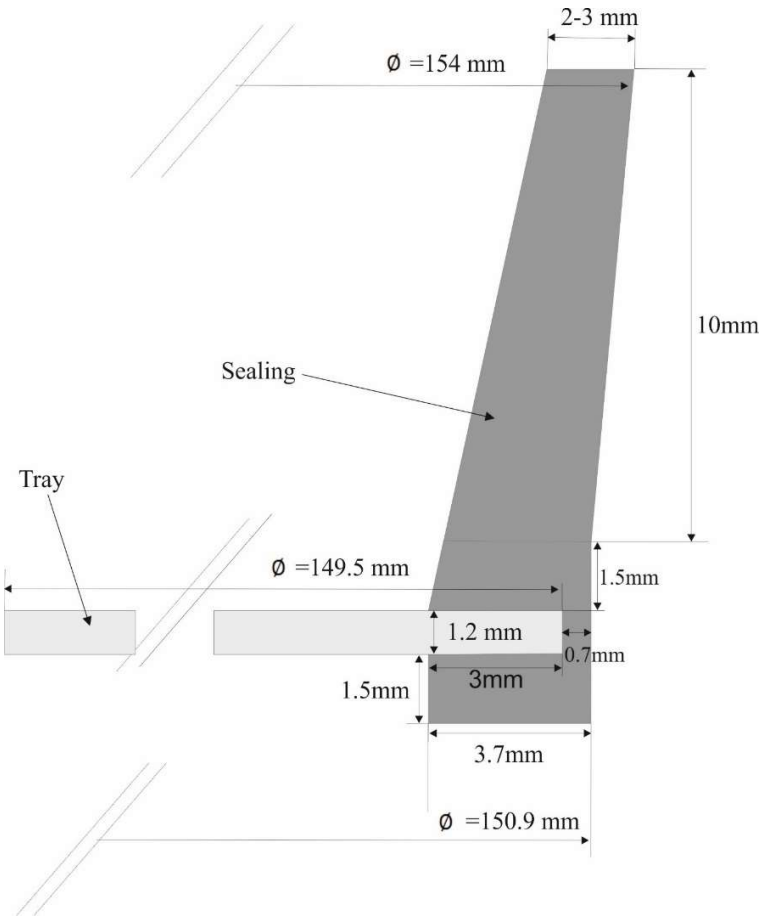

Figure 3.13 Illustration of the geometry of the flexible sealing

3.2.3 Constructing the Absorber Column

Figure 3.14 and Figure 3.15 show the designed tray absorber Column. As for the absorber's material, some liquids that enter the absorber have corrosive properties. Therefore, one requirement for the absorber must be made of corrosion-resistant materials. Several options have been presented for the material that makes up the absorption column, such as stainless steel and glass. It has been shown that both options have advantages and disadvantages. Stainless steel is much less expensive than glass, and it can withstand higher pressure and has a higher safety factor. However, stainless steel is not as transparent as glass, so the operator cannot see what is inside the absorber column. As for the glass, the cost of a glass column is higher than stainless steel, and the pressure resistance is lower than stainless steel. However, the glass can be transparent, allowing the operator to observe what is happening inside the absorption column, which allows studying the hydrodynamic characteristics of the tray. Also, choosing the glass material for making the absorber column helps the operator commission phase of the test rig, and optimize the control circuit of the liquid level at the bottom of the absorber column.

The glass column was manufactured outside the Technical University of Darmstadt. The absorber is made of a glass column with a height of 1500 mm, and its internal diameter is 152 mm. The manufactured glass column stands a maximum gas pressure of about 6 bar at a temperature of 50°C. The column has 12 glass nozzles to which metal flanges can be attached, ten nozzles used to measure pressures and temperatures in the absorber, and two nozzles for introducing the inlet gas and liquid to the absorber. The bottom and the top of the absorber column can be closed by suited metal flanges. The top flange contains the gas exit, and the bottom flange contains the exit of liquid. Five sieve trays are fixed by threaded rods and inserted inside the absorber.

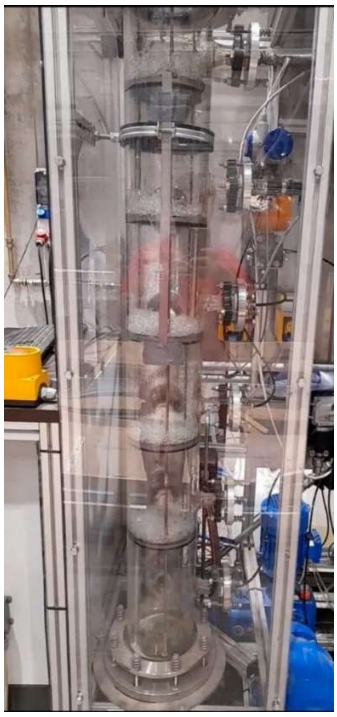

Figure 3.14 The constructed absorber

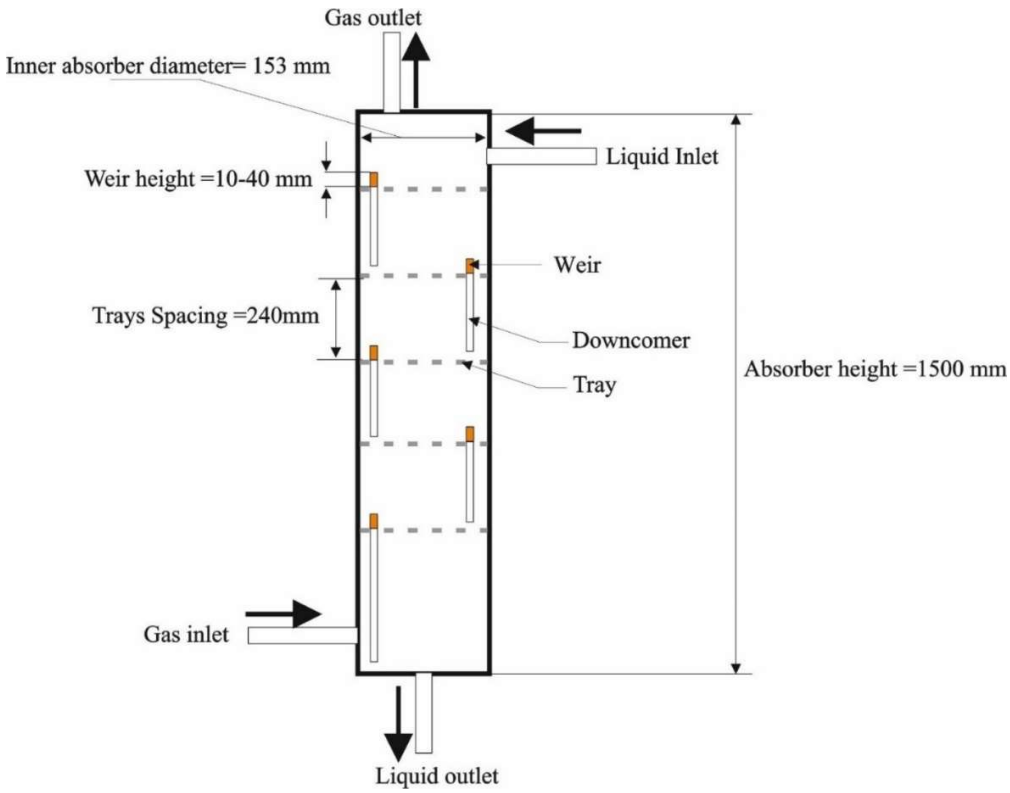

Figure 3.15 Illustration of the geometry of the absorber

3.2.4 Constructing the Regeneration Unit

Figure 3.16 shows the constructed regeneration unit. The regeneration unit aims to regenerate the absorbent and return it to the absorber as a lean absorbent. The regeneration unit consists of two heat exchangers, a reboiler, a packed column, a make-up pump, and a recycle pump. The packed column is a glass column that has a diameter of 152 mm and a height of 1300 mm. There are inside the packed column a liquid distributor, packing material, and packing support. The column has ten glass nozzles to which metal flanges can be attached. The nozzles provide the possibility to attach different measurement devices. The packing materials are from the Pall-Ring type. The height of the packing materials is about 1 m. Table 3.2 shows the characteristics of the Pall ring. The selected size of the packing material is 15 mm because the recommended size of the packing should be less than 1/8 of the column diameter to minimize liquid maldistribution [52].

Table 3.2 Characteristics of Pall-Ring

Parameters	Values
Size (diameter x length x thickness), mm	15 x 15 x 0.3
Density, kg/m^3	380
specific surface, m^2 /m^3	360
Void fraction, %	95

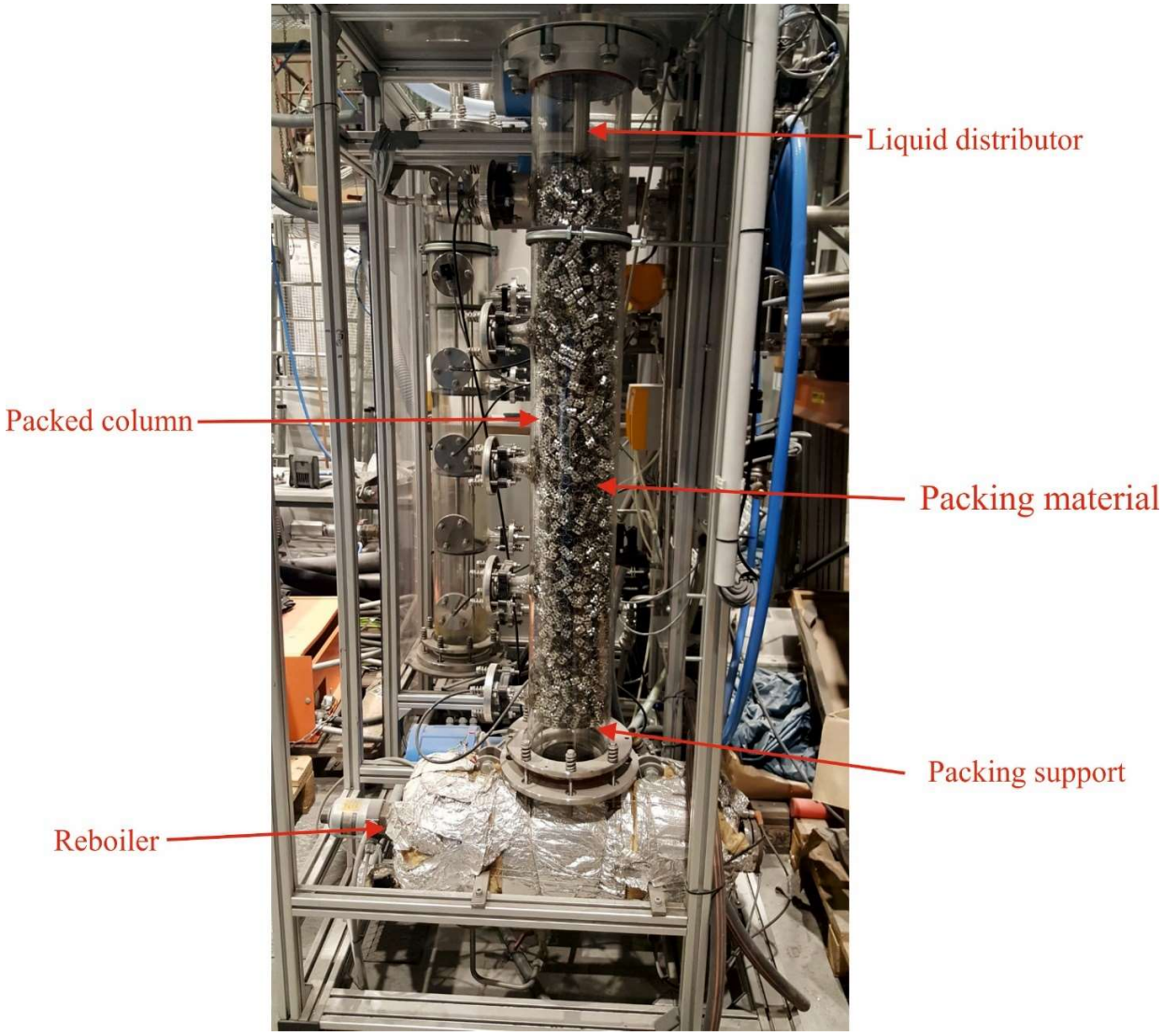

Figure 3.16 The constructed desorber

The top of the column is closed by suited metal flanges. The flange contains the inlet of rich solvent coming from the absorber and the gas outlet. The rich absorbent enters the packed column through a liquid distributor attached to the top flange of the packed column. The purpose of the liquid distributor is to spray the absorbent uniformly on the top of the packings. Figure 3.17 shows that the manufactured liquid distributor is from a spray type that contains 13 holes distributed uniformly on the liquid distributor. The diameter of the holes is about 1 mm.

Figure 3.17 The constructed liquid distributor for the desorber

The diameter of the holes, and the number of the holes, are designed by applying a Perry correlation (1984) [85] specified based on the head-flow correlation as follows [85]:

$$Q = C_D A_h n \sqrt{2gh} \tag{3.16}$$

Where Q represents the volume flow rate [m^3/s], C_D represents the coefficient of discharge, A_h represents the cross-sectional area of a hole [m^2], n represents the number of discharge holes, g represents the gravitational acceleration [m/s^2], and h represents the liquid head above the orifice [m]. Packing support is fixed at the bottom of a column as illustrated in Figure 3.18. The packing support helps to carry the packing and prevent it from falling into the reboiler and allowing the liquid to fall and the gas to flow up.

Figure 3.18 The constructed packing support for the desorber

The packed column is placed on the reboiler. The reboiler is a cylinder with a diameter of 220 mm and a length of 606 mm. The reboiler is made of stainless steel because it is corrosion-resistant to amine solvents. The volume of the reboiler is about 24 liters.

The reboiler is provided with seven nozzles. Two nozzles are used for inserting temperature sensors; one is used for the inlet of solvent into the reboiler, one is used for the outlet of solvent, and one is used for the inlet of makeup solvent. There is a nozzle for inserting the heating coil. The inserted heating coil has a heat capacity of 4500 kW.

The recycle pump is connected directly to the reboiler, which pumps the solvent from the reboiler to the absorber. The lean solvent is precooled in the first heat exchanger by exchanging heating with the solvent which comes out from the absorber. After that, the precooled solvent cools down in the second heat exchanger, by exchanging heating with cool water.

3.2.5 Equipment and Instrument of the Test Rig

The test rig is provided with various equipment and instruments that continuously measure the basic parameters of the absorption process. Table 3.3 illustrates the equipment and instrument used in the absorber test rig.

Table 3.3 Equipment and instrument used in the absorber test rig

Measured Parameter	**Used instrument**	**Number of instruments**	**Location of fixing**	**Working principle**
Temperature	Temperature sensor+ Coriolis Flow meter	Ten Temperature sensor+ one Coriolis Flow meter	Five sensors at the absorber, one sensor at the inlet of the desorber, two sensors at the desorber, two sensors at the reboiler, and a Coriolis Flow device at the liquid inlet into the absorber	(Appendix)
Pressure	Pressure sensor	One	on the absorber (between the first and the second tray)	(Appendix)
Pressure reducer	Pressure reducer regulator	four	On the upstream of the gas mixer unit	(Appendix)
Pressure difference	Pressure difference transmitter	two	One is installed on the absorber (at the third tray), and the other one is installed at the absorber (at the sump of the absorber)	(Appendix)
The flow rate of the gas	Mass flow controller	three	at the gas mixing unit	(Appendix)
The flow rate of the liquid	Coriolis Flow meter	one	at the liquid inlet of the absorber	(Appendix)
Controlling the liquid flow rate	Piston pump	one	At downstream of the reboiler	
Control Valve	Pneumatic Control Valve	two	One is installed at the gas outlet of the absorber, and the other one is installed at the liquid outlet of the absorber	Appendix
CO_2 volume fraction	Gas analysis unit	one	At the gas outlet of the absorber	
Mackup pump for water and MDEA	Peristaltic pump	two	Connected with the reboiler	(Appendix)
	Safety pressure control valve		At the gas outlet of the absorber	

3.2.6 Design Control Circuits of the Test Rig

Five control circuits were designed for the test rig. These control circuits aimed to control the absorption process in the absorber test rig and fulfill the operation's safety requirement. Below, the design of the control circuits will be illustrated.

3.2.6.1 Pressure Control Circuit

The first control circuit is aimed at controlling the pressure to the set point. Figure 3.19 illustrates the structure of the pressure control circuit. The pressure control circuit consists of a pressure transmitter and a pneumatic control valve. The pressure transmitter sensor is fixed at the top of the tray column (between the first and the second tray, numbered from above), whereas the pneumatic control valve is installed at the absorber's gas outlet. The pressure control circuit controls the pressure after the gas enters the absorber. The pressure sensor sends a signal with the actual pressure value to a PID controller. The PID controller compares the set point of pressure and the actual value of pressure and signals the pneumatic control valve to open or close to maintain the pressure at its set point. For safety reasons, a safety pressure valve is installed in the gas outlet of the absorber column, as seen in Figure 3.20. The manufacturer calibrated the safety pressure valve to a value of 0.45 MPa. Thus, when the pressure reaches a value of 4.5 and above, the safety pressure valve opens to release the gas in the absorption column, helping to reduce the pressure to a value lower than 0.45 MPa.

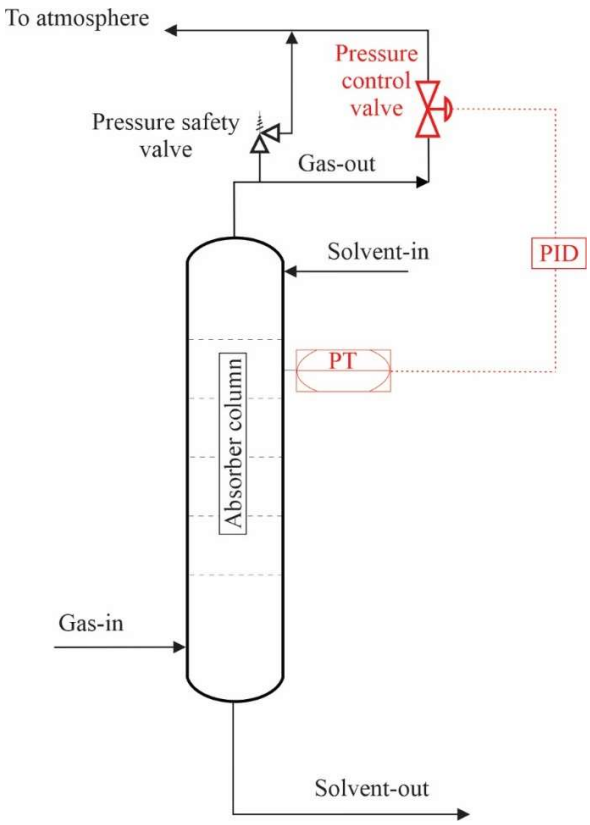

Figure 3.19 Illustration of the structure of the pressure control circuit

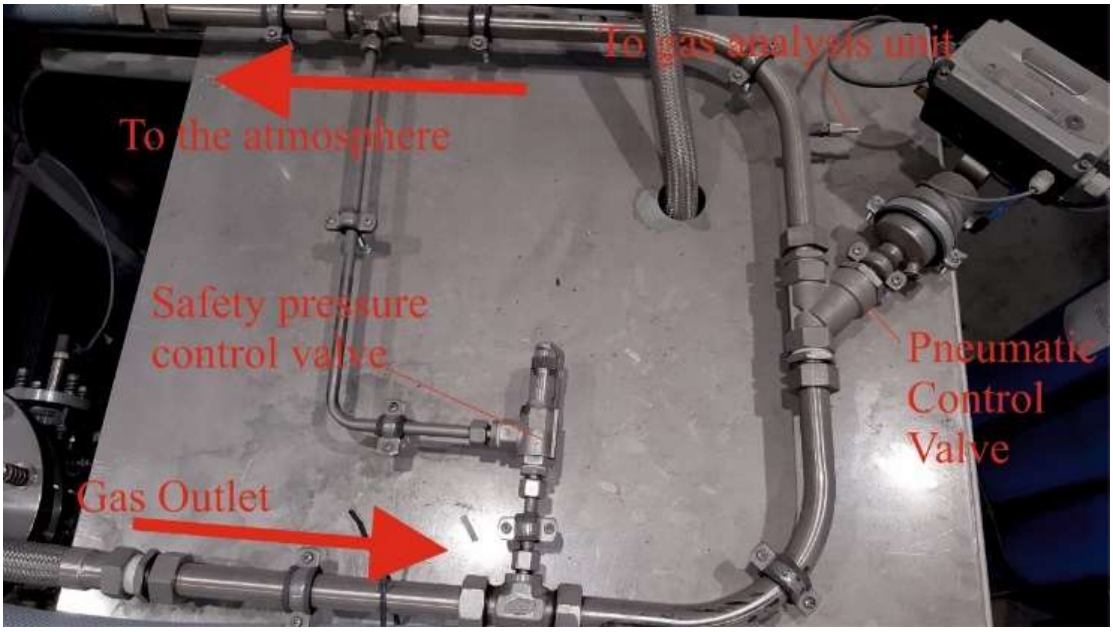

Figure 3.20 Pressure maintenance at the outlet of the absorber

3.2.6.2 Liquid Level Control Circuit in the Sump of the Absorber

The second control circuit controls the liquid level in the sump of the absorber column to its set point. Controlling the liquid level is essential since it prevents the gas from exiting from the liquid outlet and prevents the accumulation of the liquid inside the absorber to a high level. Without a level controller, the accumulated liquid causes the closing of the inlet of the gas or the possibility of immersing the trays of the absorber with the liquid. In this case, the operation of the test rig stops.

Figure 3.21 illustrates the structure of the liquid level control circuit. The liquid level control circuit consists of a pressure differential transmitter and a pneumatic control valve. A pressure differential transmitter is installed at the sump of the column, whereas the pneumatic control valve is installed at the liquid outlet of the absorber.

The pressure differential transmitter sends a signal with the actual pressure difference value (equivalent to a hydrostatic level) to a PID controller. The PID controller compares the set point of pressure difference and the actual value of pressure difference and signals the control valve to open or close to maintain the pressure difference at its set point.

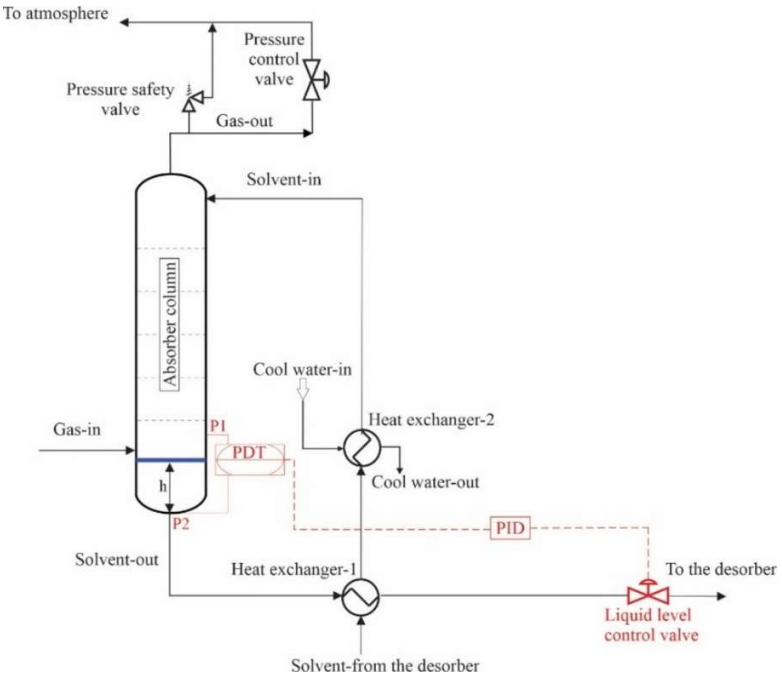

Figure 3.21 Illustration of the structure of the liquid level control circuit in the absorber

3.2.6.3 Temperature Control Circuit in the Reboiler

The third control circuit controls the absorbent's temperature inside the reboiler. Controlling the absorbent's temperature is essential for the regeneration of the absorbent by heating the absorbent to a specific hot temperature which leads to breaking the bond between the acid gases and the absorbent. Figure 3.22 illustrates the structure of the absorbent's temperature control circuit in the reboiler. This control circuit consists of a temperature controller, a heater coil, and two temperature sensors installed at the reboiler's top and bottom. The temperature sensor signals the actual value of the temperature. The controller compares the actual value of the temperature inside the reboiler and the set point and signals the heater to heat the absorbent if the absorbent temperature is below the set point.

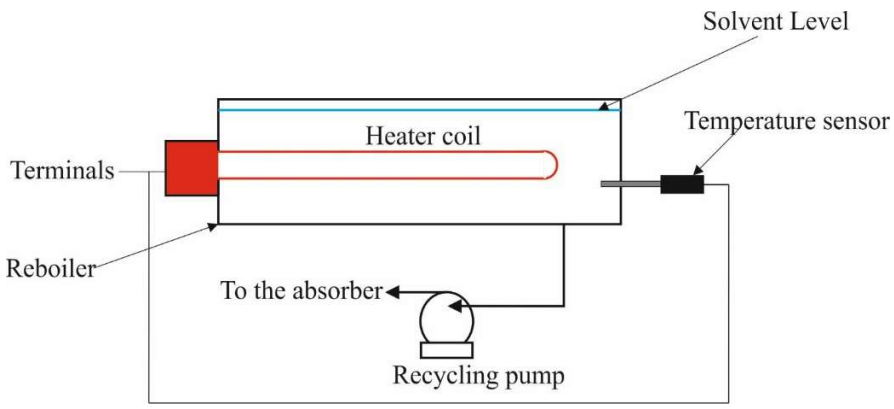

Figure 3.22 Illustration of the structure of the absorbent's temperature control circuit in the reboiler

3.2.6.4 Liquid Level Control Circuit in the Reboiler

The fourth control circuit adjusts the level of the liquid or the absorbent in the reboiler to its set point. Controlling the liquid level is essential in the reboiler. Without this liquid level control circuit, the liquid level decreases during the absorption experiments due to absorbent loss by stripping or evaporation. Decreasing the liquid level in the reboiler will affect the recycling pump's behavior, as seen later in chapter 4. Figure 3.23 illustrates the structure of the liquid level control circuit in the reboiler. The control circuit consists of a level sensor, an automatic on/off switch, and a make-up pump. The level sensor is inserted inside the reboiler at a specific level, which considers a set point. If the level of liquid decreases below the set point, the level sensor signals an automatic on/off switch which leads to running the make-up pump to supply a new liquid inside the reboiler and vice versa.

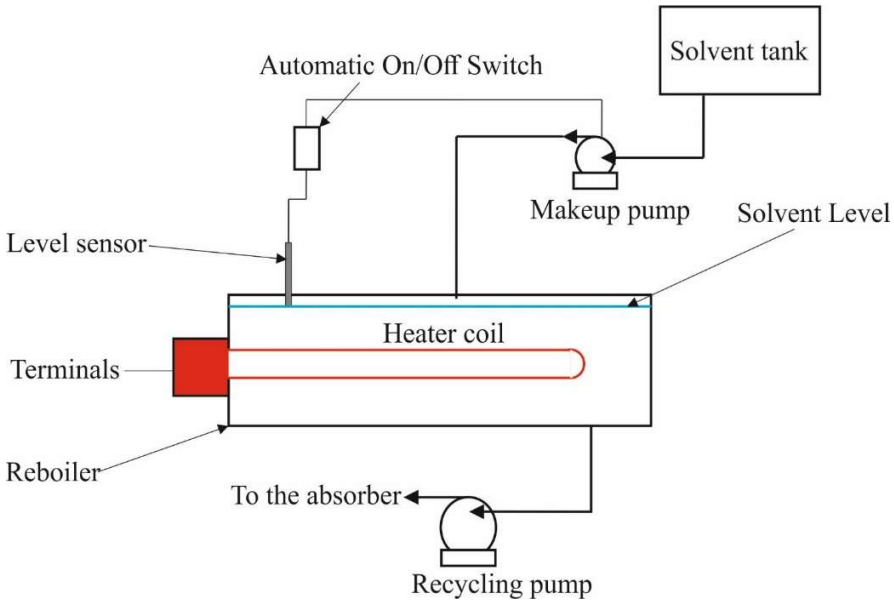

Figure 3.23 Illustration of the structure of the liquid level control circuit in the reboiler

3.2.6.5 Safety Control Circuit for the Heater Coil in the Reboiler

The fifth control circuit is used to save the heater coil in the reboiler from damage. Sometimes the level control circuit (The fourth control circuit) does not work correctly. As a result, the absorbent level inside the reboiler decreases below the heater coil, which may damage the heater coil. As a safety procedure, a safety control circuit for the heater is installed at the reboiler. Figure 3.24 illustrates the structure of the safety control circuit for the heater. The control circuit consists of a level sensor and an automatic on/off switch. The level sensor signals an automatic on/off switch to shut down when the liquid level inside the reboiler decreases below the set point of the level sensor and vice versa. This control circuit is protected from any unexpected decrease in the absorbent level during operation.

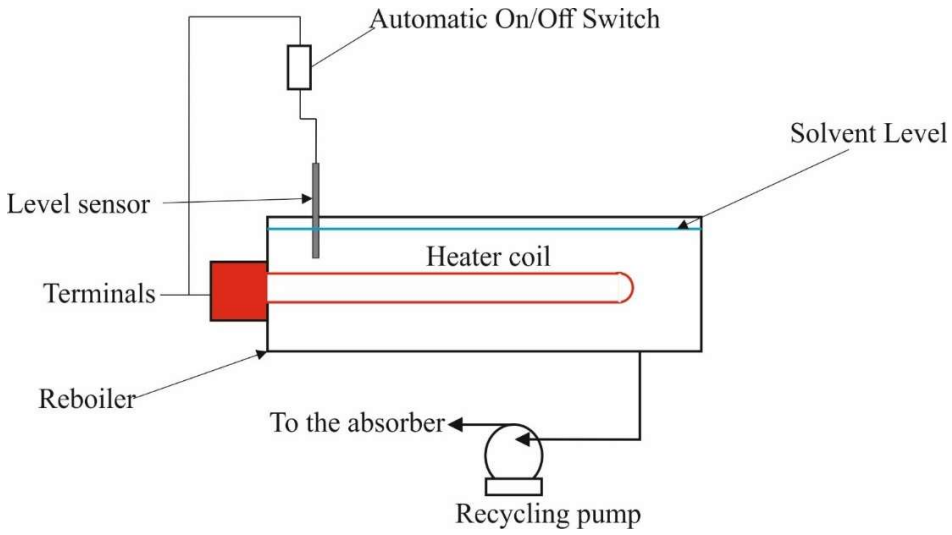

Figure 3.24 Illustration of the structure of the safety control circuit for the heater

3.2.7 Programming the Control System

3.2.7.1 Introduction

The absorber test stand contains devices, instruments, and control circuits that must be monitored, controlled, and their measurements are recorded. These tasks can be solved by programming the control system. The goal of the control system programming can be summarized as follows:

- For continuous measurement and recording of all process parameters as a function of time.
- For simple configuration of the control loops.
- For easy operation, monitoring, and control of the test stand.
- For easy execution of stationary and unstationary experiments.

The control system programming consists of hardware and software components. The hardware consists of a PLC, a PC integrated with WinCC, and a Coriolis device. The PLC consists of a central processing unit (CPU) and windows for the inputs and outputs for electrical signals to/from the absorber test bench. The central processing unit (CPU) is the interface between all electrical connections of the absorber test bench, the PC system, and the Coriolis devices. The PC and the Coriolis device are connected to the PLC via a data cable. The PLC device receives and sends the electrical signals to the absorber test rig as an electrical current between 0 and 20 mA.

The software used for programming the control system is Tia Portal V14 (Totally Integrated Automation). The software was carried out on a PC. Tia portal has a wide range of functions that can be used to program the control system as follows:

- Creation of a flow chart for the test stand, which can be used to operate, monitor, and control the test stand.
- Setting up the control loops.

- Scaling and converting of the measured electrical signals from the unit mV or mA to a physical unit such as m^3/h, °C, or bar.
- Recording the measurements performed as a time function.

3.2.7.2 Programming the Interface of the Absorber Test Rig

Figure 3.25 shows the flowchart model of the interface of the absorber test rig programmed for the test rig using the Tia portal software. It can be considered as an interface for a test bench through which the operator can operate, monitor, and control the test rig. From the flowchart in Figure 3.25, it can be seen most components that make up the test rig and the parameters that need to be measured and controlled.

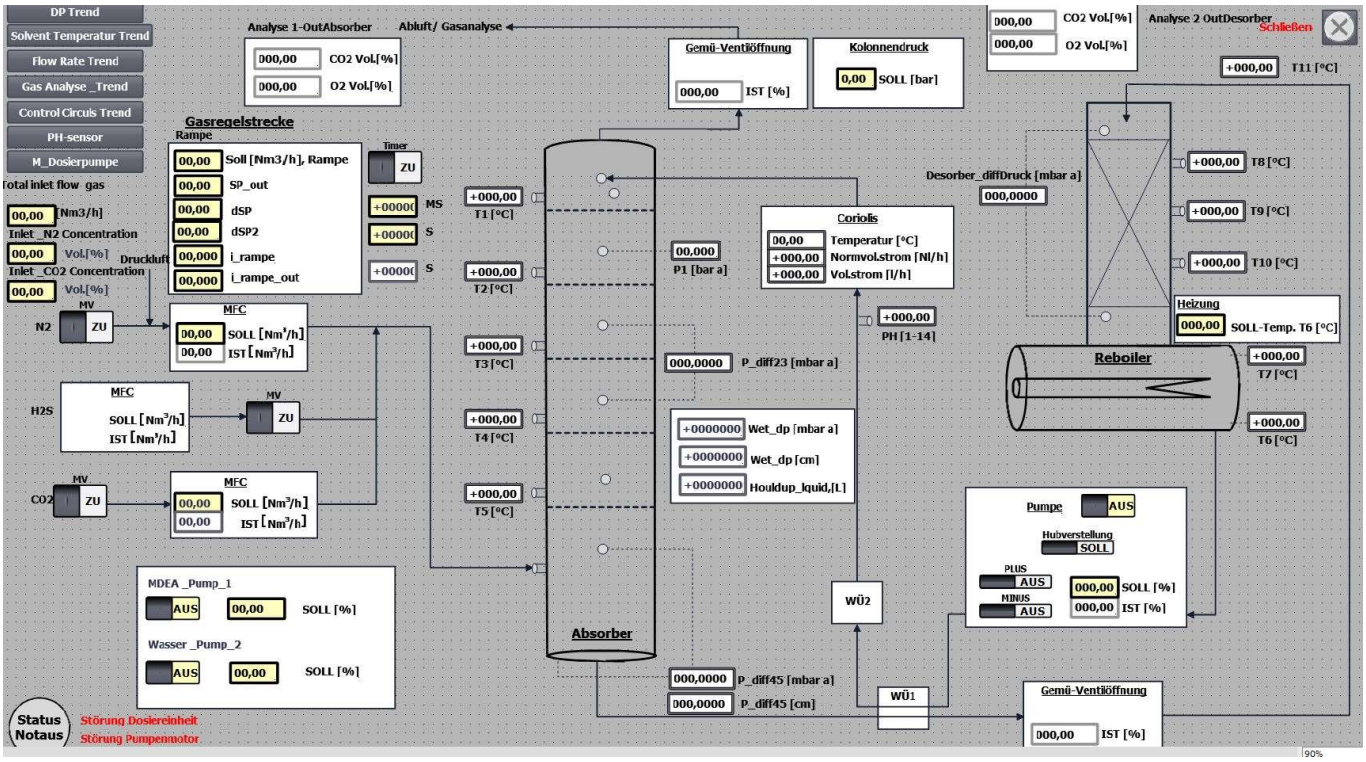

Figure 3.25 Interface of the absorber test rig

To operate the gas mixing unit, firstly, the outlet pressure of the pressure reducer, which is not drawn in the flow diagram, must be set to a value of 0.5 MPa. The next step is to open the solenoid valve for each gas that enters the absorber column. Introducing a small amount of the gas first is recommended to avoid a shock to the absorber column. The MFC can measure and control the instantaneous value of the inlet gas flow rate.

As for the absorber, the flowchart model for the test bench in Figure 3.25 displays the following parameters:

- The value of the absorber pressure in the point between the first and the second tray.
- The values for five temperature sensors along the absorber, one temperature for each tray

- The pressure drop at the third tray.
- The values of the liquid level at the sump of the absorber.
- The opening value of the pressure control circuit.
- The set value of the absorber pressure.

To control the absorber pressure after entering the gas, the pressure can be set with values between 0.1-0.3 MPa. The control loops automatically adjust the pressure using a pressure control loop shown in Figure 3.19.

The regeneration unit consists of a desorber, a reboiler, a pump, and two heat exchangers. The flowchart model for the test rig displays the following parameters for the regeneration unit:

- The temperatures at the entrance of the desorber
- The temperatures along the desorber
- The set point of the temperature in the reboiler
- The temperatures inside the reboiler
- The set point of the recycling pump
- The set point of the make-up pumps
- The actual value of the load of the recycling pump
- The PH value of the inlet liquid to the absorber
- The temperature of the inlet liquid to the absorber

To operate the regeneration unit, the reboiler can be set to a temperature between 20-95C°. The coil starts to heat the absorbent. Then the recycling pump should run by setting a value between 1 and 100%. The inlet temperature of the absorbent can be controlled by opening the valve of the cool water connected to the second heat exchanger. The temperature of the inlet absorbent into the absorber should not exceed 50 C° for the safety of the glass absorber column.

After the absorbent enters the absorber, it flows along the absorber and then exits from the liquid outlet of the absorber. The first heat exchanger preheats it, then it enters into the desorber from the top through a liquid distributor and flows along the packing material. The rising hot steam heats the absorbent, then the absorbent enters the reboiler where it heats to a specific temperature.

3.2.7.3 Implementation of the Measurement Technology

Implementing the measurement technique is based on sending the sensor or device an electrical signal through the cable to PLC. The electrical signal is current between 0-20 mA. The strength value of the current depends on the measured value. The PLC receives the current and converts the strength of the current to an integer between 0 and 27648. To convert the integer to a physical unit, the Tia portal can use the scale function to convert the integer to the physical unit. For this function, one needs the measurement range specified by the manufacturer. Figure 3.26 shows the scale function used to

measure the PH of the inlet liquid. The measured signal enters a window (1) as an integer between 0 and 27648. The operator enters the operating range for the instrument in windows (2) and (3), which are 0-14. The scale function processes the input data and outputs the results in the window (4), which displays the actual value of PH.

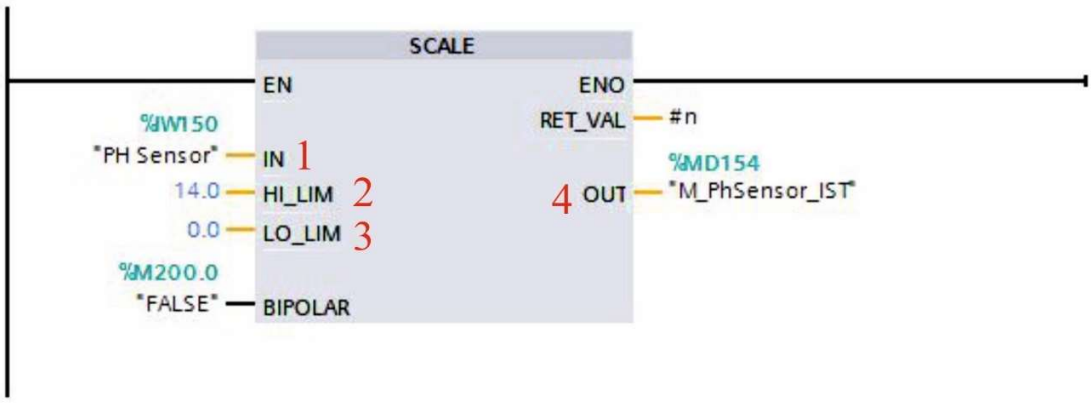

Figure 3.26 Function block of the PH measurement of the inlet solvent

The scale functions for implementation of the measurement of the temperature and CO_2 mole fractions are shown in the appendix.

3.2.7.4 Implementation of the Control Circuits

Figure 3.27 shows the function for implementing the control circuit for the liquid level. The proportional component (P) can be activated by the window (1). The integration component (I) can be activated by window (2). The derivative component (D) has been canceled or deactivated by setting window (3) to false. In this way, the controller was converted to a PI controller. The derivative component expresses the controller's response with minor changes in the level of the liquid, and because this is unnecessary, it has been canceled. By window (5), the set point of the pressure difference can be set. The controller's call time (CYCLE) can be set by window (4). GAIN or can be set by window (8). Integration time can be set by window (9).

The mechanism of controlling the liquid level in this function is as follows: the pressure difference transmitter signals the PI Controller in the window (6). Based on the setting input from gain, cycle time, integration time, and the set point, the controller calculated the opening percent of the level control valve in the window (10).

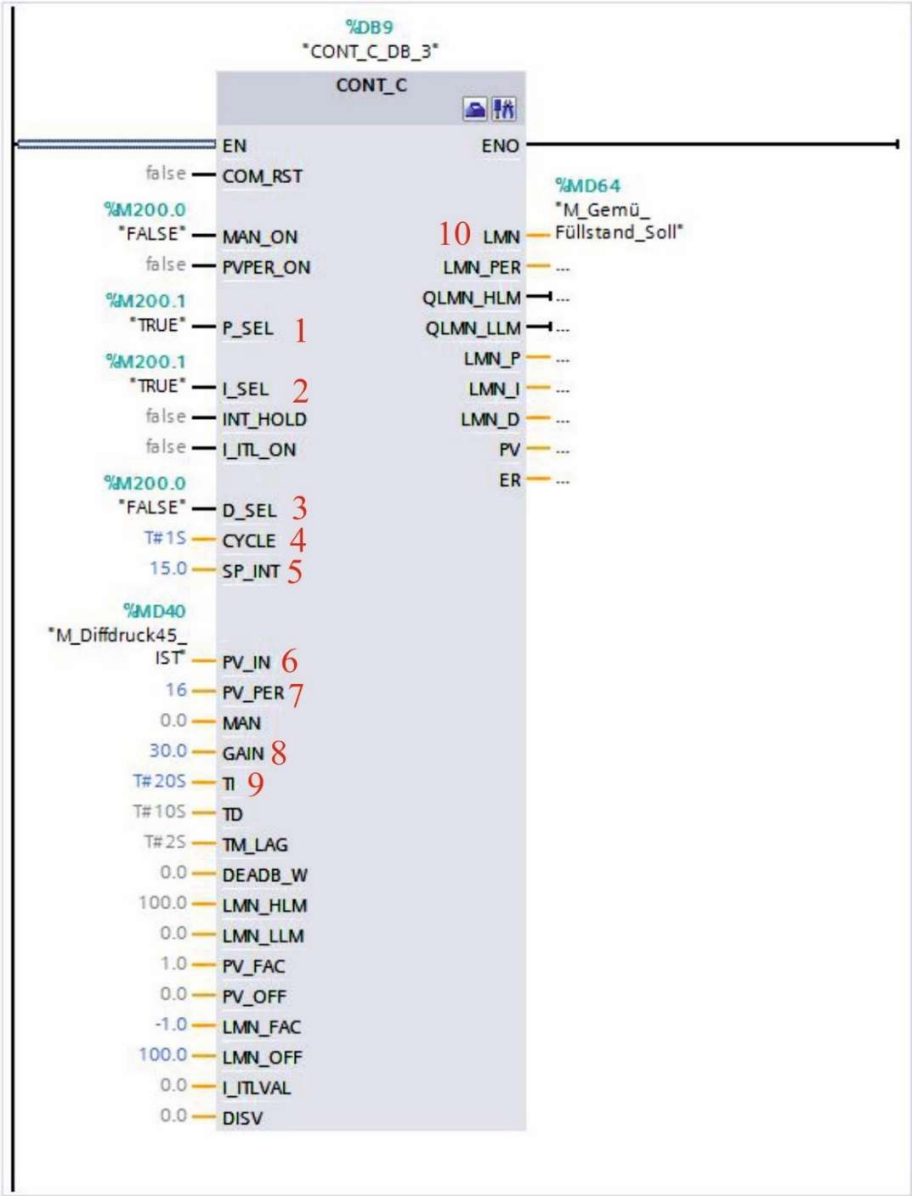

Figure 3.27 Function block of the PI controller for liquid level

Implementing the control circuits by Tia Software Portal for absorber pressure, the liquid level in the reboiler, safety heating coil, and mass flow controller of gas are shown in the appendix.

Chapter 4 : **Commissioning the absorber test rig**

This chapter summarizes the commissioning of an absorber test rig built at the Institute of Energy Systems and Technology (EST) at Technical University of Darmstadt to verify that it operates safely and meets the experimental requirements for which it was built.

4.1 Introduction

After the absorber test rig construction was completed and before the experiments started, some tests had to be performed to ensure that the test rig was ready for both steady-state and unsteady-state experiments. Thus, there was a commissioning phase of the test rig. The derived Objectives of commissioning can be surmised as follow:

- To investigate the performance of the control circuits and optimize them.
- To investigate the performance of the regeneration unit.
- To investigate the safety and experimental aspects of the test rig.
- To visualize the operating conditions where the test rig can be operated.

4.2 Test of the Pressure Control Circuit

This test evaluates the performance of the pressure control circuit. It determines its ability to control the pressure value to be close to the set point under various test operating conditions. The pressure control circuit was evaluated by performing three tests. In the first test, the pressure set point varied between 0.17 MPa to 0.3 MPa. In the second test, the gas flow rate at the inlet was changed to 10-20 Nm^3/h. The third test has been performed at different load changes in the inlet gas flow rate.

4.2.1 Test of the Pressure Control Circuit at different Set Points of the Pressure

The first test was performed by entering water and air into the absorber and varying the set point of the pressure between 0.17 MPa and 0.3 MPa. The flow rate of the inlet gas was constant at 15 Nm^3/h. The flow rate of the inlet liquid was constant at 170 L/h. Figure 4.1 shows the actual pressure values compared to the pressure set points and the percentage values for opening the control valve on the gas outlet line.

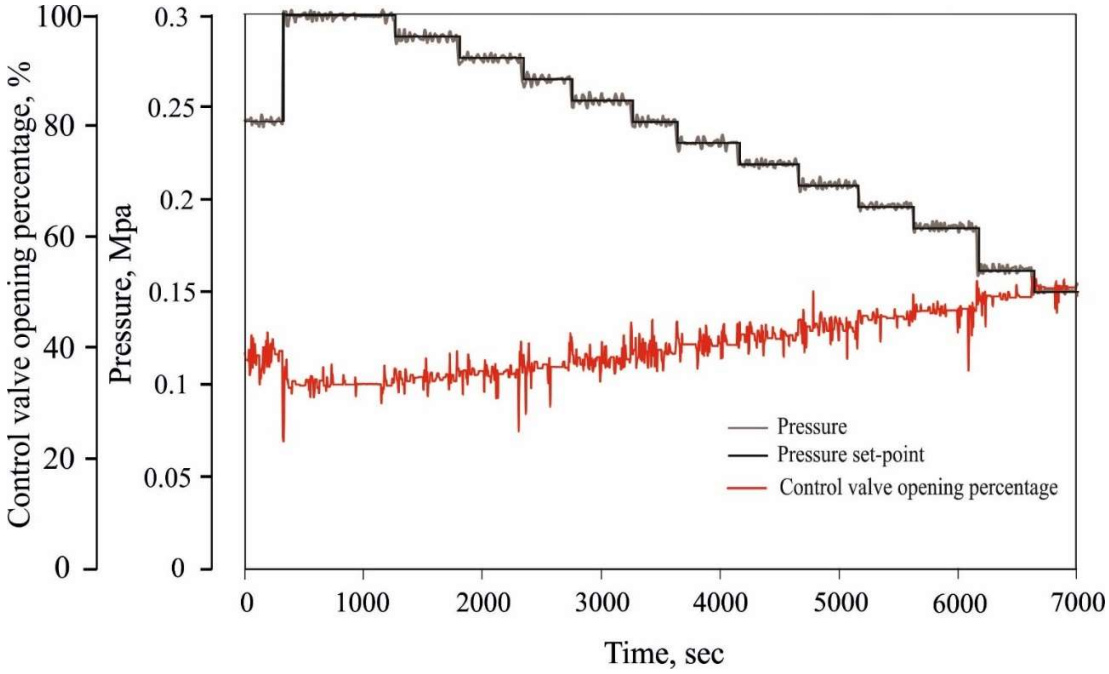

Figure 4.1 Commissioning pressure control circuit at different pressure set points

It can be seen that the deviation between the actual pressure and the set point of the pressure is too small, indicating the satisfactory performance of the pressure control circuit.

4.2.2 Test of the Pressure Control Circuit at different Inlet Gas Flow Rate

This test was performed to evaluate the performance of the control circuit when the gas inlet flow rate was changed. Figure 4.2 shows the actual pressure values compared to the pressure set points at different inlet gas flow rates. Figure 4.2 shows also the percentage values for opening the control valve on the gas outlet line. It can be seen that the deviation between the actual pressure and the set point of the pressure is too small, indicating the satisfactory performance of the pressure control loops under operating conditions of changing of inlet flow rate.

In the transient state of changing the load of the inlet flow rate, the pressure takes about 25-30 seconds to be adjusted to the set point, which is satisfactory for steady-state experiments but not suitable for dynamic experiments where the pressure should be adjusted in 10 seconds or less. Therefore, it should adjust the parameters of the PI controller when the operator wants to study the different load changes in inlet gas flow.

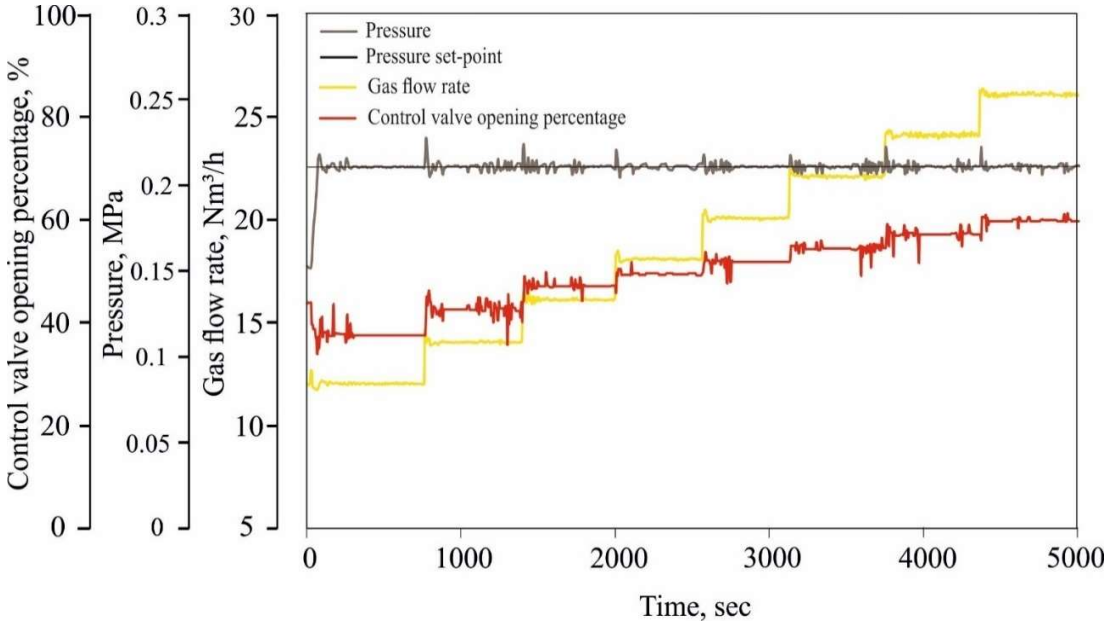

Figure 4.2 Commissioning pressure control circuit at different gas flow rates

4.2.3 Test of the Pressure Control Circuit at Different Load Changes in Inlet Gas Flow Rate

To perform ramp-up or ramp-down tests of different load changes of the inlet gas flow rate, the parameters of the PI controller must be readjusted to improve the response of the pressure control loop during the transient state of different load change tests. In addition, the response of the mass flow controllers for the CO_2 and N_2/air gases must be adjusted to control different rates of change in the inlet gas flow rate. A programming code was developed to adjust the behavior of the mass flow controllers for CO_2 and N_2/air. The programming code is shown in the Appendix. Its performance was satisfactory.

Figure 4.3 and Figure 4.4 shows the actual pressure values compared to the pressure set points at different load changes in inlet gas flow rate (ramp-up and ramp-down tests). The time to control the pressure during the transient state has been improved from 25 sec to 10 sec.

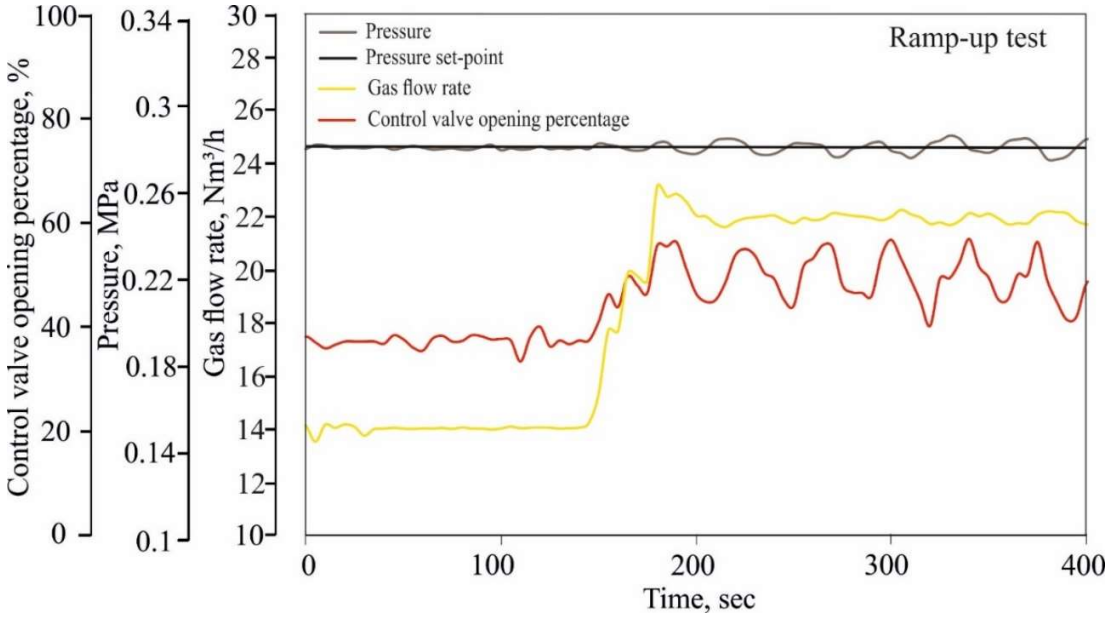

Figure 4.3 Commissioning pressure control circuit at different load changes of gas flow rate (Ramp-up test)

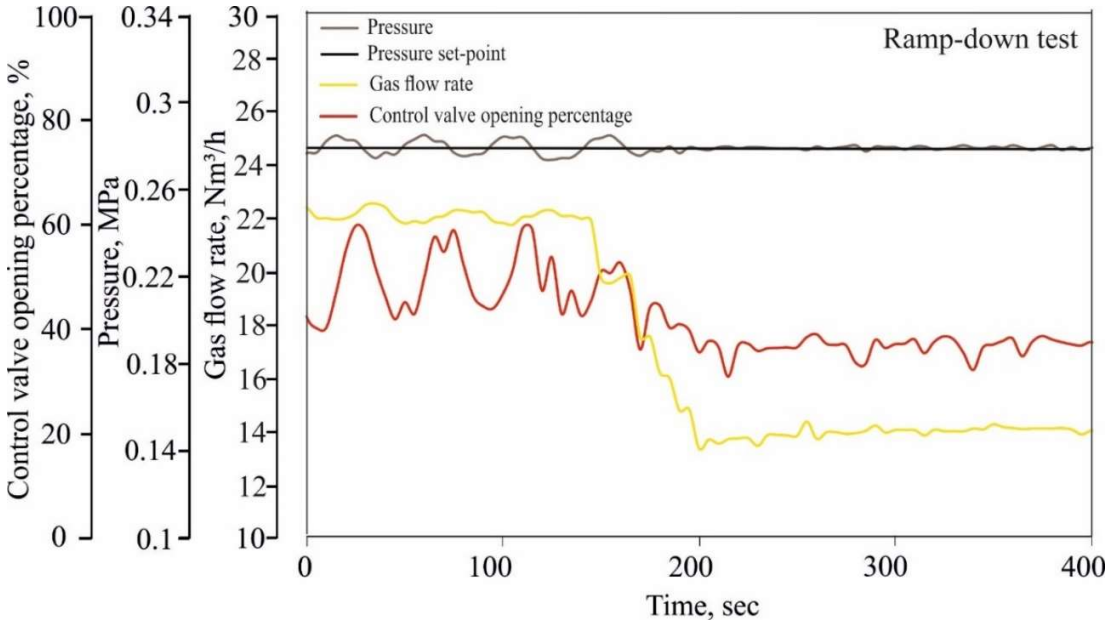

Figure 4. 4 Commissioning pressure control circuit at different load changes of gas flow rate (ramp-down test)

Based on these performed tests, the performance of the pressure control circuit is suitable for the conditions of steady state and unsteady state experiments.

4.3 Test of the Liquid Level Control Circuit at the Sump of the Absorber

The liquid level in the sump of the absorber is influenced by the pressure of the absorber and the solvent flow rate at the inlet. Two tests were performed to evaluate the level control loop under different operating conditions. In the first test, the pressure set point was varied between 0.2 MPa to 0.3 MPa. The second test was performed by changing the inlet of the gas flow rate between 100-200 L/h.

4.3.1 Test of the liquid Level Control Circuit at the Sump of the Absorber at Different Pressures

The first test was performed by introducing water and air into the absorber and varying the set point of the pressure between 0.2 MPa and 0.3 MPa. Figure 4.5 shows the actual liquid level compared to the liquid level set points (16 cm) and the percentage values for opening the control valve on the liquid outlet line. It can be seen that the deviation between the actual liquid level and the set point of the liquid level is too small, indicating the satisfactory performance of the liquid level control circuit.

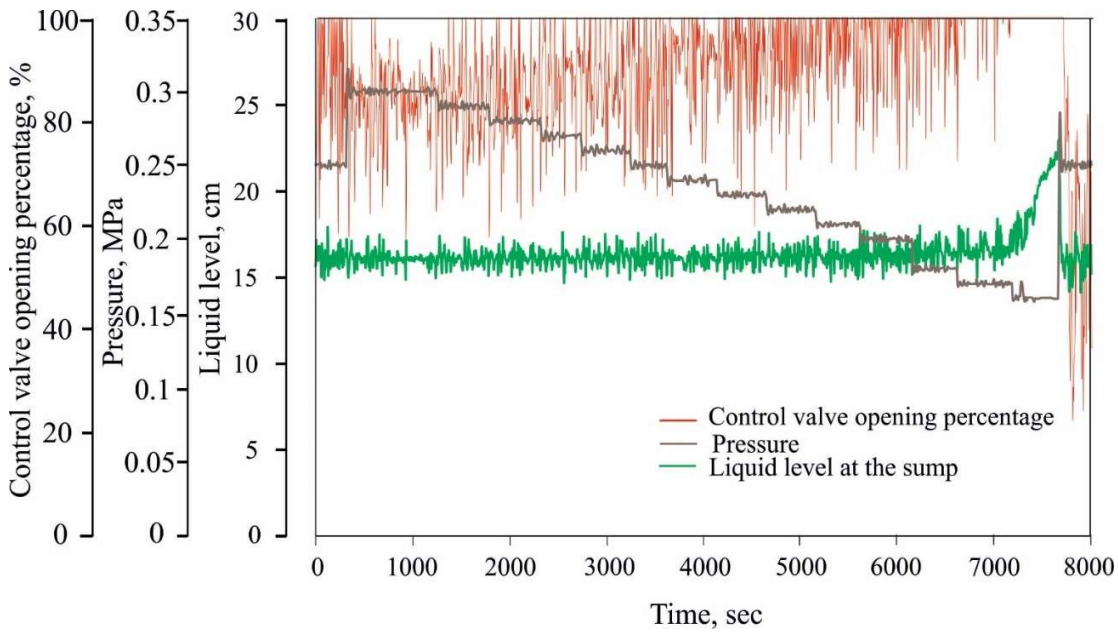

Figure 4.5 Commissioning level control circuit for the sump of the absorber at different pressure

4.3.2 Test of the Liquid Level Control Circuit at the Sump of the Absorber at Different Inlet Liquid Flow Rates

The second test was performed to evaluate the performance of the liquid level control circuit when the inlet liquid flow rate was changed. Figure 4.6 shows the liquid level in the sump of the absorber compared to the liquid level set points (16 cm) when the inlet liquid flow rate is changed. It can be seen that the deviation between the actual liquid level and the set point of the pressure is too small, indicating the satisfactory performance of the level control loops under operating conditions of changing the inlet liquid flow rate.

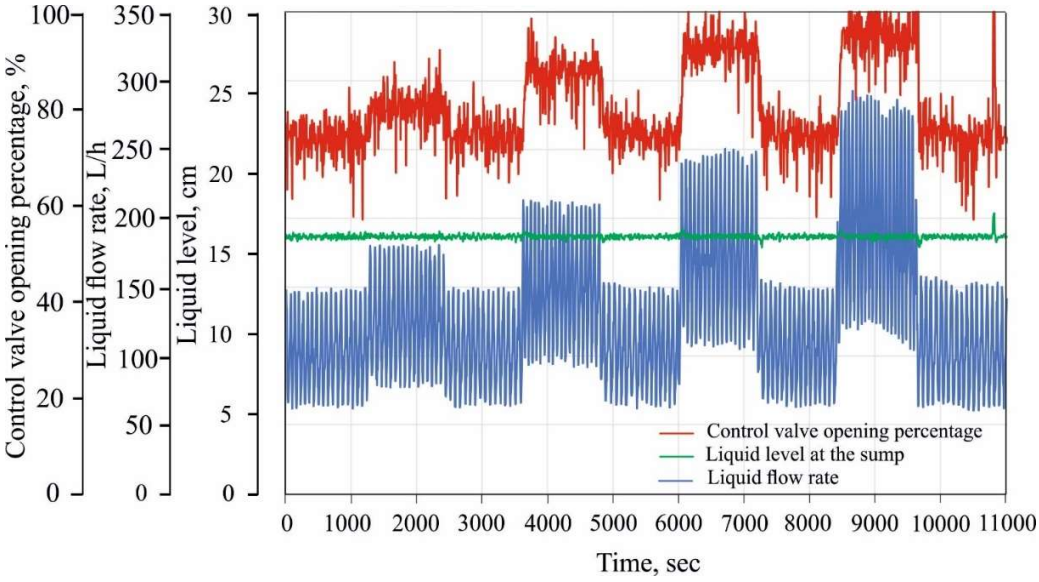

Figure 4.6 Commissioning level control circuit at different liquid flow rates

4.4 Test of the Liquid Level Control Circuit in the Reboiler

As explained above, the control circuit must maintain a level higher than the set point measured by a level sensor at a distance of 4 cm above the heater. However, there are no measurements of the level in the heater, so no results are available for the liquid level in the reboiler. During the test of the control circuit, things went as follows: When the liquid level drops to the set point, the compensation pump connected to the circuit works automatically and continues its work until the liquid level rises above the set point; then, the pump automatically shuts off, and so on.

As proof of the satisfactory performance of the control circuit, Figure 4.7 and Figure 4.8 show a comparison of the liquid flow rate with and without the control circuit. It can be seen that without the level control circuit in the reboiler, the performance of the pump changes over time even though the set point for the load of the pump has been fixed. In comparison, the pump's performance does not change with the presence of the control circuit. The flow rate of the pump is influenced by the hydrostatic height of the liquid in front of the pump. If the hydrostatic height is constant, the flow rate of the liquid is constant. In contrast, the flow rate of the liquid changes if the hydrostatic height changes with time.

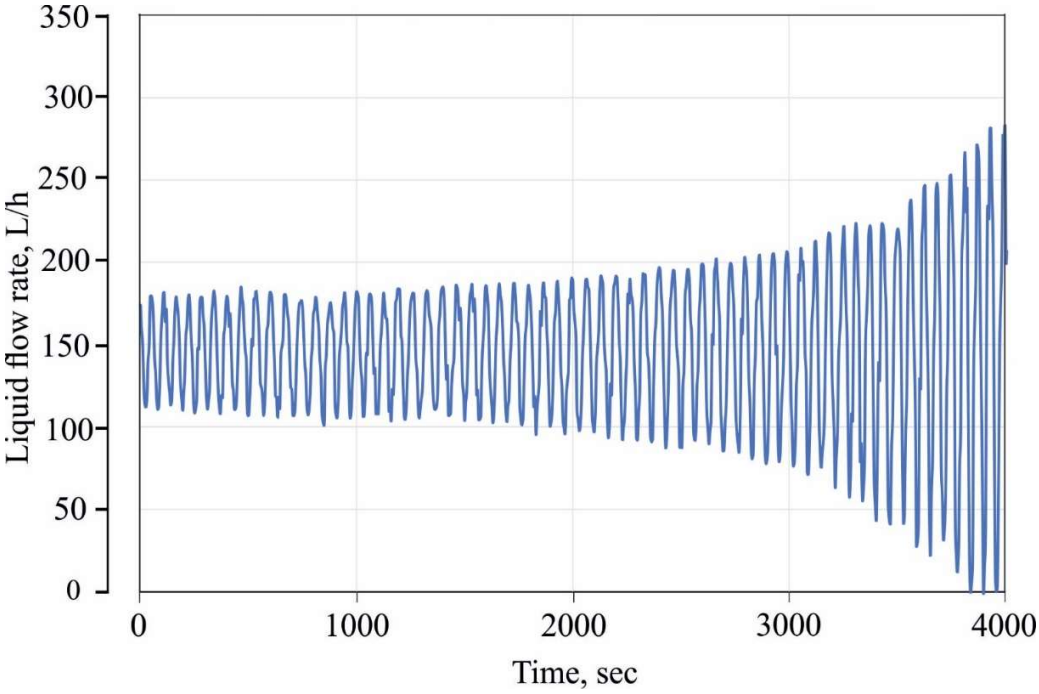

Figure 4. 7 Flow rate of the liquid pumping by the recycling pump (without a level control circuit)

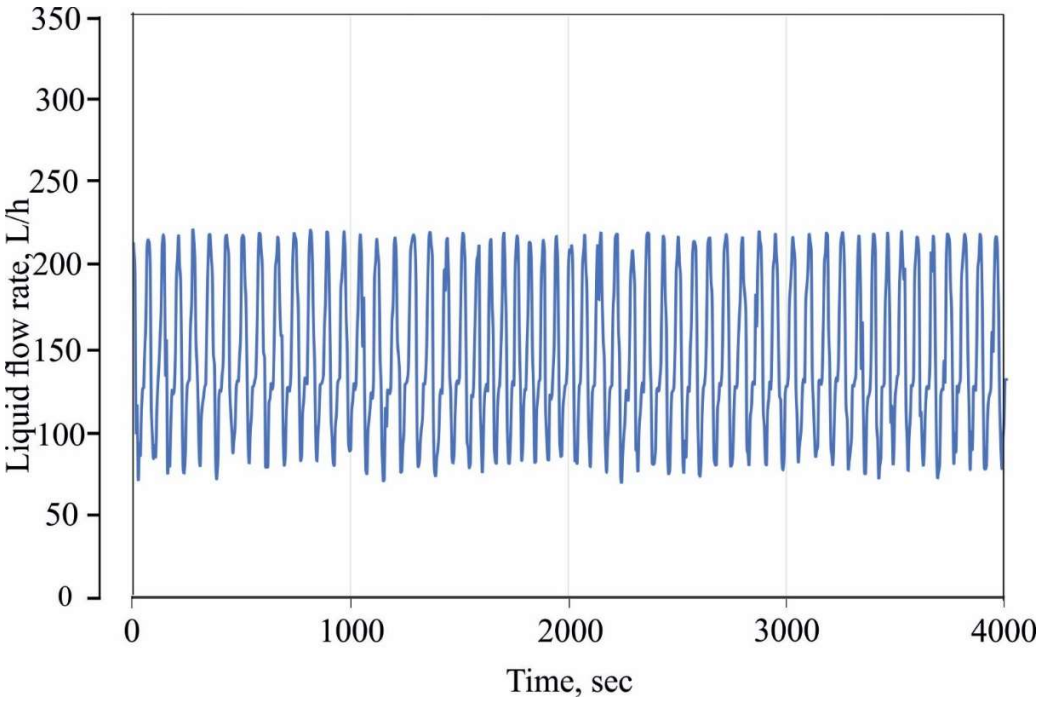

Figure 4.8 Flow rate of the liquid pumping by the recycling pump (with a level control circuit)

4.5 Test of Regeneration Unit

The objective of the regeneration unit is to regenerate the solvent by heating it to a specific temperature to release the absorbed gases, then pumping the solvent back into the absorption column after cooling it to a specific temperature. Two tests have been performed to evaluate the performance of the temperature control circuit in the reboiler. The first test is performed by changing the temperature set point of the reboiler. The second test is by changing the flow rate of the liquid.

Figure 4.9 shows the performance of the regeneration unit when the temperature set point of the solvent is changed between 30 °C and 60 °C. It can be seen that the deviation between the actual temperature of the solvent and the temperature set point is small, indicating the satisfactory performance of the temperature control loops.

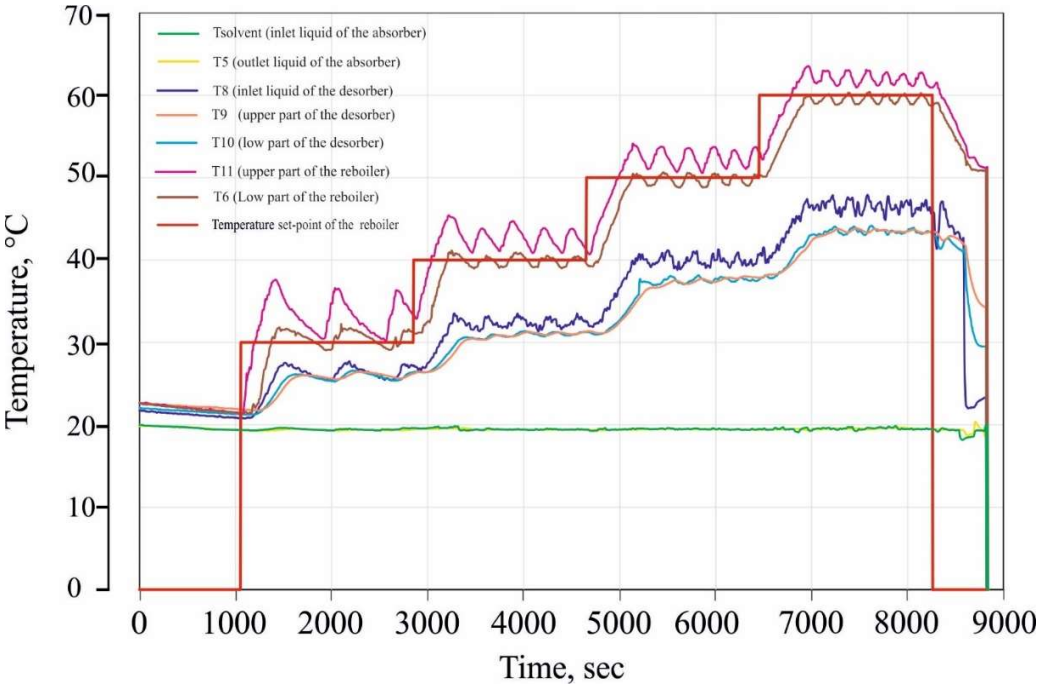

Figure 4.9 Commissioning regeneration unit at different temperature set points

Figure 4.10 shows the performance of the regeneration unit at different load changes of the inlet liquid flow rate. It can be seen that the deviation between the actual temperature of the reboiler and the set point of the temperature is small, indicating the satisfactory performance of the temperature control circuit.

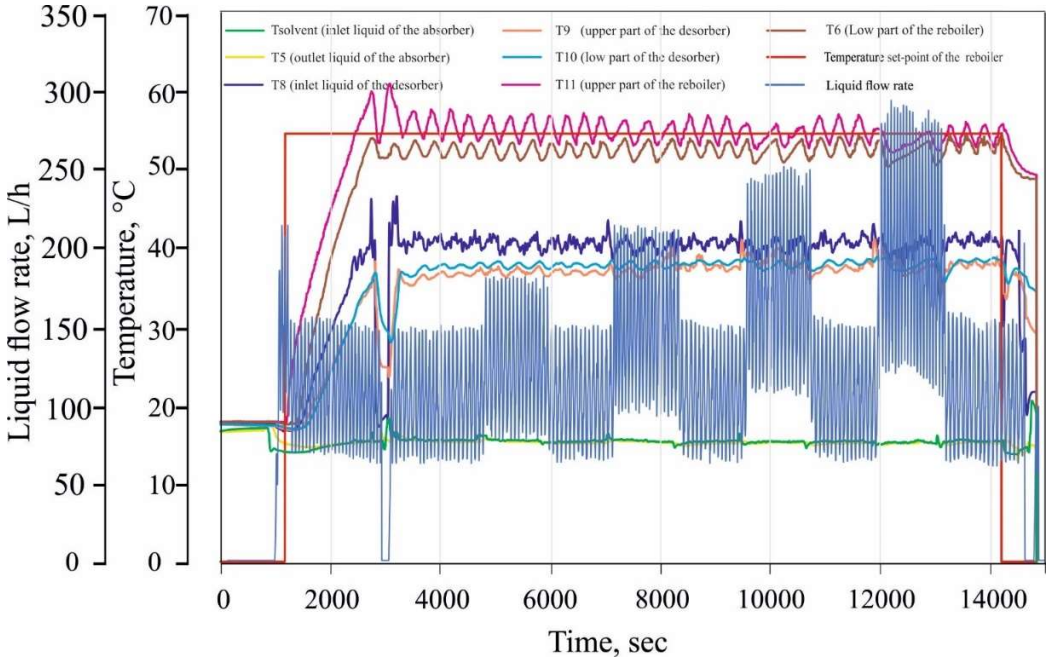

Figure 4.10 Commissioning regeneration unit at different liquid flow rates

4.6 Commissioning the Recycling Pump

The pump used is of the piston pump type. The load of the pump can be changed between 0-100%. Increasing the load increases the flow rate of the pumped liquid. The flow rate of the liquid is in the form of pulses. The pulse range increases as the load increases. To test the recycling pump, it was operated with variable loads between 10-95%. At the same time, the liquid flow rate corresponding to these loads was measured with the Coriolis flow meter. Figure 4.11 shows the operation of the recycling pump at various loads and the actual liquid flow rate pumped by the recycling pump. Since the flow rate of the liquid is in the form of pulses, the median value of the flow was computed. Figure 4.12 shows the median liquid flow rate as a function of the pump load.

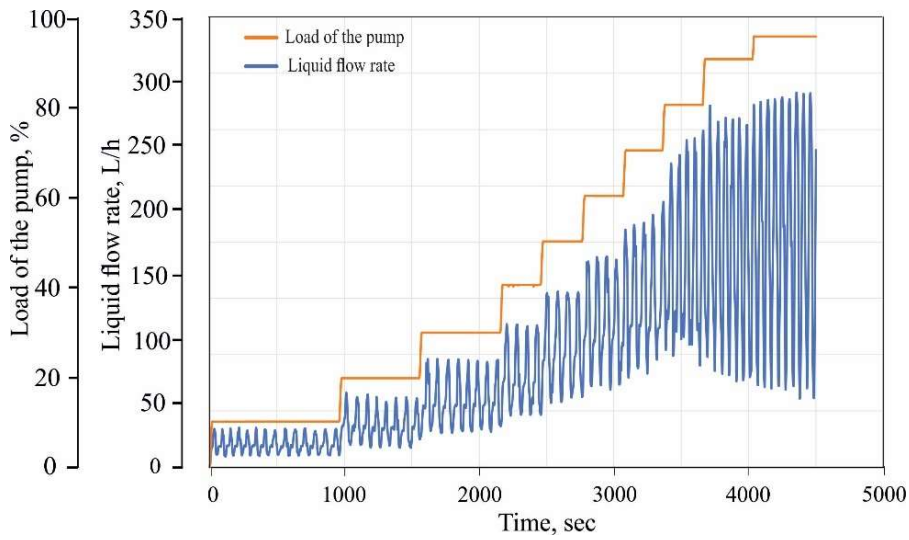

Figure 4.11 Actual liquid flow rate (Pulses)

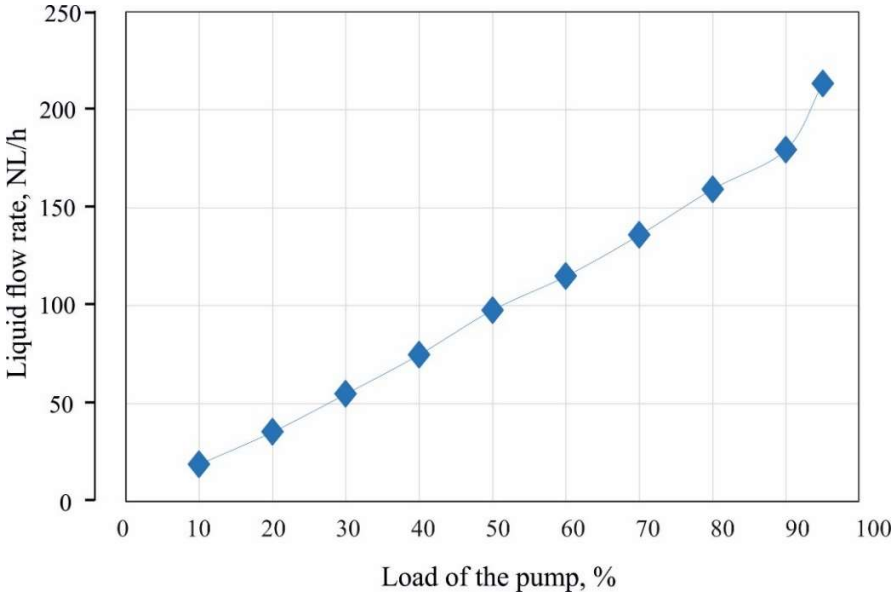

Figure 4.12 Median flow rate as a function of the pump load

4.7 Test of the pH Sensor

As explained, the ability of an amine to absorb acid gases depends on its alkalinity [74]. Therefore, a pH sensor was installed in the absorber at the liquid inlet. The pH sensor used, and its working principle is shown in the Appendix. The pH sensor was tested while performing the experiments. Figure 4.13 shows some measurements of the pH value for an aqueous methyl diethanolamine (MDEA) solution of 50% mass fraction. The pH sensor continuously measures the pH of the inlet solvent. It can be seen that the pH is constant over time. Since the pH is a function of the hydrogen ions concentration in the solvent, the constant pH value gives an idea about a constant hydrogen ions concentration in the inlet solvent. It may be essential to consider the constant value of the pH of the solvent when steady-state experiments are performed.

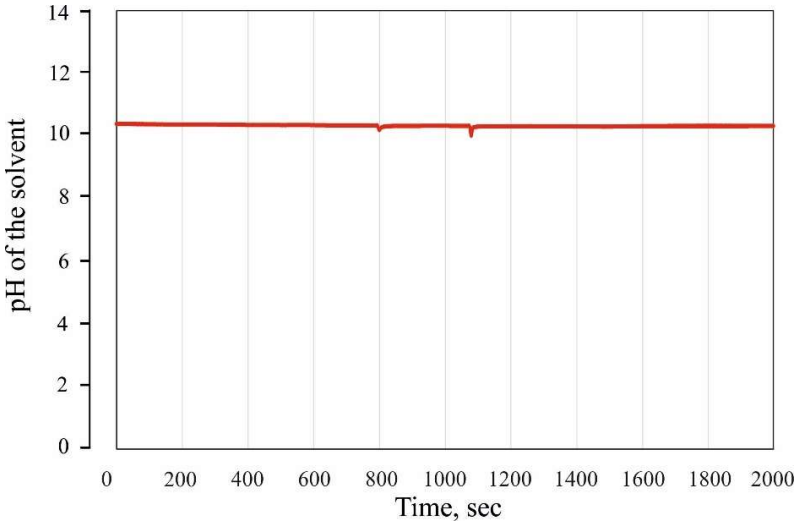

Figure 4. 13 pH of the solvent

Chapter 5 : **Modeling of the Absorption Process**

This chapter presents two mathematical models (the equilibrium model and the rate-based model) applied to simulate the absorption process. In addition, thermodynamic approaches to predict phase behavior are described. Finally, the correlations for calculating the binary mass transfer coefficients, the heat transfer coefficient, the liquid holdup, and the interface are presented.

5.1 Introduction

The importance of modeling the absorption process is well recognized. It is an effective tool for evaluating system behavior and for visualizing and understanding the process. It also saves time, money, and effort in collecting experimental data. This places high demands on both the quality of the models and their numerical solution in terms of accuracy and efficiency. In the literature, two common models are used to calculate the absorption process: the equilibrium model and the rate-based model.

5.2 Equilibrium Stage Model

The equilibrium stage model is based on dividing the absorber column into stages. The equilibrium stage model assumes that each stage in the absorption column is considered an equilibrium stage, which means that the gas or the vapor and the liquid are in thermodynamic equilibrium when leaving a stage [52]. Based on these assumptions, the equations for mass balance, energy balance, phase equilibrium, and mole fraction summation can be applied to calculate the unknown variables involved in the absorption process. Figure 5.1 shows the streams and the corresponding properties of an equilibrium stage or what is called a theoretical plate.

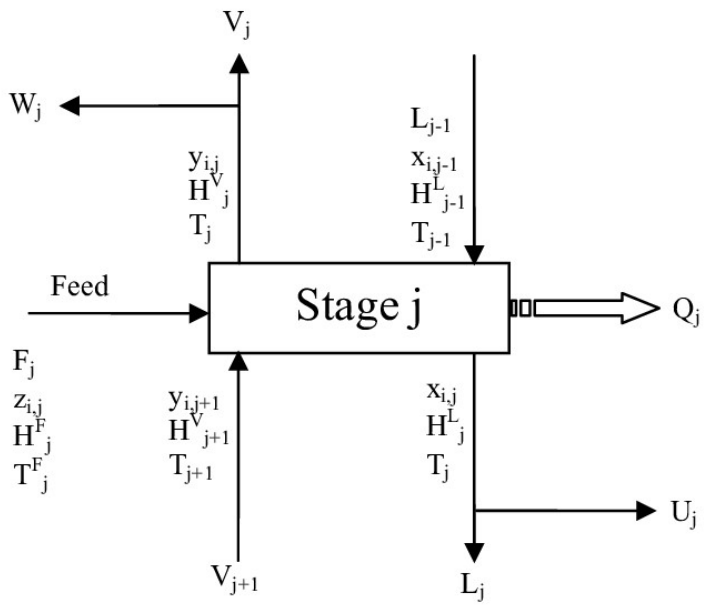

Figure 5.1 Equilibrium stage [89]

The equilibrium stage model consists of known and accepted correlations called the MESH equations, which include the material balance equations of the components, phase equilibrium equations, mole fractions summation equations, and heat (energy) balance equations for each stage as follows [90], [91]:

Material balance equations:

$$L_{i,in} + G_{i,in} - L_{i,out} - G_{i,out} = 0 \tag{5.1}$$

$$x_{i,in}\,\dot{N}_L + y_{i,in}\,\dot{N}_G - x_{i,out}\,\dot{N}_L - y_{i,out}\,\dot{N}_G = 0 \tag{5.2}$$

$$\dot{N}_L\left(x_{i,in} - x_{i,out}\right) + \dot{N}_G\left(y_{i,in} - y_{i,out}\right) = 0 \tag{5.2}$$

Mole fractions summation equations:

$$x_{i,out} = \frac{L_{i,out}}{\sum_{j=1}^{i=k} L_{j,out}} \tag{5.4}$$

$$y_{i,out} = \frac{G_{i,out}}{\sum_{j=1}^{i=} G_{j,out}} \tag{5.5}$$

$$L_{i,in} = x_{i,in}\,\dot{N}_L \tag{5.6}$$

$$L_{i,out} = x_{i,out}\,\dot{N}_L \tag{5.7}$$

$$G_{i,in} = y_{i,in}\,\dot{N}_G \tag{5.8}$$

$$G_{i,out} = y_{i,out}\,\dot{N}_G \tag{5.9}$$

Phase equilibrium equations:

$$y_i - K_i x_i = 0 \tag{5.10}$$

$$y_i \Phi_i^v P = x_i \gamma_i \Phi_{soi} P_{soi} exp\left\{\frac{1}{RT}\int_{P_{soi}}^{P} V_{oi}^L dP\right\} \tag{5.11}$$

Heat or Energy balance equations:

$$\sum_{i=1}^{i=C}\left(L_{i,in}\,h_{i,in}^L + G_{i,in}\,h_{i,in}^G - L_{i,out}\,h_{i,out}^L - G_{i,out}\,h_{i,out}^G\right) + Q = 0 \tag{5.12}$$

Where L_i represents the liquid molar flow rate of component i , G_i represents the gas molar flow rate of component i, $\dot{N}_L$ represents liquid molar flow rate, $\dot{N}_G$ represents gas or vapor molar flow rate, F represents feed molar flow rate, x represents liquid mole fraction, y represents gas mole fraction, i represents component index, j represents stage index, k represents the last stage, C represents the last component, Q represents heat input to a stage, H represents enthalpy, K_i represents equilibrium value, Φ_i^v represents fugacity coefficients, P_{soi} represents saturation vapor pressure of pure component i, γ_i represents activity coefficient, P represents vapor pressure.

According to Seader et al.2011[91], the main assumptions of the equilibrium model are as follows:

• Phase equilibrium is presented at each stage,

• There are no chemical reactions between the components of vapor and liquid,

• Entrainment of liquid drops in vapor and occlusion of vapor bubbles in the liquid is negligible.

In the real process, the equilibrium state may never be reached at every stage, so the real deposition property is described by the use of tray efficiency [92].

The efficiency of the trays is commonly evaluated as Murphree efficiency $Eff_{i,j}^{M}$, which is defined as follows [92] :

$$Eff_{i,j}^{M} = \frac{y_{i,j} - y_{i,j+1}}{K_{i,j}x_{i,j} - y_{i,j+1}} \tag{5.13}$$

Where $Eff_{i,j}^{M}$ is Murphree efficiency, x_i , y_i are mole fractions of component *i* in liquid and vapor phases respectively, $y_{i,j+1}$ is the mole fraction of component *i* in stage *j+1* (the stage numbered from top to the bottom, and K_i represents equilibrium value.

5.3 Rate-based Stage Model

The Rate-based stage model depends on the two-film theory. The two-film theory was developed by Lewis and Whitman in 1924 [93], and it explains the mass transfer between gas and liquid. The two-film theory is based on the assumption that when the gas and liquid phases contact each other, a thin stagnant film of fluid is created on each side of the gas-liquid interface [94]. Figure 5.2 illustrates the concentration gradation of component i at a gas/liquid interfacial area. It is noted that the concentration of component i decreases from $C_{i,G}$ in gas bulk to $C_{i,G*}$ in the interface. The difference of concentration creates a driving force for component i to shift it from the bulk gas to gas film and then from the gas film to liquid film, the growth of component i in the liquid film forms a concentration difference between the liquid film and the bulk liquid. Likewise, The difference creates a driving force for component i to shift it from the liquid film to the bulk liquid [94].

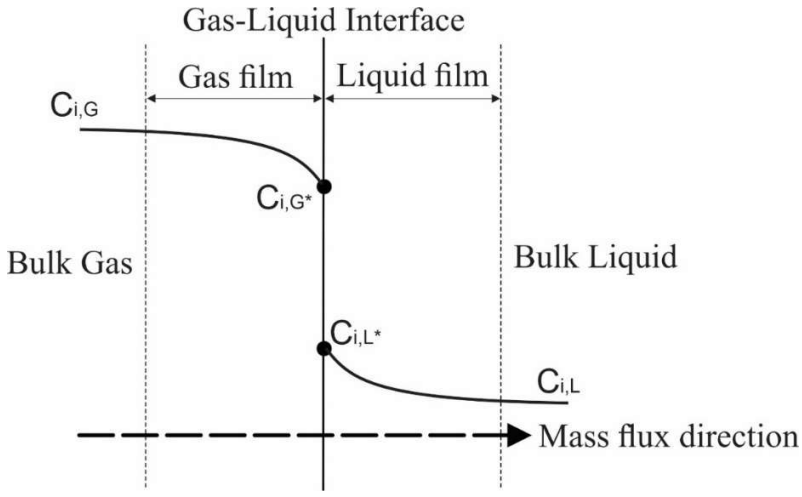

Figure 5.2 Illustration for the concentration of component i at the gas/liquid interfacial area [95]

The rate of mass transfer of component i through the gas film is calculated as follows [95]:

$$N_{i,G} = k_G a^* (C_{iG} - C_{iG*}) \tag{5.14}$$

The rate of mass transfer of component i through the liquid film is calculated as follows [95]:

$$N_{i,L} = k_L a^* (C_{iL*} - C_{iL}) \tag{5.15}$$

Where k_G , k_L are the mass transfer coefficient of the gas phase and liquid phase respectively, a^* is the interfacial area.

At a steady state, the flux of component i from bulk gas to the interface must equal the flux of component i from the interface to the bulk liquid [96]:

$$N_{i,G} = N_{i,L} \tag{5.16}$$

5.3.1 Mathematical basis of Rate-based Stage Model

The rate-based model consists of a set of well agreement correlations which calculate the mass and energy transfer across the interfacial area using mass transfer coefficients [97]. The rate-based model is based on dividing the absorber column into stages. Figure 5.3 shows a stage j of the column, which represents a tray in the column.

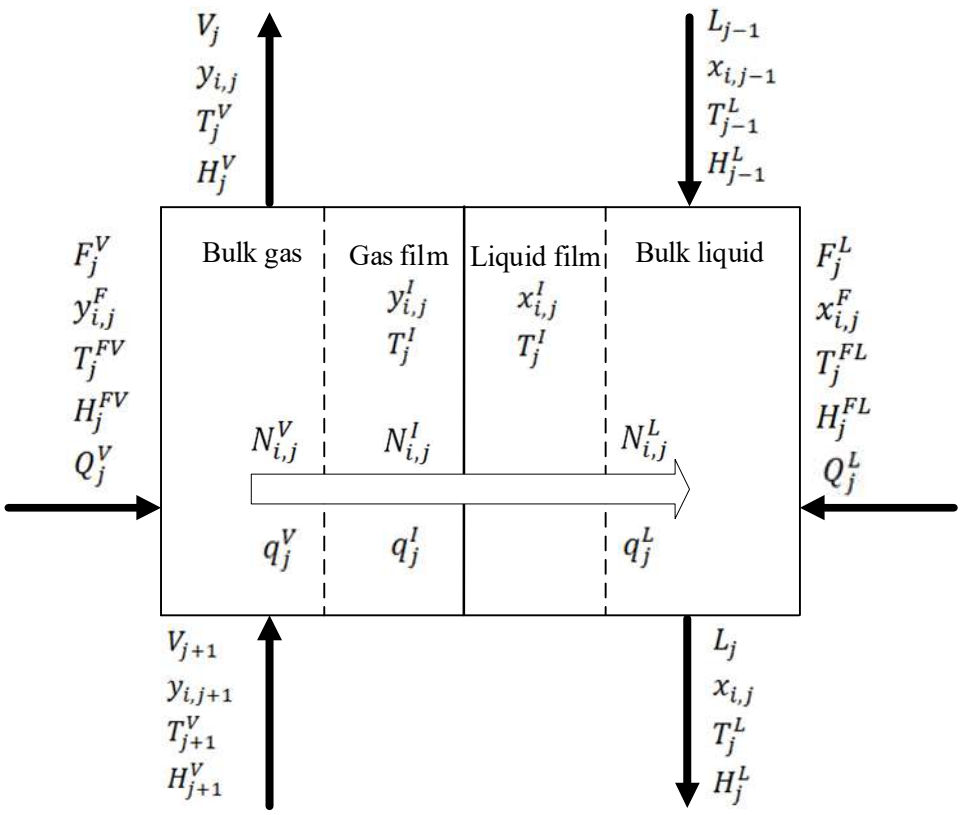

Figure 5.3 Rate-based stage model (Reproduced from ASPEN PLUS software manual)

The rate-based model consists well known and accepted correlations called MERSHQ equations presented by Taylor and Krishna (1993) [98] which calculate material balance, energy balance, mass- and heat-transfer rate, phase equilibrium equations, mole fractions summation equations, and hydraulic equations for pressure drop around a stage j as follows [98]:

Material balance for bulk vapor: $$F_j^V y_{i,j}^F + V_{j+1} y_{i,j+1} + N_{i,j}^V + r_{i,j}^V - V_j y_{i,j} = 0 \quad (5.17)$$

Material balance for bulk liquid: $$F_j^L x_{i,j}^F + L_{j-1} x_{i,j-1} + N_{i,j}^L + r_{i,j}^L - L_j x_{ij} = 0 \quad (5.18)$$

Material balance for vapor film: $$N_{i,j}^V + r_{i,j}^{fV} - N_{i,j}^I = 0 \quad (5.19)$$

Material balance for the liquid film: $$N_{i,j}^I + r_{i,j}^{fL} - N_{i,j}^L = 0 \quad (5.20)$$

Energy balance for bulk vapor: $$F_j^V H_j^{FV} + V_{j+1} H_{j+1}^V + Q_j^V - q_j^V - V_j H_j^V = 0 \quad (5.21)$$

Energy balance for bulk liquid: $$F_j^L H_j^{FL} + L_{j-1} H_{j-1}^L + Q_j^L + q_j^L - L_j H_j^L = 0 \quad (5.22)$$

Energy balance for vapor film: $$q_j^V - q_j^I = 0 \quad (5.23)$$

Energy balance for the liquid film: $$q_j^I - q_j^L = 0 \quad (5.24)$$

Phase equilibrium at the interface: $$y_{i,j}^I - K_{i,j} x_{i,J}^I = 0 \quad (5.25)$$

Summation for bulk vapor: $$\sum_{i=1}^{n} y_{i,j} - 1 = 0 \quad (5.26)$$

Summation for bulk liquid: $$\sum_{i=1}^{n} x_{i,j} - 1 = 0 \quad (5.27)$$

Summation for vapor film: $$\sum_{i=1}^{n} y_{i,j}^I - 1 = 0 \quad (5.28)$$

Summation for the liquid film: $$\sum_{i=1}^{n} x_{i,j}^I - 1 = 0 \quad (5.29)$$

Where F is the molar flow rate of feed, L and V are the molar flow rate of liquid and vapor respectively, N is the molar transfer rate, K is the equilibrium ratio, r is the reaction rate, H is enthalpy, Q is heat input to a stage, q is heat transfer rate, x_i , y_i are mole fractions of component i in liquid and vapor phases respectively.

5.3.2 Mass Transfer Models for Rate-based Stage Model

In the following, the empirical correlations are used in the rate-based model for the estimation of binary mass transfer coefficients:

AIChE Correlation [99]:

$$k_{i,k}^{L} = 19700\left(D_{i,k}^{L}\right)^{0.5}\frac{0.4F_s + 0.17}{\bar{a}} \tag{5.30}$$

$$k_{i,k}^{V} = \left(0.776 + 4.57h_w - 0.238F_s + \frac{104.8\bar{Q}_L}{l_w}\right)\frac{Sc_{V,i,k}^{-0.5}}{a^{'}t_V} \tag{5.31}$$

Gerster et al. Correlation [100]:

$$k_{i,k}^{L} = \frac{\left(4.127 \times 10^8 D_{i,k}^{L}\right)^{0.5}(0.21313F_s + 0.15)Lt_L}{\bar{\rho}^L a^I} \tag{5.32}$$

$$k_{i,k}^{V} = \left(0.776 + 4.57h_w - 0.238F_s + \frac{104.8\bar{Q}_L}{l_w}\right)\frac{Sc_{V,i,k}^{-0.5}A_b u_s^V}{a^I} \tag{5.33}$$

Chan and Fair Correlation [101]:

$$k_{i,k}^{L} = 19700\left(D_{i,k}^{L}\right)^{0.5}\frac{0.4F_s + 0.17}{\bar{a}} \tag{5.34}$$

$$k_{i,k}^{V} = \left(10300 - 8670F_f\right)F_f\left(D_{i,k}^{V}\right)^{0.5}\left(\frac{1-a}{a}\right)\frac{h_{cl}^{0.5}A_b}{a^I} \tag{5.35}$$

Chan and Fair (Rate Frac) Correlation [101], [100]:

$$k_{i,k}^{L} = \frac{\left(4.127 \times 10^8 D_{i,k}^{L}\right)^{0.5}(0.21313F_s + 0.15)Lt_L}{\bar{\rho}^L a^I} \tag{5.36}$$

$$k_{i,k}^{V} = \left(10300 - 8670F_f\right)F_f\left(D_{i,k}^{V}\right)^{0.5}\left(\frac{1-a}{a}\right)\frac{h_{cl}^{0.5}A_b}{a^I} \tag{5.37}$$

Chen and Chuang Correlation [102]:

$$k_{i,k}^{L} = \frac{14A_b}{(\mu^L)^{0.1}\phi^{0.14}}\left(\frac{\rho_t^L F_s^2}{\sigma^2}\right)^{1/3}\sqrt{D_{i,k}^{L}t_{VL}}\left(\frac{\rho_t^V}{\rho_t^L}\right)\frac{u_s^V}{a^I} \tag{5.38}$$

$$k_{i,k}^{V} = \frac{14A_b}{(\mu^L)^{0.1}\phi^{0.14}}\left(\frac{\rho_t^L F_s^2}{\sigma^2}\right)^{1/3}\sqrt{D_{i,k}^{V}t_V}\frac{u_s^V}{a^I} \tag{5.39}$$

Where $k_{i,K}^{L}$ is the binary mass transfer coefficient for the liquid which is predicted by using AICHE 1958 correlation, $k_{i,K}^{V}$ is the binary mass transfer coefficient for the vapor which is predicted by using Chan and Fair 1984 correlation, $D_{i,k}^{L}, D_{i,k}^{V}$ are diffusivity of the liquid and vapor respectively, Fs is the superficial F-factor, L is the total molar flow rate of liquid, t_L is the average residence time for the liquid (per pass), $\bar{\rho}^L$ is the molar density of the liquid, a^I is the total interfacial area for mass transfer which is calculated according to the Zuiderweg 1982 correlation, F_f is a fractional approach to flooding, a is the relative froth density, h_{cl} is the clear liquid height, A_b is the total active bubbling area on the tray, u_s^V is the superficial velocity of vapor, ρ_t^L, ρ_t^V are the density of the liquid and vapor respectively, FP is the flow parameter, $\emptyset$ is the fractional hole area per unit bubbling area, σ liquid surface tension, l_w is the average weir length (per liquid pass), Q_L, Q_V are volumetric flow rates for the liquid and vapor respectively, u_{sf}^V is the superficial velocity of vapor at flooding, l_w is average weir height, P is sieve tray hole pitch, and N_p is the number of liquid flows.

F_s, u_s^V, F_f, FP *are* Superficial F-factor, Superficial velocity of vapor, Fractional approach to flooding, and Flow parameter respectively, which can be calculated as follows [86]:

$$F_s = u_s^V (\rho_t^V)^{0.5} \tag{5.40}$$

$$u_s^V = \frac{Q_V}{A_b} \tag{5.41}$$

$$F_f = \frac{u_s^V}{u_{sf}^V} \tag{5.42}$$

$$FP = \frac{Q_L}{Q_V}\left[\frac{\rho_t^L}{\rho_t^V}\right]^{0.5} \tag{5.43}$$

5.3.3 Heat Transfer Model for Rate-based Stage Model

The heat transfer through the interfacial area is estimated using the Chilton-Colburn-Analogy. The heat transfer coefficient h is calculated *as* follows [103].

$$h^L = \bar{k}^L \bar{\rho}^L C_P^L \left(\frac{\lambda^L}{\bar{\rho}^L C_P^L \bar{D}^L}\right)^{2/3} \tag{5.44}$$

$$h^V = \bar{k}^V \bar{\rho}^V C_P^V \left(\frac{\lambda^V}{\bar{\rho}^V C_P^V \bar{D}^V}\right)^{2/3} \tag{5.45}$$

Where k_G is the mass transfer coefficient for the gas phase, ρ_G is the density of the gas, c_p is specific molar heat capacity, $M_{w,L}$ is the molecular weight of the liquid phase, λ is thermal conductivity, and D is the diffusion coefficient.

5.3.4 Liquid Holdup Correlations for Rate-based Stage Model

The liquid holdup is the amount of liquid accumulated on the tray during the operation of the absorber. The prediction of the liquid holdup is necessary to calculate the hydrostatic pressure loss in the tray. There are many correlations for Liquid holdup in the literature. Most of these equations function for liquid and gas flow rate, liquid and gas properties, and the tray's geometry. In the following, there are some common liquid holdup correlations:

Bennet Agrawal, and Cook Correlation [104]:

$$h_L = h_{cl} A_b \tag{5.46}$$

$$h_{cl} = \left(h_w + (0.5 + 0.438 e^{-137.8 h_w}) \left(\frac{Q_L}{l_w a} \right)^{2/3} \right) \tag{5.47}$$

Zuiderweg Correlation [105]:

$$h_L = h_{cl} A_b \tag{5.48}$$

$$h_{cl} = 0.6 h_w^{0.5} \left(FP \frac{\mathrm{P} A_b}{l_w N_p} \right)^{0.25} \tag{5.49}$$

Stichlmair Correlation [106]:

$$h_L = h_{cl} A_b \tag{5.50}$$

$$h_{cl} = a \left[h_w + \frac{0.49}{c_d^{0.67}} \left(\frac{Q_L}{l_w a} \right)^{0.67} + \frac{125 (u_s^V - u_b)^2 \rho_t^V}{g (\rho_t^L - \rho_t^v)(1-a)^2} \right] \tag{5.51}$$

5.3.5 Interfacial Area correlations for Rate-based Stage Model

To calculate the Interfacial area between the gas and liquid phases can be applied Zuiderweg Correlation [105] as follows:

For the Spray regime where $FP \leq 3.0 l_w h_L / A_b$ (5.52)

$$a^I = \frac{40 A_b}{\phi^{0.3}} \left[\frac{(u_s^V)^2 \rho_t^V h_L FP}{\sigma} \right]^{0.37}$$

For a mixed froth-emulsion regime where $FP > 3.0 l_w h_L / A_b$ (5.53)

$$a^I = \frac{43 A_b}{\phi^{0.3}} \left[\frac{(u_s^V)^2 \rho_t^V h_L FP}{\sigma} \right]^{0.53}$$

5.3.6 Thermodynamics Approaches for Prediction of Phase Behavior

There are two common approaches for the prediction of phase behavior; (approach (φ /γ)) and (approach (φ, φ)) [107]. In the approach (φ /γ), the Equation of state model is applied to predict the non-ideal behavior of the vapor resp. gas phase, and Activity coefficient model to predict non-ideal behavior of liquid phase [107]. The Equation of the state is applied to predict the fugacity coefficients for each component in both vapor and liquid phases [107].

The activity coefficients can be calculated from Activity Coefficients Models. The NRTL (nonrandom two-liquid) model is an activity coefficient model widely used to predict phase equilibria. The NRTL model has three adjustable parameters that are calculated by regression of experimental data for a specific system [108]. The Nonrandom two liquid model can be expressed as follows [109]:

$$\ln \gamma_i = \frac{\sum_{j=1}^{n} x_j \tau_{ji} G_{ji}}{\sum_{k=1}^{n} x_k G_{ki}} + \sum_{j=1}^{n} \frac{x_j G_{ij}}{\sum_{k=1}^{n} x_k G_{kj}} \left(\tau_{ij} - \frac{\sum_{m=1}^{n} x_m \tau_{mj} G_{mj}}{\sum_{k=1}^{n} x_k G_{kj}} \right) \tag{5.54}$$

$$G_{ij} = exp\left(-a_{ij}\tau_{ij}\right) \tag{5.55}$$

$$\tau_{ij} = \mathrm{a}_{ij} + \frac{b_{ij}}{T} + e_{ij} \ln T + f_{ij} T \tag{5.56}$$

$$a_{ij} = c_{ij} + d_{ij}(T - 273.315K) \tag{5.57}$$

Where a_{ij} , $b_{ij}, c_{ij}, d_{ij}, e_{ij}$ *and* f_{ij} are NRTL non-randomness constants for binary interaction

Chapter 6 : **Experimental Results**

In this chapter, the results of the experiments conducted on the absorber test rig are presented. First, the methodology of the experimental study is explained, then the steady state and dynamic state results of the absorption experiments are presented, and finally, the experimental results are discussed.

6.1 Research Methodology

The methodology used in this study is based on the measurement of the CO_2 outlet volume fraction and the total tray pressure drop and dry tray pressure drop at different operating conditions. The other hydrodynamic properties (the hydraulic tray pressure drop, liquid holdup level, and liquid holdup) of the sieve tray can be estimated from the total pressure drop on the sieve tray. The correlation between the hydrodynamic properties of a sieve tray and the CO_2 outlet volume fraction was investigated. The effect of changing these hydrodynamic properties on the performance of a sieve tray column for CO_2 capture was studied. Knowledge of this effect will assist how in improving the performance of a sieve tray column.

To measure the total tray pressure drop, the absorber test rig, as seen in Figure 3.2 is equipped with a pressure difference device that measures the total pressure drop at the third tray. The total pressure drop is the sum of the dry tray pressure drop and the hydraulic tray pressure drop as follows:

$$\Delta P_{total,tray} = \Delta P_{dry,tray} + \Delta P_{\mathrm{hyd}.tray} \tag{6.1}$$

Where $\Delta P_{total,tray}$ is the total tray pressure drop, $\Delta P_{dry,tray}$ is the dry tray pressure drop, and $\Delta P_{hy\ .tray}$ is the hydraulic tray pressure drop.

$\Delta P_{total,tray}$ is measured during performing the experiments when the liquid and the gas are coming into the column, whereas $\Delta P_{dry,tray}$ is measured when only the gas is coming into the column at the same other operating conditions from pressure and inlet absorbent flow rate.

By measuring $\Delta P_{total,tray}$, $\Delta P_{dry,tray}$, one can calculate the $\Delta P_{\mathrm{hyd}.tray}$ as follow:

$$\Delta P_{hyd.tray} = \Delta P_{total,tray} - \Delta P_{dry,tray} \tag{6.2}$$

Since the hydraulic tray pressure drop is equivalent to the hydrostatic height of the liquid on the tray, the hydrostatic height of the liquid on the tray can be calculated as follows:

$$h_{cl} = \Delta P_{hyd.tray} \times 0.102 \tag{6.3}$$

Where h_{cl} is liquid holdup level or the hydrostatic height of the liquid on the tray (m), $\Delta P_{\mathrm{hyd}.tray}$ is the hydraulic tray pressure drop, and 0.102 is a constant for converting the unit of pressure drop from kPa to (m).

From equation (6.3), the liquid holdup can be calculated as follows:

$$h_L = A_{tray} \times h_{cl} \tag{6.4}$$

The performance of the absorber for CO_2 capture was evaluated by estimating the absorbed rate of CO_2. The absorbed rate of CO_2 was calculated using the equation as follows:

$$N_{CO_2} = F_{gas,in} y_{CO_2,in} - F_{gas,out} y_{CO_2,out} \tag{6.5}$$

$F_{gas,out}$ can be estimated as follows:

$$F_{gas,out} = F_{gas,in} - N_{CO_2} \tag{6.6}$$

Substituting equation (6.6) into equation (6.5), one gets:

$$N_{CO_2} = F_{gas,in} y_{CO_2,in} - (F_{gas,in} - N_{CO_2}) y_{CO_2,out} \tag{6.7}$$

Or

$$N_{CO_2} = F_{gas,in} \left(y_{CO_2,in} - y_{CO_2,out}\right)/(1 - y_{CO_2,out}) \tag{6.8}$$

where N_{CO_2} is the absorbed rate of CO_2 [Nm^3/h], $y_{CO_2,in}$ is the inlet volumetric fraction of CO_2, $y_{CO_2,out}$ is the outlet volumetric fraction of CO_2, $F_{gas,out}$ is the outlet gas flow rate [Nm^3/h], and $F_{gas,in}$ is the inlet gas flow rate [Nm^3/h].

$y_{CO_2,out}$ was measured by the gas analysis unit, where $y_{CO_2,in}$ was calculated as follows:

$$y_{CO_2,in} = \frac{F_{CO_2,in}}{F_{gas,in}} = \frac{F_{CO_2,in}}{F_{CO_2,in} + F_{N_2,in}} \tag{6.9}$$

Where $F_{CO_2,in}$ is the inlet CO_2 flow rate[Nm^3/h], and $F_{N_2,in}$ is the inlet h gas flow rate[Nm^3/h].

Water and aqueous methyl diethanolamine (MDEA) solutions were used as a solvent in this study. The experiments conducted with water aimed to study the effect of the hydrodynamic properties of the tray and their effects on the performance of a tray absorber. The experiments conducted with aqueous MDEA solutions were to study the effect of different load changes and different change rates in gas flow rate.

6.2 Results of the Experiments with Water

In the experiments, distilled water was used as a solvent. The air was chosen as the carrier gas for the CO_2 gas because air is sufficiently and cheaply available in the workshop where the absorber is located. The workshop has an air compressor that can supply the required amount of air without interruption.

The objective of these experiments is to investigate the effects of operating parameters such as absorber pressure, water flow rate, and gas flow rate on the hydrodynamic properties of the sieve tray. Furthermore, to investigate the correlation between the hydrodynamic properties of the sieve tray and the performance of a tray column for CO_2 capture, and finally to estimate the operating points at which the absorber can be operated, which will help the operator to determine the operating points using the aqueous MDEA solution as a solvent.

Three experiments were conducted with water to study the hydrodynamic properties of the tray and the performance of the absorber used for CO_2 capture. In the first experiment, the gas flow rate was varied. In the second experiment, the water flow rate was varied. In the third experiment, the absorber pressure was varied.

6.2.1 Studying the Effect of Inlet Gas Flow Rate

6.2.1.1 Test Procedure

The CO_2 gas was mixed with air using the gas mixing unit before entering the absorber column. The air served as the carrier gas. The CO_2 volume fraction was 0.3 in all experiments. The input gas flow rate varied between 12-24 Nm^3/h. Three pressures of 0.22, 0.24, and 0.26 MPa were tested to investigate the effects of gas flow rate on the hydrodynamic properties of the tray. Distilled water was used as an absorbent. The feed water flow rate was nearly constant at 148 NL/h. The temperature of inlet water was controlled at 19.5 °C. The regeneration unit was operated with a heating power of 4.5 kW during all experiments.

The absorber test rig is run for 10 min under specified conditions for every measurement, resulting in time-dependent values for each measured parameter (i.e., pressure, temperature, and gas concentrations). The standard deviation, which indicates the range of variation of each measured parameter, is then calculated to estimate the random error. The systematic error of the measuring instruments is constant for all tests and is therefore not presented additionally in this chapter. In general, the measurement uncertainty of directly measured values (e.g., temperature, pressure, and flue gas concentrations) depends only on the relative uncertainty of the measuring instruments and is given by the relative error. For indirectly measured parameters or calculated values (e.g., volumetric flow rate, where the pressure difference and temperature are used in the calculation), the Gaussian error propagation method is applied, assuming normally distributed uncertainties. In this study, the volumetric concentrations are determined with the gas analysis unit, and the maximum relative error for CO_2 in the different process streams is about 3%.

6.2.1.2 Effect of the Inlet Gas Flow rate on Hydrodynamic Properties of the Sieve Tray

Figure 6.1 shows the effect of the gas flow rate on the total tray pressure drop. It can be observed that the tray pressure drop increases clearly when the inlet gas flow rate is increased between 12 and 20 Nm^3/h, while it is almost constant between 20 and 24 Nm^3/h. Figure 6.2 shows the effect of the gas flow rate on dry tray pressure drop. It can be noted that the dry pressure drop increases when the inlet flow rate increases between 12 and 24. The trend of this effect is similar for all pressure values studied.

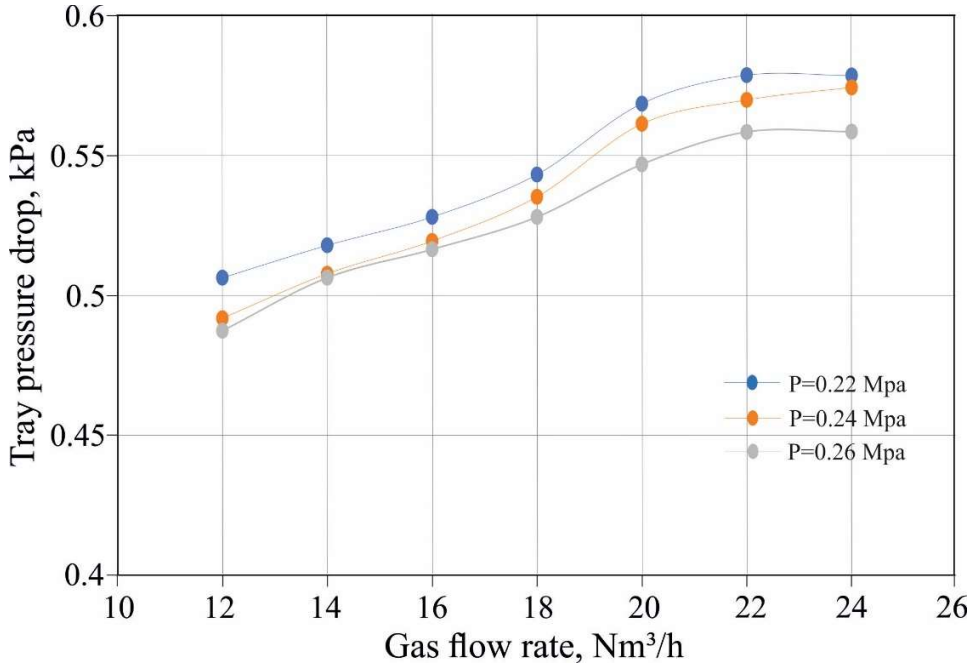

Figure 6.1 Effect of the inlet gas flow rate on total tray pressure drop

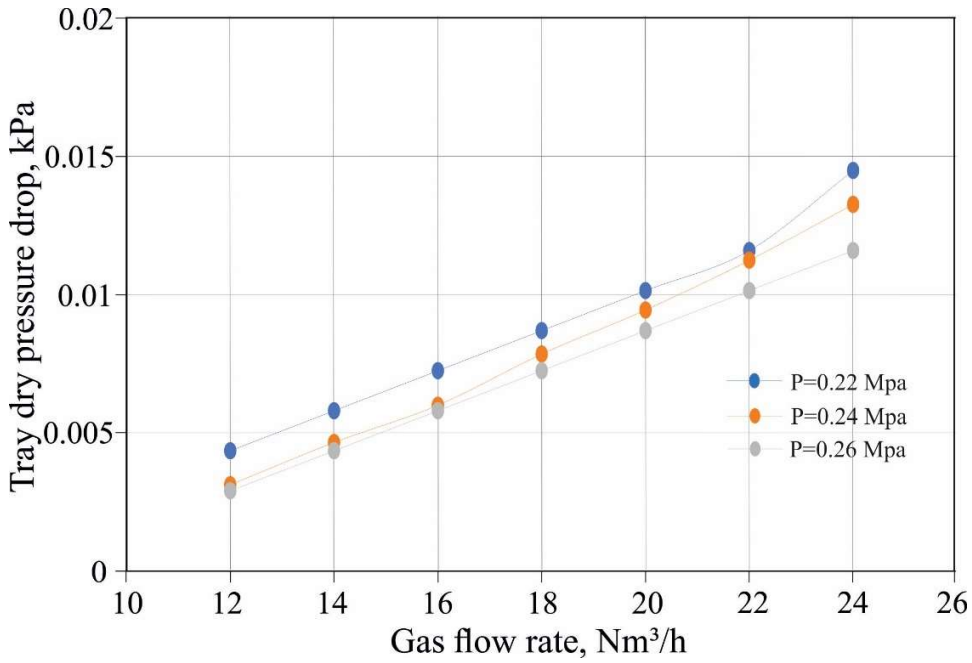

Figure 6.2 Effect of the inlet gas flow rate on dry tray pressure drop

The standard errors of the measurements of total tray pressure drop are shown in Table 6.1.

Table 6.1 Standard errors of the measurements of total tray pressure drop

Inlet Gas Flow Rate, Nm^3/h	Standard errors in the measurements		
	P = 0.22 MPa	P = 0.24 MPa	P = 0.26 MPa
12	0.00555	0.00535	0.00525
14	0.01886	0.01299	0.03397
16	0.01482	0.00982	0.01135
18	0.02145	0.01216	0.01368
20	0.02208	0.01817	0.01705
22	0.03704	0.03629	0.01956
24	0.04720	0.04783	0.03811

Figure 6.3 and Figure 6.4 show the tray liquid holdup level and tray liquid holdup when the inlet gas flow rate is increased between 12 and 24 Nm^3/h. It can be seen that increasing the gas volume flow rate has a significant effect on the tray liquid holdup level and tray liquid holdup on the tray. Both tray liquid holdup level and tray liquid holdup drastically increased when the gas volume flow rate is increased between 12 and 20 Nm^3/hr. It is noted that the increase in gas flow rate between 16 and 20 Nm^3/h is more significant than the increase in flow rate between 12 and 16 Nm^3/h, while the increase in flow rate between 20 and 24 Nm^3/h has a small effect on liquid holdup level and the liquid holdup.

The trend of this effect is similar for all pressure values studied. The possible reason for this behavior is the increase in the superficial velocity of the gas in the absorber due to the increase in the inlet gas flow rate. The increased gas velocity causes the liquid to be trapped on a tray, accumulating the liquid on the tray. As a result, the tray liquid holdup level and the tray liquid holdup will increase. It also appears that the liquid holdup is almost constant when the gas inlet flow rate is increased after 20 Nm^3/h. This trend may be due to accelerating the liquid to flow into the downcomer at the high gas velocity.

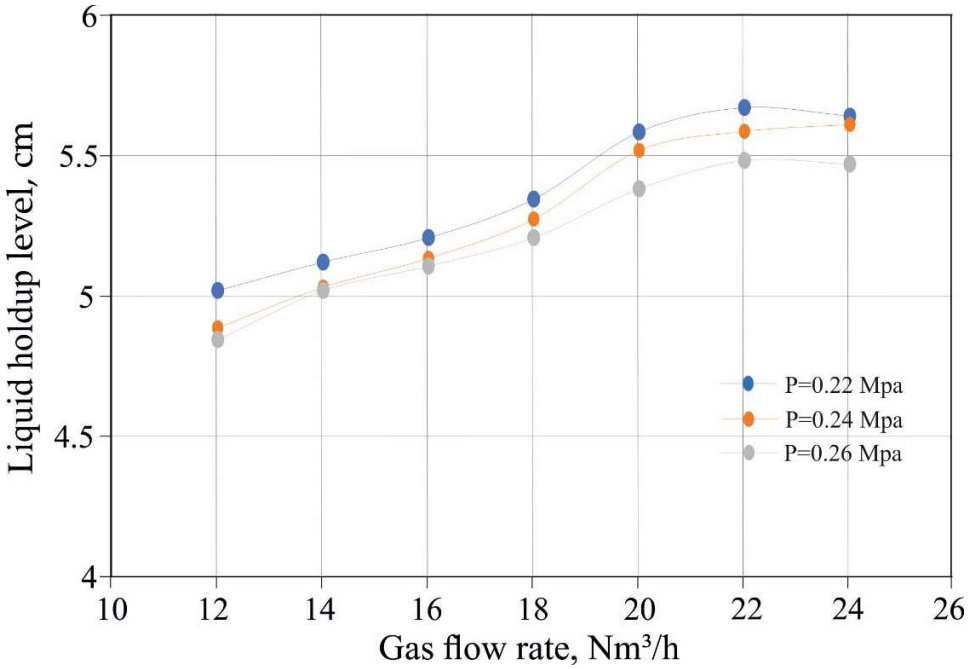

Figure 6.3 Effect of the inlet gas flow rate on tray liquid holdup level

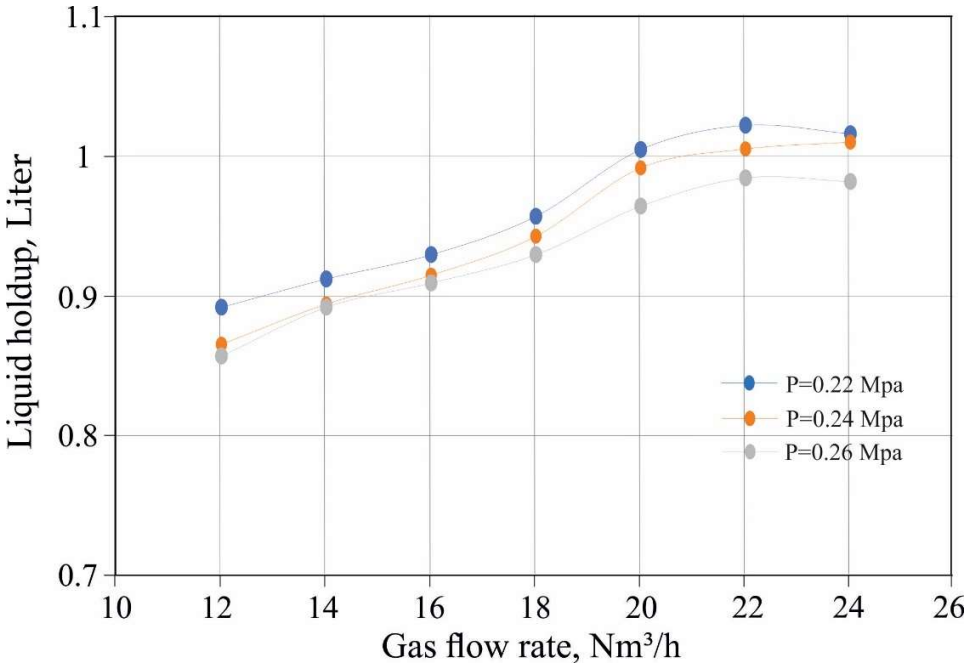

Figure 6.4 Effect of the inlet gas flow rate on tray liquid holdup

To investigate the effect of gas flow rate on froth height, the absorber was fitted with a ruler to observe froth formation above the tray. It can be seen from Figure 6.5 and Figure 6.6 that the froth height above the tray goes up as the gas flow rate is increased. The trend of this effect is similar for all pressure values studied. This trend can be explained by the increase of the superficial velocity of the gas into the absorber

through the increase of the gas flow rate, leading to an increase in the liquid holdup level and liquid holdup, as seen in Figure 6.3 and Figure 6.4. The increase of the tray liquid holdup will increase the height of the froth on the tray.

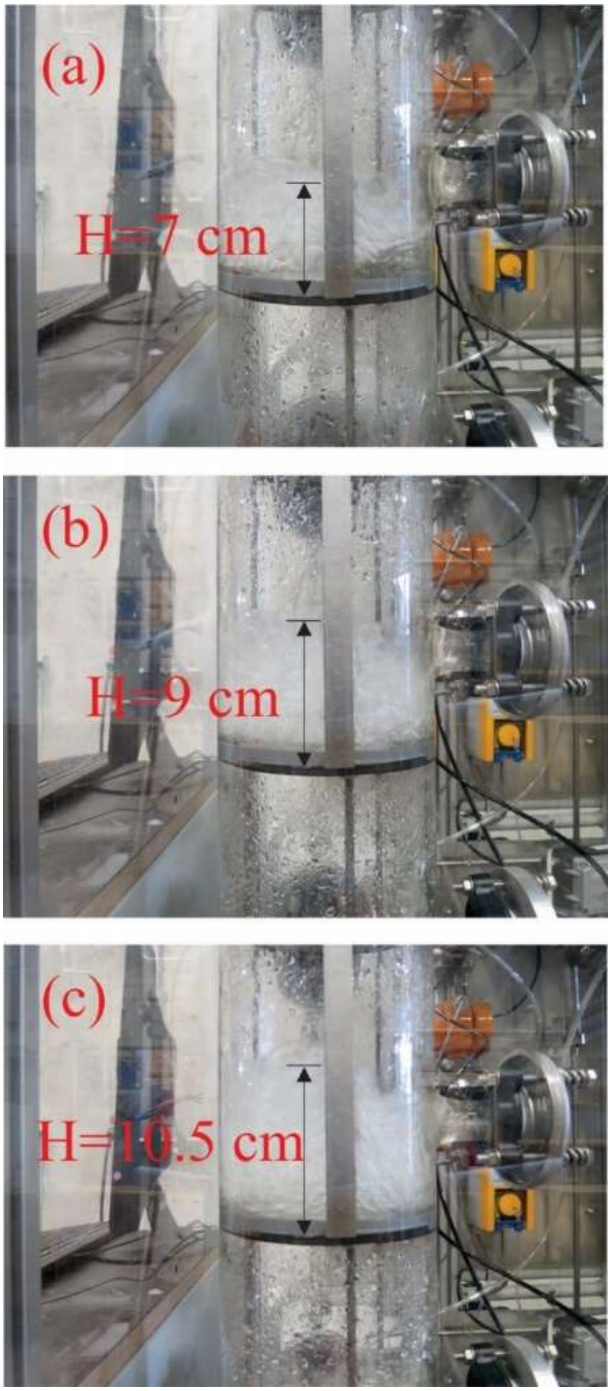

Figure 6.5 Froth height above the tray at inlet gas flow rate (a) 12 Nm^3/h, (b) 16 Nm^3/h, and (c) 18 Nm^3/h

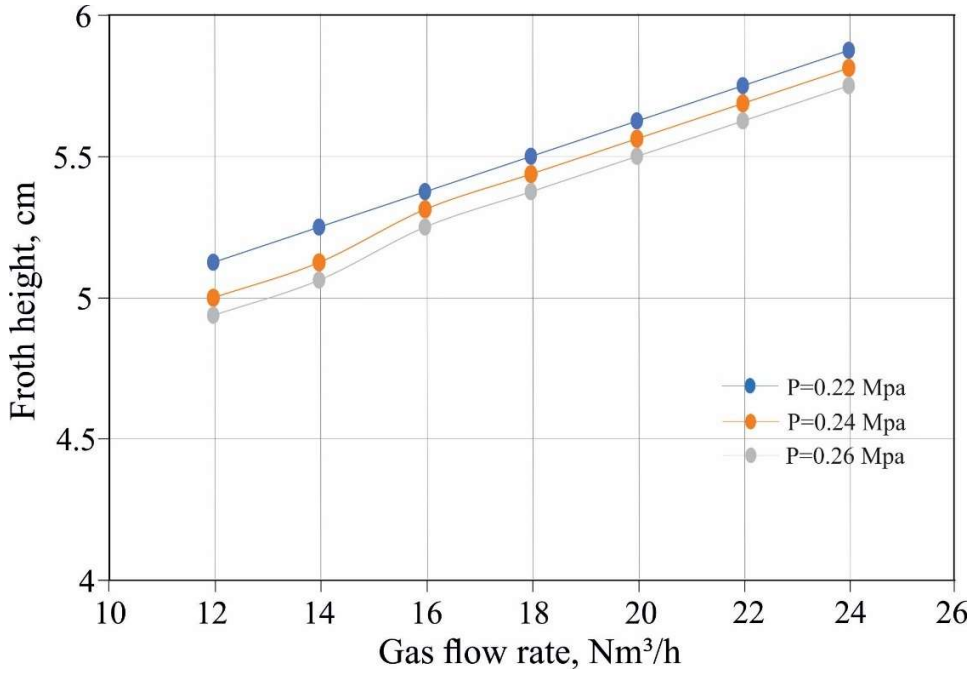

Figure 6.6 Effect of the inlet gas flow rate on froth height

6.2.1.3 Effect of the Inlet Gas Flow Rate on the Performance of the Absorber

Figure 6.7 demonstrates the effect of the inlet gas flow rate on the outlet volume fraction of CO_2 at pressures of 0.22, 0.24, and 0.26 MPa. From Figure 6.7, it can be shown that increasing the inlet gas flow rate significantly affects the volume fraction of CO_2. The volume fraction of CO_2 increases with the increase of the inlet gas flow rate from 12 to 16 Nm^3/h and 20 to 24 Nm^3/h, while an increase of the inlet gas flow rate between 16 and 20 Nm^3/h has a slight effect on the volume fraction of CO_2. The trend of this effect is similar for all pressure values investigated. The standard errors of the measurements of CO_2 volume fraction are shown in Table 6.2.

Table 6.2 Standard errors of the measurements of CO_2 volume fraction

Inlet gas flow rate, Nm^3/h	Standard errors in the measurements		
	P = 0.22 MPa	P = 0.24 MPa	P = 0.26 MPa
12	0.00043	0.00003	0.00011
14	0.00025	0.00027	0.00007
16	0.00023	0.00014	0.00024
18	0.00017	0.00017	0.00022
20	0.00011	0.00015	0.00029
22	0.00014	0.00015	0.00017
24	0.00016	0.00015	0.00025

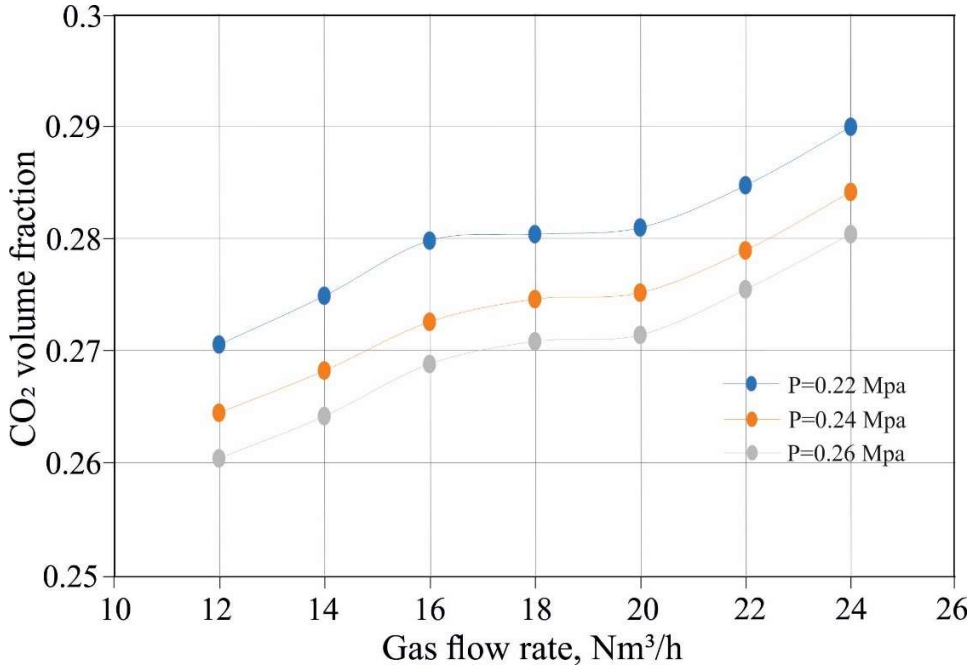

Figure 6.7 Effect of the inlet gas flow rate on the outlet volume fraction of CO_2

The principal explanation for this effect may be that a change in the gas flow rate will influence the hydrodynamic characteristics of the tray, such as liquid holdup level and liquid holdup, and the froth height on the tray.

Figure 6.8 illustrates the effect of the inlet gas flow rate on the CO_2 absorption rate when the inlet gas flow rate is changed in the range of 12–24 Nm^3/hr. There is a significant effect on the CO_2 absorption rate. The trend of this effect is similar for all pressure values studied. It can be seen that the CO_2 absorption rate is almost constant when the flow rate is changed between 12 and 16 Nm^3/h, whereas the CO_2 absorption rate increases clearly when the gas flow rate is increased between 16 and 20 Nm^3/h, while the CO_2 absorption rate decreases significantly when the flow rate is increased between 20 and 24 Nm^3/h.

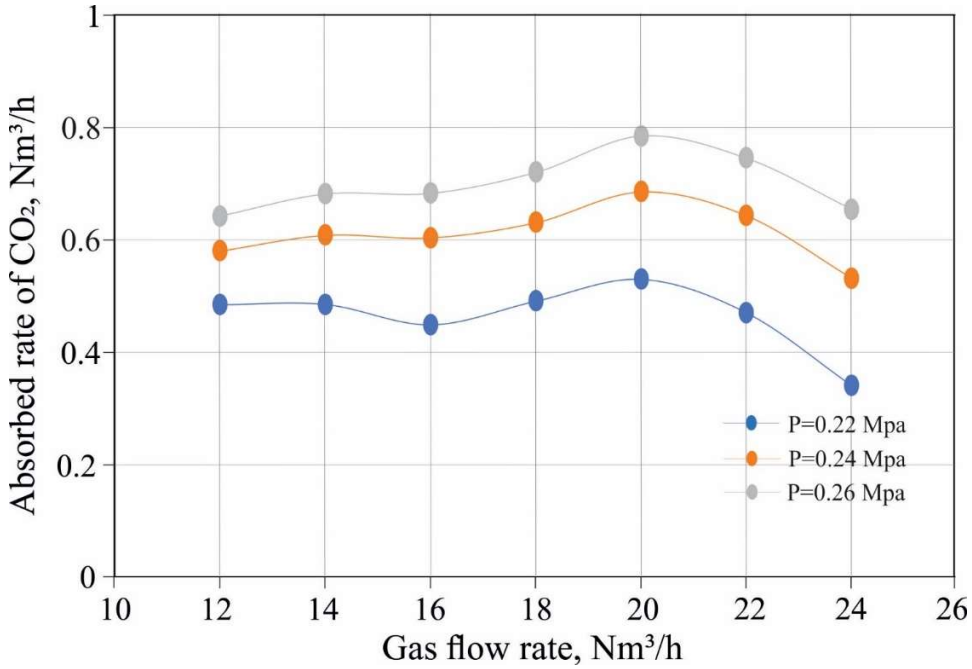

Figure 6.8 Effect of inlet gas flow rates on the absorbed rate of CO_2

The explanation for this behavior may be due to the effect of the inlet gas flow rate on the hydrodynamic characteristics of the tray, as shown in Figures 6.1–6.6. increasing the gas flow rate will improve these hydrodynamic characteristics of the tray, such as the liquid holdup level and liquid holdup and the froth height on the tray. Increasing these hydrodynamic characteristics improves the mass transfer between the liquid and gas phases. As a result, increasing the amount of CO_2 absorbed and vice versa.

On the other hand, increasing the superficial velocity will decrease the residence time of the gas in the absorber. Consequently, this decreases the contact time between the gas and liquid phases, leading to a decrease in mass transfer between the gas and liquid phases, which could explain the decrease in CO_2 absorption rate when the flow rate is increased between 20 and 24 Nm^3/h.

6.2.1.4 Results Discussion

The effect of gas flow rate on the hydrodynamic properties of a sieve tray was experimentally investigated, and an analytical study of the effect of the hydrodynamic properties of a sieve tray on the CO_2 absorption process was presented, highlighting the following points:

(1) The inlet gas flow rate is found to have a significant effect on the hydrodynamic properties of the sieve tray. Increasing the inlet gas flow rate up to a certain value increases the liquid holdup, but increasing the inlet gas flow rate above this value does not improve the liquid holdup.

(2) The increase in the gas flow rate at the inlet increases the froth height on the tray. The foam height increases the interfacial area between the gas and liquid phases. The increase in the interface contributes to increasing the mass transfer between the gas phase and the liquid phase.

(3) There is a correlation between the hydrodynamic properties of the sieve tray and the absorber's performance. An increase in liquid holdup level and liquid holdup due to an increase in inlet flow rate increases the performance of the CO_2 absorber.

(4) This study shows how the interfacial area between the gas and liquid phases changes due to a change in gas flow rate. The increase in froth height is considered a parameter that gives an idea of how big the interfacial area is between the gas and liquid phases.

(5) The study of the hydrodynamic properties of the tray can be helpful for the selection of the optimal operating conditions of the absorber. Through this study, it is possible to determine the range of the inlet gas flow rate of gas that causes a reduction in absorber performance.

6.2.2 Studying the Effect of Inlet Liquid Flow Rate

6.2.2.1 Test Procedure

The CO_2 gas was mixed with air using the gas mixing unit before entering the absorber column. The air served as the carrier gas. The CO_2 volume fraction was 0.3 in all experiments. The input gas flow rate was constant at 16 Nm^3/h. The pressure of the absorber was constant at 0.24 MPa. The inlet water flow rate varied between 101-188.5 NL/h. The temperature of inlet water was controlled at 19.5 °C. The regeneration unit was operated with a heating power of 4.5 kW during all experiments.

The absorber test rig is run for 10 min under specified conditions for every measurement, resulting in time-dependent values for each measured parameter (i.e., pressure, temperature, and gas concentrations). The standard deviation, which indicates the range of variation of each measured parameter, is then calculated to estimate the random error. The systematic error of the measuring instruments is constant for all tests and is therefore not presented additionally in this chapter. In general, the measurement uncertainty of directly measured values (e.g., temperature, pressure, and flue gas concentrations) depends only on the relative uncertainty of the measuring instruments and is given by the relative error. For indirectly measured parameters or calculated values (e.g., volumetric flow rate, where the pressure difference and temperature are used in the calculation), the Gaussian error propagation method is applied, assuming normally distributed uncertainties. In this study, the volumetric concentrations are determined with the gas analysis unit, and the maximum relative error for CO_2 in the different process streams is about 3%.

6.2.2.2 Studying the Effect of the Inlet Liquid Flow Rate on the Hydrodynamic Properties of the Sieve Tray

Figure 6.9 shows the effects of the inlet liquid flow rate on the hydrodynamic properties of the sieve tray, such as total tray pressure drop, liquid holdup level, liquid holdup, and froth height when the inlet liquid flow rate is increased between 101-188.5 NL/h. It can be observed that all the hydrodynamic properties increase remarkably when the inlet liquid flow rate is increased.

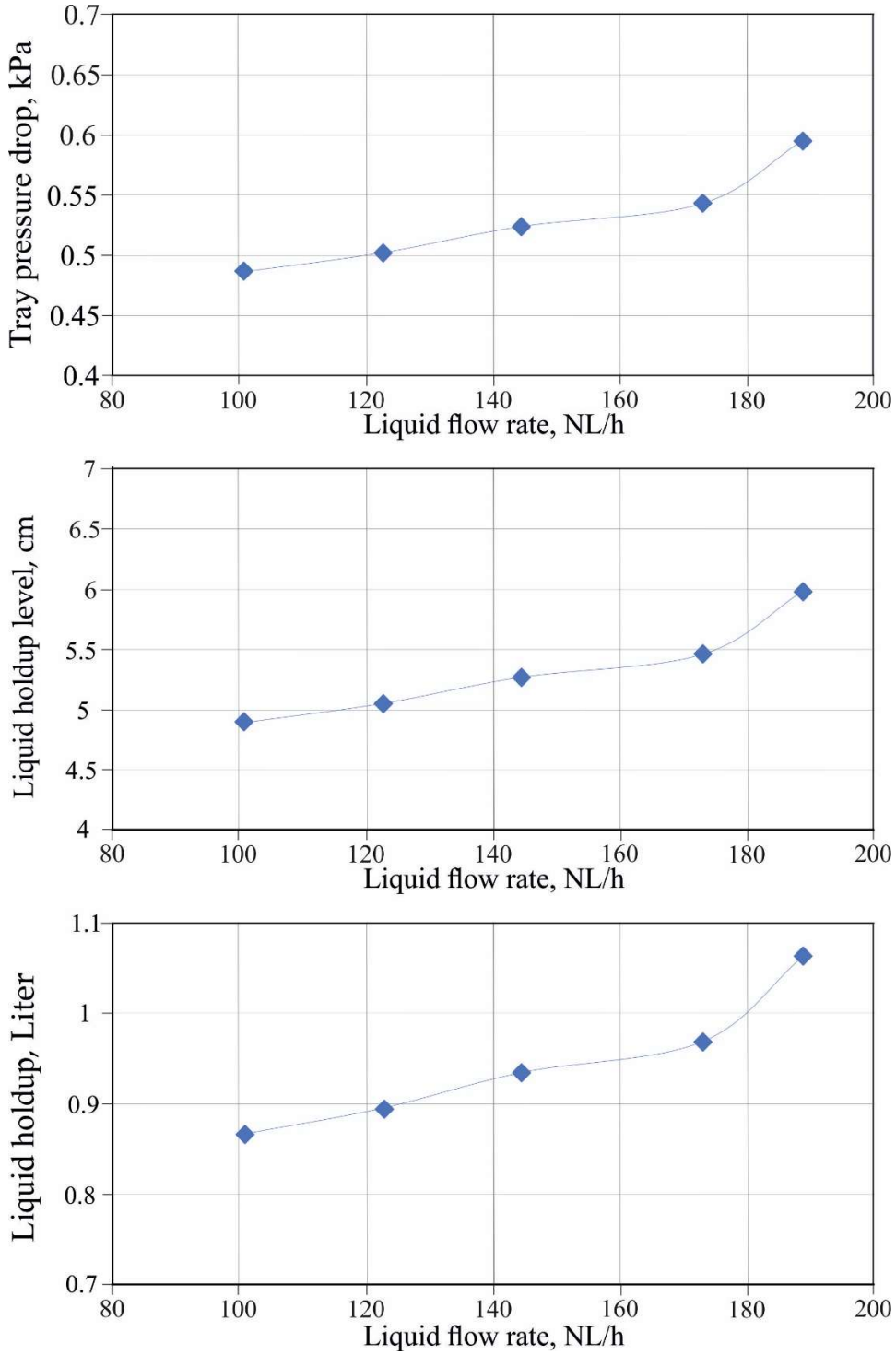

Figure 6.9 Effect of the inlet liquid flow rate on hydrodynamic properties of the sieve tray

The Standard errors in the measurements of the total tray pressure drop are listed in Table 6.3.

Table 6.3 Standard errors of the measurements of total tray pressure drop

Inlet liquid flow rate, NL/h	Standard errors in the measurements
101	0.00583
122.8	0.00660
144.5	0.01606
172.9	0.01246
188.5	0.02135

6.2.2.3 Studying the Effect of Inlet Liquid Flow Rate on the Performance of the Absorber

Figure 6.10 shows the effects of the inlet liquid flow rate on the outlet volume fraction of CO_2 when the inlet liquid flow rate is increased between 101-188.5 NL/h. It can be observed that the outlet volume fraction of CO_2 decreases remarkably when the inlet liquid flow rate is increased.

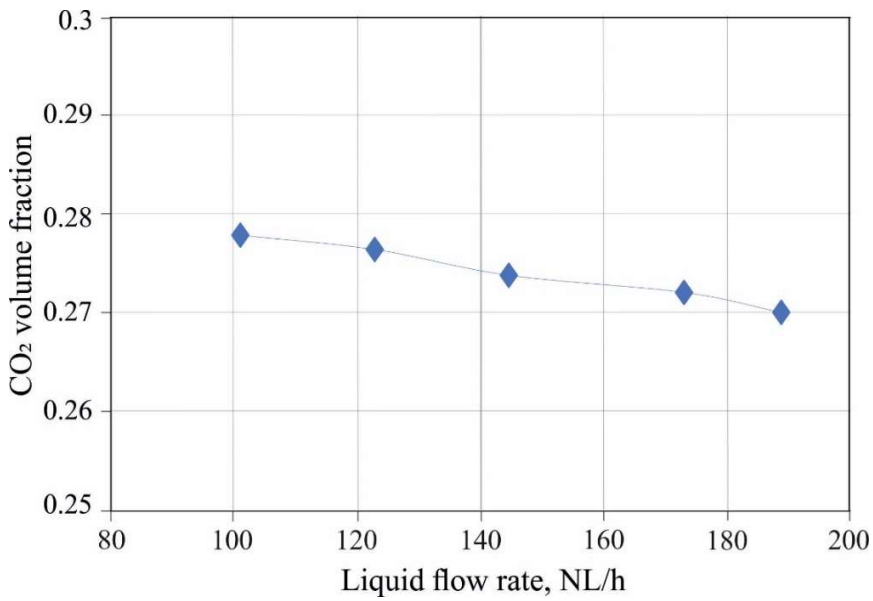

Figure 6.10 Effect of the inlet gas flow rate on the outlet volume fraction of CO_2

The maximum relative error for the volume fraction of CO_2 in the different process streams is about 3%. The standard errors of the measurements of CO_2 volume fraction are shown in Table 6.4

Table 6.4 Standard errors of the measurements of the CO_2 volume fraction

Inlet liquid flow rate, NL/h	Standard errors in the measurements
101	0.003190
122.8	0.008304
144.5	0.004063
172.9	0.002627
188.5	0.003656

Figure 6.11 shows the effects of the inlet liquid flow rate on the CO_2 absorption rate when the inlet liquid flow rate is increased between 101-188.5 NL/h. It can be observed that the CO_2 absorption rate increases remarkably when the inlet liquid flow rate is increased between 101-188.5 NL/h.

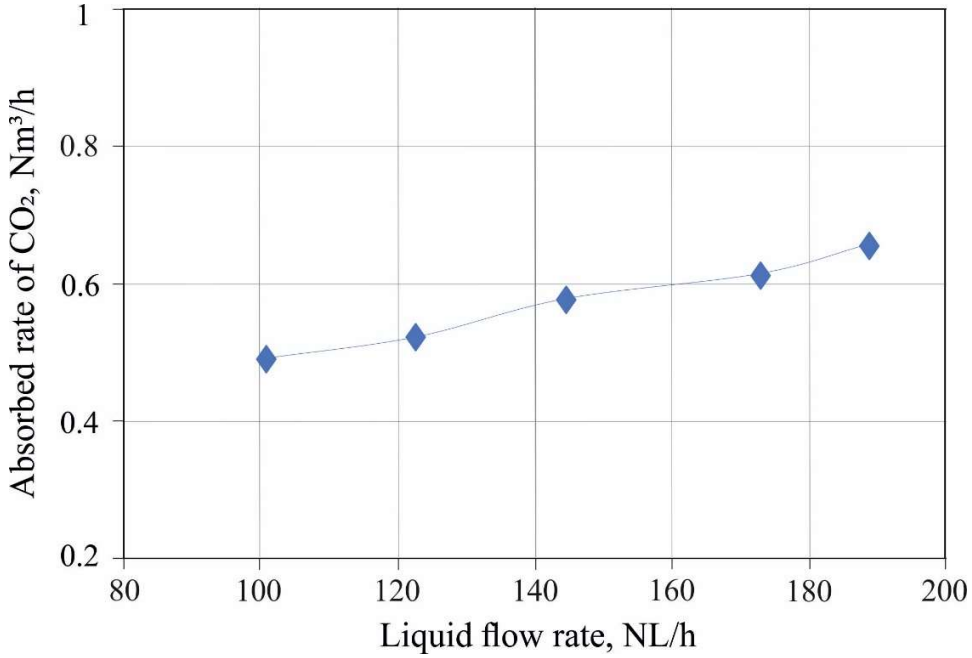

Figure 6.11 Effect of inlet gas flow rates on the absorbed rate of CO_2

The explanation for the behavior of the improvement of the CO_2 absorption rate is that the increase of the liquid flow at the inlet causes an improvement in the hydrodynamic properties of the tray. The increase in hydrodynamic properties improves mass transfer between the liquid and gas phases, and the CO_2 absorption rate increases.

6.2.2.4 Results Discussion

The effect of inlet liquid flow rate on the hydrodynamic properties of a sieve tray was experimentally investigated, and an analytical study of the effect of the hydrodynamic properties of a sieve tray on the CO_2 absorption process was presented, highlighting the following points:

(1) It was found that changing the inlet liquid flow rate has a significant effect on the hydrodynamic properties of the sieve tray, such as tray pressure drop, liquid holdup level, liquid holdup, and foam height.

(2) There is a correlation between the sieve tray's hydrodynamic properties and the absorber's performance when the fluid flow rate at the inlet is changed. The absorber's performance is similar to the hydrodynamic properties of the sieve tray when the liquid flow rate at the inlet is changed. The increase in hydrodynamic properties is increased the absorber's performance.

6.2.3 Studying the Effect of the Pressure

6.2.3.1 Test Procedure

The CO_2 gas was mixed with air using the gas mixing unit before entering the absorber column. The air served as a carrier gas. The CO_2 volume fraction was 0.3 in all experiments. The input gas flow rate was constant at 10 Nm^3/h. The pressure of the absorber varied in the ranges of 0.2-0.3 MPa. The inlet water flow rate was constant at 149 NL/h. The temperature of inlet water was controlled at 17 °C. During all experiments, the regeneration unit was operated with a heating power of 4.5 kW.

The absorber test rig is run for 10 min under specified conditions for every measurement, resulting in time-dependent values for each measured parameter (i.e., pressure, temperature, and gas concentrations). The standard deviation, which indicates the range of variation of each measured parameter, is then calculated to estimate the random error. The systematic error of the measuring instruments is constant for all tests and is therefore not presented additionally in this chapter. In general, the measurement uncertainty of directly measured values (e.g., temperature, pressure, and flue gas concentrations) depends only on the relative uncertainty of the measuring instruments and is given by the relative error. For indirectly measured parameters or calculated values (e.g., volumetric flow rate, where the pressure difference and temperature are used in the calculation), the Gaussian error propagation method is applied, assuming normally distributed uncertainties. In this study, the volumetric concentrations are determined with the gas analysis unit, and the maximum relative error for CO_2 in the different process streams is about 3%.

6.2.3.2 Studying the Effect of Pressure on the Hydrodynamic Properties of the Sieve Tray

Figure 6.12 shows the effects of pressure on the hydrodynamic properties of the sieve tray, such as total tray pressure drop, liquid holdup level, and liquid holdup when the pressure is increased between 0.2 and 0.3 MPa. All the hydrodynamic properties decrease remarkably when the pressure is increased between 0.2 and 0.26 MPa. In comparison, the hydrodynamic properties decrease slightly when the pressure is increased between 0.26 and 0.3 MPa.

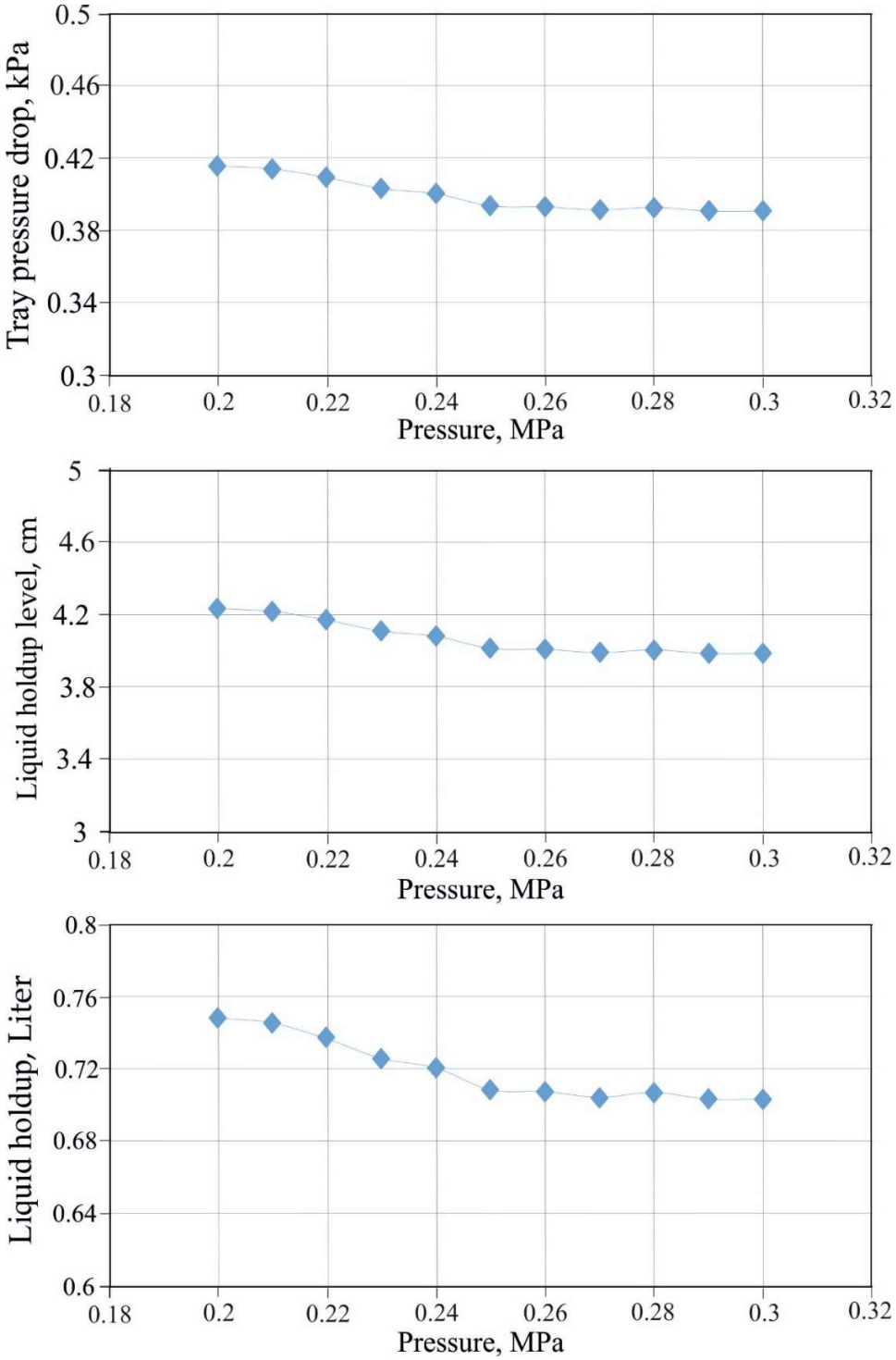

Figure 6.12 Effect of pressure on hydrodynamic properties of the sieve tray

The effect of pressure on the hydrodynamic properties of the tray can be explained by the reduction in the superficial velocity of the gas in the absorber caused by the increase in pressure. Consequently, the effect of the superficial velocity on the trapping and accumulation of the liquid on the tray is reduced. As a result, the total tray pressure drop, liquid holdup level, liquid holdup, and froth height will reduce.

The Standard errors of the measurements of the total tray pressure drop are listed in Table 6.5.

Table 6.5 Standard errors of the measurements of the total tray pressure drop

Pressure (MPa)	Standard errors in the Measurements
0.2	0.0054
0.21	0.0046
0.22	0.0049
0.23	0.0040
0.24	0.0046
0.25	0.0221
0.26	0.0044
0.27	0.0047
0.28	0.0049
0.29	0.0052
0.3	0.0056

6.2.3.3 Studying the Effect of Pressure on the Performance of the Absorber

Figure 6.13 shows the effect of pressure on the outlet volume fraction of CO_2 when the pressure is increased between 0.2 and 0.3 MPa. It can be observed that the outlet volume fraction of CO_2 decreases remarkably when the pressure is increased between 0.2 and 0.26 MPa, while the outlet volume fraction of CO_2 decreases smoothly when the pressure is increased between 0.26 and 0.3 MPa.

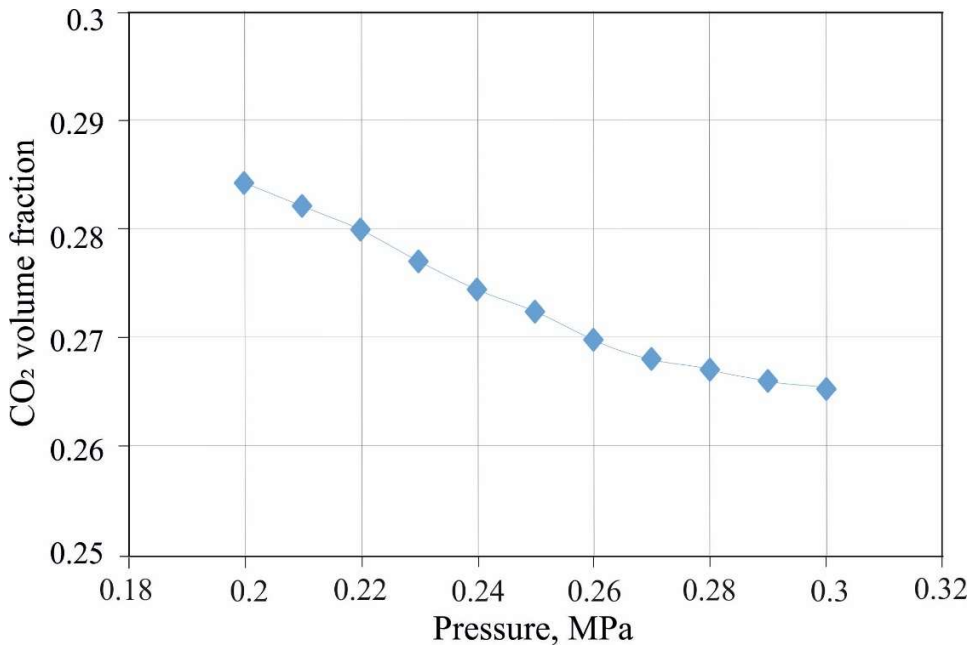

Figure 6.13 Effect of pressure on the volume fraction of CO_2 at the outlet of the absorber

The maximum relative error for the volume fraction of CO_2 in the different process streams is about 3%. The standard errors of the measurements of CO_2 volume fraction are shown in Table 6.6.

Table 6.6 Standard errors of the measurements of the CO_2 volume fraction

Pressure (MPa)	Standard errors in the Measurements
0.2	0.0003
0.21	0.0003
0.22	0.0003
0.23	0.0003
0.24	0.0004
0.25	0.0015
0.26	0.0003
0.27	0.0003
0.28	0.0004
0.29	0.0004
0.3	0.0004

Figure 6.14 shows the effect of pressure on the CO_2 absorption rate when the pressure is increased between 0.26 and 0.3 MPa. It can be observed that the CO_2 absorption rate increases remarkably when the pressure is increased between 0.2 and 0.26 MPa, while the CO_2 absorption rate increases smoothly when the pressure is increased between 0.26 and 0.3 MPa.

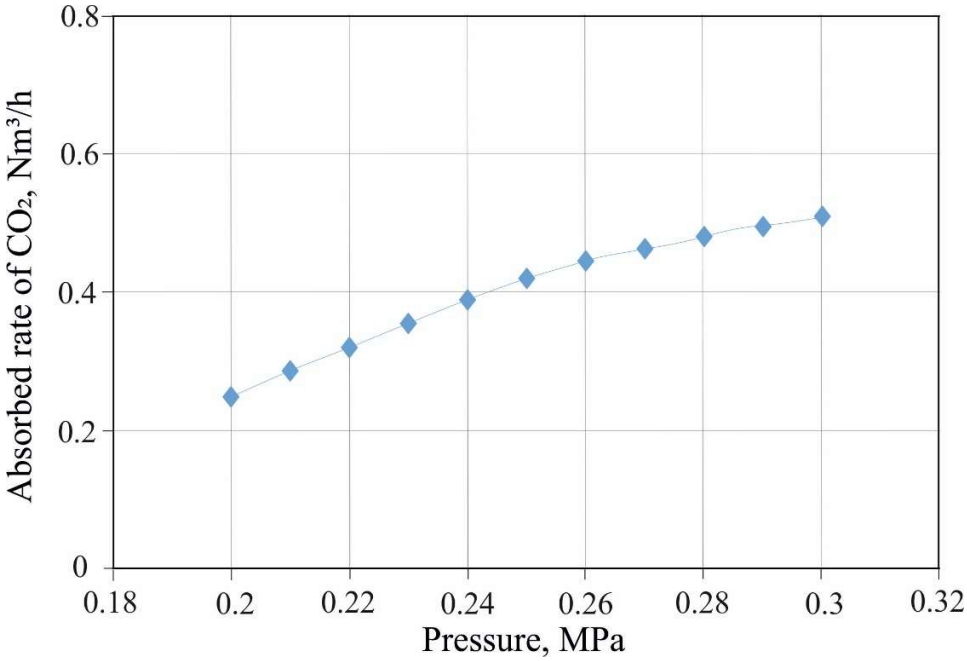

Figure 6.14 Effect of pressure on the absorbed rate of CO_2

The increase in CO_2 absorption rate can be explained by Henry's Law, which states that the amount of dissolved gas in a liquid is proportional to its partial pressure. The CO_2 absorption rate increases smoothly when the pressure is increased between 0.26 and 0.3 MPa. This may be explained by the effects of

pressure on hydrodynamic properties. As shown in Figure 6.12, the hydrodynamic properties of the tray decrease when the pressure is increased, which will affect the mass transfer.

6.2.3.4 Results Discussion

The effect of pressure on the hydrodynamic properties of the sieve tray has been experimentally investigated, and a study on the correlation between the hydrodynamic properties of a sieve tray and the CO_2 absorption rate has been presented, highlighting the following points:

(1) It has been found that increasing the absorber pressure has a remarkable influence on the hydrodynamic properties of the sieve bottom.

(2) There is a correlation between the hydrodynamic properties of the sieve bottom and the absorber's performance when the pressure is changed. It seems that the behavior of the CO_2 absorption rate follows the hydrodynamic properties of the sieve tray when the pressure is changed.

6.3 Results of the Experiments with an Aqueous Methyl Diethanolamine (MDEA) Solutions

In these experiments, aqueous MDEA solutions were used as a solvent because it is a common chemical solvent used on an industrial scale, especially in processes requiring low partial pressure. Since the maximum operating pressure of the glass column is 0.3 MPa, the chemical absorption was studied in the current research.

The objectives of the experiments using aqueous MDEA solution are, first, to investigate the performance of a tray column for CO_2 absorption during the transient state. Moreover, to investigate the relationship between a tray column's performance for CO_2 absorption and the tray's hydrodynamic properties during the transient state.

Two groups of experiments were performed on the test rig. The first group of experiments was conducted using aqueous MDEA solutions with a mass fraction of 10% as a solvent. The second group of experiments was conducted using aqueous MDEA solutions with a mass fraction of 50 % as a solvent.

6.3.1 Results of the Experiments with an Aqueous MDEA Solution with a Mass Fraction of 10%

6.3.1.1 Test Procedure

The CO_2 gas was mixed with N_2 using the gas mixing unit before entering the absorber column. The N_2 is an inert gas and serves as a carrier gas. An aqueous MDEA solution with a mass fraction of 10% was used as a solvent. The CO_2 volume fraction was 0.3 in all experiments. The input gas flow rate at the beginning was constant at 14 Nm^3/h. The pressure of the absorber was constant at 0.28 MPa. The inlet solvent flow rate was constant at 148 NL/h. The temperature of the inlet solvent was controlled at 20 °C. During all experiments, the regeneration unit was operated with a heating power of 4.5 kW. The test rig was controlled and operated under the above operating conditions for about one hour to reach the steady state of the outlet CO_2 concentration. Then, three tests were conducted to investigate the effects of

dynamic change of gas and solvent flow rate on CO_2 absorption. The first test is called "Different Load Changes" in gas flow rate, the second test is called "Different Change Rates" in gas flow rate, and the third test is called "Different Load Changes" in gas and solvent flow rate.

6.3.1.2 Results of Tests for Different Load Changes in Inlet Gas Flow Rate

The effect of different load changes is investigated by ramp-up and ramp-down tests of the gas flow rate. In the ramp-up tests, the gas flow rate was increased from a minimum load to different higher load levels. The rate of change was constant for each transient. In the ramp-down tests, the gas flow rate decreased from higher load levels to a minimum load. The rate of change was constant for each test. Figure 6.15 shows different load change tests (ramp-up and ramp-down tests) performed to investigate the effect of different load changes in the gas flow rate. In the ramp-up tests, the gas flow rate increased from 14 Nm^3/h to 18, 20, and 22 Nm^3/h by passing through a transient state between 30-60 sec. The rate of change was constant at 0.14 Nm^3/h /sec for each test. In ramp-down tests, the gas flow rate decreased from 18, 20, and 22 to 14 Nm^3/h by passing through a transient state that lasted between 30-60 sec. The rate of change was constant at 0.14 Nm^3/h /sec for each test.

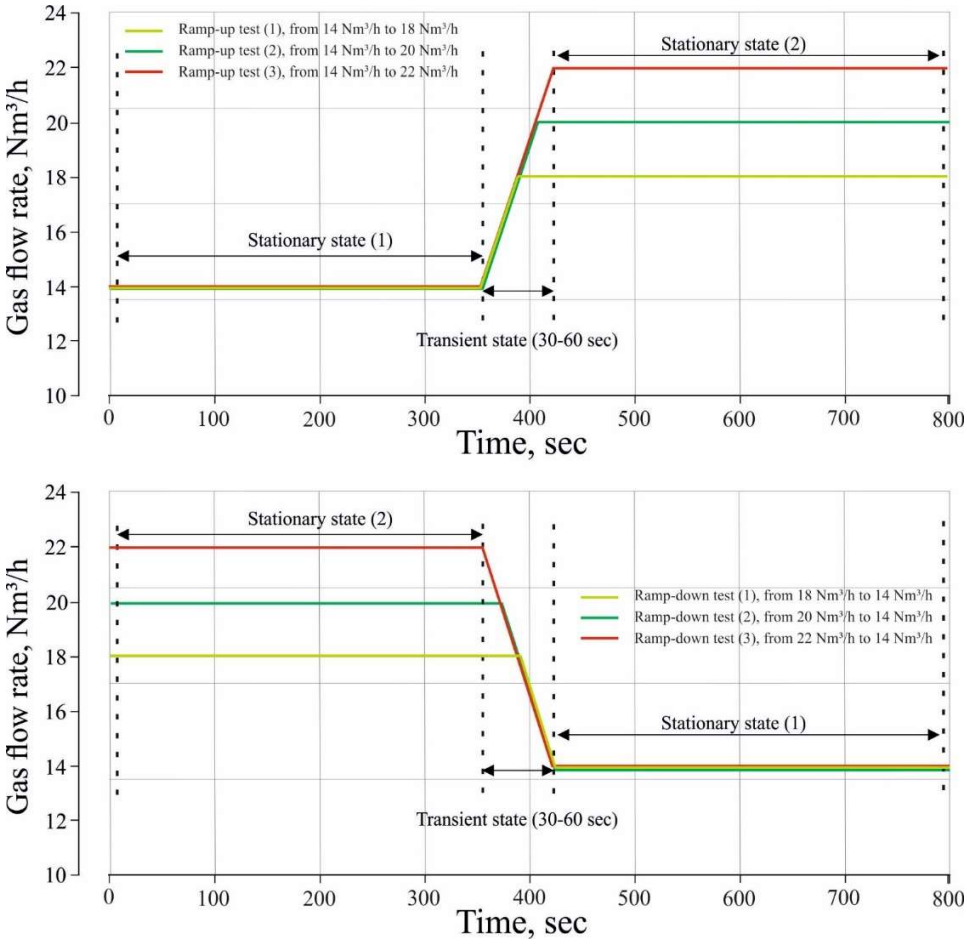

Figure 6.15 Different load changes tests

6.3.1.2.1 Effect of Different Load Changes of Gas Flow Rate on the CO_2 Volume Fraction

Figure 6.16 shows the effect of the different load changes of gas flow rate on the outlet CO_2 volume fraction during the transient state of the ramp-up tests.

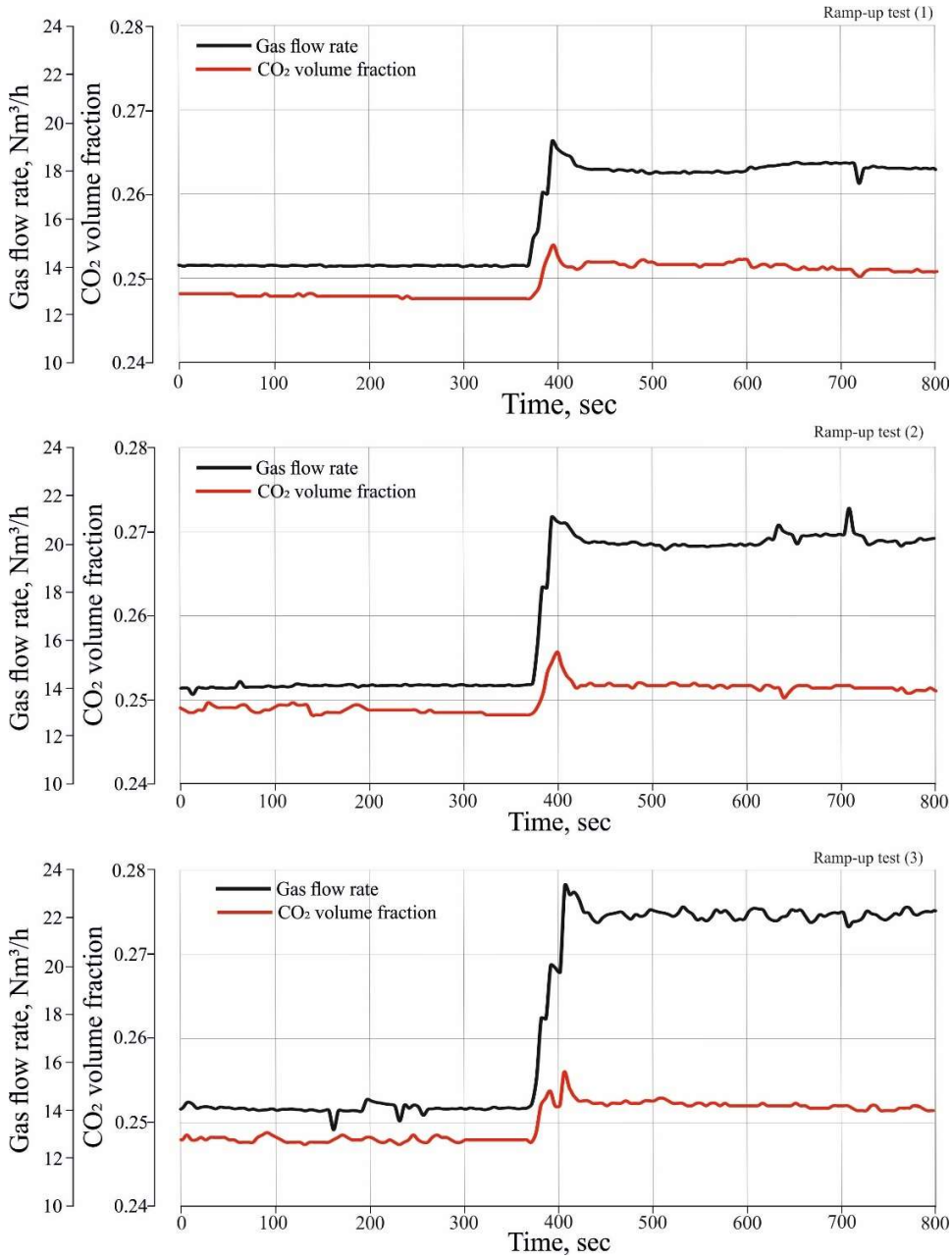

Figure 6.16 Outlet CO_2 volume fraction for different load changes of the gas flow rate in ramp-up tests

It can be seen from Figure 6.16 that different load changes of the gas flow rate in ramp-up tests have a significant effect on the volume fraction of CO_2, highlighting the following notes:

- The CO_2 volume fraction reaches a peak during the transient state at all ramp-up tests.
- The higher the different load change, the higher the peak CO_2 volume fraction.
- The higher the different load change, the longer time to reach the peak CO_2 concentration.
- After an unsteady peak of the CO_2 volume fraction, the CO_2 volume fraction settled back to the steady state level within the different times for different load changes. The higher the different load change, the longer the settling time of the CO_2 concentration.

The reason for this behavior is assumed that during the ramp-up tests, the dynamic change in gas flow rates increases the liquid holdup level and liquid holdup in the lower trays faster than in the upper trays. As a result, the lower trays have low efficiency during the ramp-up tests which reduces the performance of the absorber.

Figure 6.17 shows the effect of the different load changes of gas flow rate on the outlet CO_2 volume fraction which were performed by the ramp-down tests.

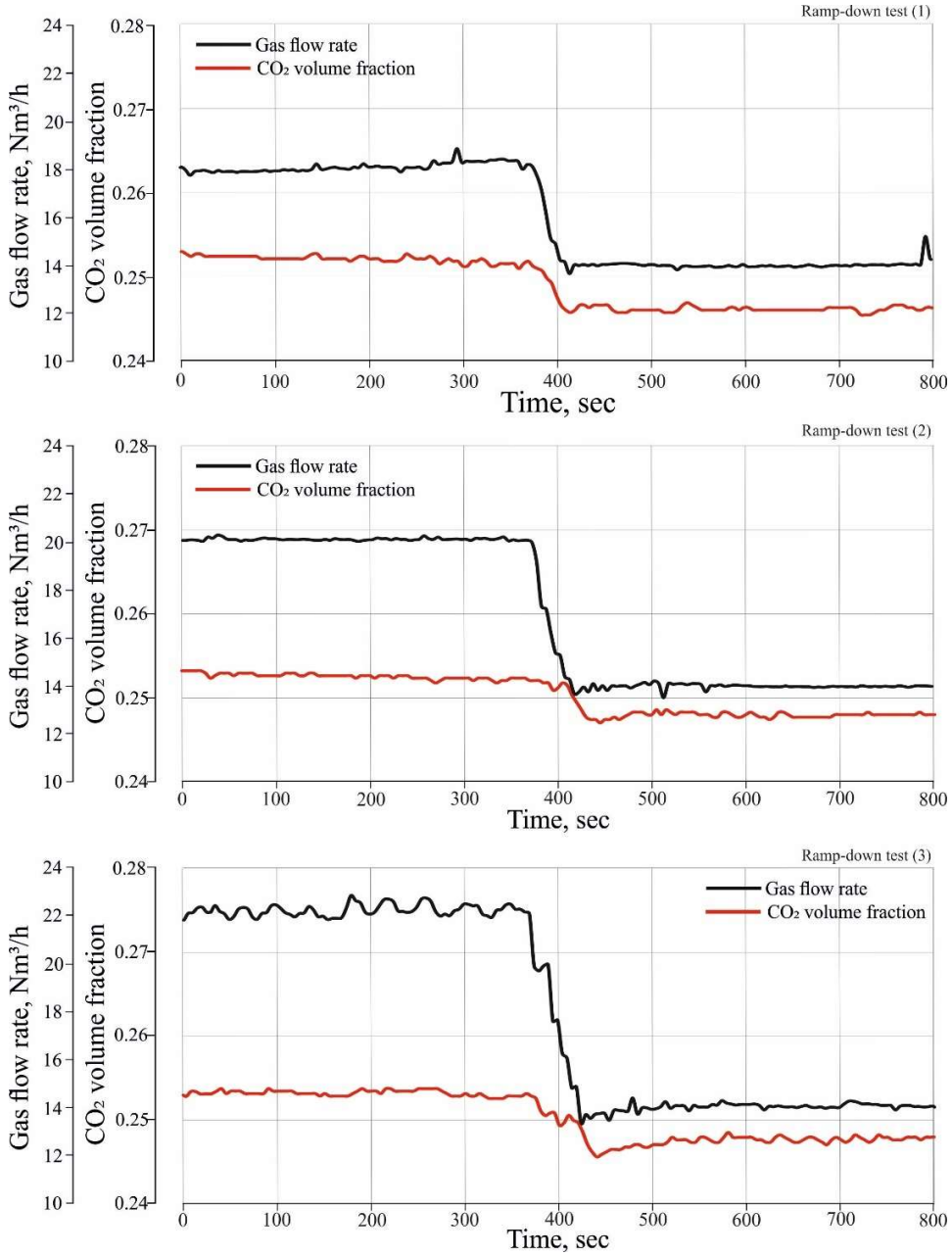

Figure 6.17 Outlet CO_2 volume fraction for different load changes of the gas flow rate in ramp-down tests

It can be seen from Figure 6.17 that different load changes of gas flow rate on the outlet CO_2 volume fraction during the transient states of the ramp-down tests have a significant effect on the volume fraction of CO_2, highlighting the following notes:

- The CO_2 volume fraction reaches a trough during the transient state at all ramp-down tests.
- The higher the different load change, the deepest the trough of CO_2 volume fraction.
- The higher the different load change, the longer time to reach the trough CO_2 volume fraction.

- After the unsteady trough of the CO_2 volume fraction, the CO_2 volume fraction settled back to the steady-state level at different times for different load changes. The higher the different load change, the longer the settling time of the CO_2 concentration.

This behavior is related to the effect of dynamic change in gas on the hydrodynamic characteristics of the tray, which will be studied later.

6.3.1.2.2 Effect of Different Load Changes of the Gas Flow Rate on the Hydrodynamic Characteristics of the Sieve Tray

Figure 6.18, Figure 6.19, and Figure 6.20 show the effect of different load changes of the gas flow rate on the total tray pressure drop, tray liquid holdup level, and tray liquid holdup sequentially during the transient states of ramp-up tests. It can be seen that all the above hydrodynamic characteristics of the sieve tray increase rapidly during the transient state. The explanation for this behavior can be illustrated as follows: An increase in the flow rate of the gas leads to an increase in the superficial velocity of the gas. The increase in the superficial velocity of the gas will improve trapping the liquid on a tray and causes the liquid to accumulate on the tray, which leads to increased hydrodynamic characteristics of the sieve tray.

It can also be noted from Figure 6.18, Figure 6.19, and Figure 6.20 that the settling time of the hydrodynamic characteristics of the sieve tray on the third tray is longer than the time of the transient state of different load changes in the inlet gas (30-60 seconds). Although the transient state of the gas flow continued for 30-60 seconds, the hydrodynamic properties continued to change for about 60 seconds after the transient state ended. It is assumed that the delay of settling time of the hydrodynamic characteristics influences the absorber's performance during the transient state.

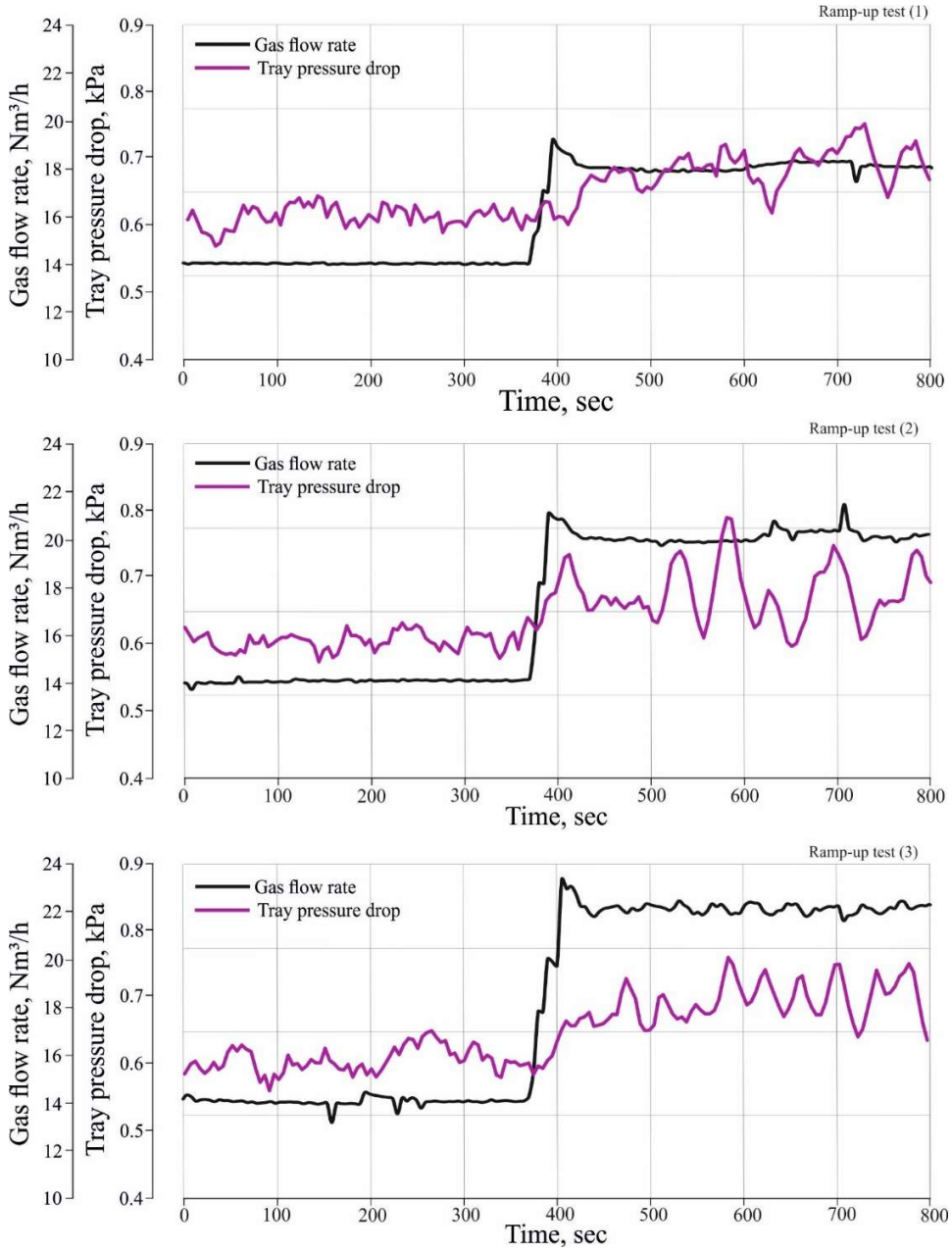

Figure 6.18 Total tray pressure drop for different load changes in inlet gas in ramp-up tests

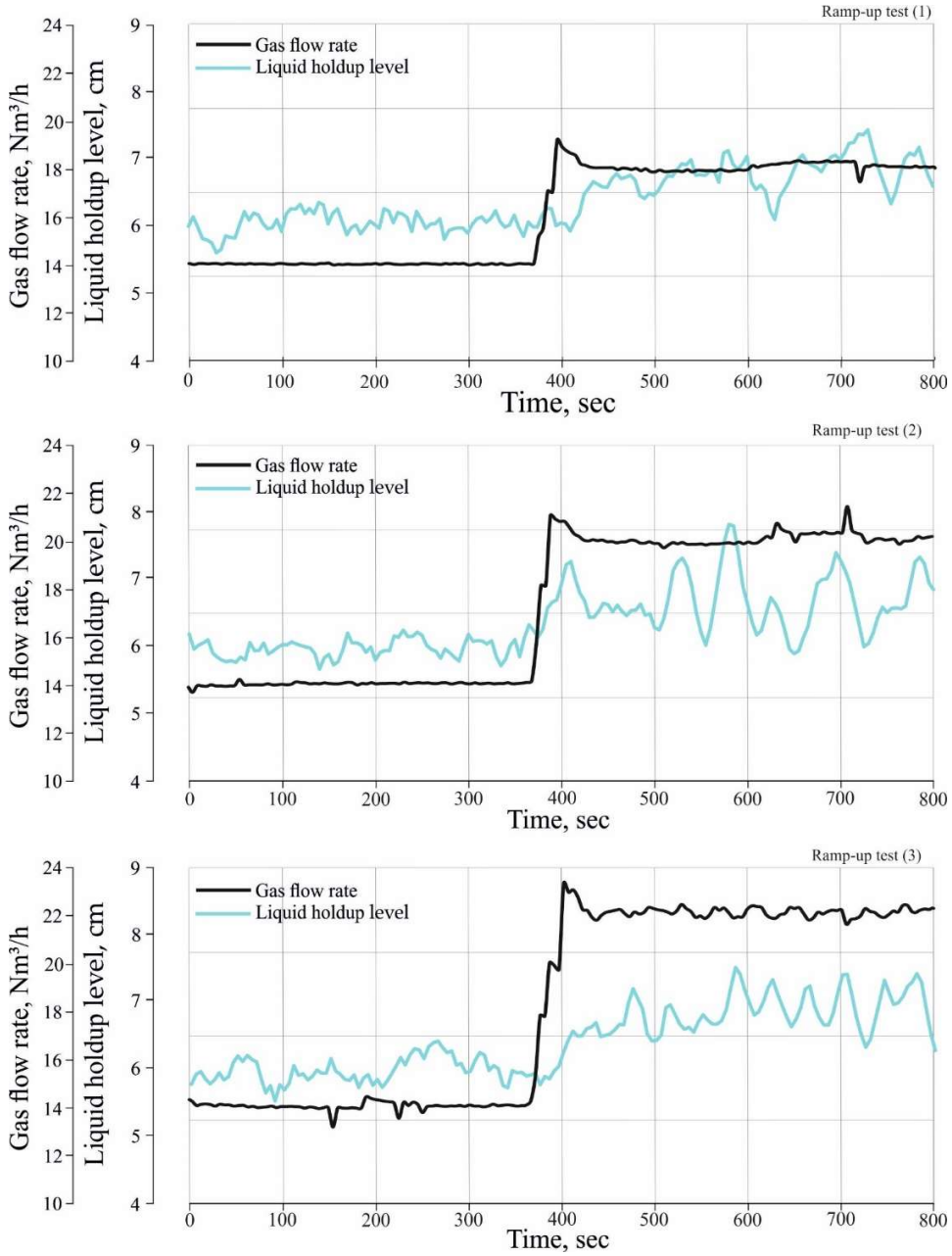

Figure 6.19 Tray Liquid holdup level for different load changes in the inlet gas in ramp-up tests

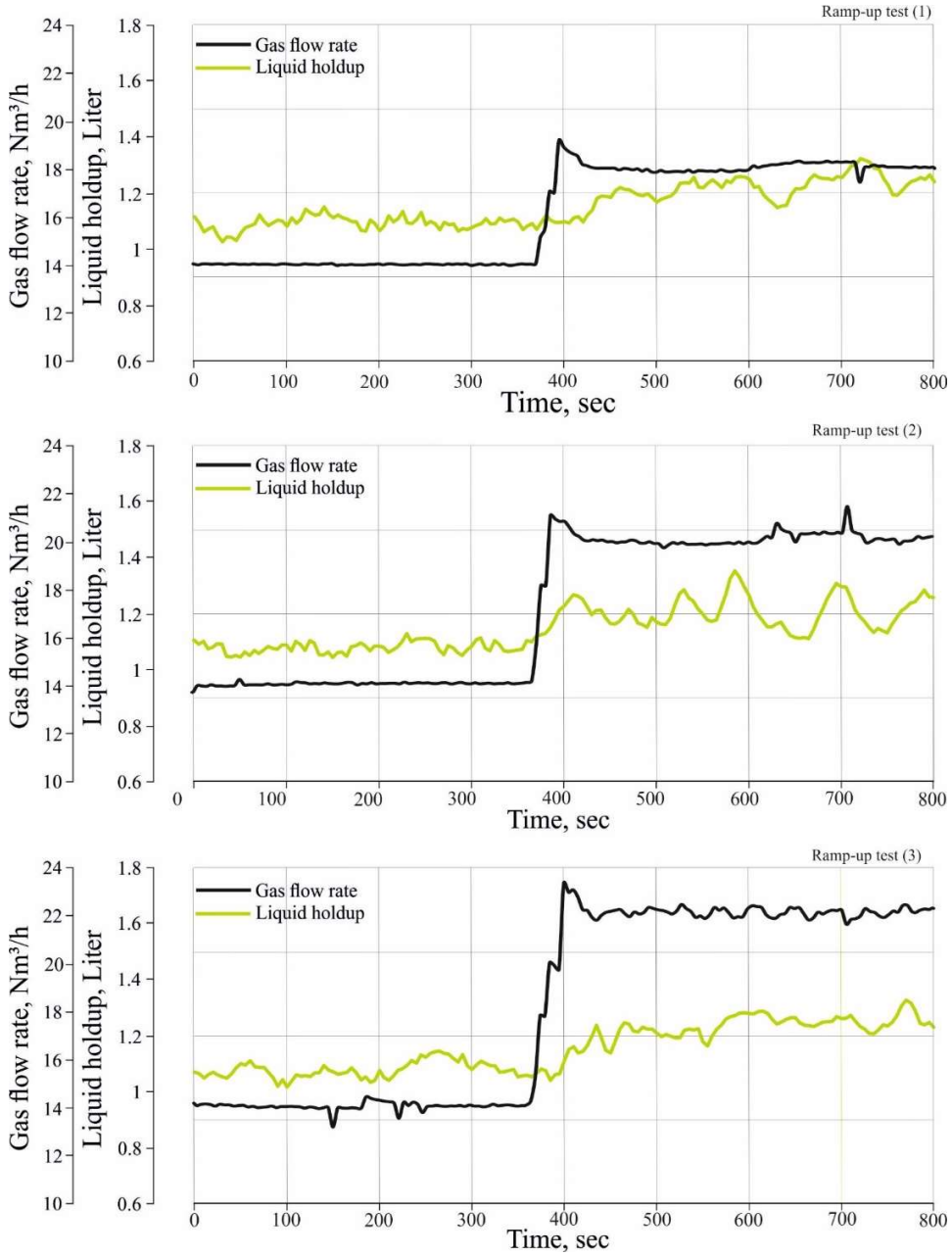

Figure 6.20 Tray Liquid holdup for different load changes in the inlet gas in ramp-up tests

Figure 6.21, Figure 6.22, and Figure 6.23 show the effect of different load changes of the gas flow rate on the total tray pressure drop, tray liquid holdup level, and tray liquid holdup sequentially during the transient states of ramp-down tests. It can be seen that all the above hydrodynamic characteristics of the sieve tray decrease rapidly during the transient state. The explanation for this behavior can be illustrated as follows: a decrease in the flow rate of the gas leads to a decrease in the superficial velocity of the gas. The decrease in the superficial velocity of the gas will decrease trapping the liquid on a tray and causing the liquid to accumulate on the tray, which leads to decreased hydrodynamic characteristics of the sieve tray.

It can also be noted from Figure 6.21, Figure 6.22, and Figure 6.23 that the settling time of the hydrodynamic characteristics of the third tray is longer than the time of the transient state of different load changes in the inlet gas, which is about 30-60 seconds. Although the transient state of the gas continued for 30-60 seconds, the hydrodynamic properties continued to change for about 60 seconds after the transient state ended. It is assumed that the delay of settling time of the hydrodynamic characteristics influences the absorber's performance during the transient state.

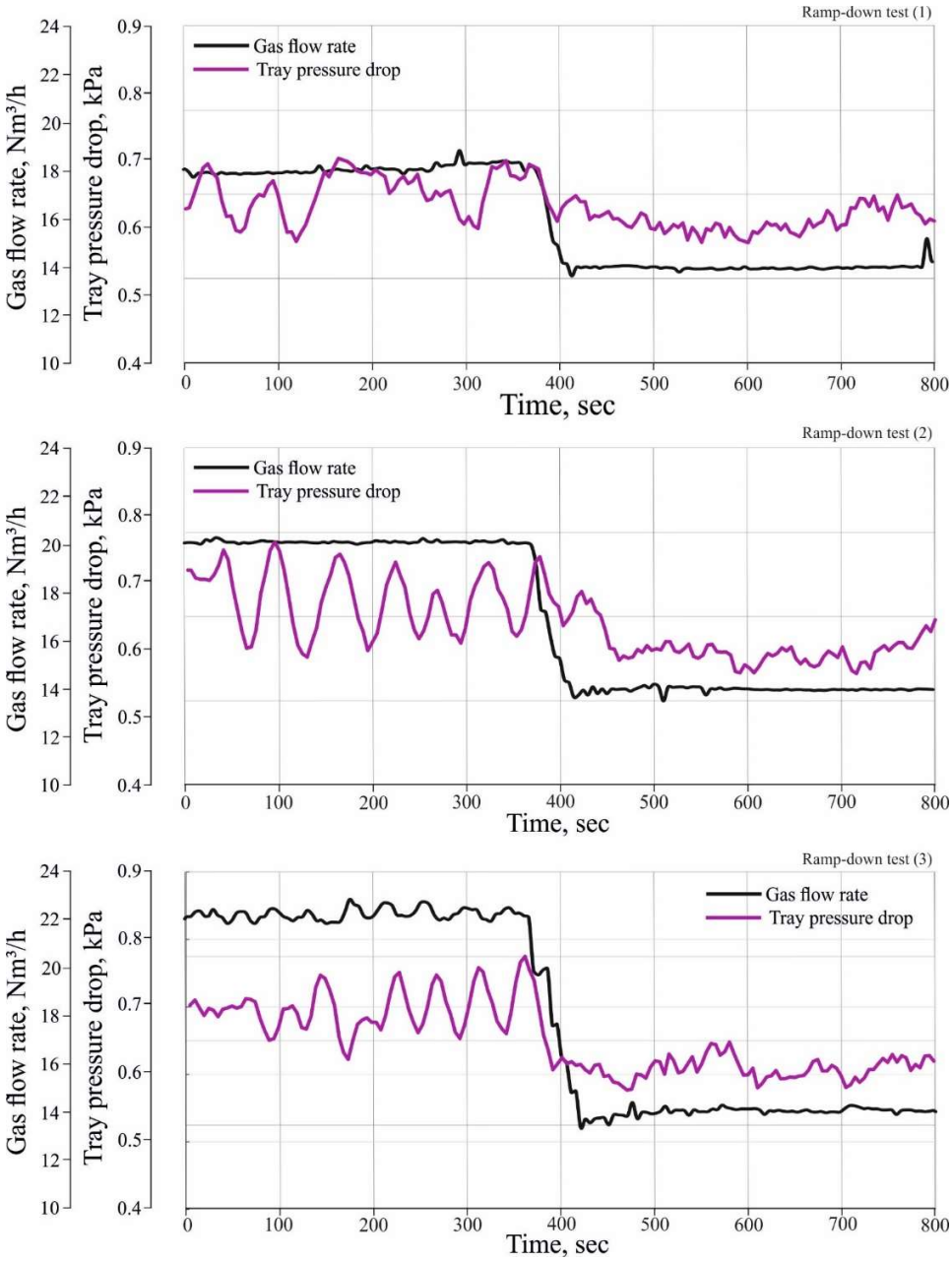

Figure 6.21 Total pressure drop for different load changes of the gas flow rate in ramp-down tests

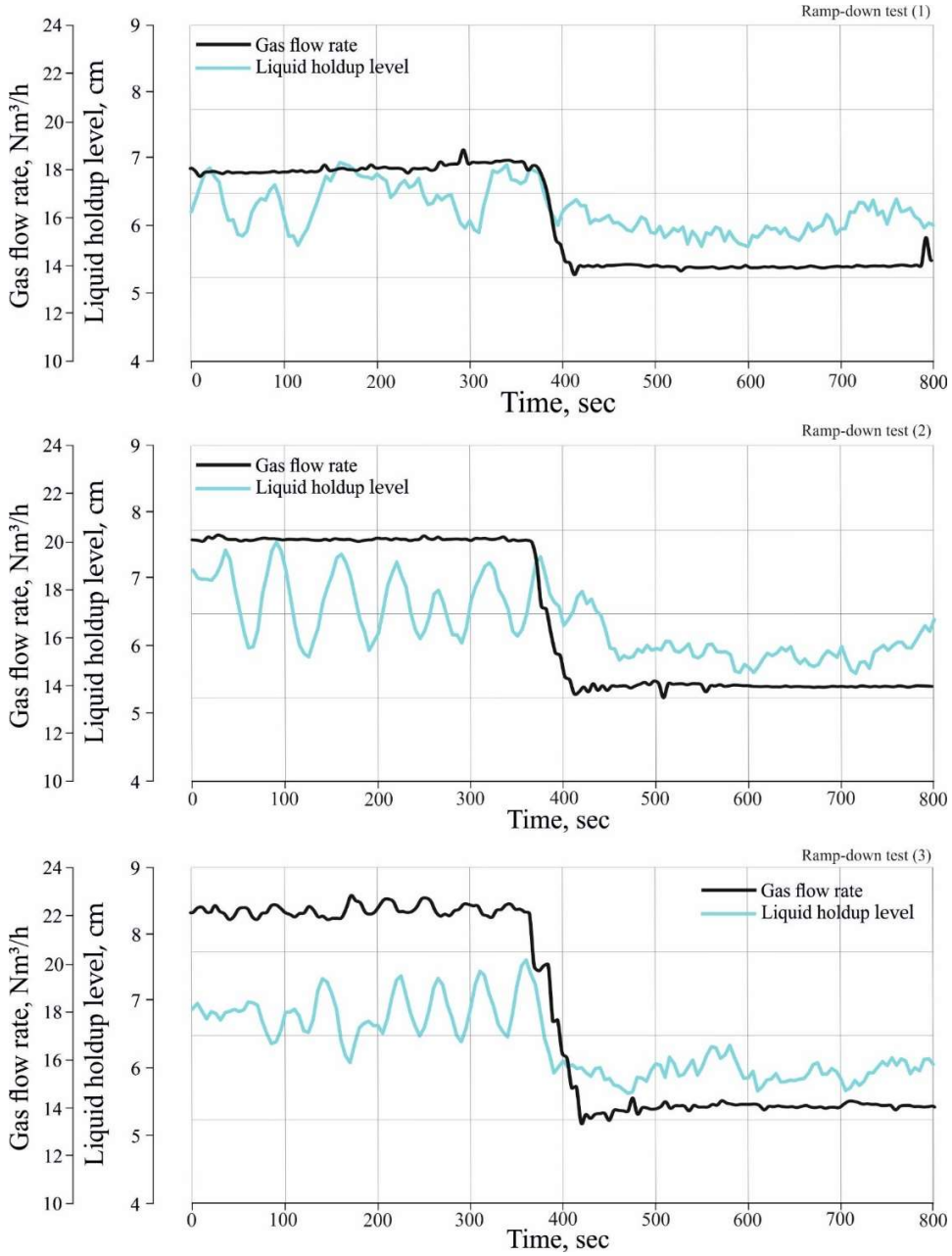

Figure 6.22 Tray liquid holdup level for different load changes of the gas flow rate in ramp-down tests

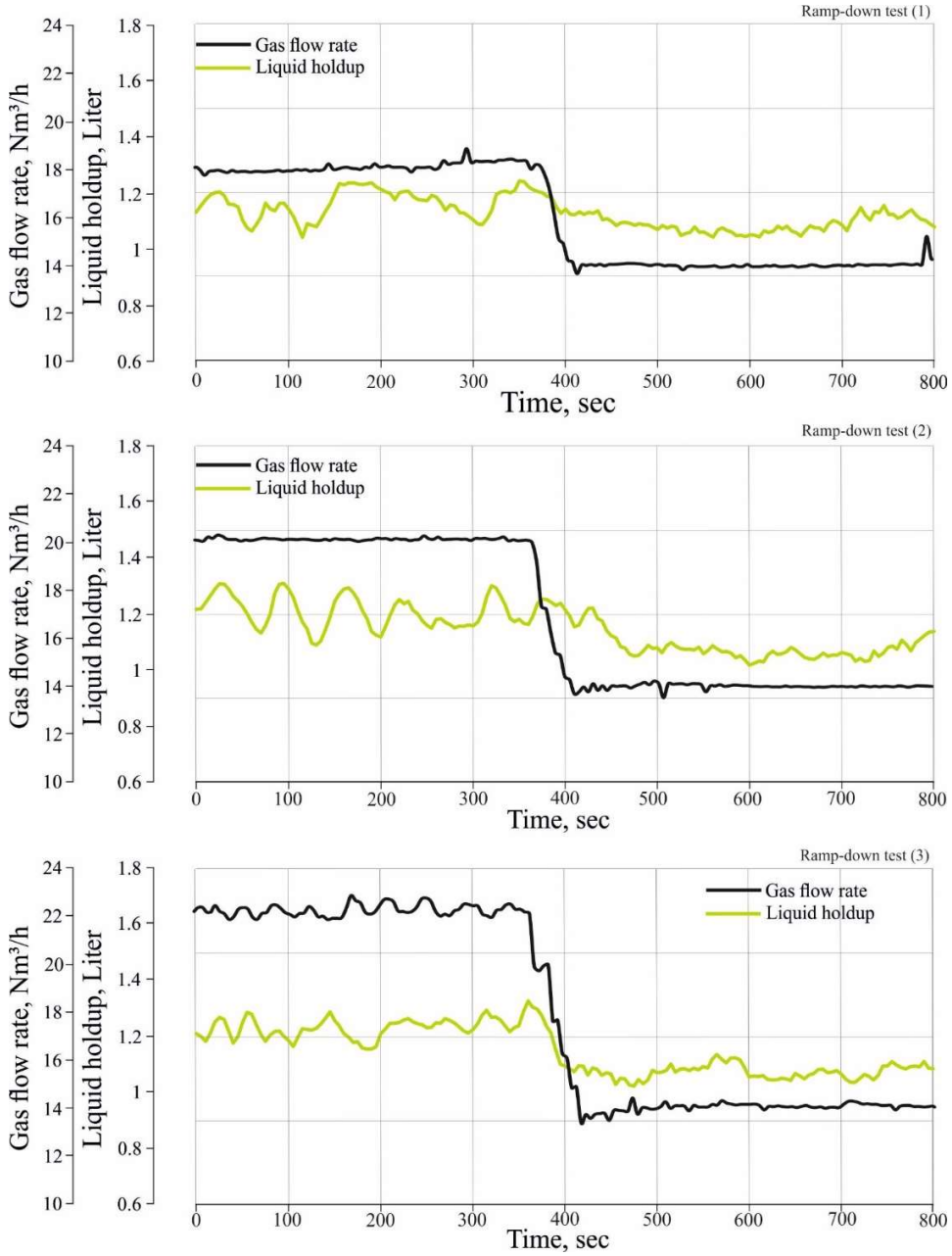

Figure 6.23 Tray liquid holdup for different load changes of the gas flow rate in ramp-down tests

6.3.1.3 Conclusion

From the experimental results, it can be concluded that the performance of the absorber was not satisfactory during the transient state at different load changes. The reason for this behavior is the delay in the settling time of the hydrodynamic properties of the tray. It can also be observed that the lower different load change results in a lower peak of CO_2 concentration at the outlet.

6.3.1.4 Results of Tests for Different Change Rates of Gas Flow Rate

The effect of different change rates is investigated by ramp-up and ramp-down tests of the gas flow rate. In the ramp-up tests, the gas flow rate increased from a minimum to a higher load. The rate of change was different for each test. In the ramp-down tests, the gas flow rate was decreased from a higher load level to a minimum load. The rate of change was different for each test. Figure 6.24 shows the tests of different change rates (ramp-up and ramp-down tests) performed to investigate the effect of dynamic change in the gas flow rate. In the ramp-up tests, the gas flow rate was increased from 14 Nm^3/h to 20 Nm^3/h by passing through a transient state. The rates of change were different at 0.2, 0.13, and 0.1 Nm^3/h /sec for ramp-up tests (1), (2), and (3) sequentially. In ramp-down tests, the gas flow rate decreased from 20 Nm^3/h to 14 Nm^3/h by passing through a transient state. The rate of change was different at 0.2, 0.13, and 0.1 Nm^3/h /sec for the ramp-up tests (1), (2), and (3) sequentially.

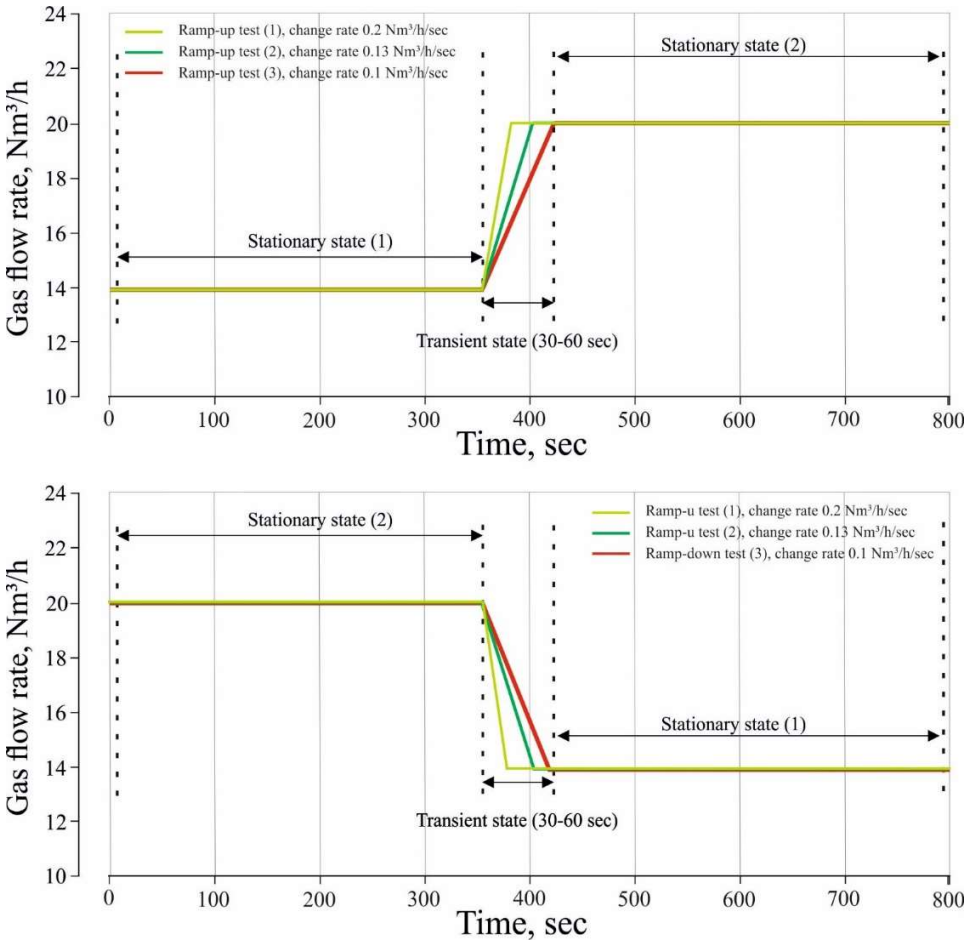

Figure 6.24 Different Change Rates tests

6.3.1.4.1 Effect of Different Change Rates of Gas Flow Rate on the CO_2 Volume Fraction

Figure 6.25 shows the effect of the different change rates of gas flow rate on the outlet CO_2 volume fraction during the transient states of the ramp-up tests. It can be seen that the different change rates in gas flow rates have a significant effect on the volume fraction of CO_2, highlighting the following notes:

- The CO_2 volume fraction reaches a peak during the transient states at all ramp-up tests.
- The higher the change rate, the lower the peak CO_2 volume fraction.
- The lower the change rate, the longer time to reach the peak CO_2 volume fraction.
- After the unsteady peak of the CO_2 volume fraction, the CO_2 volume fraction settled back to the steady-state level at different times for different change rates. The lower the change rate, the longer the settling time of the CO_2 volume fraction.

The reason for this behavior is assumed that during the ramp-up tests, the dynamic change in gas flow rates increases the liquid holdup level and liquid holdup in the lower trays faster than in the upper trays. As a result, the lower trays have low efficiency during the ramp-up tests which leads to reduce the performance of the absorber during the transient state.

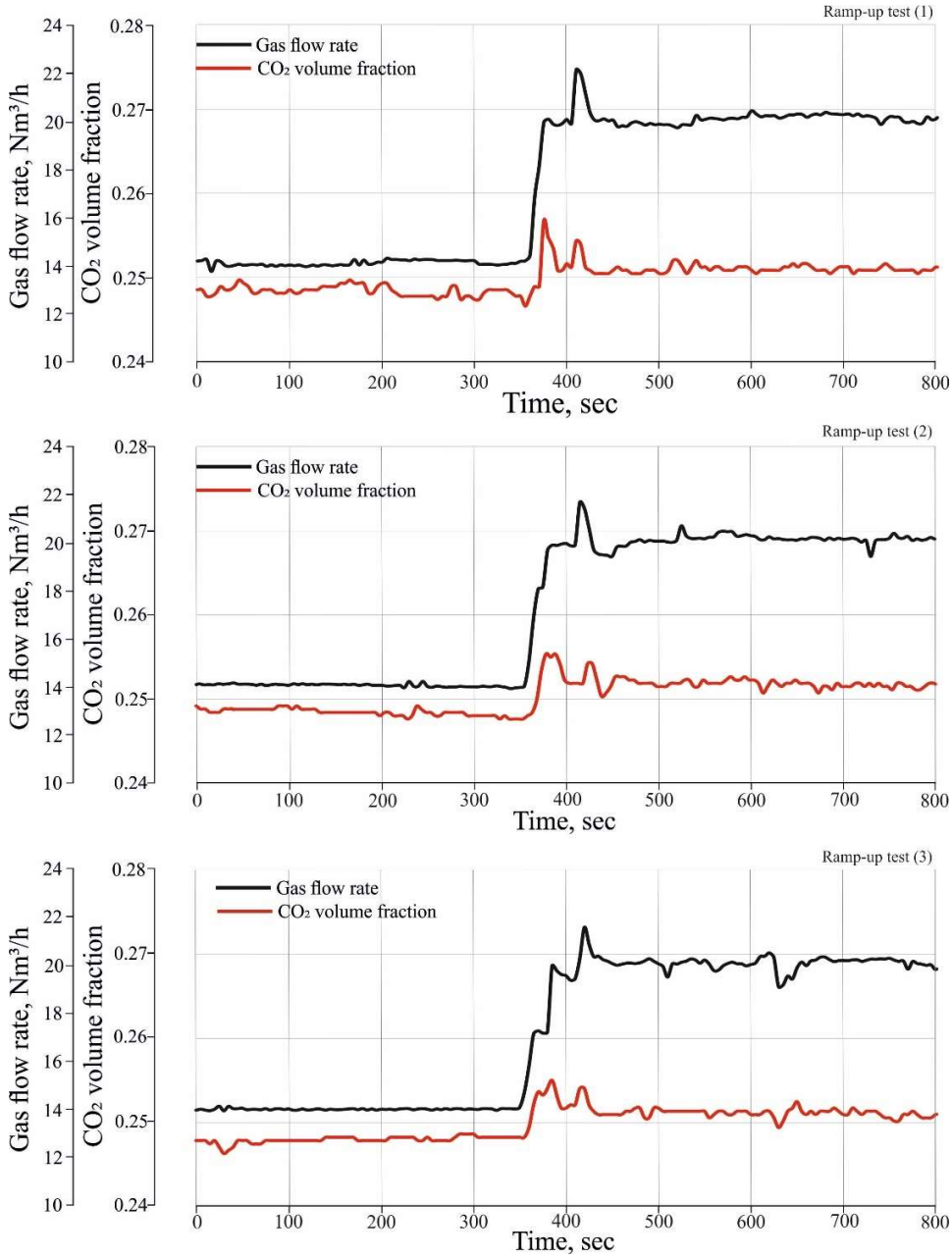

Figure 6.25 Outlet CO_2 volume fraction for different change rates of the gas flow rate in ramp-up tests

Figure 6.26 shows the effect of the different change rates of gas flow rate on the outlet CO_2 volume fraction during the transient states of the ramp-down tests. It can be seen that the different change rates in gas flow rates have a significant effect on the volume fraction of CO_2, highlighting the following notes:

- The CO_2 volume fraction reaches a trough during the transient state at all ramp-down tests
- The higher the change rate, the deepest trough of the CO_2 volume fraction.
- The higher the change rate, the shorter time to reach the trough of the CO_2 volume fraction.

- After the unsteady trough of the CO_2 volume fraction, the CO_2 volume fraction settled back to the steady-state level at different times for different change rates. The lower the change rate, the longer the settling time of the CO_2 volume fraction.

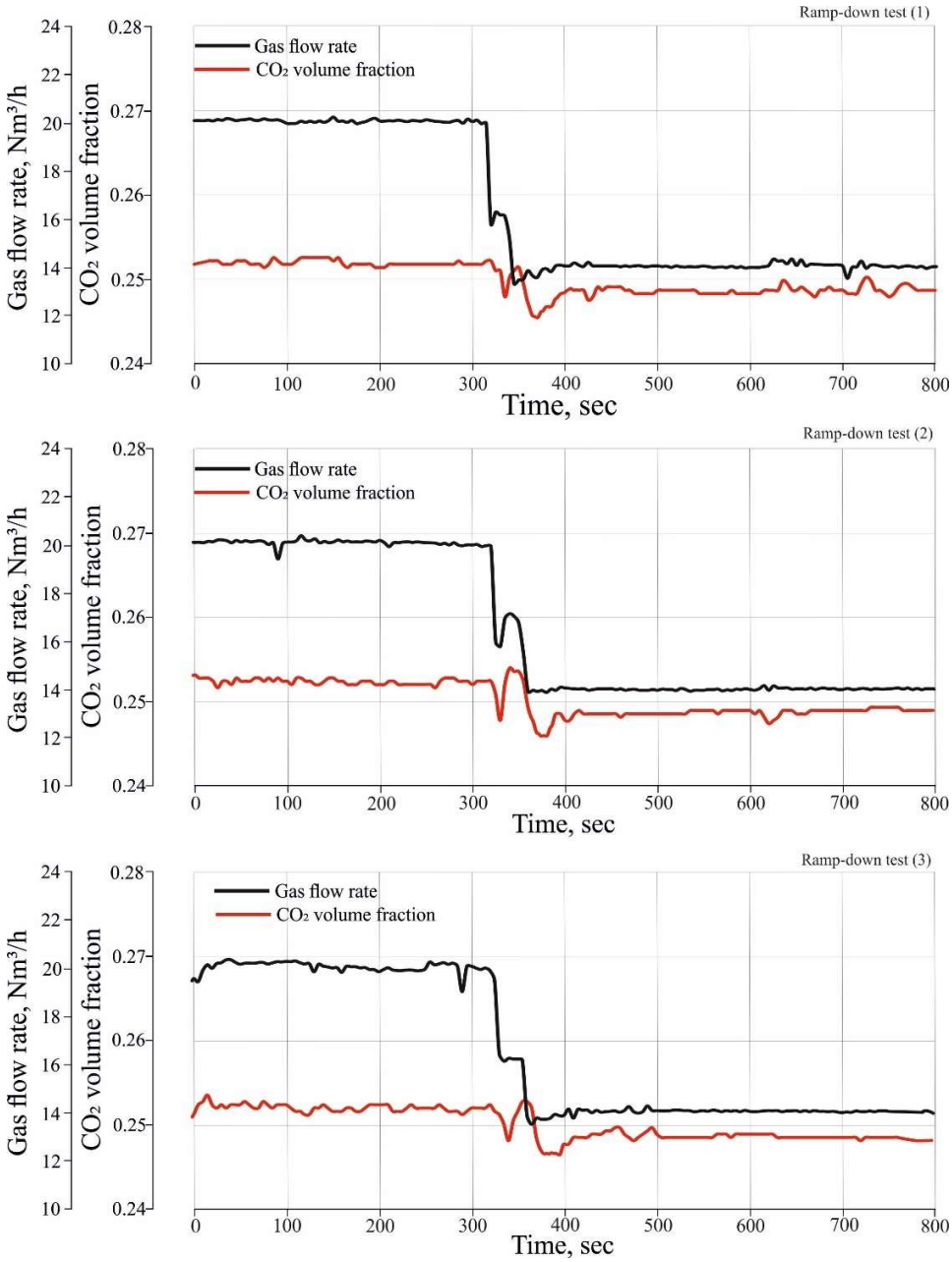

Figure 6.26 Outlet CO_2 volume fraction for different change rates of the gas flow rate in ramp-down tests

This behavior is related to the effect of dynamic change in gas on the hydrodynamic characteristics of the tray, which will be studied later.

6.3.1.4.2 Effect of Different Change rates of the Gas Flow Rate on the Hydrodynamic Characteristics

Figure 6.27, Figure 6.28, and Figure 6.29 show the effect of different change rates of the gas flow rate on the total tray pressure drop, tray liquid holdup level, and tray liquid holdup sequentially during the transient states of ramp-up tests. It can be seen that all the above hydrodynamic characteristics of the sieve tray increase rapidly during the transient state. The explanation for this behavior can be explained as follows: An increase in the flow rate of the gas leads to an increase in the superficial velocity of the gas. The increase in the superficial velocity of the gas will improve trapping the liquid on a tray and causes the liquid to accumulate on the tray, which leads to increased hydrodynamic characteristics of the sieves tray.

It can also be noted from Figure 6.27, Figure 6.28, and Figure 6.29 that the settling time of the hydrodynamic characteristics of the sieve tray on the third tray is longer than the time of the transient state of different change rates in the inlet gas flow rate (30-60 seconds). Although the transient state of different change rates in the inlet gas flow rate continued for 30-60 seconds, the hydrodynamic properties continued to change for about 60 seconds after the transient state ended. It is assumed that the delay of settling time of the hydrodynamic characteristics influences the absorber's performance during the transient state.

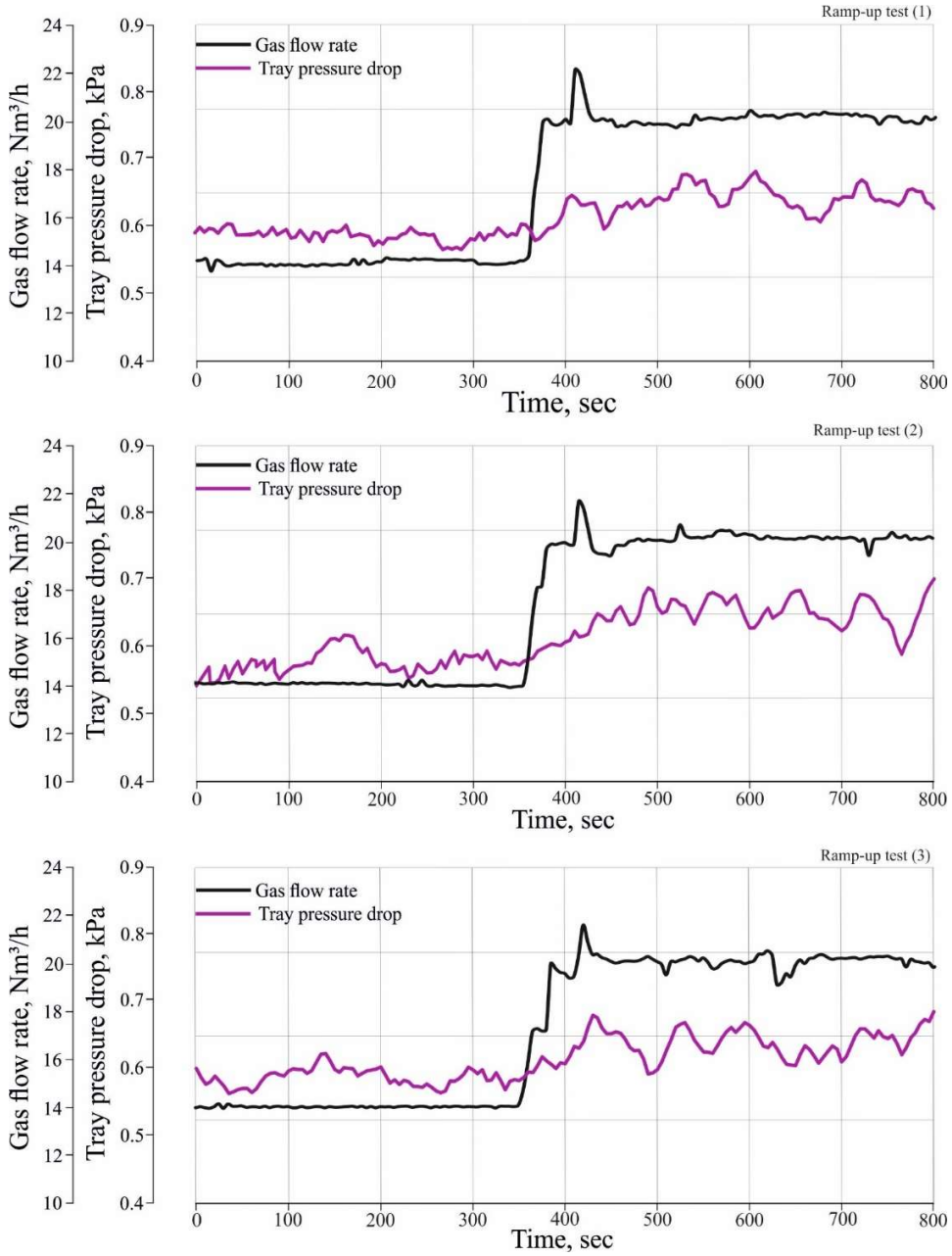

Figure 6.27 Total tray pressure drop for different change rates in the gas flow rate in ramp-up tests

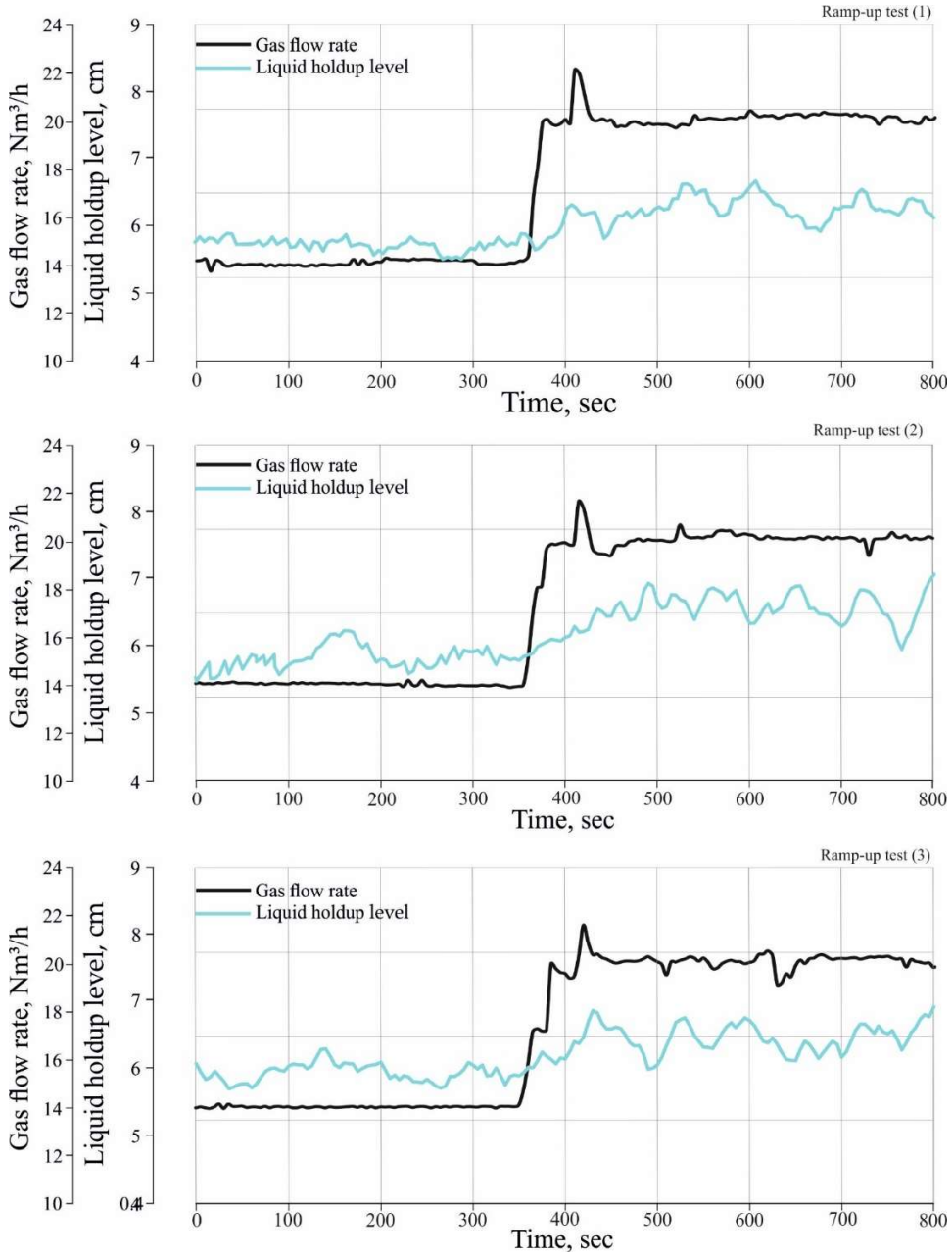

Figure 6.28 Tray liquid holdup level for different change rates in the gas flow rate in ramp-up tests

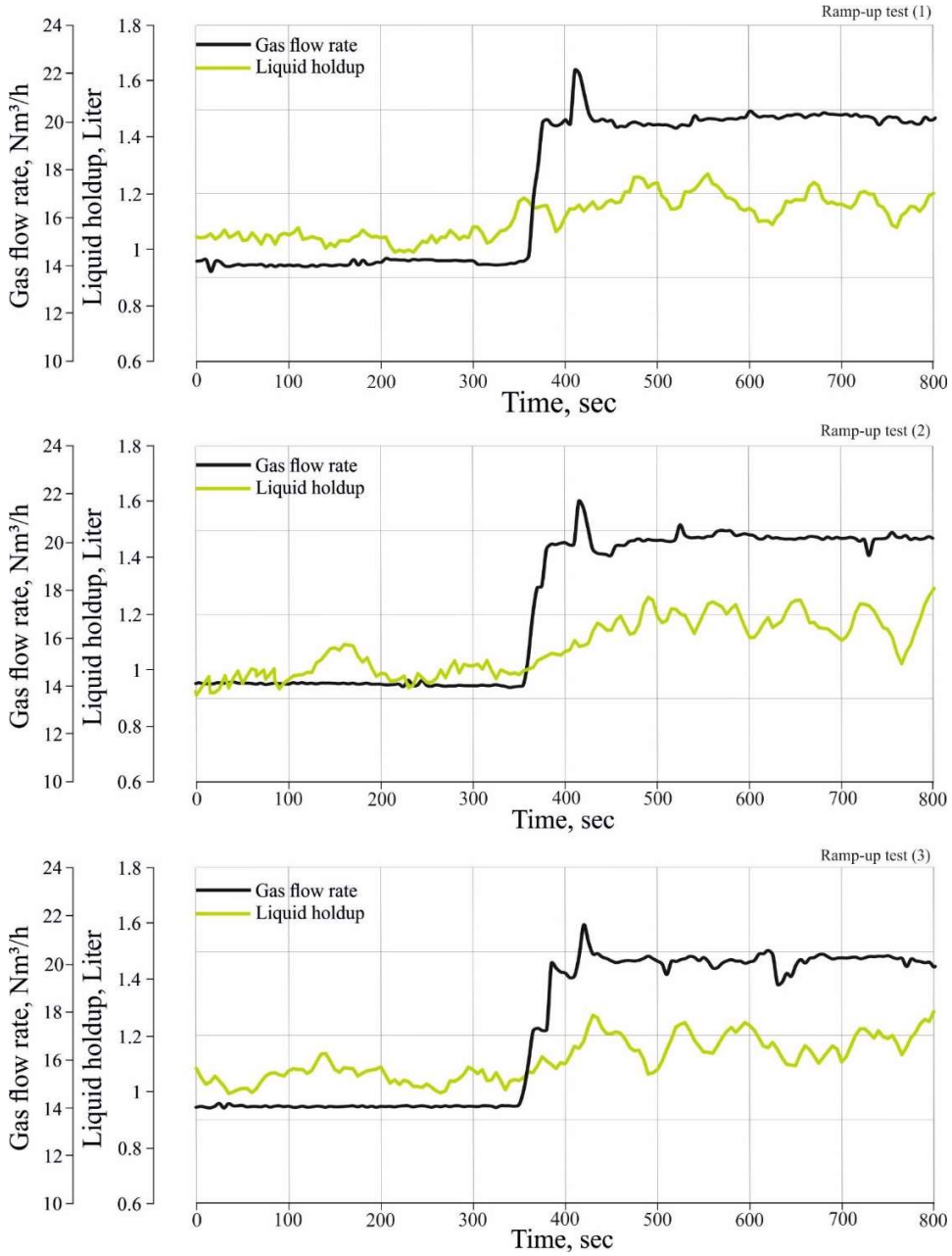

Figure 6.29 Tray liquid holdup for different change rates of the gas flow rate in ramp-up tests

Figure 6.30, Figure 6.31, and Figure 6.32 show the effect of the different change rates of the gas flow rate on the total tray pressure drop, tray liquid holdup level, and tray liquid holdup sequentially during the transient states of ramp-down tests. It can be seen that all the above hydrodynamic characteristics of the sieve tray decrease rapidly during ramp-down tests. The explanation for this behavior is as follows: a decrease in the flow rate of the gas leads to a decrease in the superficial velocity of the gas, and the decrease in the superficial velocity of the gas will decrease the trapping and accumulating of the liquid on the tray, which leads to decrease the hydrodynamic characteristics of the sieves tray.

.

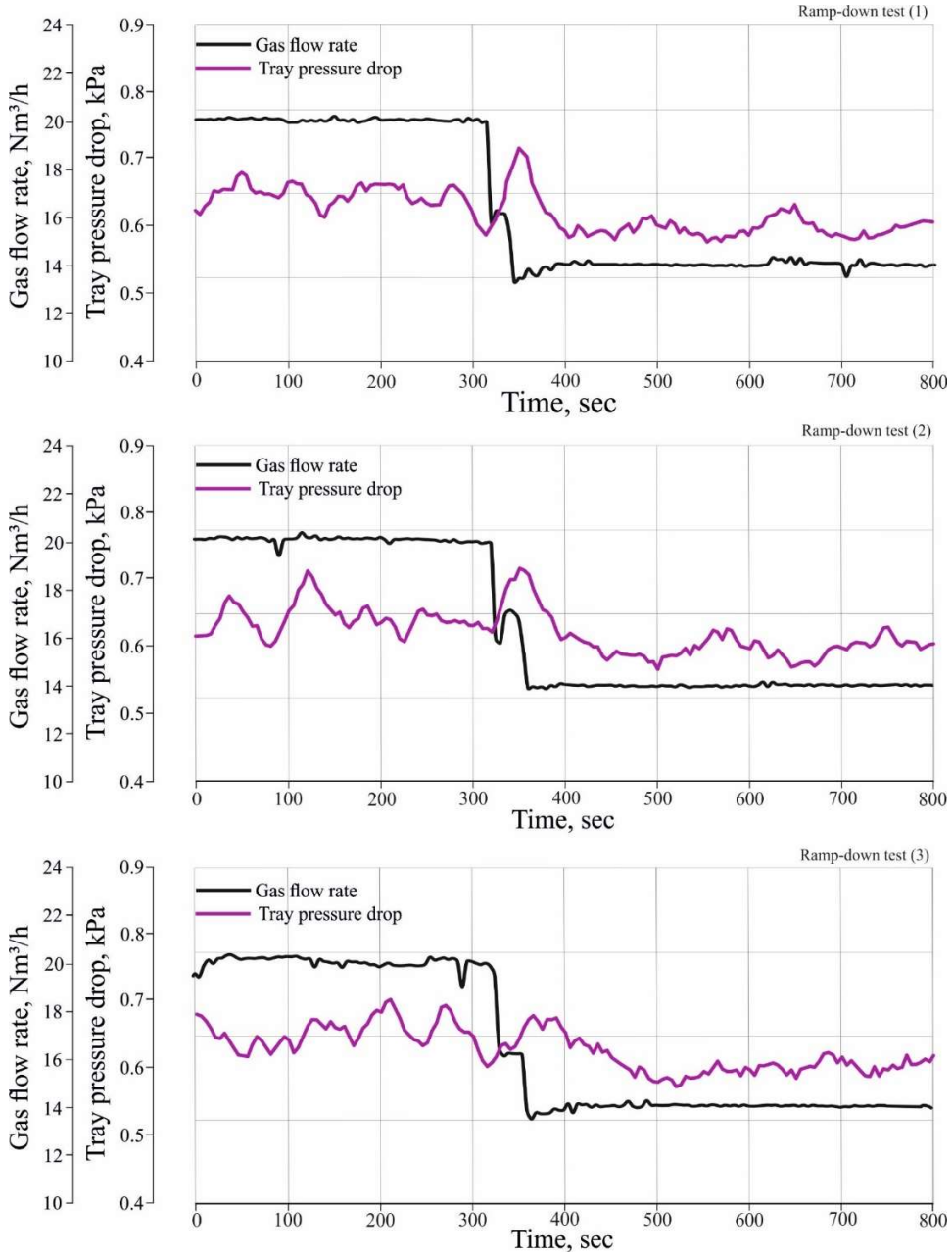

Figure 6.30 Total Tray pressure drop for different change rates of the gas flow rate in ramp-down tests

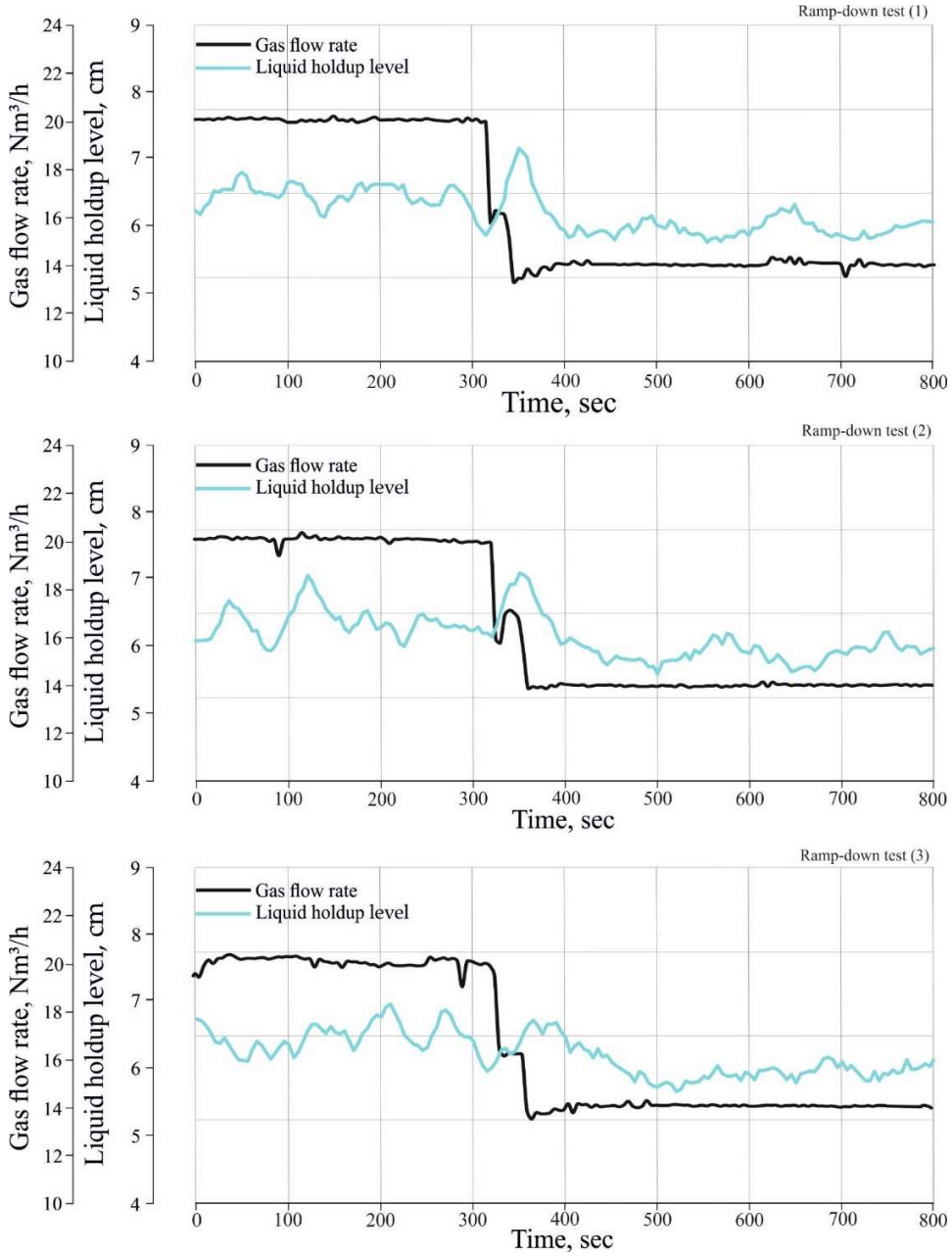

Figure 6.31 Tray liquid holdup level for different change rates of the gas flow rate in ramp-down tests

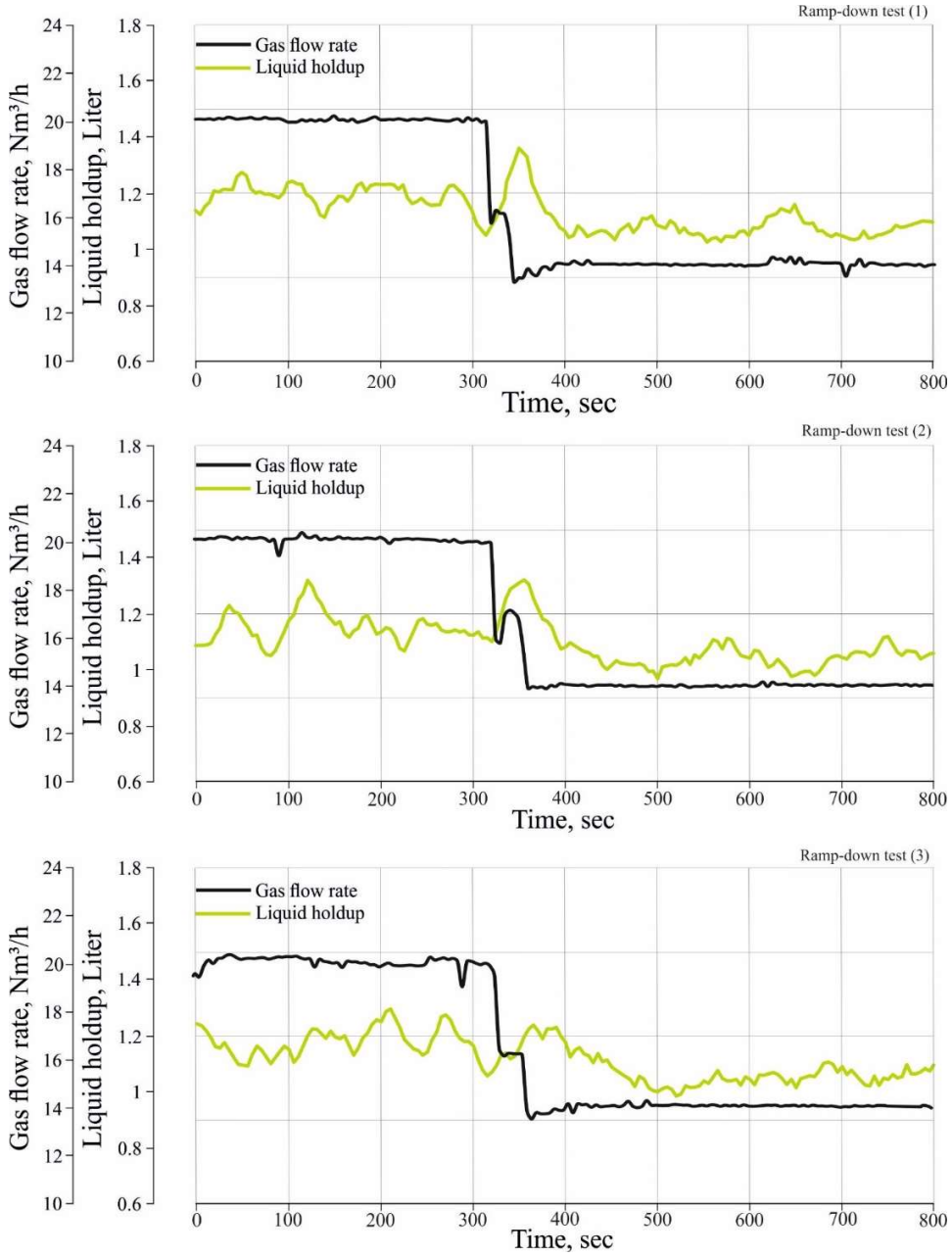

Figure 6.32 Tray liquid holdup for different change rates of the gas flow rate in ramp-down tests

6.3.1.4.3 Conclusion

From the experimental results, it can be concluded that the absorber's performance was not satisfactory during the transient state of different change rates in the gas flow rate. The reason for this behavior is the delay in the settling time of the hydrodynamic properties of the tray. It can also be observed that the lower change rate results in a lower peak of CO_2 concentration at the outlet.

6.3.1.5 Results of tests for Different Load Changes in Inlet Gas and Solvent Flow Rate

The effect of different load changes is investigated by ramp-up and ramp-down tests of the gas and solvent flow rate. Figure 6.33 and Figure 6.34 show different load change tests (ramp-up and ramp-down tests) were performed to investigate the effect of dynamic change in the gas and solvent flow rate. In the ramp-up tests, the operation of the absorber is changed from a stationary state (1) to a stationary state (2) by going into a transient state. During the transient state, both the gas and solvent flow rates are gradually increased between the stationary state (1) and stationary state (2) with a certain rate of change in the flow rate. The gas flow rate was increased from 14 Nm^3/h to 20 Nm^3/h with a rate of change of about 0.1 $Nm^3/h/s$, where the median flow rate of the incoming solvent was increased from 94 NL/h to 114 NL/h for ramp-up test (1), and to 131 NL/h and N150 L/h for ramp-up test (2) and (3) sequentially. The rate of change of solvent flow rate is about 0.7 NL/h/s.

In the ramp-down tests, the gas and solvent flow rates are gradually decreased between the stationary state (2) and stationary state (1) with a certain rate of change in the flow rate. In the transient state of the ramp-down tests, the gas flow rate decreased from 20 Nm^3/h to 14 Nm^3/h with a rate of change of about 0.1 $Nm^3/h/s$, where the median flow rate of the incoming solvent decreased from 114 NL/h,131 NL/h, and 150 NL/h for ramp-up test (1), (2) and (3) sequentially to 94 NL/h. The rate of change of solvent flow rate is about 0.7 NL/h/s.

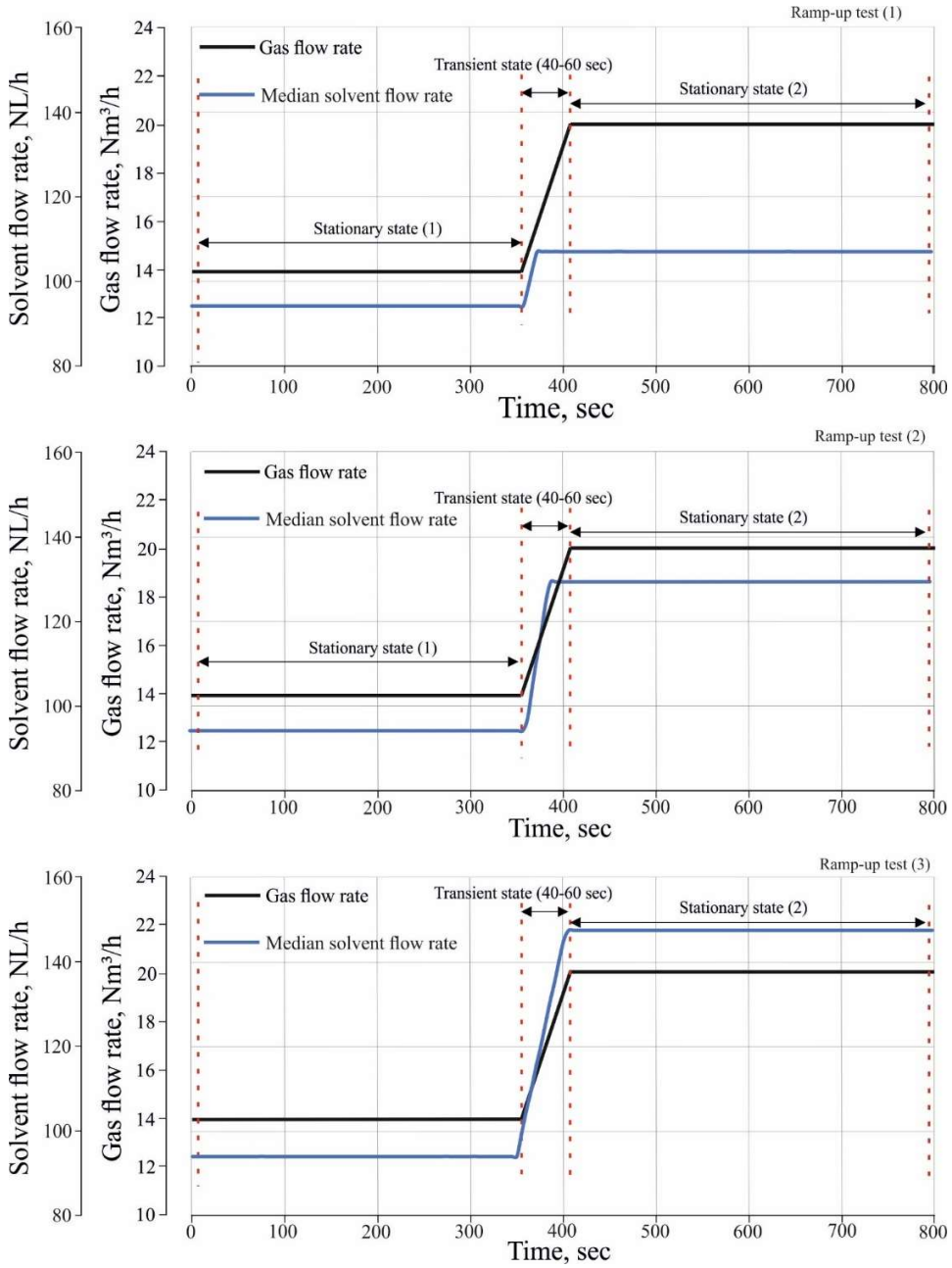

Figure 6.33 Different load changes in inlet gas and solvent flow rate in ramp-up tests

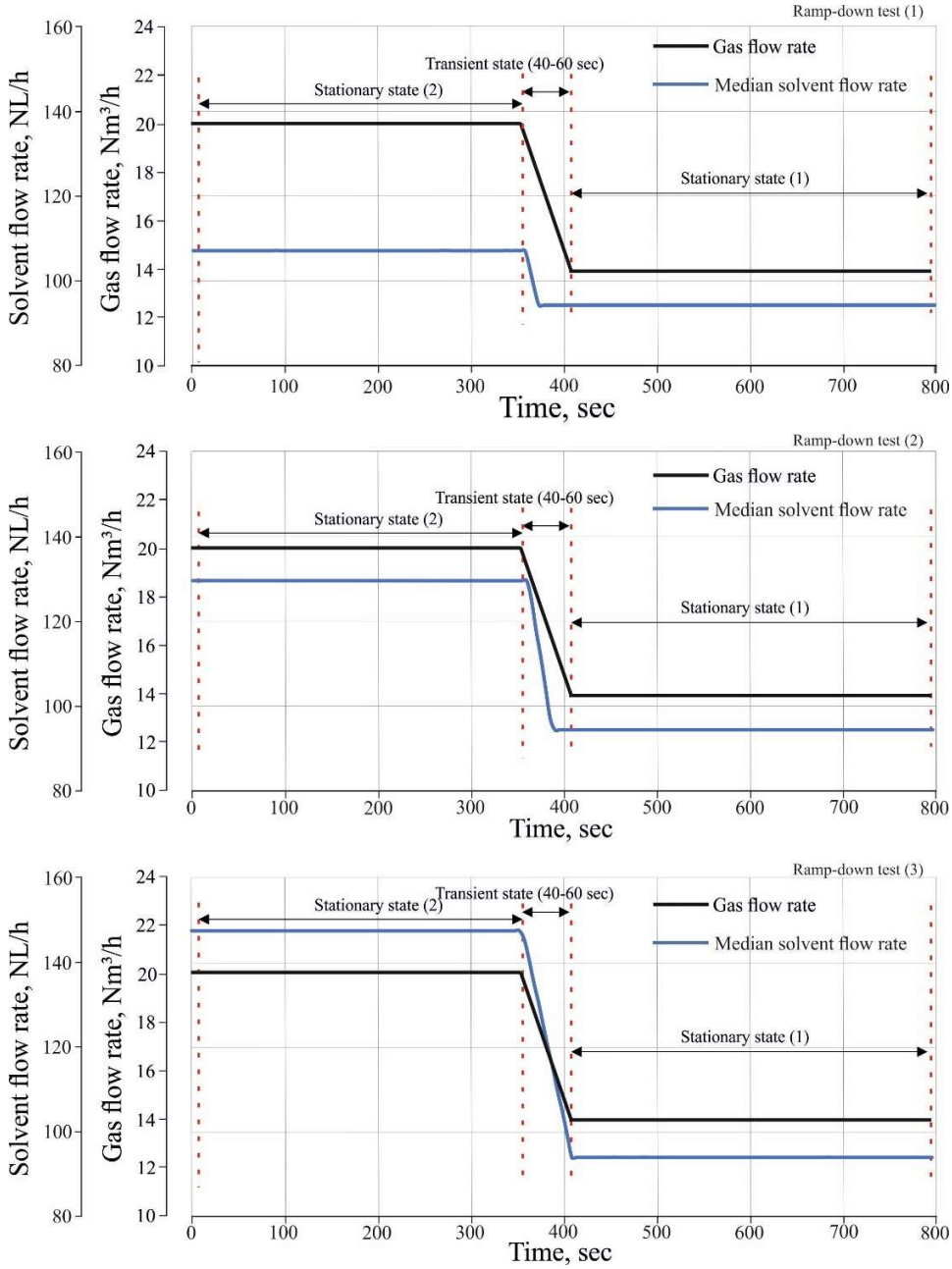

Figure 6.34 Different load changes in inlet gas and solvent flow rate in ramp-down tests

6.3.1.5.1 Effect of Different Load Changes in Inlet Gas and Solvent Flow Rate on the CO_2 Volume Fraction

Figure 6.35 shows the effect of the different load changes in inlet gas and solvent flow rate on the outlet CO_2 volume fraction during the transient states of the ramp-up tests. It can be seen that different load changes have a significant effect on the volume fraction of CO_2, highlighting the following notes:

- The CO_2 volume fraction reaches a peak during the transient state at all ramp-up tests.

- The higher the different load changes in solvent flow rate, the lower the peak CO_2 volume fraction.
- After the unsteady peak of the CO_2 volume fraction, the CO_2 volume fraction settled back to the steady state level.

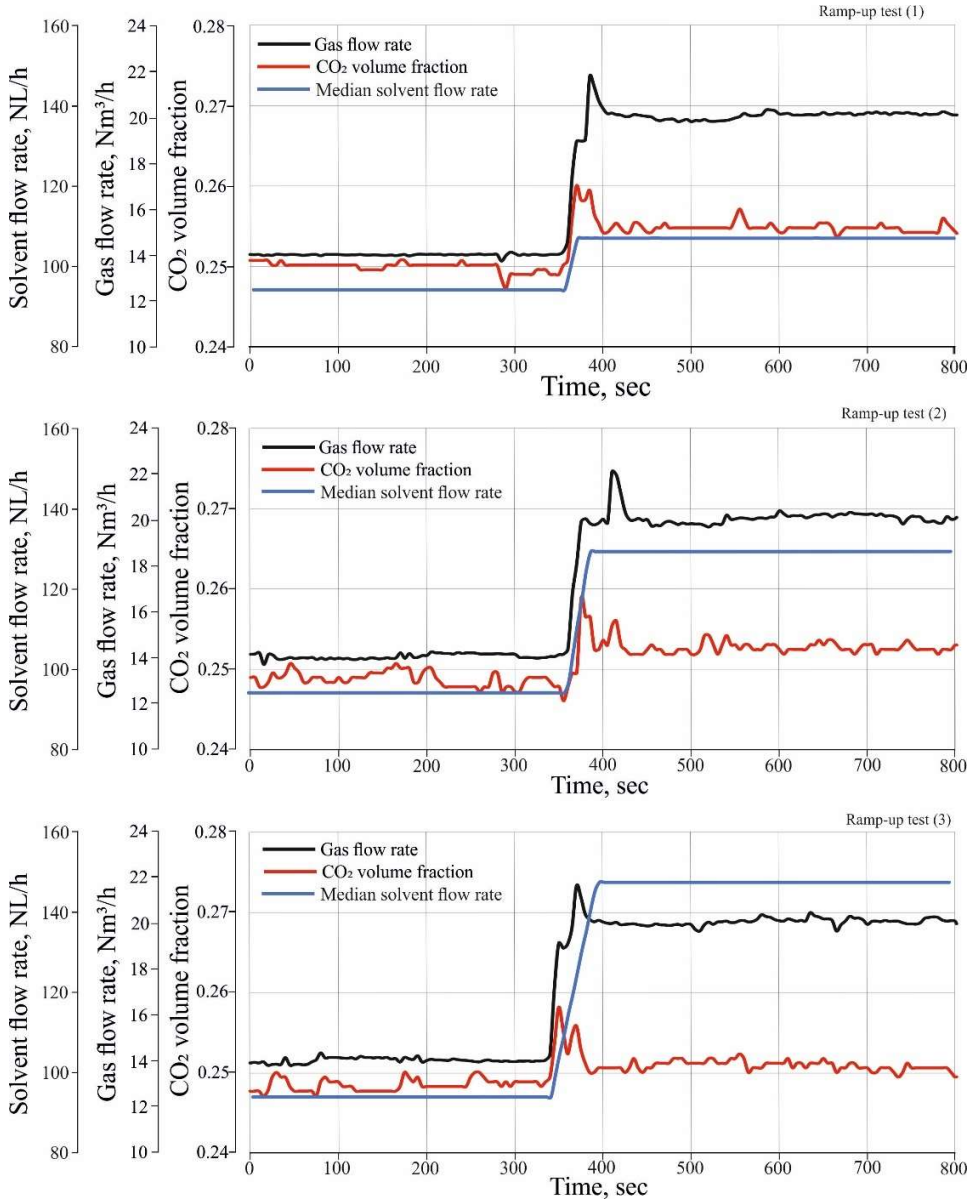

Figure 6.35 Outlet CO_2 volume fraction for different load changes of the gas flow rate and solvent flow rate in ramp-up tests

The reason for this behavior is assumed that during the ramp-up tests, the dynamic change in gas flow rates increases the liquid holdup level and liquid holdup in the lower trays faster than in the upper trays. As a result, the lower trays have low efficiency during the ramp-up tests which leads to reduce the absorber performance.

Figure 6.36 shows the effect of the different load changes of gas flow rate and solvent flow rate on the outlet CO_2 volume fraction during the transient states of the ramp-down tests. It can be seen that the different load changes have a significant effect on the volume fraction of CO_2, highlighting the following notes:

- The CO_2 volume fraction reaches trough during the transient states at all ramp-down tests.
- The higher the different load changes in solvent flow rate, the deepest the trough CO_2 volume fraction.

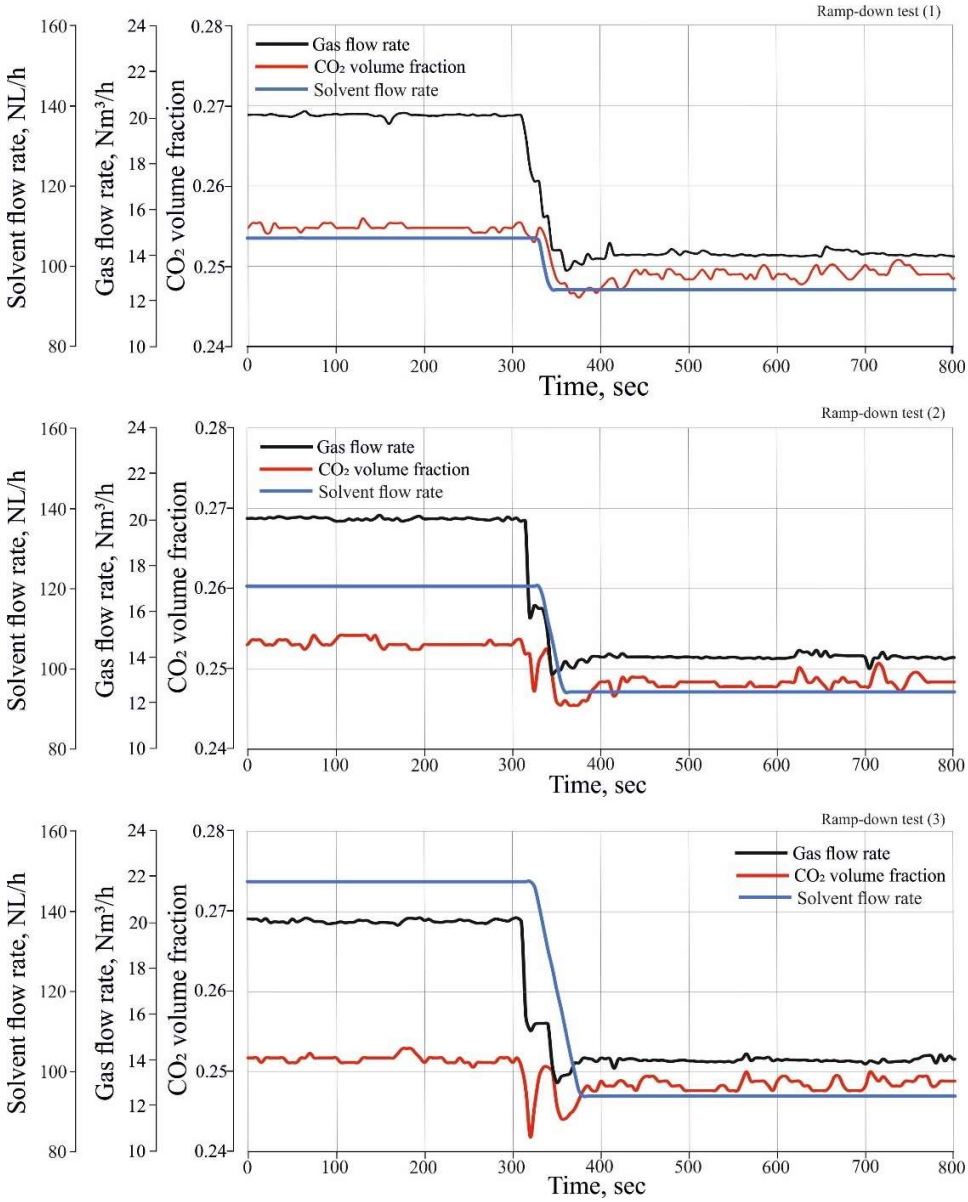

Figure 6.36 Outlet CO_2 volume fraction for different load changes of the gas flow rate and solvent flow rate in ramp-down tests

6.3.1.5.2 Studying the Effect of Different Load Changes of Inlet Gas and Solvent Flow Rate on Hydrodynamic Properties of the Sieve Tray

Figure 6.37, Figure 6.38, and Figure 6.39 show the effect of different load changes of inlet gas and solvent flow rates on the total tray pressure drop, tray liquid holdup level, and tray liquid holdup sequentially during the transient states of ramp-up tests. It can be seen that all the above hydrodynamic characteristics of the sieve tray increase rapidly during the transient state. The explanation for this behavior can be explained as follows: An increase in the flow rate of the gas leads to an increase in the superficial velocity of the gas. The increase in the superficial velocity of the gas will improve trapping the liquid on a tray and causes the liquid to accumulate on the tray, which leads to increased hydrodynamic characteristics of the sieve tray.

It can also be noted from Figure 6.37, Figure 6.38, and Figure 6.39 that the settling time of the hydrodynamic characteristics of the sieve tray on the third tray is longer than the time of the transient state of different load changes in the inlet gas rate (40-60 seconds). Although the transient state of the gas flow continued for 40-60 seconds, the hydrodynamic properties continued to change for about 60 seconds after the transient state ended. It is assumed that the delay of settling time of the hydrodynamic characteristics influences the absorber's performance during the transient state. To check this assumption, it is necessary to study the absorber's performance during the transition state, which will be discussed later.

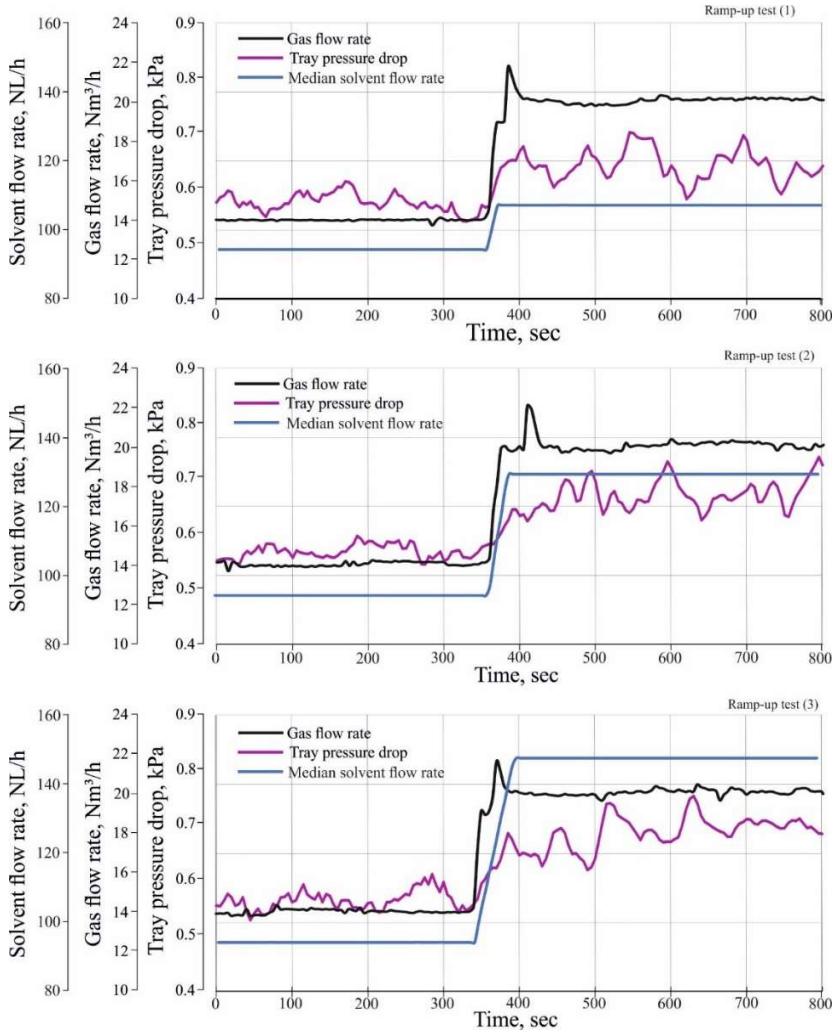

Figure 6.37 Total tray pressure drop for different load changes of the gas and solvent flow rate in ramp-up tests

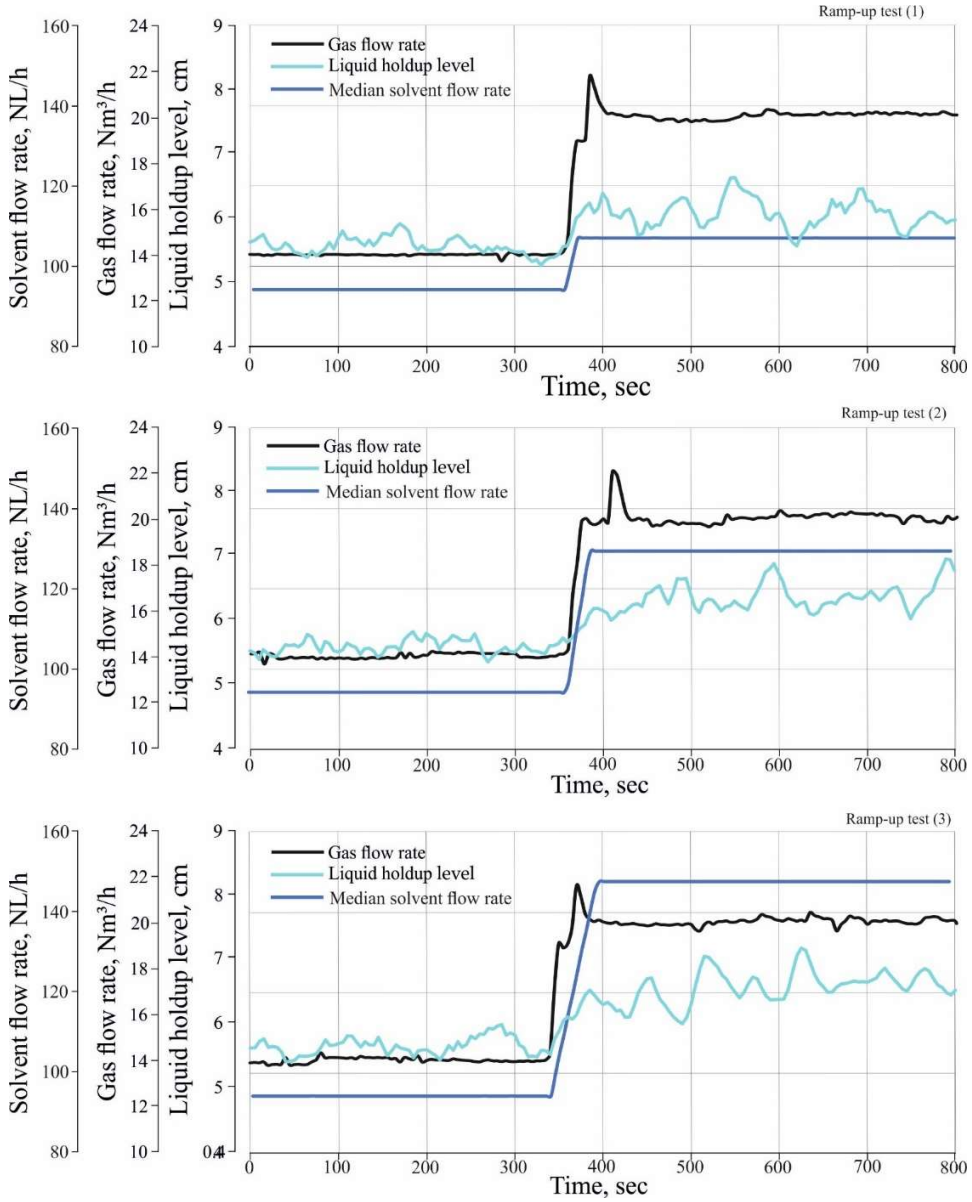

Figure 6.38 Tray liquid holdup level for different load changes of the gas and solvent flow rate in ramp-up tests

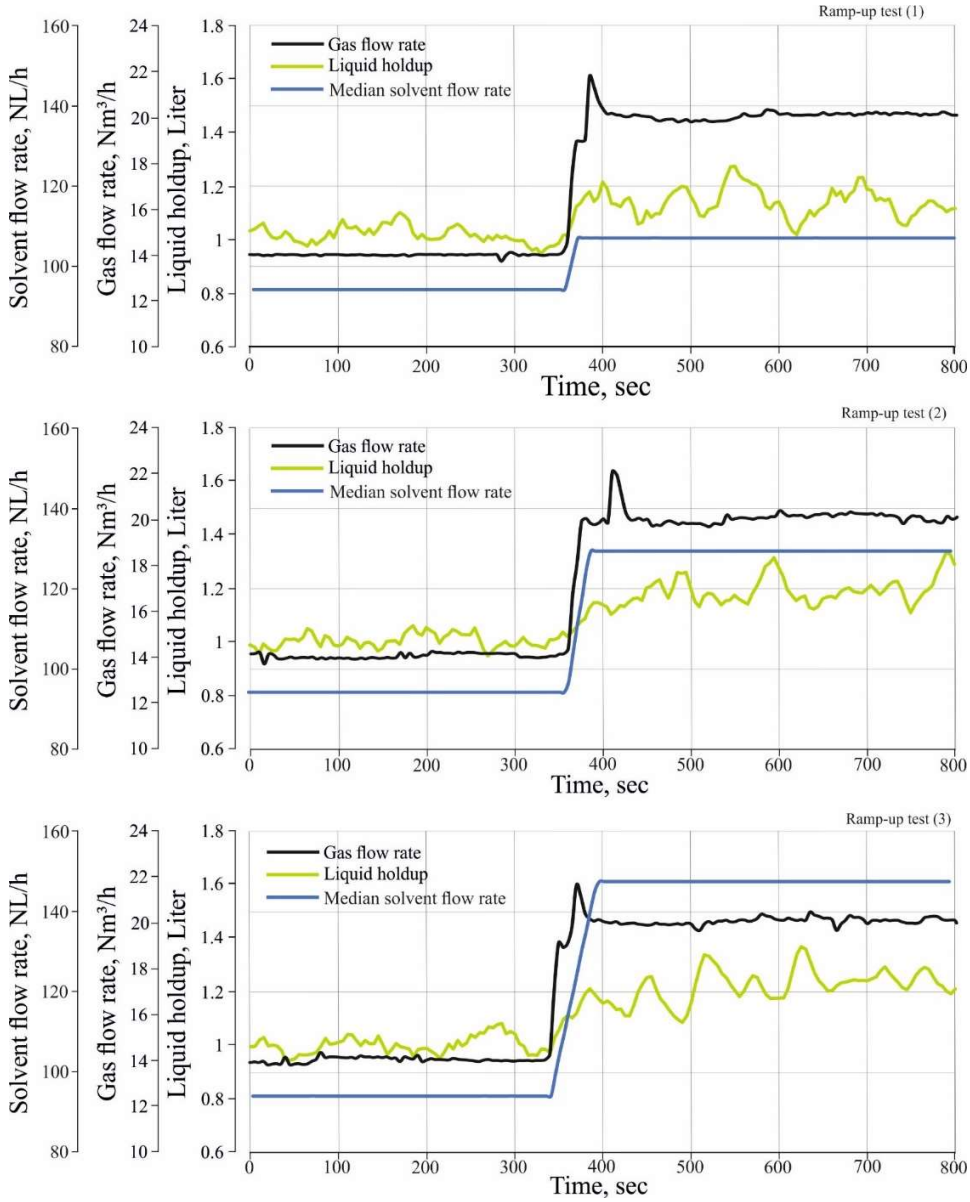

Figure 6.39 Tray liquid holdup for different load changes of the gas and solvent flow rate in ramp-up tests

Figure 6.40, Figure 6.41, and Figure 6.42 show the effect of the different change rates of inlet gas and solvent flow rate on the total tray pressure drop, tray liquid holdup level, and tray liquid holdup sequentially during the transient states of ramp-down tests. It can be seen that all the above hydrodynamic characteristics of the sieve tray decrease rapidly during ramp-down tests. The explanation for this behavior is as follows: a decrease in the flow rate of the gas leads to a decrease in the superficial velocity of the gas, and the decrease in the superficial velocity of the gas will decrease the trapping and accumulating of the liquid on the tray, which leads to decrease the hydrodynamic characteristics of the sieves tray.

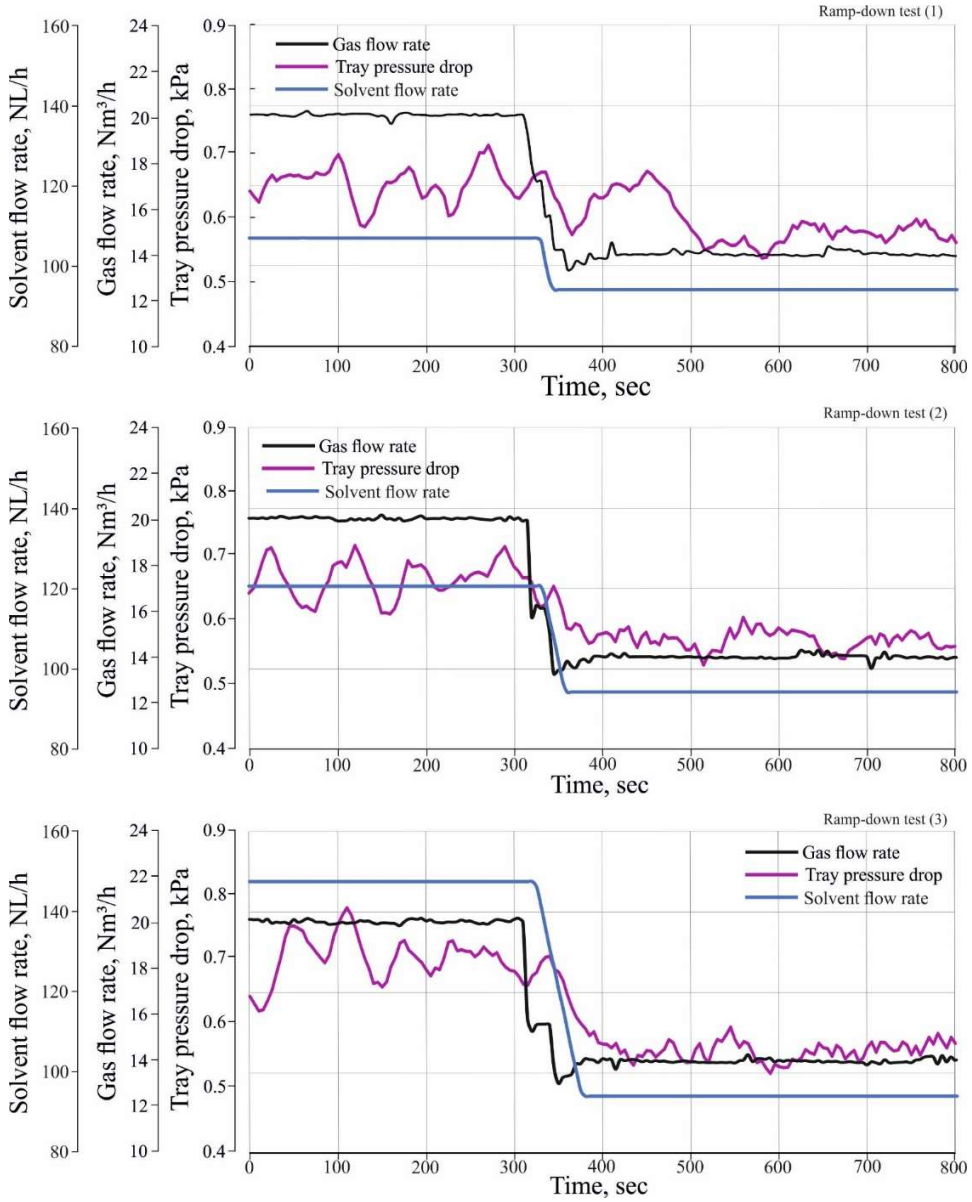

Figure 6.40 Total tray pressure drop for different load changes of the gas and solvent flow rate in ramp-down tests

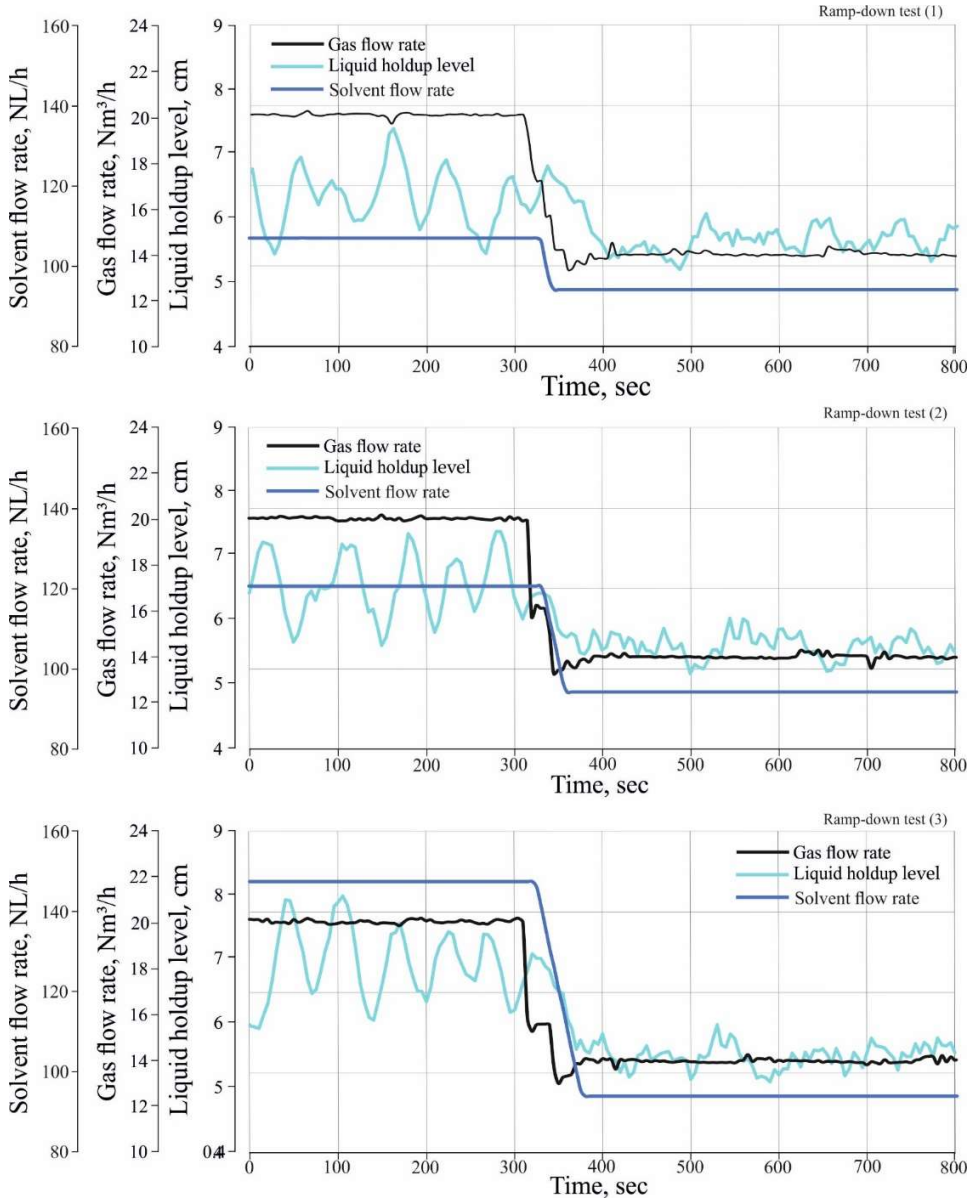

Figure 6.41 Tray liquid holdup level for different load changes of the gas and solvent flow rate in ramp-down tests

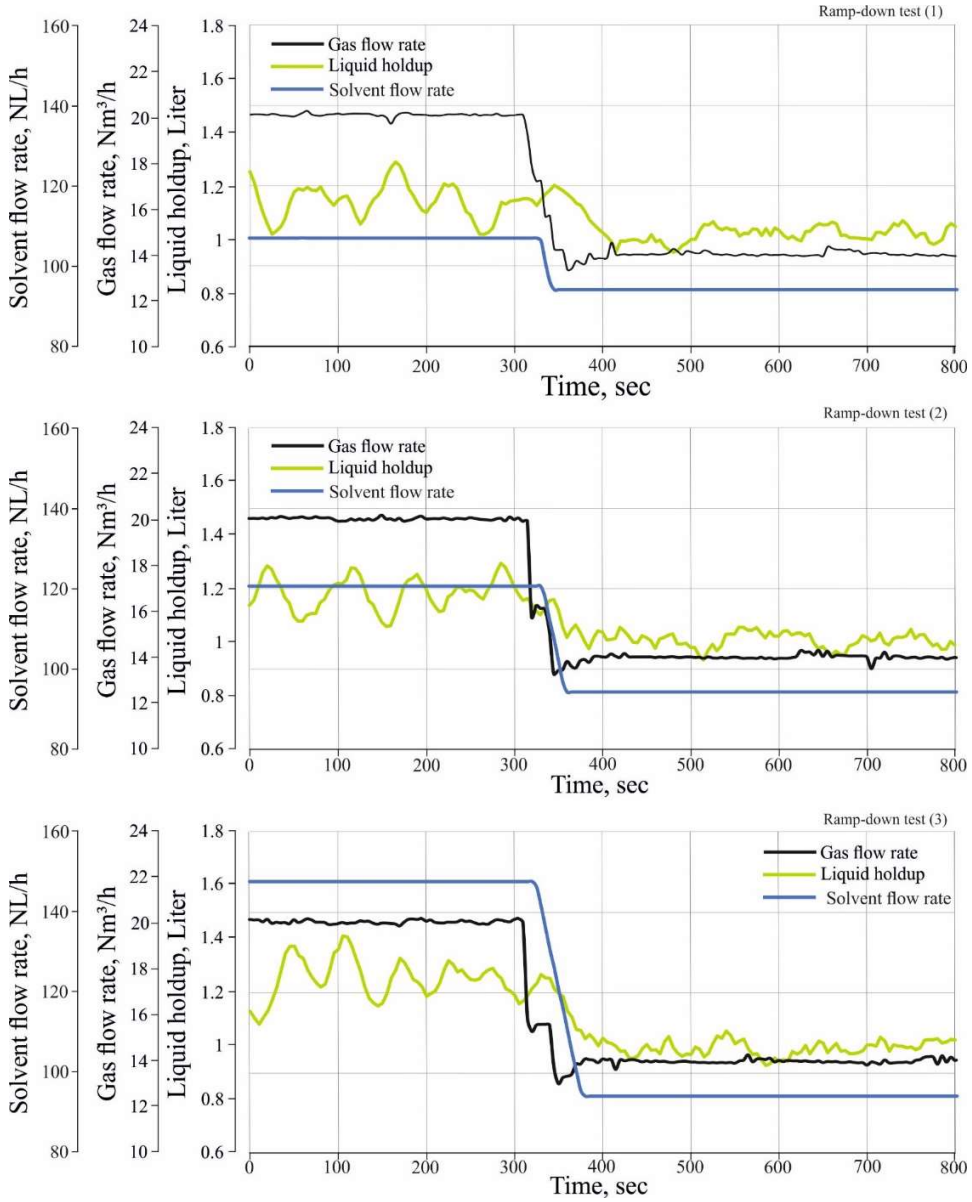

Figure 6.42 Tray liquid holdup for different load changes of the gas and solvent flow rate in ramp-down tests

6.3.1.5.3 Effect of Different Load Changes in the Inlet Gas and Solvent Flow Rate on the Performance of the Absorber

Figure 6.43 illustrates the effects of different load changes in the inlet gas and solvent flow rate on the absorption percentage of CO_2. It can be seen that different load changes have a significant effect on the absorption percentage of CO2. During the transient state, the absorption percentage of CO2 decreased rapidly during the transient state.

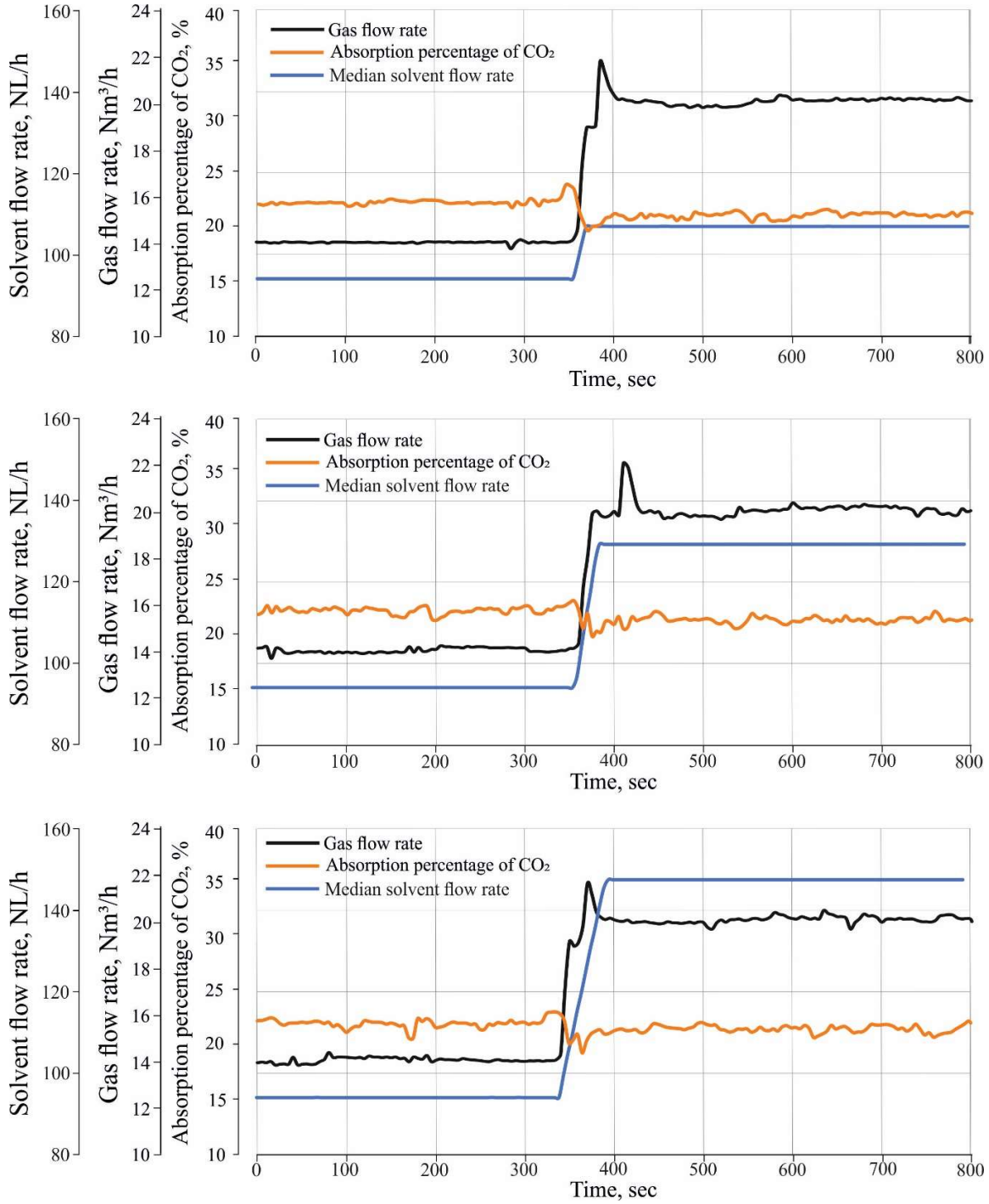

Figure 6.43 Effect of different load changes in the inlet gas and solvent flow rate on the absorbed rate of CO_2

6.3.1.6 Conclusion

To evaluate the absorber's performance during the transient state, it can be observed that the CO_2 volume fractions reached a peak value in all ramp-up tests though the solvent flow rate was increased during the transient state. The main reason for this behavior is the delayed response of the absorber to the absorption of excess CO_2 during the transient state because of the delay of the settling time of the tray hydrodynamic properties during the ramp-up tests as seen in Figure 6.37, Figure 6.38, and Figure 6.39. It can be seen that the settling time of the hydrodynamic characteristics of the tray is longer than the time of the transient state of different load changes in the inlet gas and solvent flow rate. Thus, it can be concluded that there is a significant relationship between the trays' hydrodynamic properties and the absorber's performance. During the transition state, the liquid level in the upper trays increases faster than in the lower trays, so the lower trays contain less liquid during the transient state and thus have a lower efficiency. It can also be concluded that the absorber's performance during the transient state of the ramp tests is not satisfactory.

6.3.2 Results of the Experiments With an Aqueous MDEA Solution with a Mass Fraction of 50%

6.3.2.1 Test Procedure

The CO_2 gas was mixed with N_2 using the gas mixing unit before entering the absorber column. The N_2 is an inert gas and serves as a carrier gas. An aqueous MDEA solution with a mass fraction of 50 % was used as a solvent. The CO_2 volume fraction was 0.3 in all experiments. The input gas flow rate at the beginning was constant at 14 Nm^3/h. The pressure of the absorber was constant at 0.25 MPa. The inlet solvent flow rate was constant at 40 NL/h. The regeneration unit was operated with a heating power of 4.5 kW during all experiments. The test rig was controlled and operated under the above operating conditions for about one hour to reach the steady state of the outlet CO_2 concentration. Then, two kinds of tests were conducted to investigate the effects of different load changes and different change rates in inlet gas flow rate on CO_2 absorption.

6.3.2.2 Results of Tests for Different Load Changes in Inlet Gas Flow Rate

Figure 6.44 shows the effect of the different load changes in the inlet gas flow rate on the outlet CO_2 volume fraction during the transient states of the ramp-up tests and the ramp-down tests. It can be seen from Figure 6.44 that different load changes in the gas flow rate during the transient states of ramp-up tests have a significant effect on the volume fraction of CO_2, highlighting the following notes:

- The CO_2 volume fraction reaches a peak during the transient state at all ramp-up tests.
- The higher the different load change, the higher the peak CO_2 volume fraction.
- The higher the different load change, the longer time to reach the peak CO_2 concentration.
- After the unsteady peak of the CO_2 volume fraction, the CO_2 volume fraction settled back to the steady state level at different times for different load changes. The higher the different load change, the longer the settling time of the CO_2 concentration.

It can be seen also from Figure 6.44 that the different load changes in the gas flow rate during the transient states of the ramp-down tests have a significant effect on the volume fraction of CO_2, highlighting the following notes:

- The CO_2 volume fraction reaches a trough during the transient state at all ramp-down tests.
- The higher the different load change, the deepest the trough of CO_2 volume fraction.
- The higher the different load change, the longer time to reach the trough CO_2 volume fraction.

After the unsteady trough of the CO_2 volume fraction, the CO_2 volume fraction settled back to the steady-state level at different times for different load changes. The higher the different load changes, the longer the settling time of the CO_2 concentration.

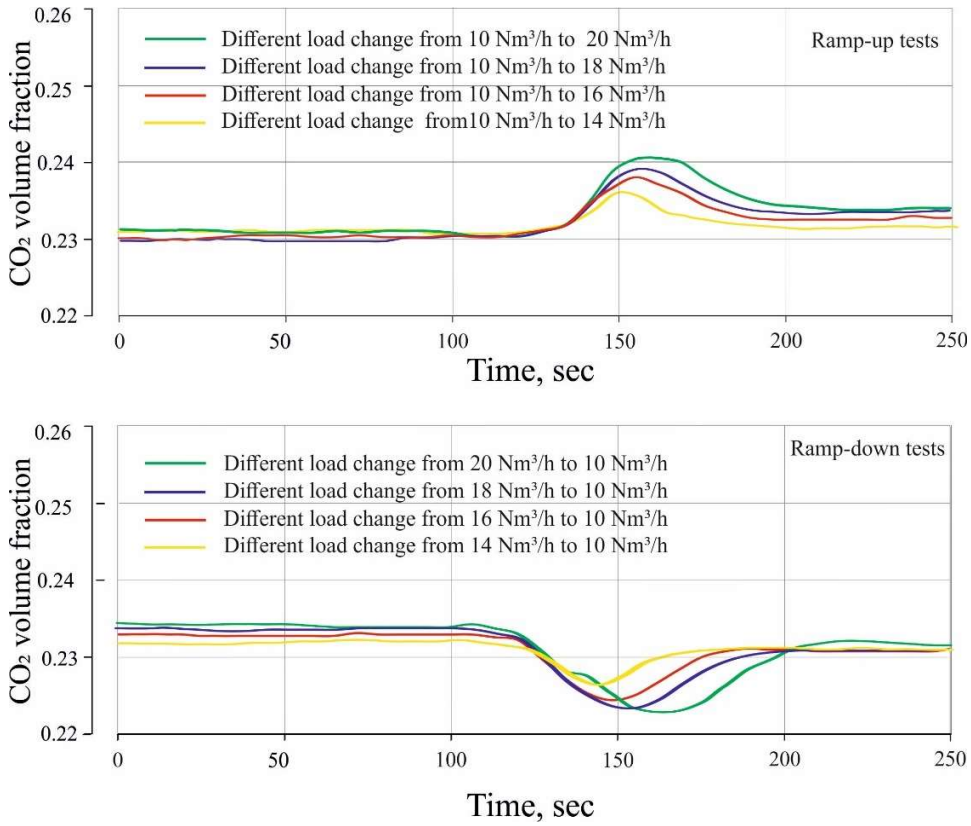

Figure 6.44 Outlet CO_2 volume fraction for different load changes in gas flow rate

6.3.2.3 Results of Tests for Different Change Rates in Inlet Gas Flow Rate

Figure 6.45 shows the effect of the different change rates of gas flow rate on the outlet CO_2 volume fraction during the transient states of the ramp-up tests and the ramp-down tests. It can be seen from Figure 6.45 that the different change rates in gas flow rates during the transient states of the ramp-up tests have a significant effect on the volume fraction of CO_2, highlighting the following notes:

- The CO_2 volume fraction reaches a peak during the transient state at all ramp-up tests.
- The higher the change rate, the higher the peak CO_2 volume fraction.

- The lower the change rate, the longer time to reach the peak CO_2 volume fraction.
- After the unsteady peak of the CO_2 volume fraction, the CO_2 volume fraction settled back to the steady-state level at different times for different change rates. The lower the change rate, the longer the settling time of the CO_2 volume fraction.

It can be also seen from Figure 6.45 that the different change rates in gas flow rates during the transient states of the ramp-down tests have a significant effect on the volume fraction of CO_2, highlighting the following notes:

- The CO_2 volume fraction reaches trough during the transient state at all ramp-down tests.
- The higher the change rate, the deepest trough of the CO_2 volume fraction.
- The lower the change rate, the longer time to reach a trough of CO_2 volume fraction.
- After the unsteady trough of the CO_2 volume fraction, it settled back to the steady-state level at different times for different change rates. The lower the change rate, the longer the settling time of the CO_2 volume fraction.

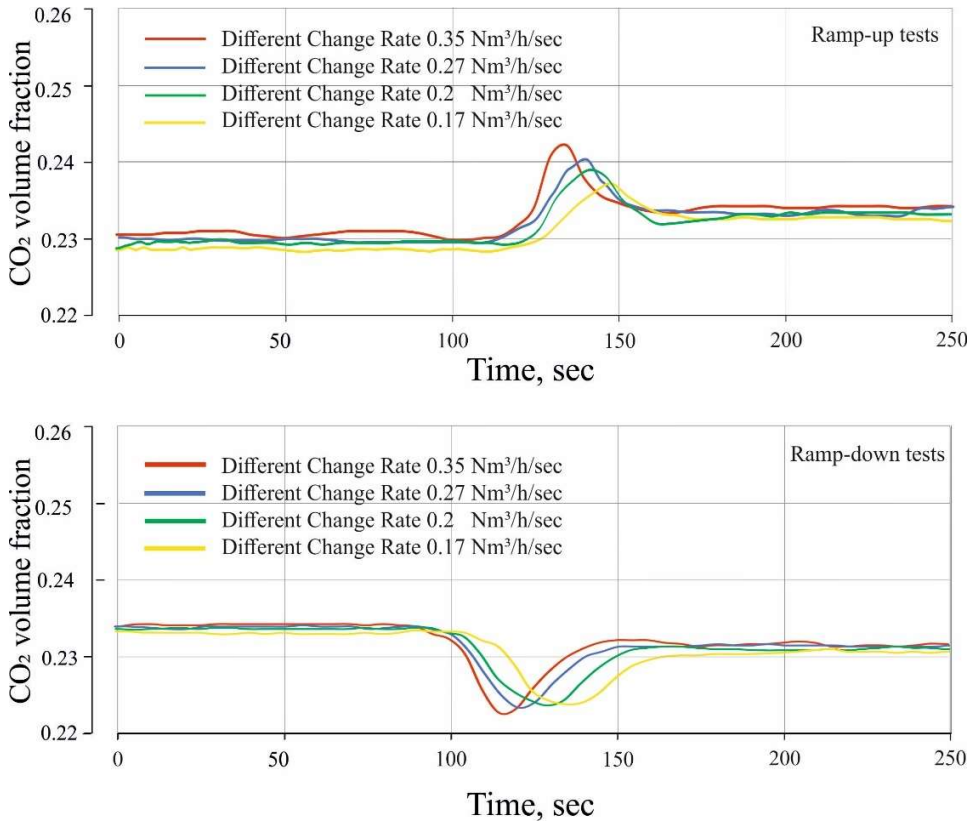

Figure 6.45 Outlet CO_2 volume fraction for different change rates in gas flow rate

6.3.3 Suggested Solutions for Improving the Performance of the Absorber

From the experimental results, it can be concluded that the performance of the solvent was not satisfactory during the transient state. The reason for this behavior is thought to be that during the ramp-up tests, the dynamic change in gas flow rates increases the liquid holdup level and liquid holdup in the upper trays faster than in the lower trays. As a result, the lower trays have low efficiency during the start-up tests which reduces absorber performance during the transient state. The following solutions are proposed to improve the absorber performance during the transient state.

6.3.3.1 Suggested Solution (1)

One of the proposed solutions to improve the performance of the sieve bottom absorber is to start ramping up the solvent flow rate before starting ramping up the gas flow rate. The period between the start of the solvent ramp-up and the gas ramp-up can be estimated based on the time it takes for the solvent to pass through the absorber. A method based on performing an excited state of the solvent temperature has been proposed to estimate the time it takes for the solvent to pass the absorber. This method is based on performing an excited state of the solvent temperature, such as increasing or decreasing the temperature of the entering solvent for a few seconds and calculating the time to reach a peak or a trough of solvent temperature caused by the excited state to the lowest tray.

Figure 6.46 shows an example of the method described above. From Figure 6.46, it can be seen how long the peak of the solvent temperature is transferred along the trays. The peak of the solvent temperature takes about 70 seconds to pass through the absorber. Figure 6.47 illustrates the proposed ramp-up of the solvent flow before ramping up the gas flow for 70 seconds. This way, it is assumed that the absorber's performance will be better than the conventional method when the gas and liquid flow rates are ramped up simultaneously.

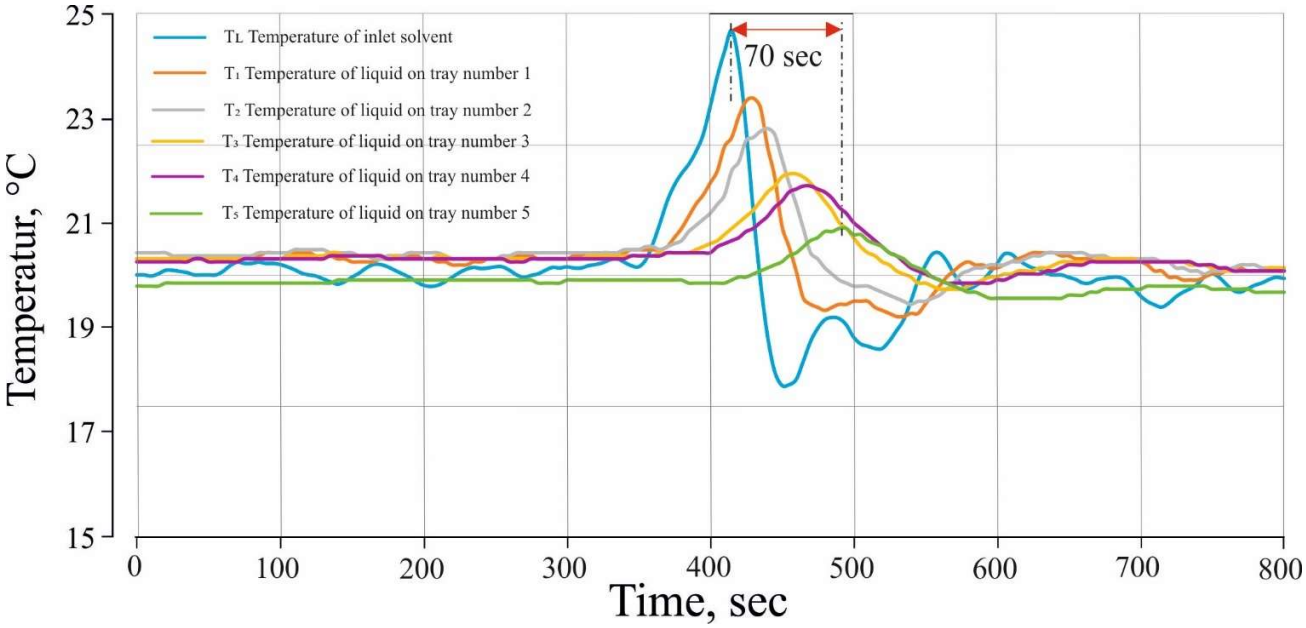

Figure 6.46 Temperatures of the input solvent and the liquid on the trays during the excited state of the temperature

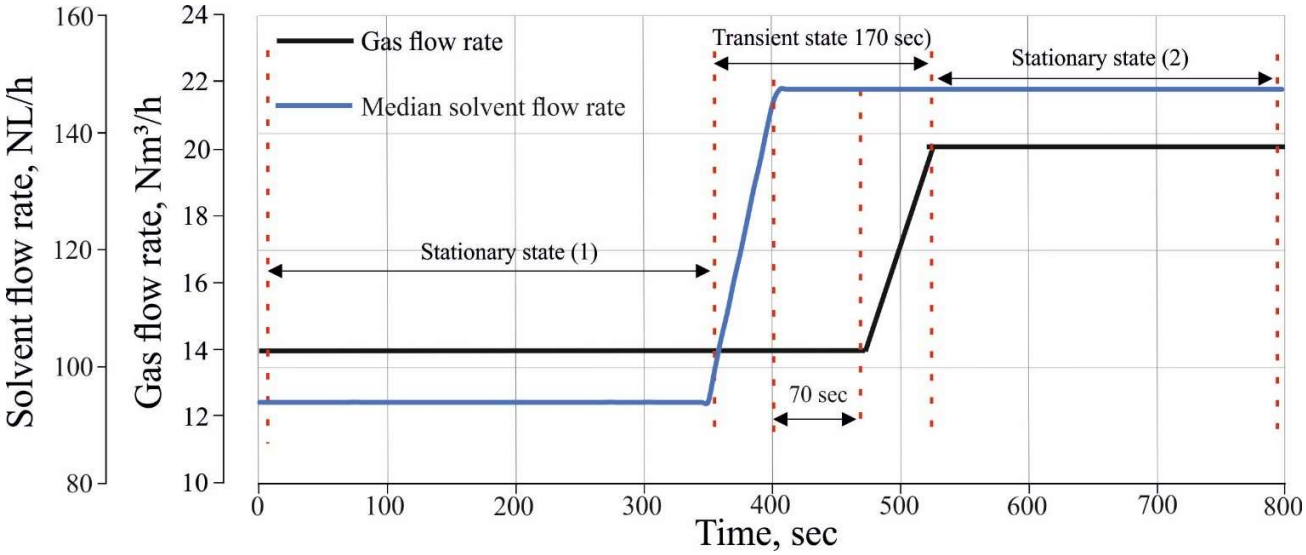

Figure 6.47 Different load changes in inlet gas and solvent flow rate in ramp-up tests

6.3.3.2 Suggested Solution (2)

It is proposed to use an absorber column consisting of trays and packing materials. The trays are located in the lower part of the absorber, while the packing materials are located in the upper part, as seen in Figure 6.48. This arrangement is expected to make the absorber perform better than the traditional absorber which consists only of trays. It is assumed that the liquid will not accumulate in the upper part of the absorber during the transient state since it is assumed that the packing material will reduce the

effects of the different load changes of the incoming gas. In this way, the liquid holdup during the transient state will be almost homogeneous along the absorber, which is expected to improve the absorber's performance.

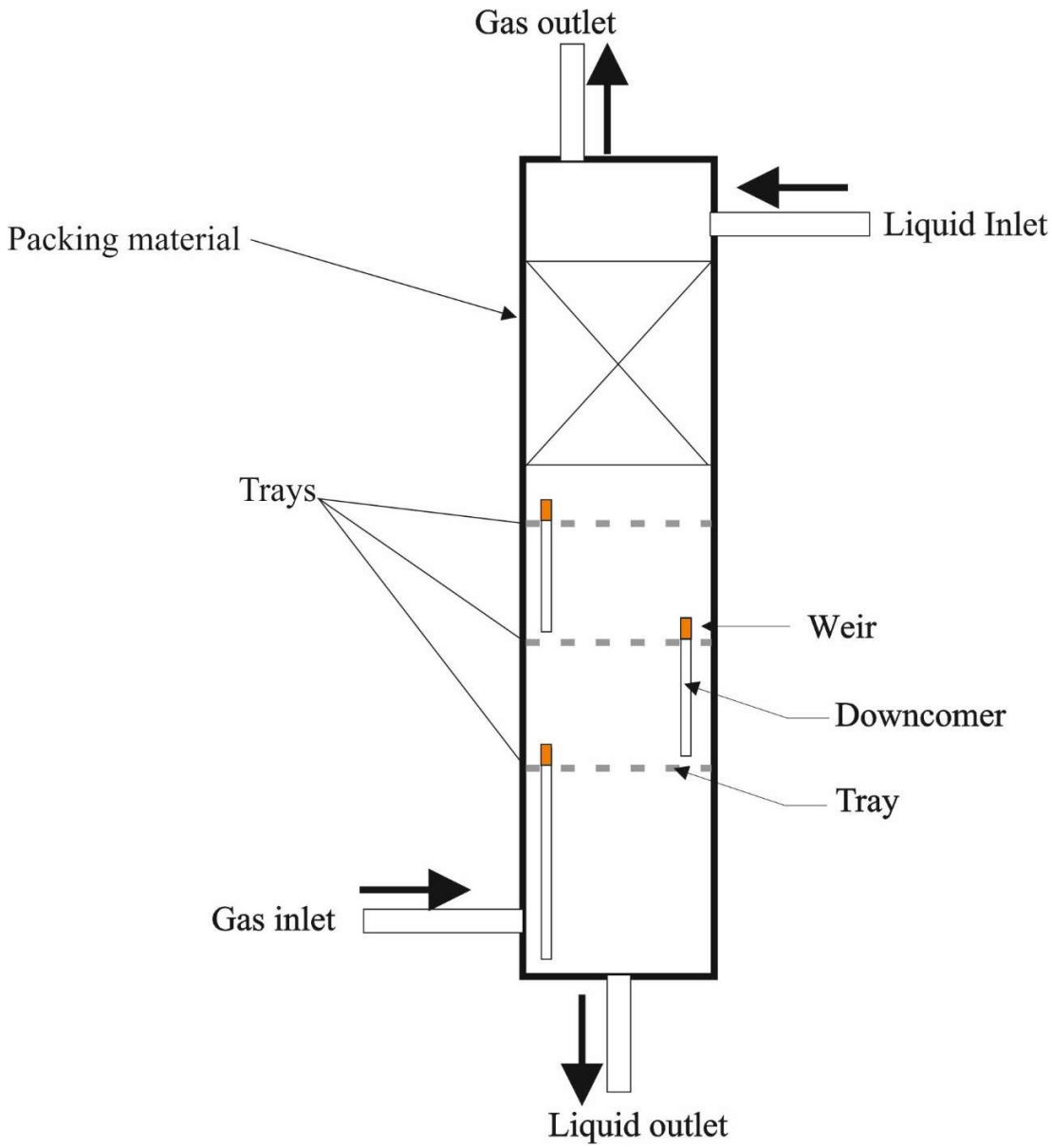

Figure 6.48 Illustration of an absorber column with packing material and trays

6.3.3.3 Suggested Solution (3)

This proposal is a tray absorber with different downcomer areas so that the downcomers in the upper trays have a larger area than the lower trays, as shown in Figure 6.49. In this way, it is expected that the liquid will not accumulate too much on the upper trays during the transient state. The performed

experimental results indicate that the trays with a small area for downcomers can slow the flow of liquid from the upper trays to the lower trays. Although the tray with a small area of liquid drain can be more efficient in the steady state of the absorber, in the dynamic state, the delay of liquid drain to the lower trays has been proved by experiments, which reduces the performance of the absorber.

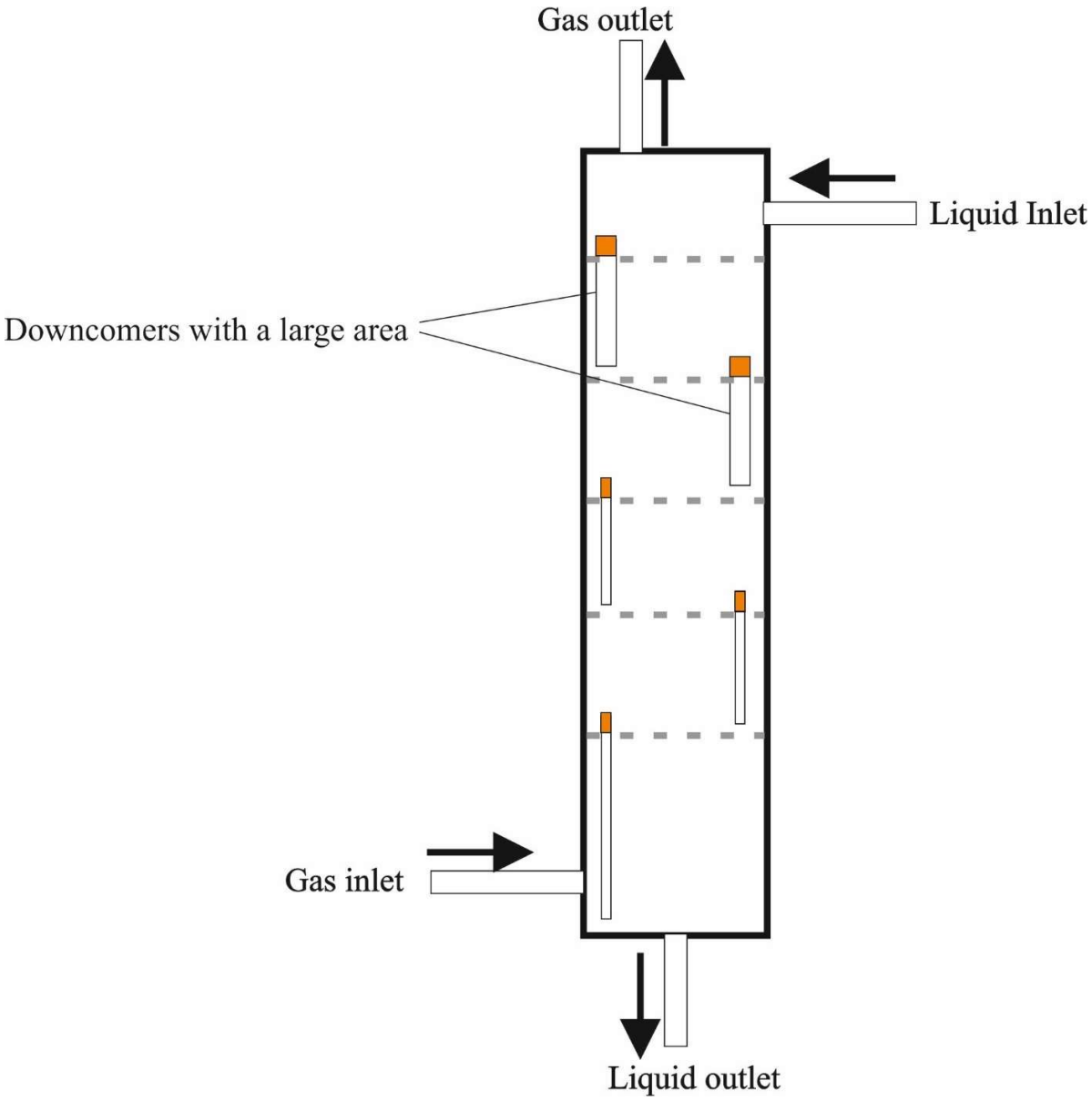

Figure 6.49 Illustration of an absorber column with different downcomers areas

Chapter 7: **Simulation Results**

In this chapter, a steady-state simulation for the absorption process is performed. The validation of the steady-state model using the experimental data is shown. Finally, the simulation of the dynamic absorption process was performed and the validation of the dynamic model is presented.

7.1Introduction

The steady state simulation is important for the design and operation of the plant under nominal conditions, while the dynamic simulation is essential for the safety analysis, risk assessment, and optimization of the systematic process, as well as for the improvement of the control strategies and control system.

Dynamic simulation models' importance for evaluating operating systems' behavior is widely recognized. Such simulation models are an effective tool for evaluating system behavior when operating systems are in a transient state, during startup, or shutdown. This makes high demands on both the quality of the models and their numerical solution in terms of accuracy and efficiency.

7.2 Steady State Simulation Model of the Absorber

To create a dynamic model, a steady-state model must first be created, which is later converted to the dynamic model. The steady-state model of the absorber is modeled by using Aspen Plus software which is a modeling tool widely recognized as an effective tool, especially for chemical process simulation. The steady-state model is built in five steps. In the first step, the chemical components were defined. The components involved in the absorption process are CO_2, N_2, H_2O, and MDEA. These components are included in the database of the aspen plus software. The second step is selecting the method to determine the physical properties. Each property method has its approach to calculating the equilibrium ratios (K values). The appropriate property method is selected to ensure the good accuracy of the simulation results. The method recommended in the Aspen Plus User's Guide for the absorption process of acid gas with MDEA solution is the electrolyte non-random two-liquid model (ENRTL). ENRTL method is applied to calculate the thermodynamic properties of the system CO_2–H_2O-MDEA. ENRTL method applies the activity coefficient model to calculate the thermodynamic properties of the liquid phases. For the calculation of the thermodynamic properties of the gas phase, the equation of state is applied. The third step is the definition of the flow diagram. The flow model is shown in Figure 7.1. It consists of the absorber column, two input streams, namely "Gas-in", and "Lean amin-in" and two output streams, namely "Gas-out" and “Rich amine-out”.

In the fourth step, the material streams are defined. The mass flow rate, composition, and conditions such as temperature and pressure should be specified as input data for each stream. This step is performed for all the inputs (Gas-in) and (lean amin-in).

Finally (step 5), the operating models of the units are defined. The absorber column and desorber are modeled by the "RadFrac" model type, which provides a suitable model for simulating all multi-stage

vapor-liquid fractionation processes. The required input data for this model are the number of trays, the stages at which the input streams enter, the output streams leave the column, and the temperature and pressure.

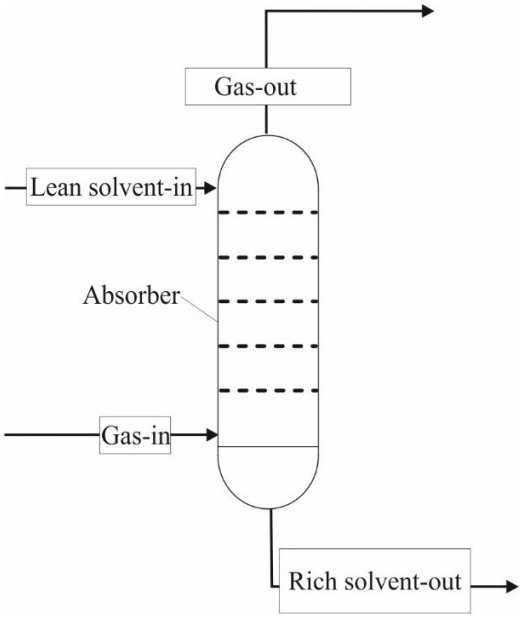

Figure 7.1 Flowsheet of the steady-state model

In addition to this basic data, there are several other optional inputs to tune the model. First, Aspen Plus offers two options for the calculation type, either equilibrium or rate-based. The rate-based approach is the more rigorous, as it accounts for heat and mass transfer rates in each phase. However, since the model will later be exported to Aspen Plus Dynamics, and Aspen Plus Dynamics does not support rate-based calculations, the equilibrium type was chosen, and the rate-based calculations were only used for comparison. Aspen Plus allows the definition of tray efficiencies (Murphree efficiencies) when using the equilibrium model. Other optional inputs include column height and diameter, geometry, type of trays, and calculation options for pressure drop and hold-up for each stage.

7.3Validation of the Steady State Simulation Model of the Absorber

Figure 7.2 shows a comparison between the results obtained from The rate-based model and the experimental data. It can be seen that there is an agreement between both results. The rate-based model was chosen for validation because it is more accurate and based on the widely accepted experimental correlation of mass and heat transfer.

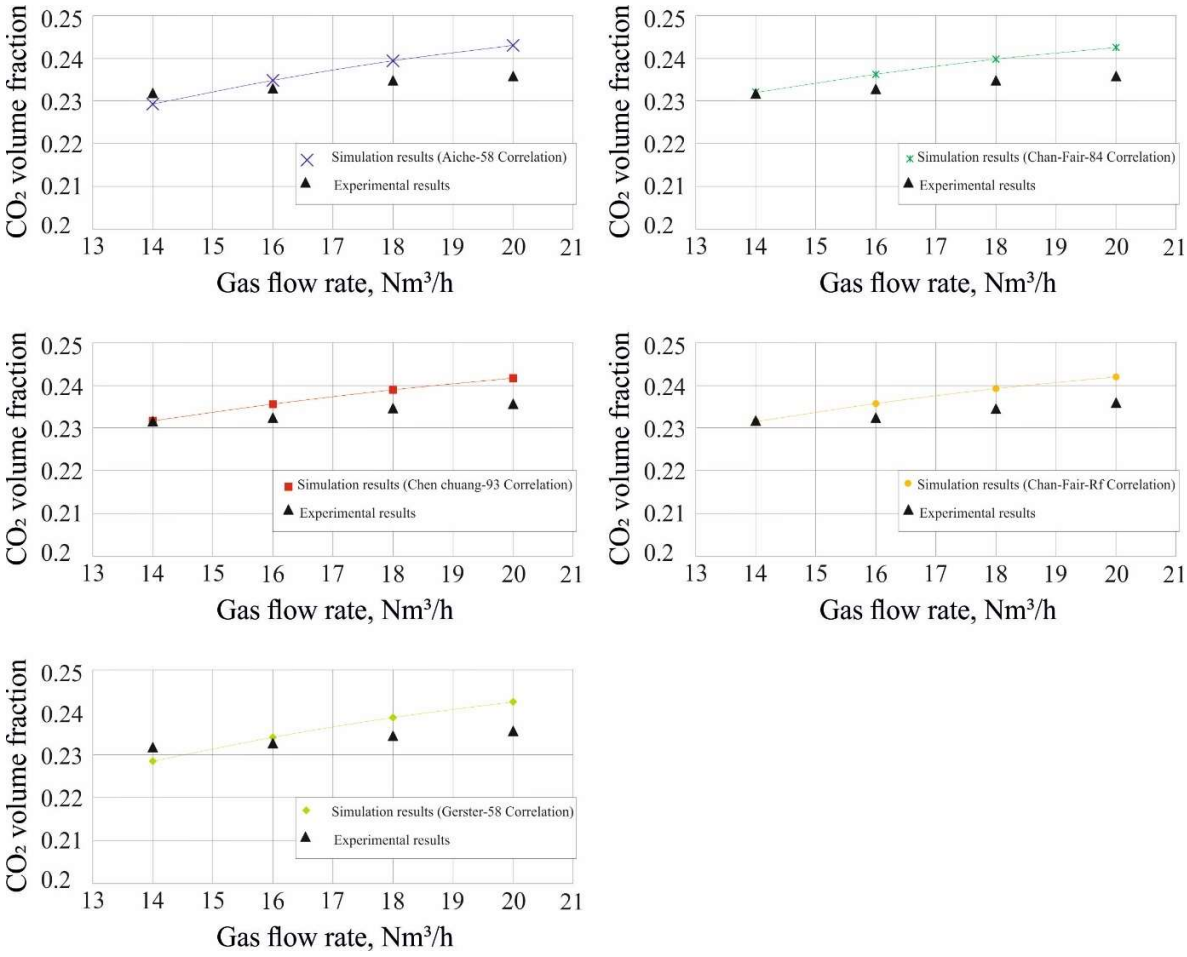

Figure 7.2 Comparison between the experimental data and simulation results

7.4 Dynamic Simulation Model of the Absorber

Because the Aspen dynamic software does not support the rate-based model, to convert the steady-state model into a dynamic model, at first an equilibrium model for the absorber should be built, then, it can be converted into Aspen dynamic model, to estimate the Murphree efficiency of the tray, the CO_2 mole fraction was plotted over the trays for both the rate-based and equilibrium models. The results are shown in Figure 7.3. It can be seen that both approaches give a similar profile at a steady state. Therefore, it is assumed that the results of an equilibrium approach can also be used for the dynamic simulation if an appropriate Murphree efficiency is applied.

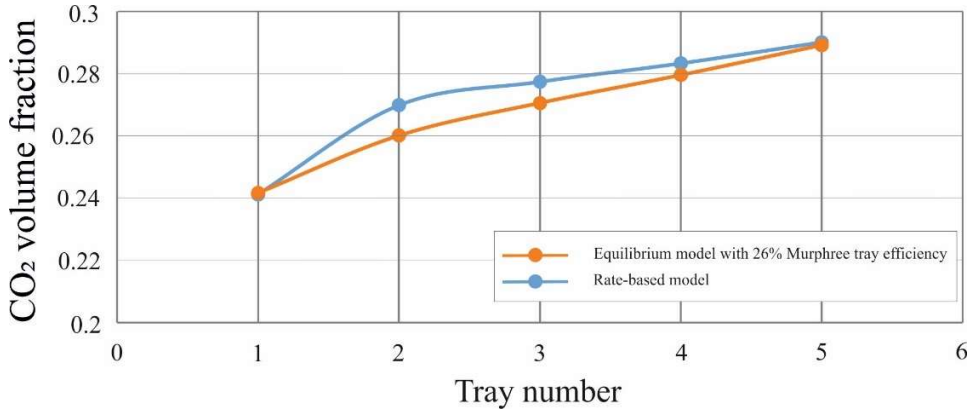

Figure 7.3 Comparison of rate-based and equilibrium approach

The steady-state model generated in ASPEN Plus was exported into Aspen PLUS Dynamics to create a dynamic model. In this way, Aspen PLUS Dynamics automatically inserts control loops into the flowsheet to control the pressure at the top of the column and the liquid levels at the sump of the absorber, as seen in Figure 7.4.

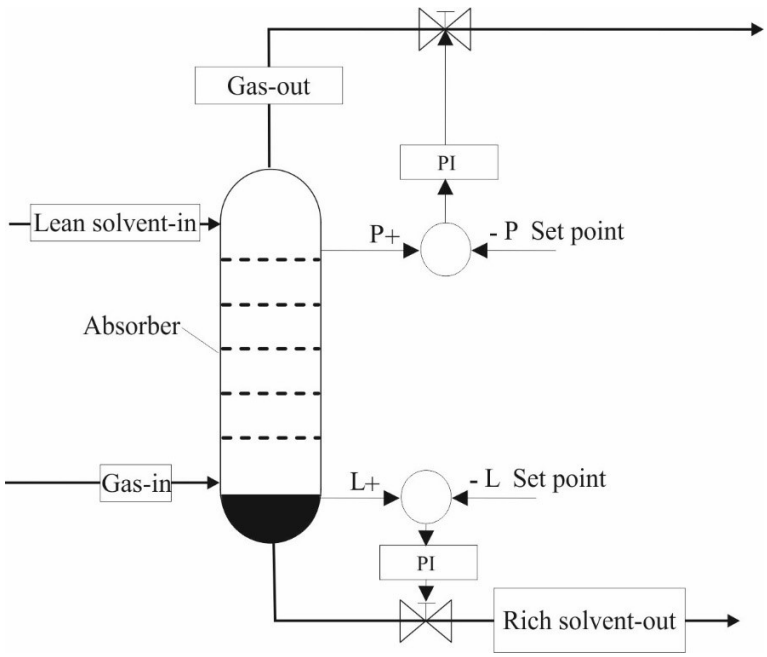

Figure 7.4 Flowsheet of the dynamic model

7.5Validation of the Dynamic Simulation Model of the Absorber

To validate the created dynamic model, a different load change in gas flow rate has been performed. Figure 7.5 shows a comparison between the experimental data and simulation results. It can be seen that there is a good agreement between both results. The CO_2 volume fraction in both results reaches a peak during the transient state. After the unsteady peak of the CO_2 volume fraction, it settled back to the steady state level.

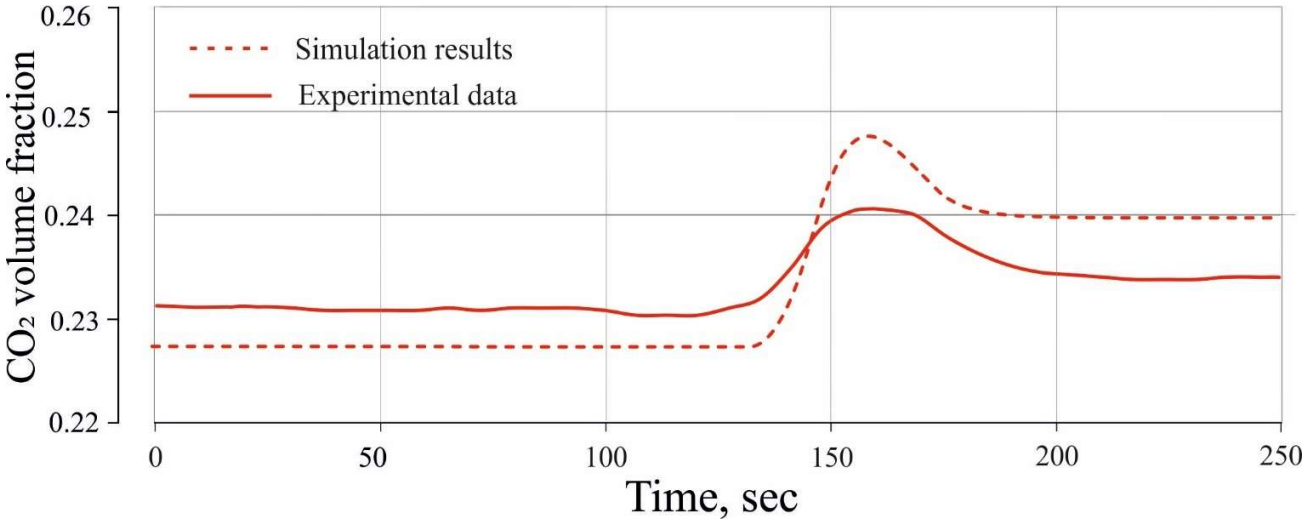

Figure 7. 5 Comparison between the experimental data and simulation results

Chapter 8: **Conclusion and Outlook**

This chapter summarizes the conclusions of the present research and provides an outlook for future research.

The concept of the polygeneration plant to produce petroleum products such as naphtha and diesel, or generate power in parallel is a promising approach for handling power fluctuating demands. The absorption process of the acid gas encounters problems resulting from the different load changes of the raw syngas.

As part of this work, a laboratory-scale absorber test rig was built at the Institute of Energy Systems and Technology (EST) at Technical University of Darmstadt. The absorber test rig was commissioned to verify it operates safely and meets the experimental requirements for which it was built. The steady-state and the dynamic state of CO_2 absorption experiments were conducted in the absorber test rig. The absorption process models are presented. A dynamic process simulation of the CO_2 absorption was performed using Aspen PLUS Dynamics software. The simulation results were validated using the obtained experimental results.

In the following, conclusions of the present study are presented, and an outlook on future research is given.

8.1 Evaluation of the Construction of the Absorber Test Rig

As part of this work, a laboratory-scale absorber test rig was built. The construction of the test rig included a variety of work that can be summarized as follows:

- Design, construction, sizing, and selection of many of parts the test rig.
- Installation of the glass absorption column on the test rig, combination of the sieve trays with rods, and installation of the sieve trays in the glass absorption column.
- Design and selection of suitable sealings for the sieve trays and their fixing to the trays.
- Construction of the packed desorber and their connections.
- Modifying the reboiler and their connections.
- Installation of most instruments on the test rig, such as temperature sensors, pressure difference transmitters, make-up pumps, and pH sensors.
- Construction and improvement of the control loops in the test rig, such as level control loops, level control loops in the reboiler, and safety control loops in the reboiler.
- Improvement of the pressure control loop in the absorber column.
- Integration of the gas analysis unit into the test stand.
- PLC programming for a large part of the test rig using the Siemens software Tia Portal.

- Integration of the gas cylinders into the absorber test rig.
- Preparation of operating instructions for the absorber test rig. In addition, the safety procedures for using Methyl diethanolamine as a solvent are presented.
- Preparation of the required equipment to convert the absorption column from a tray column to a packed column.

With the above-completed work, the building of the test rig has been completed. The test rig has been built according to experimental and safety standards. The constructed test rig is expected to contribute to experimental research on acid gas absorption. The constructed test rig device can perform most chemical sorption experiments with amine solvents.

The constructed test rig has high flexibility to be modified. There is a possibility to convert the absorber column from a tray column to a packed column. The required equipment (liquid distributor and packing support) was prepared and constructed for this purpose. The test rig has been designed and constructed so the operator can install additional equipment.

It is recommended in this work to install another pressure difference transmitter to measure the pressure drop at tray No.1, so the operator can compare the differences in pressure drop between tray No.1 and No.3.

8.2 Evaluation of Commissioning the Absorber Test Rig

As part of this work, the absorber test rig was put into operation to verify that it operates safely and meets the experimental requirements for which it was built. The absorber test rig was operated roughly for more than 200 hours, yielding the following conclusions:

- The control circuits were examined. The performance of the built-in control circuits is satisfactory. During the operation of the device, some technical problems and defects occurred, but most of these problems have been solved.
    - As for the pressure control loop in the absorber, the performance of the built-in control loop is satisfactory. A problem occurs when the flow rate of the inlet gas is higher than 24 Nm^3/h. The pressure starts to fluctuate around the pressure set point with a deviation of about 0.01 MPa. This problem can be solved by resetting the parameters of the PI controller when the input gas flow rate is higher than 24 Nm^3/h.
    - As for the level control circuit in the sump of the absorber, the performance of the built-in control loop is satisfactory. In rare cases, the gas collects in the tube connected to the high-pressure side of the pressure difference transmitter, resulting in an incorrect measurement of the pressure difference connected to the level control loop, causing the level to be improperly controlled. This problem can be solved by shutting down the absorber test rig and then draining the accumulated liquid in the tube.
    - As for the temperature control circuit in the evaporator, the performance of the built-in control circuit is satisfactory. A technical deficiency occurs when the operator must

control the temperature in the reboiler at a high temperature and high flow rate of the incoming solvent. The capacity of heating coil is not capable of heating the solvent to a high temperature of over 80°C at a high inlet flow rate. For this reason, it is recommended that the current 4.5 kW heating coil be replaced with a higher capacity heating coil suitable for the required operating conditions in the test rig.

- Regarding the level control circuit of the solvent in the reboiler, the performance of the built-in control loop is satisfactory. Nevertheless, a problem has arisen. when the solvent in the reboiler is replaced with another solvent, it may be necessary to adjust the electrical resistance measuring range for the solvent, to make the level sensor sensitive to the level of solvent in the reboiler.
- As for the mass flow controller of inlet CO_2 gas, there was a technical problem with the mass flow controller for the CO_2 gas. The minimum gas flow rate of CO_2 that can be controlled with the mass flow controller is 3 Nm^3/h. The problem occurs when the operator wants to input gas vapor with a CO_2 flow rate of less than 3 Nm^3/h, so the current mass flow controller is unsuitable. It is recommended to replace the current mass flow controller with another one that can control CO_2 flow of less than 3 Nm^3/h.

- Based on this work, the absorber works without problems in the range of 10-35 Nm^3/h gas flow rate and when water is used as a solvent. When the aqueous MDEA solution is used as a solvent, the absorber works without problems in the range of 10-22 Nm^3/h gas flow rate. At higher gas flow rates, a flooding problem occurs caused by foaming. It is recommended to mix Antifoam with the amine solvent solution to avoid foaming. Also, it has been noted that the performance of the pump decreases when using an amine solution as a solvent. The reason may be the accumulation of gas in front of the section valve of the pump. It is recommended to solve this problem in the future.
- By assessing the safety performance criteria of the test rig, the absorber test stand works with no safety problems, provided the safety regulations and the operation instruction are observed. Based on this work, it is recommended that before operating the absorber, the pressure reducer regulators on the gas streams upstream of the gas mixing unit should be set to a value not exceeding 0.5 MPa. For safety reasons and to avoid a chock at the absorber test rig, it is recommended that, during the startup of the test rig, the gas be entered at a low rate of change, not exceeding 0.7 Nm^3/h /s. Based on this work, it is interesting to perform the H_2S absorption process. It is recommended to follow the safety rules regarding the permissible H_2S content in the hall where the test rig is located.

8.3 Evaluation of the Performance of the Absorber Sieve Tray Column during the Transient State

As part of this work, the experiments of different load changes and different change rates in gas flow and solvent flow rate were conducted, concluded the following point:

- The different load changes and the different change rates of the gas and solvent have a significant effect on the CO_2 concentration at the outlet of the absorber. The correlation between the behavior of the absorber during the transient state and the hydrodynamic properties of the absorber trays was investigated. It was found that the tray's hydrodynamic properties significantly influence the absorber's performance during the transient condition.
- The performance of the tray absorber during the transient state of the different load changes at ramp-up tests is not satisfactory. It was found that the tray absorber shows a delayed response to absorb the excess CO_2 which is entered into the absorber during the transient state of the ramp-up tests. The CO_2 volume fractions peak in all tests even though the solvent flow rate is increased during the transient state. The main reason for this behavior is that, during the transient state, the liquid level in the upper trays increases faster than in the lower trays. Since the lower trays contain less liquid during the transient state as a result the lower trays have lower efficiency which reduces the overall performance of the absorber column.
- There is a significant relationship between the hydrodynamic properties of a sieve tray and the absorber's performance in the transient state. Improving the hydrodynamic properties of a sieve tray, such as tray liquid holdup and tray liquid holdup level, is key to improving the performance of the absorber during the transient state.
- One of the proposed solutions to improve the performance of the sieve tray absorber is to start the ramp-up of the solvent flow rate before starting the ramp-up of the gas flow rate. The period between starting the ramp-up of the solvent and the ramp-up of gas can be estimated based on the time the solvent needs to pass through the absorber. To estimate the period of passing the solvent through the absorber, a method based on performing an excited state of the solvent temperature was proposed.

Based on this work, it is interesting to investigate the following topics for further research:

- Conducting CO_2 absorption experiments using trays with different downcomer areas. The trays with a large downcomer area are located in the upper part of the absorber, while the trays with a small downcomer area are located in the lower part of the absorber column.
- Conducting CO_2 absorption experiments using trays with different geometries, such as variation weir height. Literature indicates that the geometry of the tray, such as the height of the weir, plays an important role in determining the hydrodynamic properties of the tray.
- Conducting CO_2 absorption using various amine solutions.
- Conducting a CO_2 absorption experiment using a packed absorber.
- Conducting a CO_2 absorption experiment using an absorber with trays and packing material. The packing materials are located in the upper part of the absorber, while the trays are located in the lower part of the absorber.
- Conducting experiments with acid gases (CO_2 and H_2S) in the constructed experimental unit.

8.4 Dynamic Absorption Process Simulation

As part of this work, two steady-state models, the rate-based stage and the equilibrium stage, have been applied to simulate the tray absorber column using Aspen PLUS simulation software. The steady-state models have been validated against the experimental data. The equilibrium model is converted to the dynamic model using Aspen PLUS Dynamics. There was a good agreement between the dynamic simulation results and the experiment date. Based on this work, it is interesting to develop the Aspen simulation model, which is expected to help improve the behavior of the tray absorber during the transient state.

The results of this study are important for the development of operating strategies that ensure safe, stable, and optimal dynamic operation.

References

[1] Q. Zhong, Q. Mao, J. Xiao, A. van Duin, and J. P. Mathews, "Sulfur removal from petroleum coke during high-temperature pyrolysis. Analysis from TG-MS data and ReaxFF simulations," *J. Anal. Appl. Pyrolysis*, vol. 132, pp. 134–142, 2018.

[2] E. Ortega, "An Overview of Hydrotreating," *Chem. Eng. Prog.*, vol. 117, no. 10, pp. 29–33, 2021.

[3] J. Wang, E. J. Anthony, and J. C. Abanades, "Clean and efficient use of petroleum coke for combustion and power generation," *Fuel*, vol. 83, no. 10, pp. 1341–1348, 2004.

[4] I. J. Okeke and T. A. Adams II, "Life cycle assessment of petroleum coke gasification to Fischer-Tropsch diesel," in *Computer Aided Chemical Engineering*, vol. 46, Elsevier, 2019, pp. 1495–1500.

[5] J.-H. Shin, L.-S. Lee, and S.-H. Lee, "Economic Assessment of a Indirect Liquefaction Process Using a Gasification with Petroleum Coke/coal Mixtures," *Korean Chem. Eng. Res.*, vol. 54, no. 4, pp. 501–509, 2016.

[6] P. Costa, F. Pinto, R. N. André, and P. Marques, "Integration of Gasification and Solid Oxide Fuel Cells (SOFCs) for Combined Heat and Power (CHP). Processes 2021, 9, 254." s Note: MDPI stays neutral with regard to jurisdictional claims in published …, 2021.

[7] P. J. Reddy, *Clean coal technologies for power generation*. CRC press, 2013.

[8] L. Gao, H. Jin, Z. Liu, and D. Zheng, "Exergy analysis of coal-based polygeneration system for power and chemical production," *Energy*, vol. 29, no. 12–15, pp. 2359–2371, 2004.

[9] H. Li, H. Hong, H. Jin, and R. Cai, "Analysis of a feasible polygeneration system for power and methanol production taking natural gas and biomass as materials," *Appl. Energy*, vol. 87, no. 9, pp. 2846–2853, 2010.

[10] L. Gao, H. Li, B. Chen, H. Jin, R. Lin, and H. Hong, "Proposal of a natural gas-based polygeneration system for power and methanol production," *Energy*, vol. 33, no. 2, pp. 206–212, 2008.

[11] S. Ziaii, G. T. Rochelle, and T. F. Edgar, "Dynamic modeling to minimize energy use for CO2 capture in power plants by aqueous monoethanolamine," *Ind. Eng. Chem. Res.*, vol. 48, no. 13, pp. 6105–6111, 2009.

[12] N. Harun, T. Nittaya, P. L. Douglas, E. Croiset, and L. A. Ricardez-Sandoval, "Dynamic simulation of MEA absorption process for CO2 capture from power plants," *Int. J. Greenh. Gas Control*, vol. 10, pp. 295–309, 2012.

[13] A. Lawal, M. Wang, P. Stephenson, and H. Yeung, "Dynamic modelling of CO2 absorption for post combustion capture in coal-fired power plants," *Fuel*, vol. 88, no. 12, pp. 2455–2462, 2009.

[14] J. Gáspár and A.-M. Cormoş, "Dynamic modeling and validation of absorber and desorber columns for post-combustion CO2 capture," *Comput. Chem. Eng.*, vol. 35, no. 10, pp. 2044–2052, 2011.

[15] J. Gaspar and A.-M. Cormos, "Dynamic modeling and absorption capacity assessment of CO2 capture process," *Int. J. Greenh. Gas Control*, vol. 8, pp. 45–55, 2012.

[16] R. Wei *et al.*, "Environmental issues related to bioenergy," 2020.

[17] T. R. K. C. Doddapaneni and T. Kikas, "Thermochemical and biochemical treatment strategies for resource recovery from agri-food industry wastes," in *Valorization of Agri-Food Wastes and By-Products*, Elsevier, 2021, pp. 787–807.

[18] J. Dai, J. Saayman, J. R. Grace, and N. Ellis, "Gasification of woody biomass," *Annu. Rev. Chem. Biomol. Eng.*, vol. 6, pp. 77–99, 2015.

[19] S. Mishra and R. K. Upadhyay, "Review on biomass gasification: gasifiers, gasifying mediums, and operational parameters," *Mater. Sci. Energy Technol.*, vol. 4, pp. 329–340, 2021.

[20] J. Phillips, "Different types of gasifiers and their integration with gas turbines," *gas turbine Handb.*, vol. 1, 2006.

[21] C. He, X. Feng, and K. H. Chu, "Process modeling and thermodynamic analysis of Lurgi fixed-bed coal gasifier in an SNG plant," *Appl. Energy*, vol. 111, pp. 742–757, 2013.

[22] C. Higman, V. Der Burgt, and M. Gasification, "Gulf Professional Publishing." Oxford, UK, 2008.

[23] M. Soltani, "A comparative study of passive and active sampling methods for measuring indoor particulate matter," 2011.

[24] H. Kamiya, K. Deguchi, J. Gotou, and M. Horio, "Increasing phenomena of pressure drop during dust removal using a rigid ceramic filter at high temperatures," *Powder Technol.*, vol. 118, no. 1–2, pp. 160–165, 2001.

[25] A. Y. Al-Otoom, Y. Ninomiya, B. Moghtaderi, and T. F. Wall, "Coal ash buildup on ceramic filters in a hot gas filtration system," *Energy & fuels*, vol. 17, no. 2, pp. 316–320, 2003.

[26] P. Pastila, V. Helanti, A.-P. Nikkilä, and T. Mäntylä, "Environmental effects on microstructure and strength of SiC-based hot gas filters," *J. Eur. Ceram. Soc.*, vol. 21, no. 9, pp. 1261–1268, 2001.

[27] S. Anis and Z. A. Zainal, "Tar reduction in biomass producer gas via mechanical, catalytic and thermal methods: A review," *Renew. Sustain. energy Rev.*, vol. 15, no. 5, pp. 2355–2377, 2011.

[28] M. Bohnet, O. Gottschalk, and M. Morweiser, "Modern design of aerocyclones," *Adv. Powder Technol.*, vol. 8, no. 2, pp. 137–161, 1997.

[29] X. Shen and D. C. Ihenacho, "Design of Gas Cyclone Using Hybrid Particle Swarm Optimization Algorithm," *Appl. Sci.*, vol. 11, no. 20, p. 9772, 2021.

[30] N. L. De Freitas, J. A. S. Gonçalves, M. D. M. Innocentini, and J. R. Coury, "Development of a double-layered ceramic filter for aerosol filtration at high-temperatures: The filter collection efficiency," *J. Hazard. Mater.*, vol. 136, no. 3, pp. 747–756, 2006.

[31] M. A. Alvin, "Advanced ceramic materials for use in high-temperature particulate removal systems," *Ind. Eng. Chem. Res.*, vol. 35, no. 10, pp. 3384–3398, 1996.

[32] S. Heidenreich, "Hot gas filtration–A review," *Fuel*, vol. 104, pp. 83–94, 2013.

[33] H. Aust, "Air filtration and power generation: Flue gas desulphurisation," *Filtr. Sep.*, vol. 44, no. 10, pp. 36–37, 2007.

[34] C. Chang, Y. Chen, L. Sheng, and S. Hsiau, "A New Approach of Dedusting for IGCC by a Two-Stage Moving Granular Bed Filter," *Energies*, vol. 14, no. 9, p. 2534, 2021.

[35] S. V. B. Van Paasen and J. Kiel, "Tar formation in fluidised-bed gasification-impact of gasifier operating conditions," *Acknowledgement/Preface*, vol. 14, p. 26, 2004.

[36] T. A. Milne, R. J. Evans, and N. Abatzaglou, "Biomass gasifier''Tars'': their nature, formation, and conversion," 1998.

[37] L. Devi, K. J. Ptasinski, F. J. J. G. Janssen, S. V. B. van Paasen, P. C. A. Bergman, and J. H. A. Kiel, "Catalytic decomposition of biomass tars: use of dolomite and untreated olivine," *Renew. energy*, vol. 30,

no. 4, pp. 565–587, 2005.

[38] H. Boerrigter, S. Van Paasen, P. Bergman, J. W. Könemann, R. Emmen, and A. Wijnands, "OLGA tar removal technology. Proof-of-Concept (PoC) for application in integrated biomass gasification combined heat and power (CHP) systems," 2005.

[39] C. Unger and M. Ising, "Mechanismen und Bedeutung der Teerbildung und Teerbeseitigung bei der termochemischen Umwandlung fester Kohlenstoffträger," *DGMK-Tagungsbericht*, vol. 2, pp. 131–142, 2002.

[40] C. Li and K. Suzuki, "Tar property, analysis, reforming mechanism and model for biomass gasification—An overview," *Renew. Sustain. Energy Rev.*, vol. 13, no. 3, pp. 594–604, 2009.

[41] J. Neeft, H. A. M. Knoef, and P. Onaji, "Behaviour of tar in biomass gasification systems. Tar related problems and their solutions," 1999.

[42] M. Kübel, *Teerbildung und Teerkonversion bei der Biomassevergasung–Anwendung der nasschemischen Teerbestimmung nach CEN-Standard*. Cuvillier Verlag, 2007.

[43] U. Wolfesberger, I. Aigner, and H. Hofbauer, "Tar content and composition in producer gas of fluidized bed gasification of wood—influence of temperature and pressure," *Environ. Prog. Sustain. Energy An Off. Publ. Am. Inst. Chem. Eng.*, vol. 28, no. 3, pp. 372–379, 2009.

[44] L. Devi, K. J. Ptasinski, and F. J. J. G. Janssen, "A review of the primary measures for tar elimination in biomass gasification processes," *Biomass and bioenergy*, vol. 24, no. 2, pp. 125–140, 2003.

[45] S. Nakamura, S. Kitano, and K. Yoshikawa, "Biomass gasification process with the tar removal technologies utilizing bio-oil scrubber and char bed," *Appl. Energy*, vol. 170, pp. 186–192, 2016.

[46] J. Dyment and S. Watanasiri, "Acid gas cleaning using DEPG physical solvents: validation with experimental and plant data," *Aspen Technol. Inc. Bedford, MA, USA*, 2015.

[47] M. Pilling and B. S. Holden, "Choosing trays and packings for distillation," *Am. Inst. Chem. Eng. CEP*, vol. 105, pp. 44–50, 2009.

[48] S. Mudhasakul, H. Ku, and P. L. Douglas, "A simulation model of a CO2 absorption process with methyldiethanolamine solvent and piperazine as an activator," *Int. J. Greenh. Gas Control*, vol. 15, pp. 134–141, 2013.

[49] T. Phuphuakrat, T. Namioka, and K. Yoshikawa, "Absorptive removal of biomass tar using water and oily materials," *Bioresour. Technol.*, vol. 102, no. 2, pp. 543–549, 2011.

[50] P. C. A. Bergman, S. V. B. Van Paasen, and H. Boerrigter, "The novel'OLGA'technology for complete tar removal from biomass producer gas," 2002.

[51] A. Paethanom, S. Nakahara, M. Kobayashi, P. Prawisudha, and K. Yoshikawa, "Performance of tar removal by absorption and adsorption for biomass gasification," *Fuel Process. Technol.*, vol. 104, pp. 144–154, 2012.

[52] P. R. Bhoi, "Wet scrubbing of biomass producer gas tars using vegetable oil." Oklahoma State University, 2014.

[53] B. Ozturk and D. Yilmaz, "Absorptive removal of volatile organic compounds from flue gas streams," *Process Saf. Environ. Prot.*, vol. 84, no. 5, pp. 391–398, 2006.

[54] H. Idriss, M. Scott, and V. Subramani, "Introduction to hydrogen and its properties," in *Compendium of Hydrogen Energy*, Elsevier, 2015, pp. 3–19.

[55] J. G. Speight, *Heavy oil recovery and upgrading*. Gulf Professional Publishing, 2019.

[56] C. A. Callaghan, *Kinetics and catalysis of the water-gas-shift reaction: A microkinetic and graph theoretic approach*. Worcester Polytechnic Institute, 2006.

[57] R. Jain and R. Maric, "Synthesis of nano-Pt onto ceria support as catalyst for water–gas shift reaction by Reactive Spray Deposition Technology," *Appl. Catal. A Gen.*, vol. 475, pp. 461–468, 2014.

[58] D. S. Newsome, "The water-gas shift reaction," *Catal. Rev. Sci. Eng.*, vol. 21, no. 2, pp. 275–318, 1980.

[59] B. S. RJ, M. Loganathan, and M. S. Shantha, "A review of the water gas shift reaction kinetics," *Int. J. Chem. React. Eng.*, vol. 8, no. 1, 2010.

[60] Y. Lei, "Novel Fe2O3-Cr2O3 Catalyst for high temperature water gas shift reaction." UNSW Sydney, 2005.

[61] L. N. Baloyi, "The production of hydrogen from the Water Gas Shift Reaction through the use of a Palladium-Silver membrane reactor." Cape Peninsula University of Technology, 2016.

[62] M. M. Maroto-Valer, *Developments and innovation in carbon dioxide (CO2) capture and storage technology: carbon dioxide (CO2) storage and utilisation*. Elsevier, 2010.

[63] Y. Demirel and V. Gerbaud, "Fundamentals of equilibrium thermodynamics," *Non-equilibrium Thermodyn. 2nd Ed. Elsevier Sci. BV*, pp. 1–52, 2007.

[64] E. Smolková-Keulemansová and L. B. T.-C. A. C. Feltl, Eds., "Chapter 10 - Gas chromatography," in *Analysis of Substances in the Gaseous Phase*, vol. 28, Elsevier, 1991, pp. 223–462.

[65] J. E. Proctor and H. E. Maynard-Casely, "Miscibility in the Liquid and Supercritical Fluid States," in *The Liquid and Supercritical Fluid States of Matter*, CRC Press, 2020, pp. 153–168.

[66] C.-C. Cormos, "IGCC with carbon capture and storage," 2017.

[67] V. V Goud and A. K. Golder, "Chemical Engineering Design-II," 2014.

[68] K. Arnold and M. Stewart, *Surface production operations, Volume 2:: Design of gas-handling systems and facilities*, vol. 2. Elsevier, 1999.

[69] K. T. Chuang and K. Nandakumar, "Tray columns: design," *Encycl. Sep. Sci.*, pp. 1135–1140, 2000.

[70] M. J. Al Mehairbi, S. A. Al Mahri, and Z. E. Dadach, "Simulation of Stripper Flooding Due to the Increase of Feed Flowrate," *World J. Eng. Technol.*, vol. 8, no. 3, pp. 443–455, 2020.

[71] Y. Diao and H. Yang, "Chapter 5 - Gas-cleaning technology," H. D. Goodfellow and Y. B. T.-I. V. D. G. (Second E. Wang, Eds. Academic Press, 2021, pp. 279–371.

[72] B. G. Miller, "Clean coal technologies for advanced power generation," *Clean Coal Eng. Technol.*, vol. 7, pp. 251–300, 2011.

[73] A. Benamor, M. Nasser, and M. J. Al-Marri, "Gas Processing Technology-Treatment and Utilization," Elsevier, 2017.

[74] A. L. Kohl and R. Nielsen, *Gas purification*. Elsevier, 1997.

[75] C.-H. Yu, C.-H. Huang, and C.-S. Tan, "A review of CO2 capture by absorption and adsorption," *Aerosol Air Qual. Res.*, vol. 12, no. 5, pp. 745–769, 2012.

[76] T. L. Donaldson and Y. N. Nguyen, "Carbon dioxide reaction kinetics and transport in aqueous amine membranes," *Ind. Eng. Chem. Fundam.*, vol. 19, no. 3, pp. 260–266, 1980.

[77] P. F. Schubert, C. A. Bayens, L. Weick, and M. O. Haid, “Expanding markets for GTL fuels and specialty products,” in *Studies in Surface Science and Catalysis*, vol. 136, Elsevier, 2001, pp. 459–464.

[78] M. Gupta and J. J. Spivey, “Chapter 5-Catalytic Processes for the Production of Clean Fuels,” *New Futur. Dev. Catal. Suib, SL, Ed. Elsevier Amsterdam*, pp. 87–126, 2013.

[79] A. de Klerk and E. Furimsky, “Catalysis in the refining of Fischer–Tropsch syncrude,” *Platin. Met. Rev*, vol. 55, no. 4, pp. 263–267, 2011.

[80] D. Leckel, “Diesel production from Fischer– Tropsch: the past, the present, and new concepts,” *Energy & Fuels*, vol. 23, no. 5, pp. 2342–2358, 2009.

[81] J. G. Speight, “4 - Distillation,” J. G. B. T.-T. R. of the F. (Second E. Speight, Ed. Gulf Professional Publishing, 2020, pp. 125–159.

[82] H. Z. Kister, “Distillation design. McGraw-Hill.,” *Boston, USA*, 1992.

[83] W. L. McCabe and E. W. Thiele, “Graphical design of fractionating columns,” *Ind. Eng. Chem.*, vol. 17, no. 6, pp. 605–611, 1925.

[84] P. C. Wankat and P. C. Wankat, *Separation Process Engineering:" Formerly Published as Equilibrium Staged Separations.”*. Prentice Hall, 2007.

[85] D. W. Green and M. Z. Southard, *Perry’s chemical engineers’ handbook*. McGraw-Hill Education, 2019.

[86] Z. Švandová, J. Markoš, and L. Jelemenský, *Impact of mass transfer on modelling and simulation of reactive distillation columns*. IntechOpen, 2011.

[87] A. A. Ujile and J. T. Iminabo, “Evaluating Sieve Tray Flooding in A Distillation Column Using Kister and Haas; and Fair’s Correlations,” *Chem. Process Eng. Res. 2225-0913*, vol. 25, pp. 16–23, 2014.

[88] H. E. Eduljee, “Design of sieve type distillation plates,” *Brit. Chem. Eng*, vol. 3, no. 1, pp. 14–17, 1958.

[89] M. Errico, “Optimal retrofit and process design of distillation plants for energy saving and process intensification,” 2008.

[90] K. Ramesh, N. Aziz, S. R. Abd Shukor, and M. Ramasamy, “Dynamic rate-based and equilibrium model approaches for continuous tray distillation column,” *J. Appl. Sci. Res.*, vol. 3, no. 12, pp. 2030–2041, 2007.

[91] J. D. Seader, E. J. Henley, and D. K. Roper, “Separation Process Principles: Chemical and Biochemical Operations . Hoboken, NJ: Jon Wiley & Sons.” Inc, 2011.

[92] Q. Sun, C. Pan, and X. Yan, “Simulation and analysis of dehydration distillation column based on distillation mechanism integrated with neural network,” *Korean J. Chem. Eng.*, vol. 30, no. 3, pp. 518–527, 2013.

[93] W. K. Lewis and W. G. Whitman, “Principles of gas absorption.,” *Ind. Eng. Chem.*, vol. 16, no. 12, pp. 1215–1220, 1924.

[94] W. G. Whitman, “The two film theory of gas absorption,” *Int. J. Heat Mass Transf.*, vol. 5, no. 5, pp. 429–433, 1962.

[95] P. M. Doran, “Chapter 10 - Mass Transfer,” P. M. B. T.-B. E. P. (Second E. Doran, Ed. London: Academic Press, 2013, pp. 379–444.

[96] T. H. Ngo, “Gas absorption into emulsions.” 2013.

[97] M. Afkhamipour and M. Mofarahi, “Comparison of rate-based and equilibrium-stage models of a packed

column for post-combustion CO2 capture using 2-amino-2-methyl-1-propanol (AMP) solution," *Int. J. Greenh. Gas Control*, vol. 15, pp. 186–199, 2013.

[98] R. Taylor and R. Krishna, *Multicomponent mass transfer*, vol. 2. John Wiley & Sons, 1993.

[99] A. I. of Chemical Engineers (AIChE), *Bubble-tray Design Manual*. A.I.Ch.E., 1958.

[100] J. A. Gerster, A. B. Hill, N. N. Hochgraf, and D. G. Robinson, "Tray Efficiencies In Distillation Columns American Institute of Chemical Engineers (AIChE)," *Final Rep. from Univ. Delaware. New York*, vol. 118, 1958.

[101] H. Chan and J. R. Fair, "Prediction of point efficiencies on sieve trays. 1. Binary systems," *Ind. Eng. Chem. Process Des. Dev.*, vol. 23, no. 4, pp. 814–819, 1984.

[102] G. X. Chen and K. T. Chuang, "Prediction of point efficiency for sieve trays in distillation," *Ind. Eng. Chem. Res.*, vol. 32, no. 4, pp. 701–708, 1993.

[103] L. L. Simon, Y. Elias, G. Puxty, Y. Artanto, and K. Hungerbuhler, "Rate based modeling and validation of a carbon-dioxide pilot plant absorbtion column operating on monoethanolamine," *Chem. Eng. Res. Des.*, vol. 89, no. 9, pp. 1684–1692, 2011.

[104] D. L. Bennett, R. Agrawal, and P. J. Cook, "New pressure drop correlation for sieve tray distillation columns," *AIChE J.*, vol. 29, no. 3, pp. 434–442, 1983.

[105] F. J. Zuiderweg, "Sieve trays: a view on the state of the art," *Chem. Eng. Sci.*, vol. 37, no. 10, pp. 1441–1464, 1982.

[106] J. Stichlmair, "Dimensionierung des Gas/Flüssigkeit-Kontaktapparates Bodenkolonne, Teil I," *Chemie Ing. Tech.*, vol. 50, no. 4, pp. 281–284, 1978.

[107] S. Gebreyohannes, K. Yerramsetty, B. J. Neely, and K. A. M. Gasem, "Improved QSPR generalized interaction parameters for the nonrandom two-liquid activity coefficient model," *Fluid Phase Equilib.*, vol. 339, pp. 20–30, 2013.

[108] S. Gebreyohannes, B. J. Neely, and K. A. M. Gasem, "Generalized nonrandom two-liquid (NRTL) interaction model parameters for predicting liquid–liquid equilibrium behavior," *Ind. Eng. Chem. Res.*, vol. 53, no. 31, pp. 12445–12454, 2014.

[109] H. Renon and J. M. Prausnitz, "Local compositions in thermodynamic excess functions for liquid mixtures," *AIChE J.*, vol. 14, no. 1, pp. 135–144, 1968.

[110] E. Baralić, E. dd Sarajevo, and H. Bašić, "CALCULATION OF MEASUREMENT UNCERTAINTY IN PROVING PROCESS OF CORIOLIS FLOW-METER."

[111] J. M. Berg and T. Dallas, "Peristaltic Pumps. Encyclopedia of Microfluidics and Nanofluidics, Chap. 2." Springer, 2014.

[110] NASIR HUSSAIN 2021, Types of Trays in Distillation Columns, OIL REFINING GENERAL TOPICS https://thepetrosolutions.com/types-of-trays-in-distillation-columns/ visited on 18.08.2022

[111] https://chemistrypage.in/tertiary-amine/ visited on 18.08.2022

[112] agora-energiewende

Appendix

8.1 Pressure reducer

Figure 8.1 shows a pressure reducer regulator used in the absorber test rig. The working principle of the pressure reducer is illustrated in Figure 8.2. The working principle of a pressure reducer is based on the manual adjustment of the spring to a specific pressure value. When the gas enters the second chamber from the first chamber, the diaphragm in the second chamber shifts upward to reach a state of equilibrium with the preset value of the associated spring force. The diaphragm is connected to a valve via an axis. The valve simultaneously shifts up or down due to the displacement of the diaphragm. The valve displacement causes an adjustment of the amount of gas entering the chamber (2). When the pressure reaches a value greater than the set pressure, the diaphragm and the valve move upwards, causing the closure of the opening between the first and second chambers. This way, the maximum pressure that can be applied to the absorber test stand can be set.

Figure 8. 1 Pressure reducing regulator

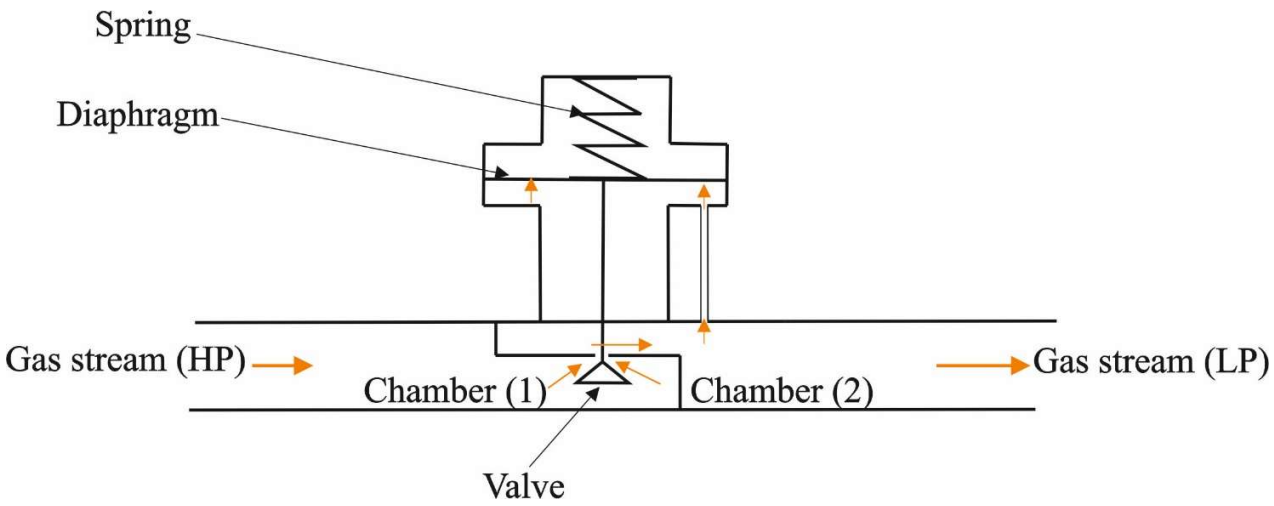

Figure 8. 2 Illustration of the working principle of pressure reducer regulator

8.2 PH sensor

Figure 8.3 shows the PH sensor used in the absorber test rig. The working principle of the PH sensor depends on the measurement of the potential difference between the measuring system and the reference system. The measuring system is a buffer filled with KCL solution. A silver-silver chloride wire is inserted into the buffer solution as an electrical conductor. The reference system is filled with KCL solution and has a silver-silver chloride wire as the electrical conductor. When the PH sensor is immersed in the solution, the hydrogen ions in the aqueous solution penetrate and accumulate on the outside of the glass membrane of the measurement system. At the same time, the hydrogen ions in the buffer solution of the measuring system penetrate and accumulate on the inside of the glass membrane. If the hydrogen ion concentration on the outside is higher than the hydrogen ion concentration, the solution is acidic; if the hydrogen ion concentration on the outside is lower than the hydrogen ion concentration, the solution is basic.

Figure 8. 3 PH sensor

8.3 Temperature sensor

Figure 8.4 shows a temperature sensor used in the absorber test rig. The working principle of the temperature is illustrated in Figure 8.5. The Temperature sensor consists of two wires of two different

types connected to a potentiometer, and connected at the other end. When exposed to a heat source, the heat conduction will be different in both wires because they are of two different metals and each metal has its conduction factor. The distribution of the electron gradient will be different in both wires, so there will be a difference in voltage between the two ends of the wire. This difference is proportional to the temperature measured in this way. The scale gives a potential difference that is then converted into a temperature.

Figure 8. 4 Temperature sensor

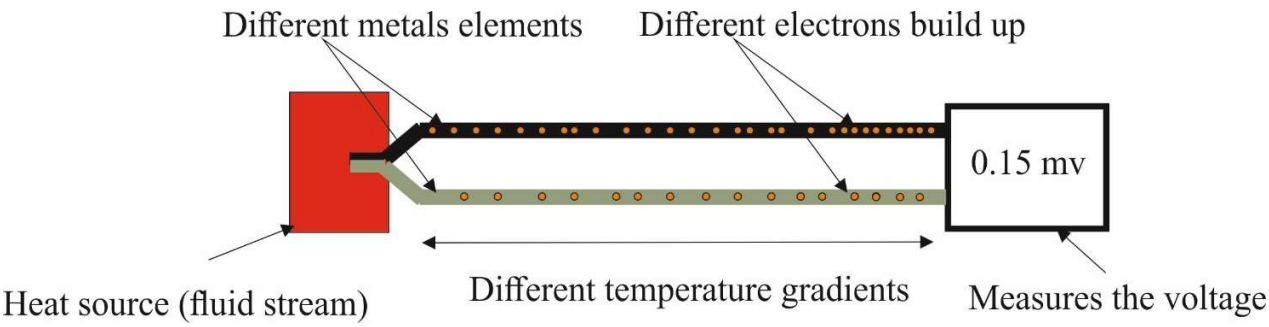

Figure 8. 5 Illustration of the working principle of a temperature sensor

8.4 Pressure sensor

Figure 8.6 shows a pressure sensor used in the absorber test rig. The working principle of the pressure sensor is illustrated in Figure 8.7. The working principle of the pressure sensor is based on the piezoelectric effect. Here, a material generates an electrical charge when twisted, bent, or subjected to a force. The electrical charge is proportional to the force. The electric charge can be measured and tuned to pressure values.

Figure 8. 6 Pressure sensor

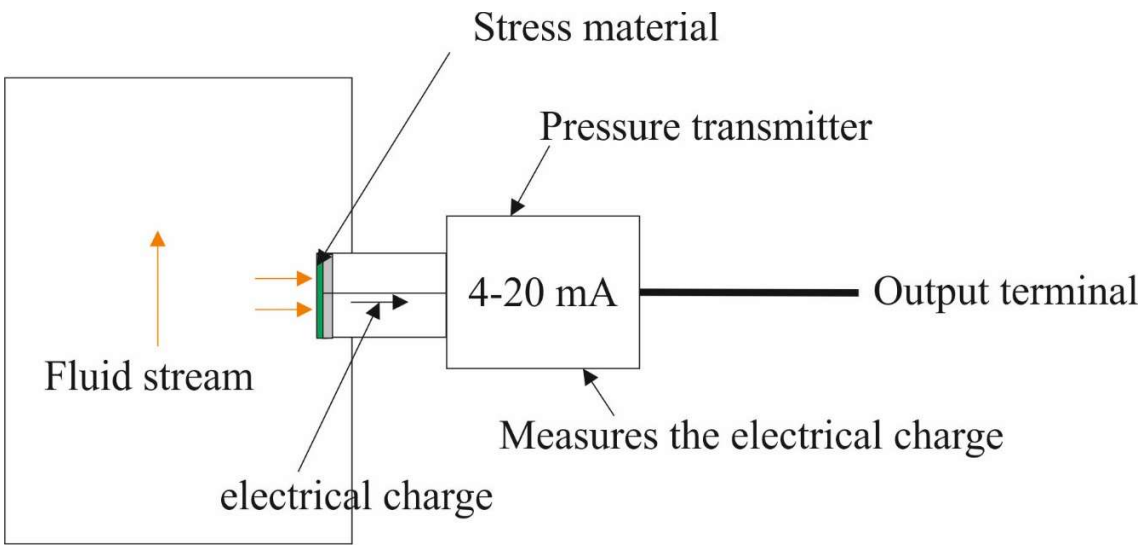

Figure 8. 7 Illustration of the working principle of Pressure sensor

8.5 Pressure differential transmitter

Figure 8.8 shows a pressure differential transmitter used in the absorber test rig. The working principle of the pressure differential transmitter is illustrated in Figure 8.9. The working principle of a pressure differential transmitter is based on the displacement of a movable plate, which is subjected to pressure from both sides. On one side is subjected to low pressure, and on the other side to high pressure. The

displacement of the moving plate depends on the pressure difference between the two sides. An electric charge is generated, which is proportional to the amount of displacement of the moving plate associated with the pressure difference. The electric charge is measured and converted into a pressure difference.

Figure 8. 8 Pressure differential transmitter

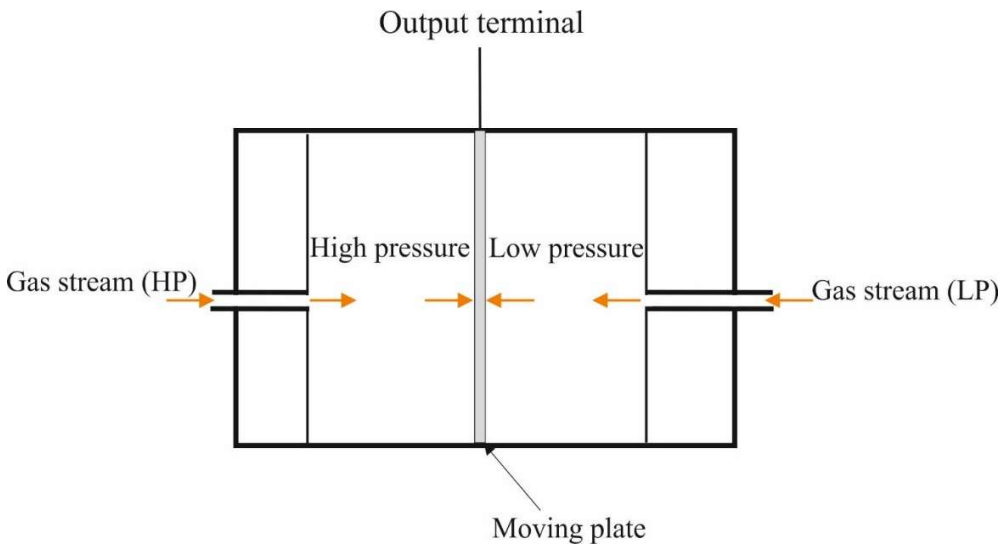

Figure 8. 9 Illustration of the working principle of a pressure differential transmitter

8.6 Mass flow controller

Figure 8.10 shows a mass flow controller used in the absorber test rig. The working principle of the mass flow controller is illustrated in Figure 8.11. The gas enters the mass flow controller and branches in a bypass. At this bypass, two temperature sensors measure the temperature difference at two different points at a distance of x. The temperature sensors send the temperature difference as an electrical signal

to the central processing unit (CPU). The CPU converts the measured temperature difference into a flow rate, compares the measured flow rate with the set flow rate, and sends an electrical signal to the flow control valve to open or close to adjust the flow rate to the set value.

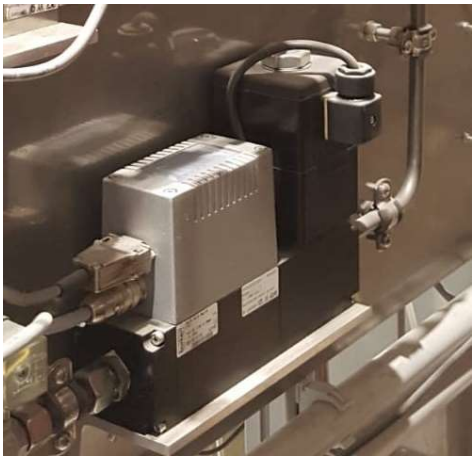

Figure 8. 10 Mass flow controller

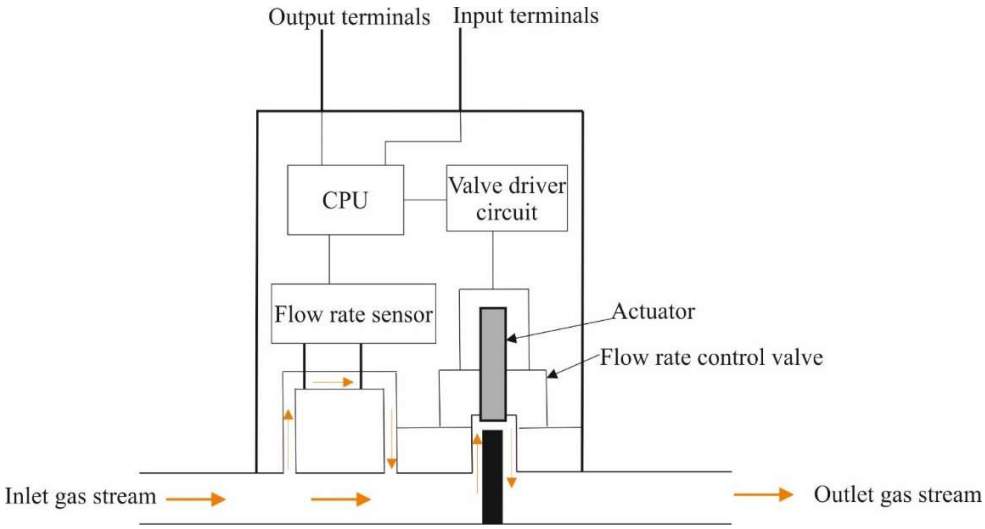

Figure 8. 11 Illustration of the working principle of the mass flow controller

8.7 Coriolis flow device

Figure 8.12 shows the Coriolis flow device used in the absorber test rig. The working principle of the Coriolis flow device is illustrated in Figure 8.13. The working principle of Coriolis flow device is based on the Coriolis force. The measurement flow pipe in Coriolis device is always oscillating. Electrodynamic sensors along the measuring tube measure the oscillation as a function of time and distance. When no fluid flows through the device, the oscillation along the measuring flow pipe is homogeneous. In contrast, when a fluid flows through the device, the oscillation is different as a function of time and distance. The measurement of oscillation can be converted to flow values.

Figure 8. 12 Coriolis flow device

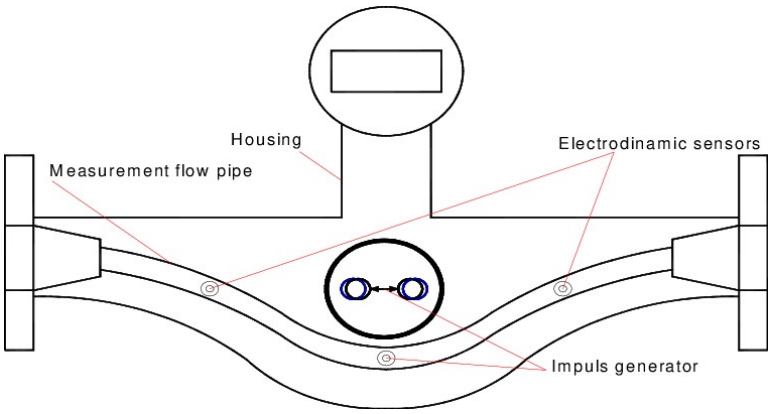

Figure 8. 13 Illustration of Coriolis flowmeter [110]

8.8 Pneumatic Control Valve

Figure 8.14 shows the pneumatic control valve used in the absorber test rig. The working principle of the pneumatic control valve is illustrated in Figure 8.15. The PLC sends an electrical signal between 4-20 mv to the Electro-pneumatic positioner in the pneumatic control valve. Electro-pneumatic positioner converts this electrical signal proportionally to a pneumatic signal. This signal goes to the pneumatic actuator. The actuator shifts up or down by helping the air supply, leading to shift up or down of the connected valve up or down depending on the received signal.

Figure 8. 14 Pneumatic Control Valve

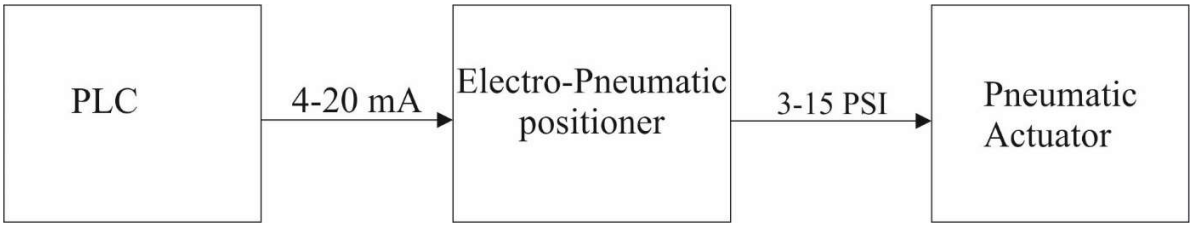

Figure 8. 15 Illustration of the operating principle of a pneumatic control valve

8.9 Peristaltic pump (makeup pump)

Figure 8.16 shows peristaltic pumps used as make up pumps for MDEA and water in the absorber test rig. The working principle of the peristaltic pump is illustrated in Figure 8.17. The working principle of peristaltic pumps is based on the circular movement of a roller on a flexible tube. The rollers compress on the flexible tube, by the circular movement of the rollers which takes this movement from the rotor, the rollers displace the fluid inside the flexible tube to the discharge of the pump.

Figure 8. 16 Peristaltic pump

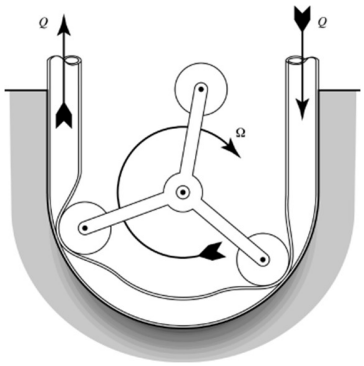

Figure 8. 17 Illustration of the working principle of the peristaltic pump [111]

8.10 Input and output variables of the CPU

PLC tags

	Name	Tag table	Data type	Address	Retain	Acces...	Visibl...	Comment
1	MV_N2	Ein-/ Ausgänge	Bool	%Q10.7		☑	☑	Magnetventil Stickstoff
2	Not_Aus	Ein-/ Ausgänge	Bool	%I10.1		☑	☑	
3	FALSE	Merker	Bool	%M200.0		☑	☑	
4	TRUE	Merker	Bool	%M200.1		☑	☑	
5	Thermo1	Ein-/ Ausgänge	Int	%IW108		☑	☑	Thermoelement 1 (oben im Absorber)
6	M_Thermo1_IST	Merker	Real	%MD0		☑	☑	
7	Thermo2	Ein-/ Ausgänge	Int	%IW110		☑	☑	
8	Thermo3	Ein-/ Ausgänge	Int	%IW112		☑	☑	
9	Thermo4	Ein-/ Ausgänge	Int	%IW114		☑	☑	
10	Thermo5	Ein-/ Ausgänge	Int	%IW116		☑	☑	Thermoelement 5 (unten im Absorber)
11	Thermo6	Ein-/ Ausgänge	Int	%IW118		☑	☑	unten im Reboiler
12	Thermo7	Ein-/ Ausgänge	Int	%IW120		☑	☑	oben im Reboiler
13	Thermo8	Ein-/ Ausgänge	Int	%IW122		☑	☑	vor Coriolismessung
14	M_Thermo2_IST	Merker	Real	%MD4		☑	☑	
15	M_Thermo3_IST	Merker	Real	%MD8		☑	☑	
16	M_Thermo4_IST	Merker	Real	%MD12		☑	☑	
17	M_Thermo5_IST	Merker	Real	%MD16		☑	☑	
18	M_Thermo6_IST	Merker	Real	%MD20		☑	☑	
19	M_Thermo7_IST	Merker	Real	%MD24		☑	☑	
20	M_Thermo8_IST	Merker	Real	%MD28		☑	☑	
21	MV_H2S	Ein-/ Ausgänge	Bool	%Q11.1		☑	☑	
22	MV_CO2	Ein-/ Ausgänge	Bool	%Q11.0		☑	☑	
23	Drucktransm	Ein-/ Ausgänge	Int	%IW102		☑	☑	Drucktransmitter (oben im Absorber)
24	M_Drucktransm_IST	Merker	Real	%MD32		☑	☑	
25	Diffdruck23	Ein-/ Ausgänge	Int	%IW106		☑	☑	Differenzdruckmessung Böden
26	M_MV_N2	Merker	Bool	%M200.3		☑	☑	
27	M_MV_H2S	Merker	Bool	%M200.4		☑	☑	
28	M_MV_CO2	Merker	Bool	%M200.5		☑	☑	
29	M_Diffdruck23_IST	Merker	Real	%MD36		☑	☑	
30	Diffdruck45	Ein-/ Ausgänge	Int	%IW104		☑	☑	
31	M_Diffdruck45_IST	Merker	Real	%MD40		☑	☑	
32	Gemü_Gas_Soll_Ausgang	Ein-/ Ausgänge	Int	%QW108		☑	☑	AO-Sollwert
33	Gemü_Gas_IST_Eingang	Ein-/ Ausgänge	Int	%IW126		☑	☑	
34	MFC_N2_Soll_Ausgang	Ein-/ Ausgänge	Int	%QW110		☑	☑	
35	M_MFC_N2_SOLL	Ein-/ Ausgänge	Real	%MD44		☑	☑	
36	MFC_N2_IST_Eingang	Ein-/ Ausgänge	Int	%IW128		☑	☑	
37	M_MFC_N2_IST	Ein-/ Ausgänge	Real	%MD48		☑	☑	
38	Gemü_Füllstand_IST_Eingang	Ein-/ Ausgänge	Int	%IW124		☑	☑	
39	Gemü_Füllstand_Soll_Ausgang	Ein-/ Ausgänge	Int	%QW106		☑	☑	
40	Temp_Coriolis	Ein-/ Ausgänge	Real	%ID281		☑	☑	
41	M_Gemü_Gas_IST	Merker	Real	%MD52		☑	☑	
42	M_Gemü_Gas_Soll	Merker	Real	%MD56		☑	☑	
43	M_Gemü_Füllstand_IST	Merker	Real	%MD60		☑	☑	
44	M_Gemü_Füllstand_Soll	Merker	Real	%MD64		☑	☑	
45	M_Temp_Coriolis	Merker	Real	%MD68		☑	☑	
46	AI_1	Ein-/ Ausgänge	Real	%ID256		☑	☑	
47	M_AI_1	Merker	Real	%MD72		☑	☑	
48	AI_2	Ein-/ Ausgänge	Real	%ID261		☑	☑	

PLC tags

	Name	Tag table	Data type	Address	Retain	Acces...	Visibl...
49	AI_3	Ein-/ Ausgänge	Real	%ID266		✓	✓
50	AI_5	Ein-/ Ausgänge	Real	%ID276		✓	✓
51	TOTAL_1	Ein-/ Ausgänge	Real	%ID286		✓	✓
52	TOTAL_2	Ein-/ Ausgänge	Real	%ID291		✓	✓
53	TOTAL_3	Ein-/ Ausgänge	Real	%ID296		✓	✓
54	M_AI_2	Merker	Real	%MD76		✓	✓
55	M_AI_3	Merker	Real	%MD80		✓	✓
56	M_AI_5	Merker	Real	%MD88		✓	✓
57	M_TOTAL_1	Merker	Real	%MD92		✓	✓
58	M_TOTAL_2	Merker	Real	%MD96		✓	✓
59	M_TOTAL_3	Merker	Real	%MD102		✓	✓
60	M_Dichte_kg_m3	Merker	Real	%MD106		✓	✓
61	M_Druck_Sollwert	Merker	Real	%MD110		✓	✓
62	Pumpe_Einschalten_Ausgang	Ein-/ Ausgänge	Bool	%Q10.1		✓	✓
63	Pumpe_Stoerung Pumpe_Eing...	Ein-/ Ausgänge	Bool	%I10.0		✓	✓
64	Pumpe_Verstellung_Auto_Man...	Ein-/ Ausgänge	Bool	%Q10.4		✓	✓
65	Pumpe_Verstellung_Man_Plus_...	Ein-/ Ausgänge	Bool	%Q10.5		✓	✓
66	Pumpe_Verstellung_Man_Minu...	Ein-/ Ausgänge	Bool	%Q10.6		✓	✓
67	Pumpe_Dosiereinheit_Stoerung	Ein-/ Ausgänge	Bool	%I10.2		✓	✓
68	Pumpe_Istwert_Eingang	Ein-/ Ausgänge	Int	%IW100		✓	✓
69	Pumpe_Sollwert_Ausgang	Ein-/ Ausgänge	Int	%QW100		✓	✓
70	M_Pumpe_Einschalten	Merker	Bool	%M200.6		✓	✓
71	M_Pumpe_Minus	Merker	Bool	%M200.7		✓	✓
72	M_Pumpe_Plus	Merker	Bool	%M201.0		✓	✓
73	M_Pumpe_Istwert	Merker	Real	%MD114		✓	✓
74	M_Pumpe_Sollwert	Merker	Real	%MD118		✓	✓
75	M_Pumpe_Auto_Man	Merker	Bool	%M201.5		✓	✓
76	M_Stoerung_Pumpe	Merker	Bool	%M201.6		✓	✓
77	M_Stoerung_Dosiereinheit	Merker	Bool	%M201.7		✓	✓
78	Dominik	Merker	Int	%MW122		✓	✓
79	Heizung_Einschalten_Ausgang	Ein-/ Ausgänge	Bool	%Q10.0		✓	✓
80	M_Heizung_Einschalten	Merker	Bool	%M202.0		✓	✓
81	M_Pumpe_Soll_Fördermenge	Merker	Real	%MD126		✓	✓
82	Heizung_Heizstatus	Ein-/ Ausgänge	Bool	%I11.1		✓	✓
83	M_Heizung_Heizstatus	Merker	Bool	%M202.2		✓	✓
84	M_Heizung_Solltemperatur	Merker	Real	%MD130		✓	✓
85	M_Achtung_Temperautrdiffere...	Merker	Real	%MD138		✓	✓
86	M_Achtung_Temperaturdiffere...	Merker	Real	%MD142		✓	✓
87	M_MFC_CO2_SOLL	Merker	Real	%MD146		✓	✓
88	M_MFC_CO2_IST	Merker	Real	%MD150		✓	✓
89	MFC_CO2_IST_Eingang	Ein-/ Ausgänge	Int	%IW130		✓	✓
90	MFC_CO2_Soll_Ausgang	Ein-/ Ausgänge	Int	%QW112		✓	✓
91	Dosierpumpe_MDEA	Ein-/ Ausgänge	Bool	%Q10.2		✓	✓
92	Dosierpumpe_MDEA_Sollwert	Ein-/ Ausgänge	Int	%QW102		✓	✓
93	Dosierpumpe_Wasser	Ein-/ Ausgänge	Bool	%Q10.3		✓	✓
94	Dosierpumpe_Wasser_Sollwert	Ein-/ Ausgänge	Int	%QW104		✓	✓
95	M_Dosierpumpe_MDEA	Ein-/ Ausgänge	Bool	%M202.3		✓	✓
96	M_Dosierpumpe_Wasser	Ein-/ Ausgänge	Bool	%M202.4		✓	✓

PLC tags

	Name	Tag table	Data type	Address	Retain	Acces...	Visibl...	Comment
97	M_Dosierpumpe_MDEA_Sollwert	Ein-/ Ausgänge	Real	%MD210		☑	☑	
98	M_Dosierpumpe_Wasser_Sollw..	Ein-/ Ausgänge	Real	%MD220		☑	☑	
99	Pumpe Ein von Füllstandsüber...	Ein-/ Ausgänge	Bool	%I11.2		☑	☑	
100	M_Pumpe Ein von Füllstandsüb..	Ein-/ Ausgänge	Bool	%M204.0		☑	☑	
101	Messwert1_Analyse1	Ein-/ Ausgänge	Int	%IW134		☑	☑	
102	Messwert2_Analyse1	Ein-/ Ausgänge	Int	%IW136		☑	☑	
103	Messwert1_Analyse2	Ein-/ Ausgänge	Int	%IW138		☑	☑	
104	Messwert2_Analyse2	Ein-/ Ausgänge	Int	%IW140		☑	☑	
105	M_Messwert1_Analyse1	Ein-/ Ausgänge	Real	%MD168		☑	☑	
106	M_Messwert2_Analyse1	Ein-/ Ausgänge	Real	%MD172		☑	☑	
107	M_Messwert1_Analyse2	Ein-/ Ausgänge	Real	%MD176		☑	☑	
108	M_Messwert2_Analyse2	Ein-/ Ausgänge	Real	%MD180		☑	☑	
109	Thermo9	Ein-/ Ausgänge	Int	%IW142		☑	☑	Mitte im Desorber
110	Thermo10	Ein-/ Ausgänge	Int	%IW144		☑	☑	Unten im Desorber
111	M_Thermo9_IST	Ein-/ Ausgänge	Real	%MD158		☑	☑	
112	M_Thermo10_IST	Ein-/ Ausgänge	Real	%MD164		☑	☑	
113	M_Desorber_Differenzdruck_IST	Ein-/ Ausgänge	Real	%MD240		☑	☑	
114	Desorber_Differenzdruck	Ein-/ Ausgänge	Int	%IW146		☑	☑	
115	M_Thermo11_IST	Ein-/ Ausgänge	Real	%MD184		☑	☑	
116	Thermo11	Ein-/ Ausgänge	Int	%IW148		☑	☑	
117	Heizung aus von Füllstandsübe..	Ein-/ Ausgänge	Bool	%I11.3		☑	☑	
118	PH Sensor	Ein-/ Ausgänge	Int	%IW150		☑	☑	
119	M_PhSensor_IST	Merker	Real	%MD154		☑	☑	
120	Rampe aktive	Merker	Bool	%M202.7		☑	☑	
121	SP_out	Ein-/ Ausgänge	Real	%ID210		☑	☑	
122	d_SP	Merker	Real	%MD244		☑	☑	
123	SP_End	Merker	Real	%MD252		☑	☑	
124	Time_in	Ein-/ Ausgänge	Time	%MD248		☑	☑	
125	Time_out	Ein-/ Ausgänge	Time	%MD188		☑	☑	
126	Rampe-out	Ein-/ Ausgänge	Bool	%M203.1		☑	☑	
127	Timer_in	Ein-/ Ausgänge	Time	%ID215		☑	☑	
128	Timer_out	Ein-/ Ausgänge	Time	%ID220		☑	☑	
129	Total Inlet flow gas to absorber	Ein-/ Ausgänge	Real	%ID225		☑	☑	
130	Inlet _CO2 Concentration	Ein-/ Ausgänge	Real	%ID230		☑	☑	
131	Inlet N2 Concentration	Ein-/ Ausgänge	Real	%ID235		☑	☑	
132	Dosierpumpe_Wasser_On/Off	Ein-/ Ausgänge	Real	%ID240		☑	☑	
133	Dosierpumpe_MEDA_On/Off	Ein-/ Ausgänge	Real	%ID245		☑	☑	
134	Rampeup_hilfe	Ein-/ Ausgänge	Real	%ID250		☑	☑	
135	Rampeup_hilfe_out	Ein-/ Ausgänge	Real	%ID255		☑	☑	
136	Wet_pressuer drop,mbar	Ein-/ Ausgänge	Real	%ID260		☑	☑	
137	Wet_pressuer drop,cm	Ein-/ Ausgänge	Real	%ID265		☑	☑	
138	Houldup_lquid,Liter	Ein-/ Ausgänge	Real	%ID270		☑	☑	
139	pressuer drop_bottom,cm	Ein-/ Ausgänge	Real	%ID275		☑	☑	
140	d_SP2	Ein-/ Ausgänge	Real	%ID280		☑	☑	
141	Rampedown_hilfe	Ein-/ Ausgänge	Real	%ID285		☑	☑	
142	Rampedown_hilfe_out	Ein-/ Ausgänge	Real	%ID290		☑	☑	
143	<Add new>					☑	☑	

8.11 Function block of the temperature measurement

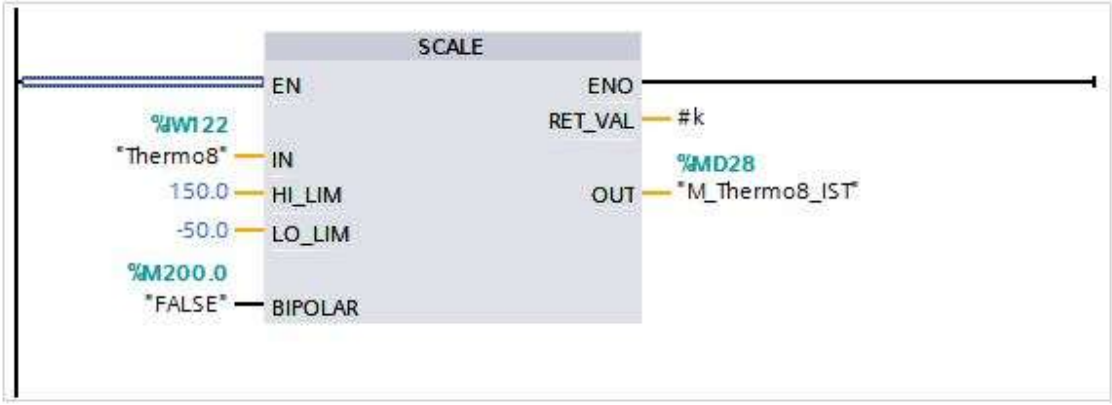

8.12 Function block of CO_2 mole fraction measurement by gas analysis

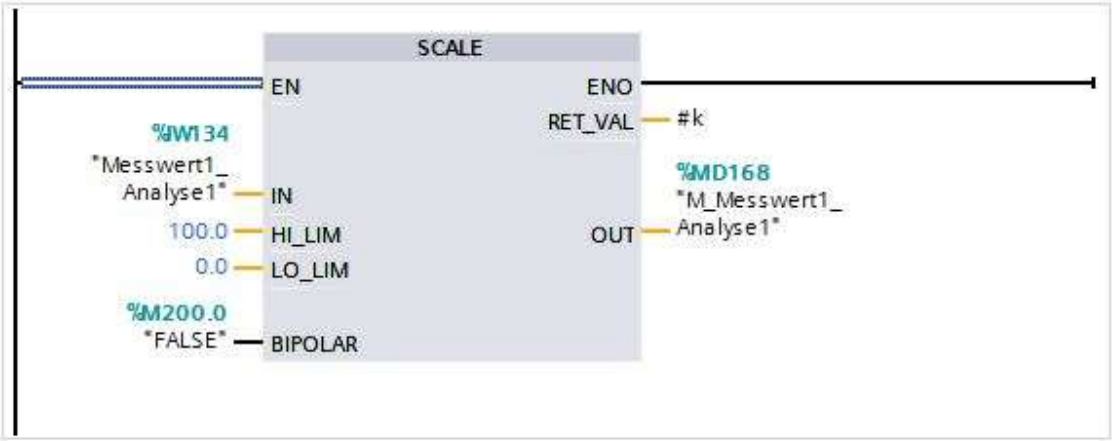

8.13 Function block of the pressure control circuit

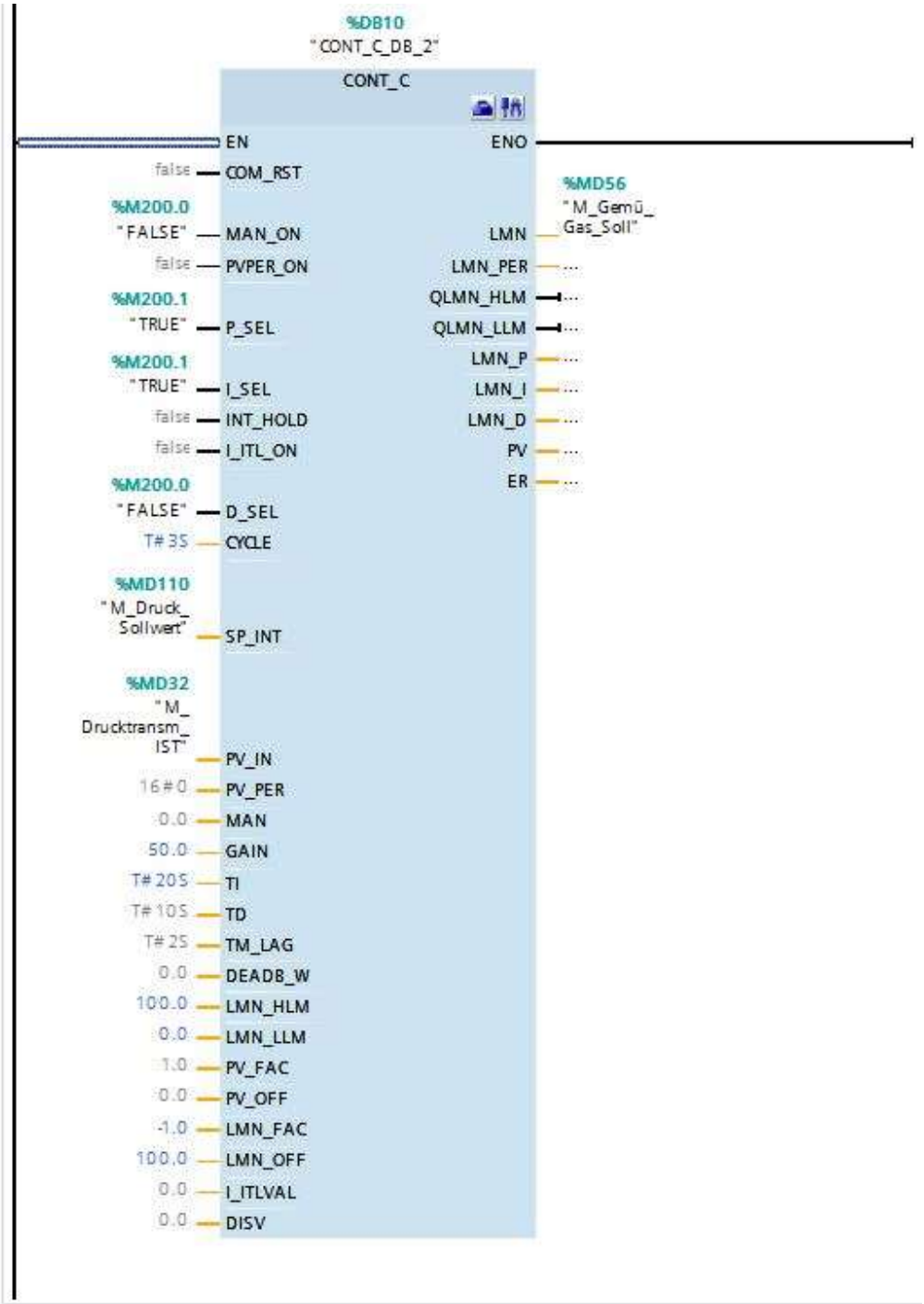

8.14 Program code of the Mass flow controller for CO_2

```
1
2  "M_MFC_CO2_SOLL" := "SP_out";
3  "d_SP" := ("SP_End" - "M_MFC_CO2_SOLL");
4  "Rampeup_hilfe" := "Rampeup_hilfe_out";
5  "d_SP2" := ("M_MFC_CO2_SOLL" - "M_MFC_CO2_IST");
6  "Rampedown_hilfe" := "Rampedown_hilfe_out";
7
8  IF "d_SP" > 0 THEN
9
10     "SP_out" := "SP_out" + ("d_SP" / 100000) + "Rampeup_hilfe_out" / 1000;
11     "Rampeup_hilfe_out" := "Rampeup_hilfe" + 0.0000001;
12
13 END_IF;
14
15
16 IF "d_SP" < 0 THEN
17     "SP_out" := "SP_out" + ("d_SP" / 100000) - "Rampedown_hilfe_out" / 1000;
18     "Rampedown_hilfe_out" := "Rampedown_hilfe" + 0.0000001;
19
20 END_IF;
21
22
23
24
25
26 #k := SCALE(IN := "MFC_CO2_IST_Eingang", HI_LIM := 48, LO_LIM := 0, BIPOLAR := 0, OUT => "M_MFC_CO2_IST");
27
28 #l := UNSCALE(IN := "M_MFC_CO2_SOLL", HI_LIM := 48, LO_LIM := 0, BIPOLAR := 0, OUT => "MFC_CO2_Soll_Ausgang");
29
```

8.15 Program code of the Mass flow controller for N_2

```
1
2  "M_MFC_N2_SOLL" := "M_MFC_CO2_IST" * 4;
3
4  IF "M_MFC_CO2_SOLL" < 0.1 THEN
5      ;
6      "M_MFC_N2_SOLL" := 0;
7
8
9  END_IF;
10
11 "Total Inlet flow gas to absorber" := "M_MFC_N2_IST" + "M_MFC_CO2_IST";
12 "Inlet _CO2 Concentration" := ("M_MFC_CO2_IST" / "Total Inlet flow gas to absorber") * 100;
13 "Inlet N2 Concentration" := ("M_MFC_N2_IST" / "Total Inlet flow gas to absorber") * 100;
14
15 #k := SCALE(IN := "MFC_N2_IST_Eingang", HI_LIM := 78, LO_LIM := 0, BIPOLAR := 0, OUT => "M_MFC_N2_IST");
16
17 #l := UNSCALE(IN := "M_MFC_N2_SOLL", HI_LIM := 78, LO_LIM := 0, BIPOLAR := 0, OUT => "MFC_N2_Soll_Ausgang");
18
19
20 "IEC_Timer_0_DB".TP(IN := "Rampe aktive",
21                     PT := "Time_in",
22                     Q => "Rampe-out",
23                     ET => "Time_out");
24 "Timer_in" := "Time_in" / 1000;
25 "Timer_out" := "Time_out" / 1000;
```

8.16 Program code of safety control circuit for the heater coil in the reboiler

```
1  "Heizung_Einschalten_Ausgang" := "M_Heizung_Einschalten";
2  "M_Heizung_Heizstatus" := "Heizung_Heizstatus";
3
4  IF "M_Heizung_Solltemperatur" - "M_Thermo6_IST" > 0.1 THEN
5      "M_Heizung_Einschalten" := "TRUE"
6      ;
7  END_IF;
8
9  IF "M_Heizung_Solltemperatur" - "M_Thermo6_IST" < 0.1 THEN
10     "M_Heizung_Einschalten" := "FALSE"
11     ;
12 END_IF;
13
14 IF "Heizung aus von Füllstandsüberwachung" = "TRUE" THEN
15     "M_Heizung_Einschalten" := "FALSE"
16     ;
17 END_IF;
18
19
20
21
22  "M_Achtung_Temperaturdifferenz_Reboiler_6_minus_7" := "M_Thermo6_IST" - "M_Thermo7_IST";
23  "M_Achtung_Temperautrdifferenz_Rebiler_7_minus_6" := "M_Thermo7_IST" - "M_Thermo6_IST";
```

8.17 Program code of MDEA make-up pump

```
1  "Dosierpumpe_MDEA" := "M_Dosierpumpe_MDEA";
2
3  #1 := UNSCALE(IN := "M_Dosierpumpe_MDEA_Sollwert", HI_LIM := 100, LO_LIM := 0, BIPOLAR := 0, OUT => "Dosierpumpe_MDEA_Sollwert");
```

8.18 Program code of water make-up pump

```
1  "Dosierpumpe_Wasser" := "M_Dosierpumpe_Wasser";
2
3
4  #1 := UNSCALE(IN := "M_Dosierpumpe_Wasser_Sollwert", HI_LIM := 100, LO_LIM := 0, BIPOLAR := 0, OUT => "Dosierpumpe_Wasser_Sollwert");
5
6
```